



UNIVERSIDAD DE GRANADA

Departamento de Química Orgánica y Farmacéutica

Programa de Doctorado en Farmacia (B15.56.1) en *Cotutela*

Escuela de Doctorado de Ciencias de la Salud

TESIS DOCTORAL

Título:

SUSTAINABLE SYNTHESIS OF BIOLOGICALLY ACTIVE MOLECULES

Autora:

Pilar María Luque Navarro

Directoras de la tesis:

Prof. Daniela Lanari and Luisa Carlota López Cara

Editor: Universidad de Granada. Tesis Doctorales
Autor: Pilar María Luque Navarro
ISBN: 978-84-1117-430-5
URI: <http://hdl.handle.net/10481/75971>

Acknowledgements.

I would like to thank my supervisors Prof. Luisa Carlota López Cara and Prof. Daniela Lanari, to bring me the possibility to follow the course of studies at this level. Their confidence has made me grow professionally and personally.

I would like to thank also to all the collaborators mentioned in this dissertation because of their patience and time to introduce me to multidisciplinary areas enriching the results herein exposed.

Difficulties and Covid-19 have tested me during these three years that now are worth, and I am glad to have found people opened and have learned so much of Italy and its culture.

I have to mention my family that, in the distance, has always supported me and trusted in me.

However, I want to highlight someone who has never left me apart, Filippo F. You always gave me the courage to believe in myself.

Thank you.

**“Behind the passion there are people
with the courage to try.”**

Table of contents.

Acknowledgements	3
Index of Figures	7
Index of Schemes	9
Index of Equations.....	9
Index of Tables	10
List of Abbreviations.....	11
Resumen.....	14
Overview	17
<i>Chapter 1</i>	19
Introduction	19
1. Choline Kinase as a therapeutic target for cancer.	19
2.1 Discovery and structure of the ChoK enzyme.....	21
2.2 The <i>Human</i> Choline Kinase structure and its mechanism.	22
3. Development-Timeline of the ChoK inhibitors.....	25
3.1 Derivatives of Hemicolinium-3.....	25
3.2. Different strategies based on SARs.	27
3.3. Inhibitors based on the crystal structure.	27
3.4. New approaches towards drug design from Academia to Pharma.	30
4. Biological effects of the inhibitors.....	32
5. The ChoK α involvement in other pathologies.....	33
Aims.....	38
Materials and methods	39
1. Synthesis of Choline Kinase inhibitors. General conditions.	39
2. Enzyme-based ChoK activity assays (IC ₅₀).	39
3. Computational studies.	40
4. Growth inhibition assay (GI ₅₀).	41
5. Physico-chemical studies.	41
6. Figures and Graphics.	42
Results and discussion.....	43
1. <i>Sustainable</i> Synthesis of Choline Kinase inhibitors.....	43
1.2. Optimization of the dithioethane and disulphide linkers.	45
1.3. Optimization of the final nucleophilic substitution.	47
1.4. Green metrics, quantification of sustainability.....	50
2. <i>HChoKα</i> enzymatic inhibition.	55
3. Modelling compound-protein interactions.....	60
3.2 Dithioethane library of compounds.....	61
3.3 Disulphide library of compounds.	67
3.4 Comparison between library's homologous and discussion.	72
4. Antiproliferative activity.....	73
5. Inhibitor's physical-chemistry properties in the PL library.	78
5.2 Absorbance and fluorescence spectra.	78
5.3 <i>FLIM</i> bioimaging on MCF-7 cells.....	82
5.4 In silico PAINS and pharmacodynamics assays.	84
Conclusions	86
Experimental part.....	87
1. Synthesized compounds characterization: ¹ H and ¹³ C NMR spectra, HRMS or Elemental Analysis, and melting point.	87

1.2	Procedure for the synthesis of the dithioethane linker:.....	87
1.3	Procedure for the synthesis of the disulphide linker.....	89
1.4	Procedure for the synthesis of the heads.....	90
1.5	General procedure A for the synthesis of the dithioethane final products.....	94
1.6	General procedure A for the synthesis of the disulphide final products.....	99
1.7	Bidimensional spectra HMBC and HSQC of Compound FP 16	103
1.8	Bidimensional spectra HMBC of Compound PL 54	105
1.9	Green metrics calculation.....	107
1.9.2	E-factor of the disulphide linker synthetic pathway.....	107
1.9.3	E-factor of the dithioethane linker synthetic pathway.....	108
1.9.4	E-factor of the diphenoxyethane linker synthetic pathway.....	108
1.10	Calculation with EcoScale.....	109
1.11	Crystallographic enzyme and search of pockets.....	113
1.12	Validation of the model.....	114
Chapter 2.....		116
Introduction.....		117
1.	Towards sustainability of processes.....	117
2.	Flow implementation in processes.....	118
3.	Heterogeneous catalyst in green chemistry.....	120
Aims.....		123
Material and methods.....		124
General conditions of synthesis.....		124
Results and discussion.....		125
1.	Green flow chemistry applied to pharmaceutical scaffolds.....	125
1.2	Optimization of the batch reaction conditions.....	126
1.3	Flow system implementation and optimized conditions.....	127
1.4	Plausible catalytic mechanism.....	128
1.5	Flow system regioselectivity and versatility.....	129
1.6	Big scale reaction and metal leaching.....	130
1.7	Green metrics comparison for batch and flow processes.....	131
Experimental part A: <i>Green</i> flow chemistry process.....		132
1.	Synthesis and characterization of the starting materials.....	132
2.	General procedure for the K-OMS-2 synthesis.....	136
3.	General procedure used in the batch reaction optimization.....	137
4.	General procedure used in flow synthesis and final products characterization.....	137
5.	Big scale flow procedure with solvent recirculation.....	140
6.	Analysis of the K-OMS-2 three-dimensional structure integrity after the catalytic reaction.....	141
7.	Calculation of the green metrics.....	142
Results and discussion:.....		144
2.	Development of sustainable synthetic pathways towards pharmaceuticals scaffolds of interest.....	144
2.2	Preliminary studies toward the manganese-catalyzed synthesis of isoquinoline-1,3,4,(2 <i>H</i>)-trione.....	145
2.3	K-OMS-2 reaction conditions optimization towards the synthesis of 11.....	149
Experimental part B: <i>Greenest</i> synthetic pathway towards pharmaceuticals scaffolds of interest.....		151
8.	Synthesis of the starting materials.....	151

9. General procedure of the optimization reaction.....	151
10. Optimized catalytic reaction with K-OMS-2 and final products characterization. .	152
Conclusions	154
Conclusiones	155
Appendix:	157
1. The search of the catalytic pocket.	157
2. The inhibitors' probability to adopt the pose.	159
3. Similarity and energetic values obtained by FLAP.	164
References.....	167

Index of Figures

Figure 1. Representation of the mutated ras protein bounded to the cell membrane (left) and the ChoK activation (right).	20
Figure 2. Kennedy pathway for the synthesis of phosphatidylcholine.	20
Figure 3. Catabolism products' of phosphatidylcholine that are involved in tumor survival.	21
Figure 4. Cristallografic structure of ChoK isolated in <i>C. elegans</i> . (<i>Left</i>) Dimeric form with detailed interface-region interactions. (<i>Right</i>) Monomer tertiary structure with N and C terminal domains from blue to orange. ²⁰	22
Figure 5. (I) Monomeric crystallographic structure of ChoK α 1 (<i>left</i>) and ChoK β (<i>right</i>) and their different conformational change in the catalytic site to place the HC-3 (α 9 and α 10 helices are in orange colour). (II) Conformational change in the N-terminal domain when the choline is phosphorylated. (III) Allosteric negative cooperativity and a broken symmetry between the monomers of the dimeric unit ²⁶	24
Figure 6. Ping-pong enzymatic mechanism of action proposed by Pollard <i>et al.</i> ²⁷	25
Figure 7. Hemicolinium-3 chemical structure in its open and cyclized forms.	26
Figure 8. FK-7 (<i>left</i>) and HC-15 (<i>right</i>) inhibitors of the first pharmacomodulation stage.	26
Figure 9. Screening of the most suitable heads (<i>up</i>) and linkers (<i>down</i>) structures.	26
Figure 10. Chemical structure of the hit to lead MN58b and TCD-717	27
Figure 11. Example of the triscationic (<i>left</i>), cyclophanes (<i>middle</i>) and biscyclophanes (<i>right</i>) structures.	27
Figure 12. ATP-mimicking inhibitors designed to bind both choline and ATP catalytic pockets.	28
Figure 13. ATP-mimicking derivatives of aminophenol and benzylthiopurine.	28
Figure 14. Asymmetrical biscationic compound's chemical structure	29
Figure 15. Bioisosteric inhibitors strategy. (<i>Left</i>) Compound 9h bioisoster of TCD-717 and (<i>right up</i>) compound 10a bioisoster of MN58b and (<i>right down</i>) 10l successfully improved the parent drugs potency	29
Figure 16. (<i>Left up</i>) Bioxazole derivate, (<i>left down</i>) JAS239 fluorophore chemical structure and (<i>right</i>) natural products derivatives from plants	30
Figure 17. Compounds developed using in-silico methods by Pharmaceuticals Companies and/or in collaboration with academia	32
Figure 18. Compounds that can inhibit the choline uptake through the membrane's transporter.	33
Figure 19. The cycle of infection and reproduction of the Plasmodium falciparum parasite. It is also highlighted the replication inhibition step due to the enzymatic inhibition of choline in the parasite	35
Figure 20. ChoK inhibitors used also as antimalarials	36
Figure 21. Compounds designed to selectively inhibit PfChoK	37
Figure 22. General structure of the new inhibitors	44
Figure 23. Disulphide linker E-factor (<i>left</i>) and EcoScale value (<i>right</i>) for the retrosynthetic pathway	51
Figure 24. Disulphide linker E-factor (<i>left</i>) and EcoScale value (<i>right</i>) for the green-by-design pathway	52
Figure 25. Dithioethane linker (green bar charts) and diphenoxyethane linker (blue bar charts) representation of calculated E-factor (<i>right part</i>) and EcoScale (<i>left part</i>) values for each synthetic step	53
Figure 26. Comparison between the dithioethane and disulphide library's homologous inhibitors.	58
Figure 27. Effect of the linker bioisosteric exchange in the inhibitory activity towards the ChoK.	58
Figure 28. Inhibitors' mainly interactions inside the catalytic pocket.	63
Figure 29. Inhibitors' mainly interactions inside the catalytic pocket.	64

Figure 30. Undocked compounds 70 , 72 and 67 . Compound 71 , an isoster of 67 , can be docked and is also doubly active than 67 .	66
Figure 31. Inhibitors' mainly interactions inside the catalytic pocket.	68
Figure 32. Inhibitors' mainly interactions inside the catalytic pocket.	70
Figure 33. Inhibitors' mainly interactions inside the catalytic pocket.	71
Figure 34. (<i>Left side</i>) Front of the choline and ATP catalytic site. (<i>Right side</i>) Back of the choline and ATP catalytic site.	72
Figure 35. Absorption spectra of compound PL 68 <i>left</i> and PL 54 <i>right</i> .	79
Figure 36. Fluorescence emission spectra of compound PL 68 dissolved in water (<i>left</i>) and dioxane (<i>right</i>) using the maximum absorption in water, 310 nm for excitation.	79
Figure 37. Fluorescence emission spectra of compound PL 54 dissolved in water (<i>left</i>) and dioxane (<i>right</i>) using the maximum absorption in water, 303 nm for excitation.	80
Figure 38. Absorption spectra recovered from the emission maximums for compounds PL 68 (<i>left</i>) and PL 54 (<i>right</i>).	80
Figure 39. Absorption spectra in dioxane of PL 68 (<i>left</i>) and PL 54 (<i>right</i>) with the laser employed in FLIM (375 nm) excite region indicated.	81
Figure 40. Compound PL 68 fluorescence emission spectra when excited at 375 nm (same wavelength of the used laser in FLIM).	81
Figure 41. PL 68 distribution on MCF-7 cells over the time.	82
Figure 42. Intensity profile of PL 68 in the cross-section of the cell over time.	83
Figure 43. Section of the cytosol selected for the PL 68 average intensity calculation (<i>at the top</i>). Bar chart with the obtained mean values (<i>right</i>).	84
Figure 44. Broadening of the aromatic region of the FP 16 HMBC spectra.	103
Figure 45. Broadening of the aliphatic region of the FP 16 HMBC spectra.	104
Figure 46. HSQC spectra of compound FP 16 .	104
Figure 47. Broadening of the aromatic region of the PL 54 HMBC spectra.	105
Figure 48. Broadening of the aliphatic region of the PL 54 HMBC spectra.	106
Figure 49. Catalytic pocket GRID MIFs.	113
Figure 50. The development of processes able to match both chemical performance and generate harmless by-products and waste for reuse.	117
Figure 51. Plausible catalytic mechanism.	128
Figure 52. Manganese leaching in flow.	130
Figure 53. E-factor of flow and batch procedures, with and without the recirculation of solvents.	131
Figure 54. X-ray diffraction path for K-OMS-2.	136
Figure 55. On the <i>left</i> , we report the XRD and HRTEM images of the fresh catalyst while on the <i>right</i> is reported the analysis of the used catalyst.	141
Figure 56. Representation of the yield obtained for each intermediate, while varying the employed amount of TBHP in decane (red) and water (blue).	147
Figure 57. Aligned crystallographic structures and their comparison to PDB: 3G15 (light blue color).	157
Figure 58. (<i>Left part</i>) Pocket designed by using the Flapsite algorithm and the poses of the docked HC-3 . (<i>Right part</i>) Pocket designed with Phe 361 merged with the latter and the poses obtained while docking the crystallographic ligand. The crystallographic ligand has yellow carbon atoms.	158

Index of Schemes

Scheme 1. Attempts for the synthesis of sulphur –containing linkers.	45
Scheme 2. Dithioethane linker synthetic pathway.	46
Scheme 3. Disulphide linker synthetic pathway.	46
Scheme 4. Yields of the final products obtained with the dithioethane linker.	48
Scheme 5. Yields of the final products obtained with the disulphide linker.	49
Scheme 6. Traditional (a) and proposed sustainable (b) procedure to achieve the brominated disulphide linker.	50
Scheme 7. Comparison of the bioisosteric linkers' synthesis.	53
Scheme 8. (Left part) cLog P of the linkers mainly used as part of the Choline Kinase inhibitors. (Right part) Bioisosteric changes in the linker.	65
Scheme 9. Dithioethane linker synthesis.	87
Scheme 10. The disulphide linker synthetic pathway.	89
Scheme 11. Assembly of the dithioethane library's final compounds.	94
Scheme 12. Assembly of the disulphide library's final compounds.	99
Scheme 13. Microfluidic flow protocol example for the synthesis of chemical libraries.	119
Scheme 14. Transformation of traditional on batch (a) towards the in-flow (b) synthesis of Cyclizine.	119
Scheme 15. Examples of the OMS-2 oxidation applications.	122
Scheme 16. Substrates scope using substituted aminophenols.	129
Scheme 17. Enzymatic substrates of HRP.	130
Scheme 18. Literature examples of the isoquinoline-1,3,4(2H)-triones synthesis.	144
Scheme 19. Proposed oxidative reaction when the salt 9a is used as starting material.	145
Scheme 20. Superimposed amino acid sequence of the Choline Kinase α 1 (PDB: 3G15) monomers A and B.	158

Index of Equations

Equation 1. E-factor calculation.	107
Equation 2. EcoScale calculation.	110

Index of Tables

Table 1. Optimization of the last synthetic step.	48
Table 2. Dithioethane (<i>at the top</i>) and disulphide (<i>at the bottom</i>) libraries' inhibitory activity and cLog P. Insoluble molecules are coloured in red.....	56
Table 3. Classification of the dithioethane library binding mode and reported S-score, IC ₅₀ and cLog P values for comparison.....	61
Table 4. Classification of the disulphide library binding mode and reported S-score, IC ₅₀ and cLog P values for comparison.....	67
Table 5. Dithioethane (<i>at the top</i>) and disulphide (<i>at the bottom</i>) libraries' antiproliferative activity. Insoluble molecules are coloured in red.	75
Table 6. Structural alert and PAINS of the synthesized libraries.....	85
Table 7. Summary of the EcoScale values calculation for the synthetic pathway 1.	110
Table 8. Summary of the EcoScale values calculation for the synthetic pathway 2.	111
Table 9. Summary of the EcoScale values calculation for the dithioethane linker synthetic pathway.....	111
Table 10. Summary of the EcoScale values calculation for the diphenoxyethane synthetic pathway.....	112
Table 11. Model A and B scores (up table), and probabilities of getting the correct (carbon atoms in pink color) or incorrect (carbon atoms in blue color) pose for the crystallographic ligand HC-3 (carbon atoms in yellow color).....	115
Table 12. Screening of the parameters in batch.	126
Table 13. Screening of oxygen pressure and concentration in flow.	127
Table 14. Conditions optimization for the further oxidation of 9a using Mn-based catalyst... 146	
Table 15. Oxidation of the bromide benzyl isoquinolinium salt (9b), under the same reaction conditions.....	147
Table 16. Optimization of the reaction conditions with the K-OMS catalyst.....	149
Table 17. Main poses obtained for the dithioethane library.	161
Table 18. Main poses obtained for the disulphide library.	164
Table 19. S-score, MIFs, and energetic values for the dithioethane compounds library.	165
Table 20. S-score, MIFs and energetic values for the disulphide library of compounds.	166

List of Abbreviations

2-MeTHF 2-Methyltetrahydrofuran

A

AA Arachidonic acid

ADME Absorption, Distribution, Metabolism, and Excretion

AE Atom economy

AIBN Azobisisobutyronitrile

AMPK AMP-activated protein kinase

API Active Pharmaceutical Ingredient

B

BBB Blood Brain Barrier

BPR Back pressure regulator

C

CCT Choline cytidyltransferase

CDP-Cho Cytidine 5'-diphosphocholine

ChoK Choline Kinase

CHT High-affinity choline transporter

CKA-2 *Caenorhabditis elegans* ChoK

CMP Cytidine monophosphate

CPME Cyclopentyl methyl ether

CPT Choline phosphotransferase

c-Src Tyrosine-protein kinase

CTL Choline transporter-like protein

CTP Cytidine triphosphate

D

DAG Diacylglycerol

dbp Dibenzoyl peroxide

dc Decomposition melting point temperature

DIBAL Diisobutylaluminum hydride

DIPEA N,N-diisopropylethylamine

DMAP 4-Dimethylaminopyridine

DMC Dimethyl carbonate

E

E-factor Environmental-factor

EGFR Epithelial Growth Factor Receptor

ENM Elastic Network Model

ES- Electrospray negative ion

ES+ Electrospray positive ion

F

FID Flame Ionization Detector

FLIM Fluorescence-Lifetime Imaging Microscopy

FLS Fibroblast-like synoviocytes

FT-IR Fourier Transform Infrared

G

GC-EIMS Gas Chromatography-Electron Impact Mass Spectrometer

GI Gastrointestinal

GLC Gas-Liquid Chromatography

GVL Gamma-Valerolactone

H

HBV Hepatitis B virus

HC-3 Hemicolinium-3

HDT Host-directed therapy

HMBC Heteronuclear Multiple Bond Correlation

HRP Horseradish peroxidase

HRTEM High-resolution Transmission Electron Microscopy

HSQC Heteronuclear Single Quantum Coherence

HTS High Throughput Screening

L

Log P Partition coefficient

LPA Lysophosphatidic acid

LTA Lipoteichoic acid

M

MAPK Mitogen-activated protein kinase

MD Molecular Dynamics

MOF Metal organic framework

MP-AES Microwave Plasma-Atomic Emission Spectrometers

MP-AES Microwave Plasma-Atomic Emission Spectrometers

MRS Magnetic Resonance Spectroscopy

MTBE Methyl tert-butyl ether

mTORC1 Mammalian target of rapamycin complex 1

MW Microwave

N

NBS N-Bromosuccinimide

NHC N-heterocyclic carbene

NIR Near Infrared

O

OCT Organic cation transporter

OCTN Organic cation/carnitine transporter

OMS Octahedral Molecular Sieves

P

PA Phosphatidic acid

PAINS Pan Assays Interference Structures

PAP Phosphatidic acid phosphohydrolase

PBS Phosphate-buffered saline

PCho Phosphocholine
PE Phosphatidylethanolamine
PET Positron emission tomography
PfChoK Plasmodium falciparum Choline Kinase
Pgp Permeability glycoprotein

PI3K/AKT Phosphatidylinositol 3-kinase

PIDA Phenyl iodine (III) diacetate

PLA2 Phospholipase A2

PLD Phospholipase D

PLimC Poly(limonene carbonate)

PPi Diphosphate

psi Pounds per square inch

PtdCho Phosphatidylcholine

PTFE Polytetrafluoroethylene

Q

QSAR Quantitative Structure Activity Relationship

R

ROS Reactive oxygen species

RSMD Root Mean Square Deviation

S

SARs Structure Activity Relationships

shRNA Short hairpin RNA

SM Sphingomyelin

S_N2 Nucleophilic substitution of second order

spp. Species

ST NMR Saturation Transfer Nuclear Magnetic Resonance

T

TAME Tert-Amyl methyl ether

TBHP Tert-butyl hydroperoxide

TCD-717 or *RSM-932A* are the same compound if search in literature.

tCho Total choline or choline-containing lipids

TEMPO 2,2,6,6-Tetramethylpiperidin-1-yl)oxyl

TLC Thin Layer Chromatography

TOF Turnover frequency

TON Turnover number

TPQ Triterpene quinone methide

V

VOCs Volatile Organic Compounds

W

WHO World Health Organization

X

XRD X-Ray Diffraction

Resumen

En la presente tesis doctoral se pone en valor el desarrollo de procesos químicos que sean sostenibles ambientalmente para la obtención de moléculas con interés farmacológico. La química verde surge de la necesidad de reducir residuos y vertidos contaminantes que pongan en riesgo ecosistemas y ríos. Sobre todo, las industrias farmacéuticas generan una gran cantidad de vertidos debidos en parte por la complejidad de los procesos sintéticos multistep que se requieren para producir APIs. Los doce principios de la química verde propuestos por Anastas y Warner en 1998 establecen como llevar a cabo el cambio hacia procesos más sostenibles. Dichos principios se basan en la reducción de sustancias auxiliares, como disolventes, la sustitución de reactivos que sean peligrosos o tóxicos por otros inocuos, en el uso de catalizadores, en la reducción de la energía necesaria y de los residuos generados y en el uso de compuestos biodegradables que cumplan su función pero que no sean persistentes en el ambiente.

Por ello, en la presente tesis hemos diferenciado dos capítulos en los que hemos implementado estos principios cuando ha sido posible, diseñando en primer lugar inhibidores de la Colino Cinasa ampliamente estudiados como compuestos antiproliferativos y sintetizándolos de manera sostenible (green-by-design), y en segundo lugar mejorando el proceso de síntesis de estructuras constituyentes de fármacos ya comercializados, usando procesos catalíticos más sostenibles e incorporando la química en fujo.

En el primer capítulo, además de un detallado análisis de la ruta sintética desarrollada y de las métricas verdes (E-factor y EcoScale) que garantizan una comparación objetiva entre procesos, se ha estudiado la efectividad de dos librerías de compuestos como inhibidores de la enzima Colino Cinasa. Dicha enzima ha suscitado interés en investigación como diana terapéutica debido a su sobreexpresión en células tumorales. Se encuentra en el citosol y está involucrada en el primer paso de la ruta de Kennedy catalizando la conversión de la colina a fosfocolina usando Mg^{2+} y ATP como cofactores. Debido al mayor requerimiento de lípidos de membrana y agentes mensajeros en las células tumorales, la inhibición de la Colino Cinasa se plantea como una estrategia para el tratamiento del cáncer de manera más selectiva.

Se han sintetizado dos librerías de compuestos bioisotéricos que se basan en estructuras ya testadas por nuestro grupo de investigación, pero con la introducción de átomos de azufre en el enlazador que une dos aminos cuaternarias cargadas positivamente. La librería **PL** contiene un puente ditioetano y la **FP** un puente disulfuro.

La actividad inhibitoria en la enzima aislada y el estudio de su posible modo de unión en el sitio catalítico, han desvelado dos compuestos como líder, **PL 55** y **FP 3**, ambos con un tiano [2,3-d] pirimidina sustituida en la posición 4 con azepano. El modo de unión de la librería **PL** parece estar correlacionado con su capacidad para desplazar los átomos de Mg^{2+} o crear impedimento estérico en su lugar de unión inhibiendo la catálisis enzimática. Los compuestos **FP** más rígidos y pequeños muestran una mayor inserción en el sitio de la colina lo que les confiere mayores valores de S-score (similaridad) a nivel computacional.

Sin embargo, es la actividad frente a líneas tumorales la que determina su capacidad para atravesar la membrana plasmática y actuar sobre la enzima en cuestión. En este caso, la librería **PL** resultó ser más activa en la inhibición del crecimiento en células neoplásticas mientras que la librería **FP** es menos eficaz posiblemente debido a la ruptura del puente disulfuro.

Además, debido a la naturaleza electrónica de los compuestos **PL**, el candidato **PL 68** presentó una emisión de fluorescencia suficiente para su posible seguimiento in vitro usando FLIM. Este ensayo fue determinante para corroborar un doble modo de acción, sea a través de la inhibición de transportadores de la colina (dada su acumulación en la membrana), que a su efectiva inhibición enzimática dada su acumulación con el tiempo en el citosol.

Los compuestos diseñados también fueron usados en un screening in-silico, para detectar posibles estructuras interferentes (PAINS) que pudieran dar lugar a una respuesta biológica inespecífica. De hecho, el puente disulfuro y la amina cuaternaria resultaron inadecuados. El primero podría ser fácilmente metabolizado, mientras que el segundo, a pesar de su mayor reactividad y la posibilidad de formar agregados, es indispensable para la unión selectiva al enzima en el sitio de la colina.

Sus propiedades farmacocinéticas, preliminarmente obtenidas in-silico, mostraron una adecuada absorción en el tracto gastrointestinal en general, pero poca solubilidad en el caso de los compuestos líder.

Por tanto, en base a los estudios realizados, esfuerzos futuros irán dirigidos hacia la síntesis de compuestos con puentes ditioetano que además de ser obtenidos con bajo impacto ambiental tengan una actividad selectiva por la enzima Colino Cinasa y buenas propiedades ADME que garanticen su futuro desarrollo en ulteriores fases clínicas.

En el segundo capítulo de la tesis, el objetivo no es la síntesis de un fármaco novedoso sino mejorar el proceso de síntesis mediante el cual se obtienen estructuras de interés farmacológico ya definido. De esta forma, se pretende potenciar el uso de metodologías más sostenibles que mejoren la síntesis y reduzcan la gestión de residuos, lo que se traduce en un menor coste del proceso.

La temática principal se basa en la implementación de catalizadores heterogéneos a base de Manganeseo, en concreto catalizadores de óxido de manganeseo con estructura del tipo criptomelano (OMS-2). Su heterogeneidad y baja lixiviación los hace idóneos para su implementación en la industria farmacéutica debido a su poca citotoxicidad, a la abundancia y al bajo coste de este material. Además, este catalizador ha sido ampliamente utilizado en reacciones de oxidación, descomposición, y condensación oxidativa.

En la presente tesis, se estudia la aplicación de dicho catalizador como alternativa a reacciones enzimáticas llevadas a cabo por oxidasas y peroxidasas (como las enzimas Lacasa o HPR), que dan lugar a la formación de fenoxacinas y fenacinas a partir de 2-aminofenol, o-fenilendiaminas y sus derivados. Estas estructuras se encuentran presentes en una gran variedad de fármacos como agentes quimioterapéuticos y antibióticos.

Basándonos en estudios previamente desarrollados por los colaboradores del Departamento de Química de la Universidad de Perugia, hemos optimizado las condiciones de reacción con el catalizador en baño, usando diferentes solventes considerados sostenibles, diferentes atmósferas (inerte u oxidante), temperatura y tiempo que diesen lugar a la conversión cuantitativa del producto final.

Después, se desarrolló un sistema en flujo en el que la fuerza motriz era un flujo de oxígeno que guiaba al producto de partida, previamente disuelto en CPME junto al peróxido de hidrógeno, a través del sistema. Una vez alcanzado el reactor, donde estaba empaquetado el catalizador y que se mantiene la temperatura optimal (50 °C), tiene lugar la C-H activación/dimerización, obteniendo el producto final en el tubo colector con rendimientos cuantitativos.

En esta fase se optimizaron la presión (bar) de la bombona de oxígeno, el tipo de regulador contrapresión (psi) y la concentración del producto de partida en disolución, para conseguir un tiempo de retención suficiente en el reactor para la total conversión del producto de partida.

El sistema resultó eficaz usando 5 bar de oxígeno, un regulador contrapresión de 75 psi y una concentración de 2-aminofenol de 0.5 M, obteniendo el producto final en 30 min. Concentraciones superiores de producto de partida dieron lugar al envenenamiento y obturación del catalizador.

La regio-selectividad del catalizador en esta transformación se evaluó mediante el ensayo con derivados del 2-aminofenol en orto, para y N-sustituídos. El catalizador mostró selectividad por la sustitución en orto independientemente de la naturaleza electro -donadora o -aceptora del sustituyente.

Otros productos de partida, substratos de la enzima HPR, se usaron para corroborar la capacidad de OMS-2 de mimar la reacción enzimática. O-fenilendiaminas y pirogalol fueron convertidos satisfactoriamente en fenazinas y purpurogalina, respectivamente. Solo el producto de partida 2-amino-3-hidroxipiridina no mostró reactividad.

También se evaluó la capacidad del sistema para producir a gran escala, en este caso de modo continuo, y de recuperar su estructura cristalina gracias al flujo de oxígeno, permitiendo su reutilización. Además, se analizó la lixiviación que con el tiempo se estabilizó a 0.17 ppm y garantizó la recirculación del disolvente utilizado en el sistema.

Los cálculos de E-factor, AE, TON y TOF confirmaron la competitividad del sistema en flujo y del catalizador utilizado frente a otros procesos usados en literatura.

En una segunda parte dentro de este capítulo, decidimos estudiar la capacidad del OMS-2 para oxidar isoquinolinas a isoquinolinones. Al usar como producto de partida la sal, yoduro de 2-metilisoquinolina, se observó la formación de tres productos principales, la 2-metil isoquinolinona, la 4-iodo-2-metil isoquinolinona y la 2-metilftalimida. La facilidad para derivatizar la 4-iodo-2-metil isoquinolinona y obtener una amplia gama de productos químicos de interés, nos llevó a la optimización de la reacción para lograr una mayor selectividad.

Usando como oxidante el TBHP en decano en lugar de al 70% en agua, no se formaba ftalimida como subproducto. Se probaron diferentes oxidantes a base de iodo, temperaturas y tiempos de reacción. Otras sales y medios de reacción dieron lugar a conversiones más bajas, siendo la reacción sin disolvente la mejor opción.

A pesar de la implementación de condiciones de reacción catalíticas, sin disolvente y al uso de temperatura y tiempo moderados, la reacción siempre formaba la 4-metilisoquinolinona como subproducto. Debido a la necesidad de la separación mediante cromatografía del derivado iodado y al moderado rendimiento de la reacción en comparación con otros procesos descritos en literatura, decidimos concluir el estudio. De hecho, ulteriores pruebas se podrían llevar a cabo con OMS-2 dopados o con H⁺-OMS-2 obtenido mediante intercambio iónico, que potenciasen su capacidad oxidativa dando lugar a una completa conversión de la sal.

Overview

The herein exposed dissertation is conceived based on the implementation and use of Green Chemistry.

The increased interest in this branch of chemistry has involved not only academia but also companies that are required to be more environmentally sustainable. The urge to reduce the environmental impact of the chemical processes and consequently the pollutions sources related to them has prompted the scientific community to define new greener methodologies for the synthesis of fine chemicals, pharmaceuticals and polymers.

In a chemical process, the parameters that have to be carefully optimized from a point of view of sustainability are the chemical efficiency, amount and origin of the solvents, reaction conditions (e.g. temperature and pressure), the need and the number of purification steps, and the over stoichiometric use of reagents and promoters.

The present work aims to develop novel synthetic protocols for the synthesis of biologically active molecules able to minimize energy misuse and waste production.

This PhD thesis is divided into two chapters connected by the common green approach to the synthesis of molecules of pharmaceutical interest. In *Chapter 1*, two libraries of antiproliferative drugs were synthesized using a green by design approach. A thorough study of their biological efficacy in cells and their Structure-Activity-Relationships (SARs) have been evaluated.

On the other hand, in *Chapter 2*, well-known drug scaffolds were synthesized using innovative and greener procedures. In particular, the use of Manganese OMS-2 as heterogeneous catalyst in C-H activation and oxidative reactions was exploited. Its reusability and low leaching allowed the integration of such system into a flow apparatus.

The multidisciplinary scenario in which this thesis has evolved is mostly thanks to our collaborators.

In *Chapter 1*, the biological assays (enzyme inhibition and cell growth proliferation) were carried out by Prof. María Paz Carrasco Jiménez of the Department of Biochemistry in the Faculty of Sciences at the University of Granada. The fluorescence spectra and the use of FLIM equipment were as well the main work of the PhD. Laura Espinar Barranco, who set up the experiment to be recorded.

In *Chapter 2*, the first part was developed hand in hand with Dr Francesco Ferlin and under the supervision of both Prof. Vaccaro of the Department of Chemistry, Biology and Biotechnology at the University of Perugia and my PhD supervisor Prof. Lanari. However, while I was responsible for the synthesis of starting materials to be tested, Dr Ferlin designed the flow system and set up conditions for its use.



SUSTAINABLE SYNTHESIS OF CHOLINE KINASE INHIBITORS

Chapter 1

Introduction

1. Choline Kinase as a therapeutic target for cancer.

One of the most studied disorders in research is the abnormal cell growth, generally known as cancer. It affects worldwide and like the latest WHO report collects, in 2018, 18.1 million of new cases and 9.6 million of deaths due to cancer were estimated.¹

Responsible for one in six deaths globally, the predicted global burden is not promising. According to the United Nations projections, based on population growth and ageing, in 2040 about 29–37 million new cancer cases will be diagnosed.

These numbers are also a reflection of the urgent need for investment and effort to take this disease under control.

A lot of progress has been done in the study of the biological changes that cancer produces, to design pharmaceutical strategies able to interrupt its development and ultimately induce apoptosis in neoplastic cells. The origin of this condition seems to reside in personal genetic factors and their behaviour when interacting with external agents as physical carcinogens (UV or ionizing radiation), chemical carcinogens (e.g. components of tobacco smoke) and biological carcinogens (infection from certain viruses, bacteria, or parasites).

Even if the cellular machinery is able to fix the effects of those agents, with ageing the cellular repair mechanisms are less effective and the risk increases.

Cancer cells follow several strategies that allow their survival and rapid growth. Differences in their metabolism regarding normal cells surged as an opportunity to develop selective therapies with fewer side effects than the current chemotherapy. In tumours, there is an upregulated consumption of glucose, amino acids, and lipids to compensate for the energetic requirements and synthesize proteins and membranes, respectively. The inhibition of the enzymes that regulate the synthesis or conversion of such substrates arises as a great therapeutic target. For example, there are strategies like the use of antimetabolites that inhibits the activity of enzymes involved in nucleotide base synthesis to produce DNA damage or the inhibition of *de novo* synthesis of fatty acids and phospholipids used by neoplastic cells.²

The latter is the object of our study. Numerous articles highlight the presence of high choline and choline-containing lipids (tCho) levels in different cancer types. It can be effectively measured using non-invasively techniques like PET (Positron emission tomography) and MRS (Magnetic Resonance Spectroscopy).^{3,4} The choline phenotype has become a common fingerprint observed in breast, prostate, bladder, colon, and lung tumorigenic cells.⁵ However, the importance of lipids was not only due to their role as membrane building blocks but also are mitogenic agents and second messengers.

One of the biological origins of this lipidic disorder has been assigned to the proto-oncogene Ras.⁶ The Ras gene encodes for ras proteins, a family of GTPases, that are in charge of the transduction of the extracellular signals in an intracellular response.

They regulate cell growth, cell motility, metabolism, and communication (through secretion of microvesicles and exosomes) by an “on” - “off” state.

Those proteins get attached to the plasmatic membrane where they receive the extracellular signal and activate the intracellular downstream. When the signal is suppressed, the “on” GTP-bound state of the ras proteins change to the “off” GDP-bound state. The proto-oncogene Ras and the mutated ras proteins can't regulate the cell growth due to the permanent GTP bound

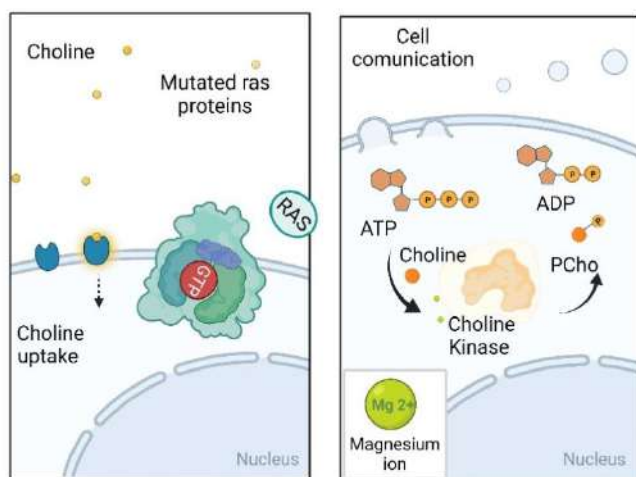


Figure 1. Representation of the mutated ras protein bounded to the cell membrane (left) and the ChoK activation (right).

state, being unable to *switch off* the cell growth signal.⁷ The constant cellular demands have proven to upregulate the Choline Kinase (ChoK) expression to supply the need for membrane lipids (Figure 1).

Lacal *et al.*,⁸ first observed the deregulated synthesis of phosphatidylcholine in tumoral cells and point out the ChoK as a therapeutic target for chemical inhibition⁹.

The ChoK is a cytosolic enzyme and belongs to the family of phosphotransferases. There are three isoforms of the human ChoK, the ChoK α 1 (457 residues), the

ChoK α 2 (439 residues), both encoded by splicing of the *choK- α* gene, and the ChoK β (395 residues) originate by the *choK- β* gene. The α and β isoforms are expressed in different tissues, and in spite of their catalytic site homology (higher than 60%) the β isoform is selective for the ethanolamine and is not involved in cell transformation and cancer development, while the α isoform can carry out the phosphorylation of both choline and ethanolamine.¹⁰ In the physiological media the ChoK is not active as a monomer, instead, it is found as a dimer or a tetramer.

The ChoK catalysed the phosphorylation of choline in the first step of the Kennedy route, with the ATP and Mg²⁺ as cofactors, and produces phosphocholine (PCho) (Figure 2). Then, the PCho is transformed in cytidine 5'-diphosphocholine (CDP-Cho) by the enzyme choline phosphate cytidyltransferase (CCT). The latter constituted the rate-limiting step and is accomplished through the dephosphorylation of the CTP. Finally, the CDP-Cho suffer the substitution of the cytidine monophosphate by DAG (1,2-*sn*-diacylglycerol) giving room to phosphatidylcholine (PtdCho), which is mediated by the enzyme diacylglycerol choline phosphotransferase (CPT).¹¹

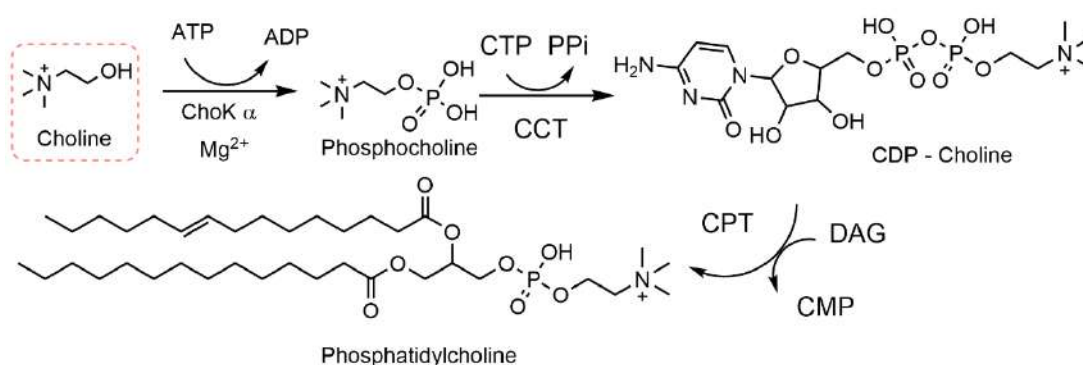


Figure 2. Kennedy pathway for the synthesis of phosphatidylcholine.

In fact, the proposed strategy suggests the inhibition of the first link in the Kennedy route that will lead to lower levels of PtdCho. It has two important effects, the decrement of scaffolding building blocks for the cellular membrane and of mitogenic second messengers from the PtdCho catabolism (Figure 3). For example, it is highlighted the role that the phosphatidic acid, produced by the phospholipase D (PLD) hydrolysis, has as a growth factor.¹² The latter could still be deacetylated by the phosphatidic acid phosphohydrolase (PAP) giving room to DAG or by the phospholipase A2 (PLA2) generating lysophosphatidic acid (LPA) and arachidonic acid (AA). Both

of them DAG and LPA, mainly working as lipidic metabolites with mitogenic activity due to the activation of protein kinase C (that ultimately induces DNA synthesis).¹³

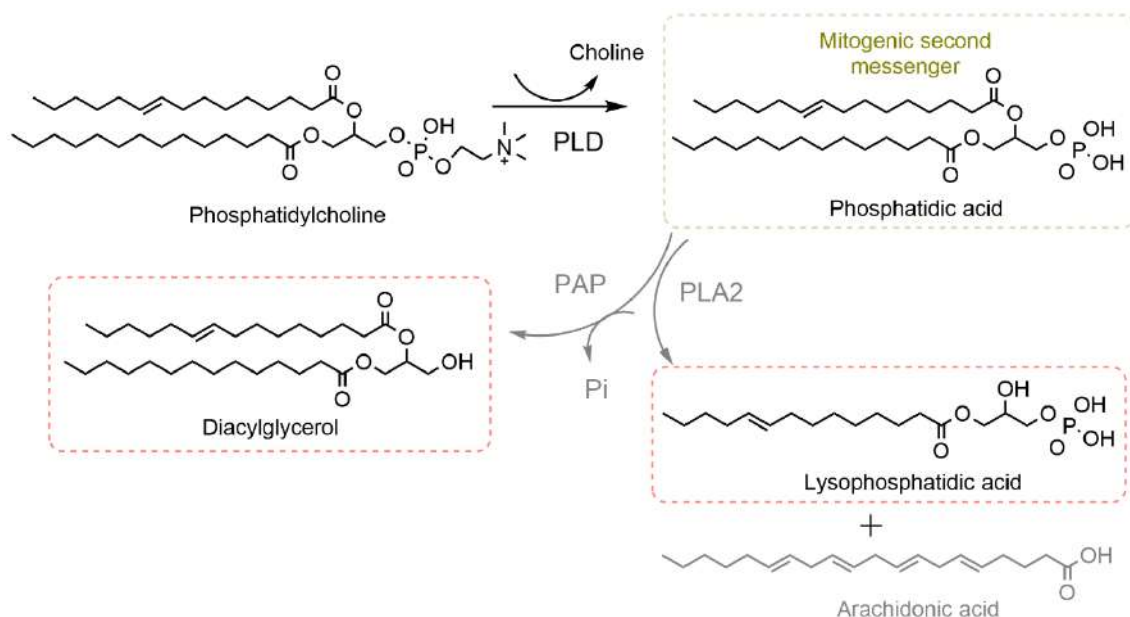


Figure 3. Catabolism products' of phosphatidylcholine that are involved in tumor survival.

To further support the focus on the ChoK α inhibition, it was assayed the influence that its depletion had on normal and tumoral cells. Studies confirmed that the specific blockage of the ChoK α signalling using shRNA (short hairpin RNA) caused apoptosis in tumoral cells and an arrest of the cell cycle in the non-tumoral cell of the same type.¹⁴ In addition, the overexpression of ChoK α in normal cells is a sufficient condition to promote neoplastic transformation.^{15,16} Actually, in breast cancer cells the ChoK enzyme is 38% overexpressed, and the concentration of PCho is 26 times higher in comparison with normal cells of the same tissue. As well, in prostate tumoral cells, ChoK is 48% overexpressed and the production of PCho is 19 times higher than in normal prostate cells.^{4,17}

All this evidence is enough to affirm that the ChoK is a valid therapeutic target, and its inhibition is a more selective antitumoral strategy than chemotherapy.

2.1 Discovery and structure of the ChoK enzyme.

Wittenberg and Kornberg first isolated the enzyme Choline Phosphokinase from yeast in 1952. They first evaluated the kinetics of the phosphocholine transformation and determined the formation of a ternary complex between choline, ATP, and the enzyme, suggesting a random Bi Bi catalytic mechanism. Meaning that each substrate (choline and ATP) can bind the catalytic pocket and release it without an established order. Their study also arose light to the hypothesis that the phospholipid's precursors were nitrogen bases (as choline and ethanolamine) instead of phosphoesters.¹⁸ At the time, it was already established the importance of the Mg²⁺ ions for the catalysis, which form a complex with the ATP stabilizing it in the catalytic site. However, the isolation and purification of the ChoK enzyme from the yeast of brewer was difficult and the enzyme could suffer from proteolysis giving room to difficult reproducible results.^{19,20}

Nevertheless, with the increasing interest of the human ChoK as an antitumoral target, new models were studied to try to understand the way the enzyme works. Due to the easy purification of the *Caenorhabditis elegans* ChoK (CKA-2) expressed in *E. coli*, it was first crystallized to understand the structural characteristics of the enzyme and the mechanism of its catalysis (PDB: 1NW1).²¹ In that way, the well-studied and conserved regions identified in other

transferases like the Aminoglycoside 3'-Phosphotransferase and c-AMP Protein Kinase, were also localized in the CKA-2 structure. Thus, it was identified the phosphotransferase Brenner's motif, that forms the ATP binding site, and the choline kinase motif characteristic of the choline/ethanolamine kinase family.

It was also verified the dimeric nature of the choline kinase and characterized the dimer interface mostly stabilized by salts bridges, hydrogen bonds and to a lesser extent by hydrophobic interactions, between the two alpha helices (Figure 4, left). However, it was still unknown the catalytic role that the amino acids played in the Brenner and choline pockets.

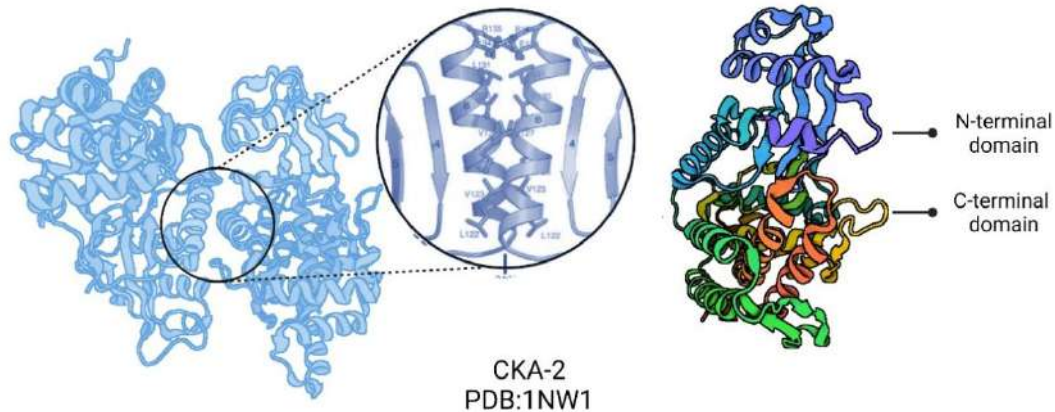


Figure 4. Cristallografic structure of ChoK isolated in *C. elegans*. (Left) Dimeric form with detailed interface-region interactions. (Right) Monomer tertiary structure with N and C terminal domains from blue to orange.²¹

Kent and Yuan's group carried out mutagenesis studies over CKA-2.²² They recognized the role of key residues, which was essential for the development of a *Human* homology model of the Choline Kinase.²³

For example, it was observed that the Asp305 was necessary for the deprotonation of the incoming hydroxyl group of the substrate. Arg145 and Ser120 were responsible for binding with the ATP phosphate groups, while Asn310 and Asp329 were involved in binding to the ATP-Mg complex via coordination with the Mg^{+2} ions. The mutation of those residues was translated into a lack of catalytic activity and improved the understanding of the enzymatic model existing at that moment.

2.2 The *Human* Choline Kinase structure and its mechanism.

All the structural data already available, and the CKA-2 crystal structure served as a guideline to the consolidation of the Human ChoK α 2 crystal.²⁴ The difference between the ChoK isoforms α 1 and α 2, reside in a sequence of 18 amino acids missing in the latter. However, those residues do not take part in the conformation of the catalytic pockets.

The HChoK α 2 was crystallized in its apo form (PDB: 2CKO) and as a complex with ADP and PCho catalysis products (PDB: 2CKP and PDB: 2CKQ, respectively). It was confirmed that each monomer of the dimeric enzyme, was constituted by two main domains. A smaller N-terminal domain and a larger C-terminal domain are connected by a short β -strand. Residues of both N and C-lobes form a large cavity where the nucleotide (ATP or ADP) binds at the N-terminal domain. Howbeit the choline-binding site was placed in a hydrophobic groove with a rim composed of negatively charged residues in the C-terminal domain.

As so the ATP binding site was mainly constituted by interactions in which the adenine rest of ADP or ATP was stabilized by H-bond with Glu206, Gln207 and Ile209, by hydrophobic interactions with Leu144 and Leu313, and by π - π interaction with Phe208. The ribose also interacts with the active site by H-bonds (Ser211 and Arg213) and hydrophobic interactions

(Leu124 and Leu313). Finally, the phosphate groups are mainly recognized by the enzyme through H-bond with residues Arg117, Asn122 and Arg146, and metals bonds by coordination with the two Mg^{+2} ions.

Potential structural roles of some residues near the nucleotide binding site were highlighted for *Arg117* that pointed toward the β -phosphate thereby positioning the nucleotide for enzymatic catalysis and *Asp330* that participate directly in the coordination of the magnesium ions.

The choline pocket was constituted by hydrophobic residues as Tyr333, Tyr354, Trp420, Trp423, Tyr440 and Phe435, with whom the substrate could establish π -cation interactions and the positive charge was also stabilized by negative residues as Glu215, 217, 218, 309, 349, 357, 434 and Asp353, 306.

The crystals of the ChoK α 1 and ChoK β in complex with the HC-3 inhibitor arrived in 2010 (PDB: 3G15 and PDB: 3FEG, respectively).²⁵ They constituted the first crystals in complex with a ChoK inhibitor and supported the hypothesis of a binding mode similar to the choline substrate. The biscationic HC-3 was observed in the choline pocket mainly interacting with one oxazinium ring while the other remained exposed to the solvent.

Interestingly, the inhibitor was phosphorylated when crystallized in the ChoK β isoform, even if it showed a less binding affinity for it. The reason for this behaviour was that the steric hindrance caused when the HC-3 was binding the β isoform gives room to a flip out of the loop connecting helices α 9 and α 10. This affected the overall contact of the protein with the inhibitor molecule, giving an extra space where the HC-3 opened conformation fixes better and was easily attacked for phosphorylation. The ChoK α isoform, instead, is able to hold the inhibitor due to the more flexible residues (Leu419 in α 1 and Phe352 in β).

As usually observed in the kinase family the conformational changes of the tertiary structure regulate the catalytic activity, and it was also evidenced in the ChoK.

The N-terminal domain changed its orientation from an open to a close conformation when was in complex with the PCho.²⁴ In that way, the choline substrate enters the active site when the N-terminal domain is opened and once phosphorylated the N-lobes turn out to the close conformation (Figure 5, I and II).

This open-close regulatory mechanism was further studied. Using MD (Molecular Dynamics) and ENM (Elastic Network Model), it was observed an allosteric negative cooperativity and a broken symmetry between the monomers of the dimeric unit. For that study, it was used the inhibitor 1 able to interact with both the choline and the ATP binding sites (Figure 5, III). This inhibitor first binds to one monomer, reducing the binding at the active site of the coupled monomer, due to a conformational change that goes through the dimeric interface to the catalytic site of the second monomer. The two monomers alternatively assume an open/semi-open or closed state with a fast interconversion rate, recovering on average the symmetry. In the open conformation, there are more water molecules inside the catalytic site that make the binding of the inhibitor to the choline pocket less effective.²⁶

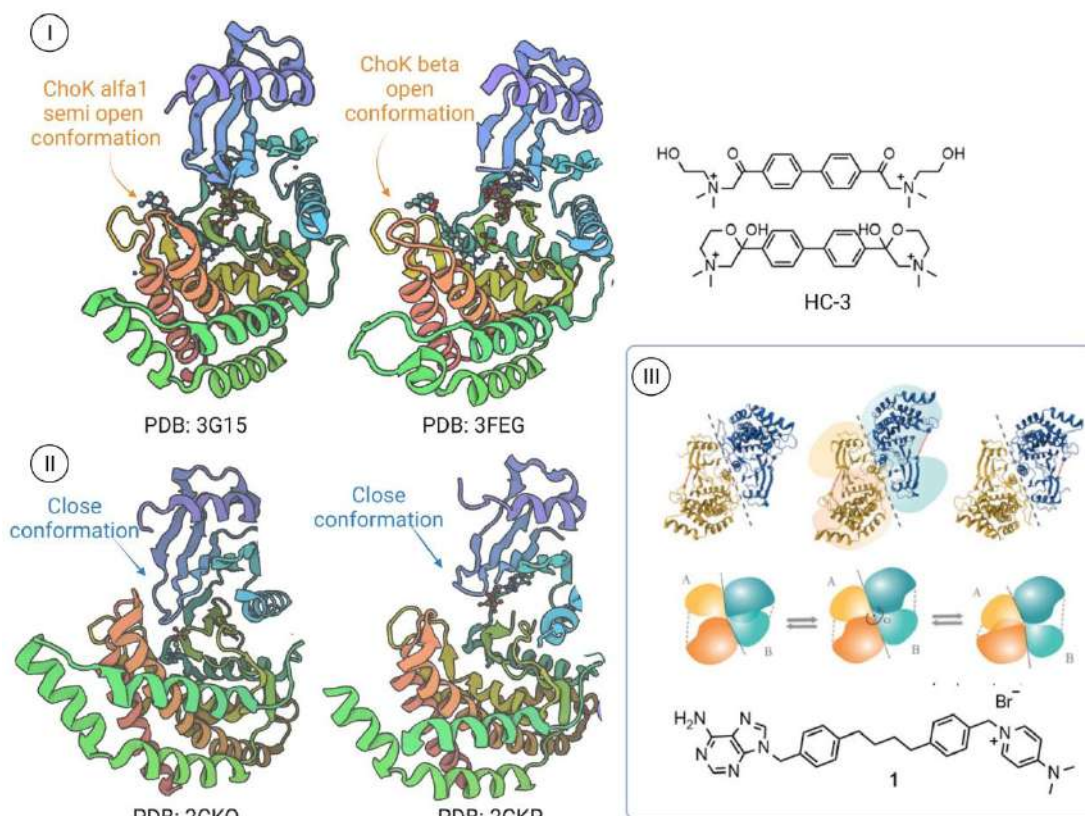


Figure 5. (I) Monomeric crystallographic structure of ChoK α 1 (*left*) and ChoK β (*right*) and their different conformational change in the catalytic site to place the HC-3 (α 9 and α 10 helices are in orange colour). (II) Conformational change in the N-terminal domain when the choline is phosphorylated. (III) Allosteric negative cooperativity and a broken symmetry between the monomers of the dimeric unit.²⁷

Contemporary, in 2013 Pollard *et al.* broach again the mechanistic issue. The kinetic studies showed parallel double reciprocal plots, which is indicative of a ***ping-pong mechanism***. Thus, classifying the Choline Kinase as an “atypical” kinase because they usually form ternary complexes.

ChoK is able to form firstly a phosphorylated intermediate that subsequently is transferred to the choline and that goes with a conformational change able to release the phosphorylated product. It was highlighted the role of Asp 306, located in the catalytic surroundings, and was proposed as a key residue for the phosphotransfer activity, also verified by mutagenesis studies.^{22,23} Asp 306 is able to form H-bonds with the γ -phosphate of the ATP, giving room to the enzyme intermediate. The ADP is released and the phosphated-enzyme interacts with the choline assuming a new conformation that changes the pKa in the catalytic site, breaking the H-bond with Asp 306 and releasing the phosphocholine (Figure 6).²⁸

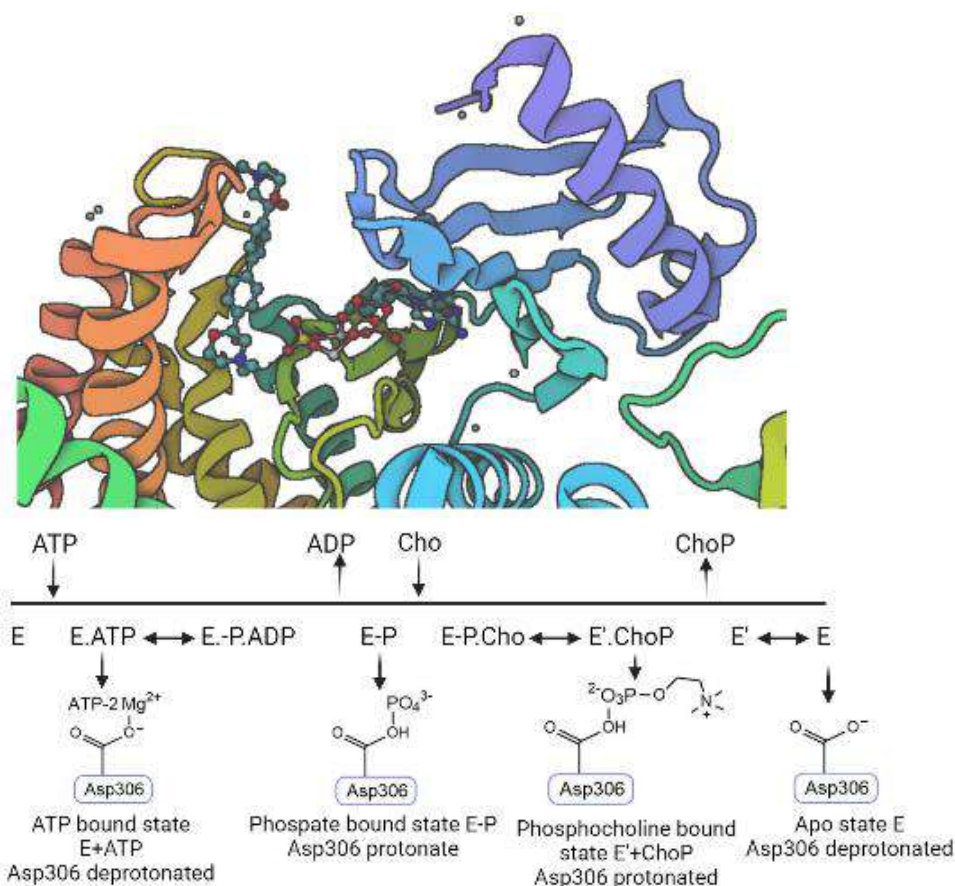


Figure 6. Ping-pong enzymatic mechanism of action proposed by Pollard *et al.*²⁸

All these conclusive discoveries together with the availability of crystal structures to make docking studies allows for the determination of new potent inhibitors.

3. Development-Timeline of the ChoK inhibitors.

The first ChoK inhibitor dates back to 1994 and since then, the rational design of more potent and selective inhibitors has not stopped. The initial rational design of inhibitors has evolved with technological advances. The availability of crystal structures of the ChoK isoforms allows the implementation of docking, MD and computational studies. Those have developed at the same time in the massive computational screening of chemical fragments and databases able to select chemical entities that best fits the catalytic pocket. The latter high-tech methodologies constituted a big step towards resource harnessing due to the synthetic libraries reduction previously optimized in-silico.²⁹

3.1 Derivatives of Hemicolinium-3.

The HC-3 (hemicolinium-3) was first proposed inhibitor of the *HChoK* enzyme.³⁰ Structurally, it consists of a biphenylic ring with two choline chains in *para*-position, that in solution cyclized forming oxazinium rings (Figure 7). The aromatic rings have a quaternary ammonium and a hydroxyl group that makes the molecule very polar and able to cross the BBB (blood-brain-barrier). Thus, it shows toxicity in the therapeutical window as well as interference with the cholinergic system and competitive inhibition with the choline transporters. However, it was used as a template for further pharmacomodulation in an effort to obtain safer and selective molecules.³¹ Two significant features involved in the efficacy: the biphenyl "spacer" that ensures the distance between the positive charges and the oxazinium rings, whose polarity strongly influences the activity were distinguished.

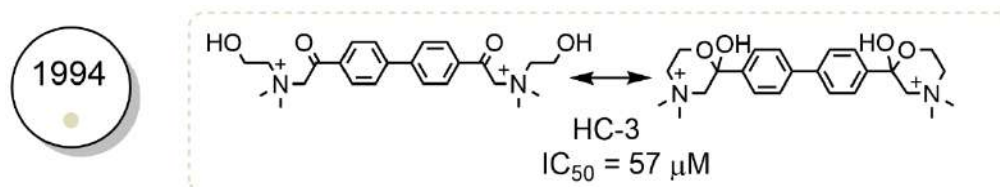


Figure 7. Hemicolinium-3 chemical structure in its open and cyclized forms.

The first efforts towards structural improvements were done together with in-vitro inhibitory and antiproliferative assays to completely understand the behaviour of the drug. Hernández-Alcoceba *et al.*³² ruled out the adequacy of the pyridinium cationic heads (Figure 8, left). Regardless of the linker, the pyridinium heads showed to have a targeted effect over the ChOK inhibition in accordance with the reduction in the cell growth and avoiding the side effects presented in HC-3. Then, the necessity of the two cationic charges was questioned. Half monoquaternized derivatives were synthesized, showing moderated activities as ChOK inhibitors (Figure 8, right). In fact, also the natural substrate choline has only one positive charge, but it was emphasised that the biscationic inhibitors allowed better affinity.

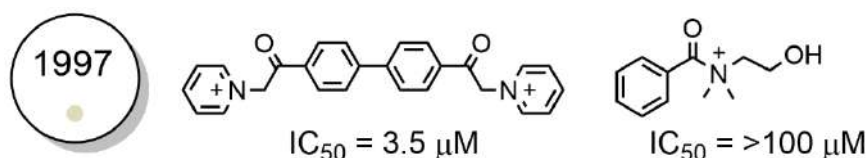


Figure 8. FK-7 (left) and HC-15 (right) inhibitors of the first pharmacomodulation stage.

A huge effort was carried out to rationally explain, using QSAR analysis³³, how the linker and the heteroaromatic heads modulation could lead to a hit. Starting from the dibenzyl scaffold, several heads were tested (Figure 9, up). From pyridinium, quinolinium and isoquinolinium heads derivatives, it was concluded the favourable substitution of the pyridinium heteroaromatic head, substituted in *para* position by electro-releasing groups able to delocalize the charge.³⁴ Overall, cyclic or aromatic amines in 4-position improve the antiproliferative values due to their greater lipophilicity. The next step was the size optimization of the linker (Figure 9, down). A series of six different spacers from cyclopropane to biphenyl were tested with the previously screened heads. The results pointed out toward the biphenylic spacer substituted in 3- or 4-position as the better spacer for inhibition and antitumoral potency.³⁵

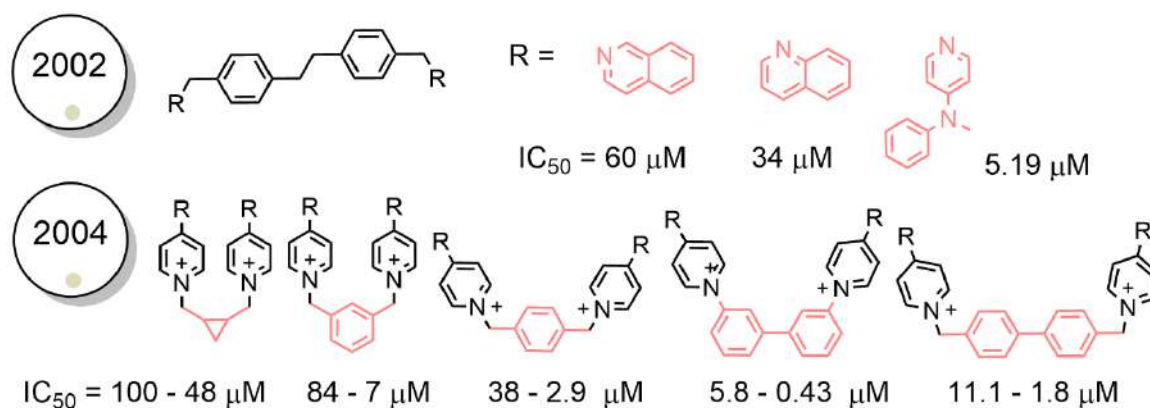


Figure 9. Screening of the most suitable heads (up) and linkers (down) structures.

However, further QSAR studies concluded that the antiproliferative behaviour was not so dependent on the latter parameters. On the contrary, it was highlighted the role of lipophilicity over cell growth that improved when using quinolinium and longer linkers.³⁶

As a result of all this research, two potent inhibitors were discovered (Figure 10). MN58b and TCD-717 became the new hits to lead for further development. They inhibited the enzyme

activity at 5 and 2 micromolar, respectively, and shed light on the biological mechanism of action.^{37,38} TCD-717 also known as RSM932A, showed the best results in vitro and in vivo, becoming the first *HChokα* inhibitor reaching Phase I clinical trials for advanced solid tumour treatment.³⁹

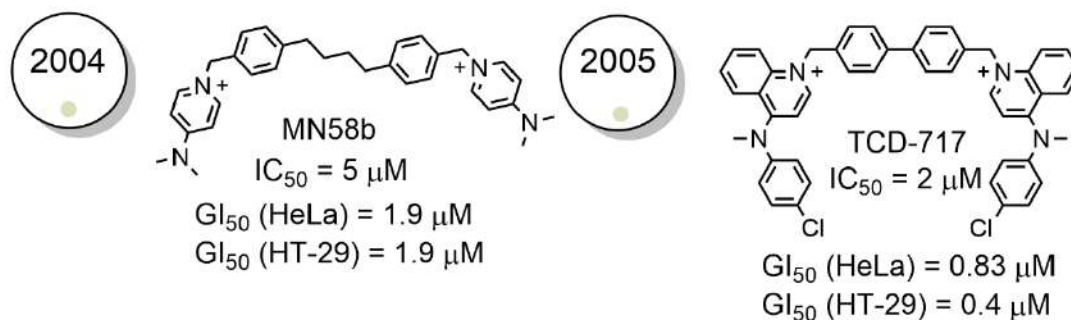


Figure 10. Chemical structure of the hit to lead MN58b and TCD-717.

3.2. Different strategies based on SARs.

Meanwhile the crystallographic structures of ChoK were resolved, other strategies were tested to increase the affinity towards the catalytic pocket.

The insertion of a third cationic charge gave room to compounds with higher affinity towards the enzyme (Figure 11, left). Nevertheless, they were so polar that couldn't pass through the membrane and were worse antiproliferative inhibitors.⁴⁰ Then, rigid scaffolds were synthesized to lock a particular inhibitor conformation and reduce the side effects, but they just showed moderate antiproliferative values (Figure 11, middle).⁴¹ In addition, it was also tested a mix of both proposals, a triple-bridged triscationic bicyclophanes (Figure 11, right). However, the latter compounds were inactive both as enzyme inhibitors and antiproliferative.⁴²

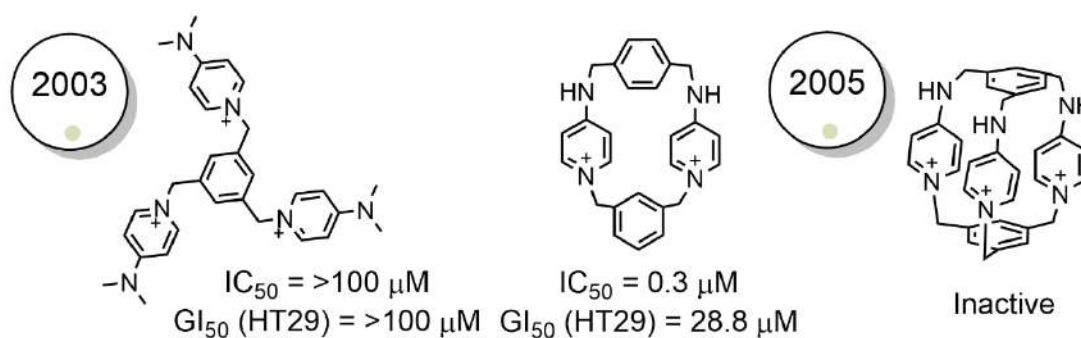


Figure 11. Example of the triscationic (left), cyclophanes (middle) and bicyclophanes (right) structures.

3.3. Inhibitors based on the crystal structure.

At the beginning of the first decade of the XXI century, the crystallographic model of the ChoK and its different isoforms were resolved. Since then, the design approach had been based on the crystallographic information of the binding sites. The proximity of the choline and ATP regions make researchers think about the possibility of new inhibitors able to bind both pockets.

Rubio *et al.* first synthesized asymmetrical inhibitors that connected an adenine and a pyridinium moiety as heads, with the purpose of seeing if the inhibitors could bind the ATP and choline binding sites (Figure 12, left).⁴³ Those derivatives show proper inhibitory values but were not as active as previous inhibitors. Trousil *et al.* also synthesized a family of similar derivatives

with longer linkers and demonstrated that their low activity was due to the inability to displace and compete with the ATP in its active site (Figure 12, right).⁴⁴

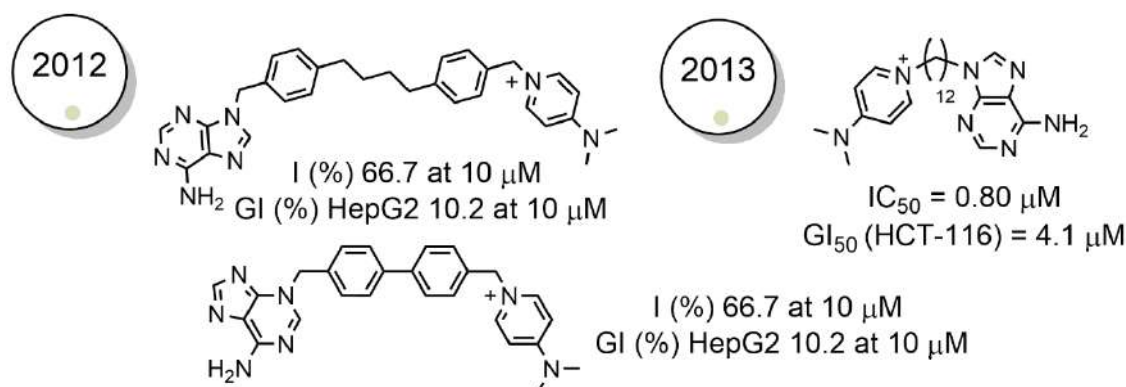


Figure 12. ATP-mimicking inhibitors designed to bind both choline and ATP catalytic pockets.

In this direction, new modifications in the adenine head were introduced, i.e. the replacement by 3-aminophenol or benzylthiopurine substituents as an attempt to reach a better antiproliferative profile (Figure 13). However, this strategy was not successful and some of them show cytotoxicity.^{45,46} Nevertheless, further experiments were recently carried out in the aminophenol asymmetrical inhibitors to determine their SARs.⁴⁷ It was observed that N-atom connected to the linker derivatives were better as ChoK inhibitors while the O-connected were better antiproliferative compounds, which comes together with their higher lipophilicity. Also, it was observed an improvement in their inhibitory and antiproliferative values due to the use of a purer ChoK enzyme instead of cell homogenates, and the wide range of neoplastic cells studied, respectively.

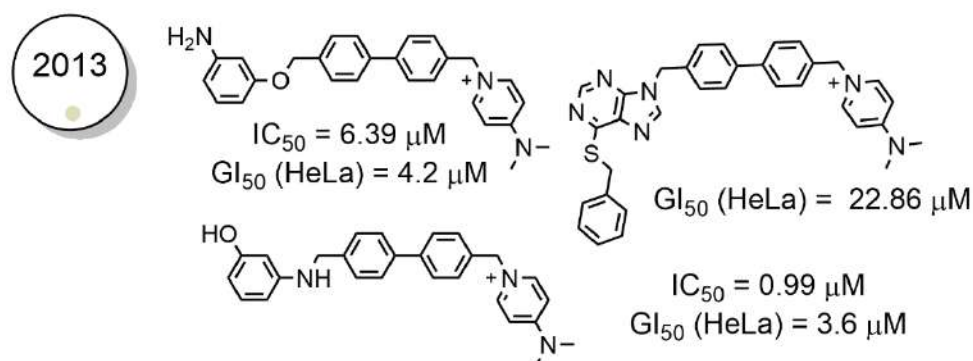


Figure 13. ATP-mimicking derivatives of aminophenol and benzylthiopurine.

These results gave room to the design of new non-symmetrical bis-cationic compounds. Due to the inability to occupy the ATP site, the new inhibitors were designed with the objective of binding new cavities in the surroundings of the choline pocket. Those compounds bind deeply in the hydrophobic groove of the choline pocket and when substituted with the 4-chloro-N-methyl aniline showed the opening of a new cavity at the back, with whom that fragment is able to bind (Figure 14, left). The access of this new binding site was enhanced by longer linkers and allows for better antiproliferative and inhibitory values without showing cytotoxicity.⁴⁸

In 2018, this strategy was redefined and asymmetrical bis-cationic molecules were designed using a (7-chloro)-4-substituted quinolinium and pyridinium moieties (Figure 14, right). Longer linkers gave room for better results, and inhibitory and antiproliferative values in the low micromolar range, inducing senescence in tumoral cells.⁴⁹

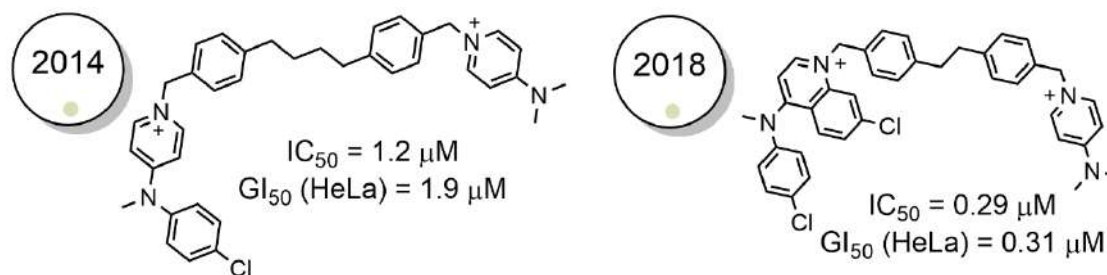


Figure 14. Asymmetrical bicationic compound's chemical structure.

An interesting methodology adopted in the last years has been the design of bioisosteric inhibitors (Figure 15). Bioisosterism consists of the replacement of some atoms of the structure by others that will allow the establishment of new H-bonds or could improve the lipophilic-hydrophilic balance enhancing the solubility and the pharmacodynamic of the molecule. In 2015, Castro-Navas *et al* synthesized a new library of compounds by the replacement of the biphenyl linker with a bipyridinic one (Figure 15, left).⁵⁰ Unfortunately, the inhibition towards the enzyme didn't improve with respect to its bioisoster TCD-717, but the antiproliferative values and the safer profile of non-tumoral cells did.

Similarly, in the search for newer anchor points to establish H-bonds, it was synthesized an oxygen-containing linker diphenoxyethane (Figure 15, right). It consisted of a longer spacer between the biphenylic rings in which two carbon were replaced by two oxygen atoms with free electron pairs able to interact with the enzyme pocket and improve the solubility while maintaining the activity of its predecessors.⁵¹ The linker adopted a gauche conformation that favours a deep insertion in the choline pocket improving its inhibitory and antiproliferative potency.

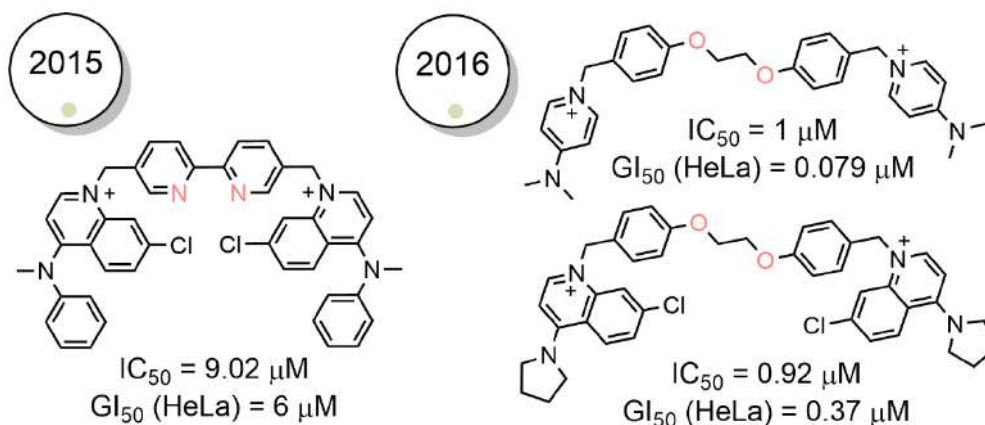


Figure 15. Bioisosteric inhibitors strategy. (Left) Compound 9h bioisoster of TCD-717 and (right up) compound 10a bioisoster of MN58b and (right down) 10l successfully improved the parent drugs potency.

Lately, a small molecule library of inhibitors comes to prove the suitability of the rational design (two cationic heads better than one or the linker improvement of affinity). It was declared that a greater contribution to the antiproliferative activity was due to the choline uptake inhibition rather than to a targeted effect.⁵²

Most of the contribution to the drug design and optimization has been done by the Department of Organic and Pharmaceutical Chemistry at the University of Granada (Spain), but also other groups have proposed new inhibitors from different scaffolds or using the HC-3 as a template.

For example, the group of Estévez-Braun *et al.* tested the efficacy of triterpene quinone methides (TPQ) bioactive compounds isolated from plants of the Celastraceae family and its

derivatives (Figure 16, right). They thought that due to the hydrophobic characteristics of the choline active site, this family of 5 fused aromatic rings could work as potent inhibitors. They observed that the most active compounds were able to bind similarly to the HC-3 and formed a cluster with the Mg^{2+} atoms hindering the ATP stabilization.⁵³

Other groups build their libraries from the HC-3 as template, giving room to different structures. For example, a family of 4,4'-bispyridyl-2,2'-bisoxazoles derivatives were synthesized due to the biological activity of oxazole and bisoxazole building blocks (Figure 16, left up). Those compounds showed potency as ChoK inhibitors and antiproliferative agents in the micromolar range, but SARs were difficult to establish.⁵⁴

An interesting proposal was also the design of a carbocyanine equivalent of the symmetrical biscationic ChoK inhibitors, able to emit fluorescence when irradiated with NIR light (Figure 16, left down).⁵⁵ The synthesized compound JAS239 showed comparable potency with MN58b and allowed tracking the accumulation of the inhibitor in the cell and evaluating the membrane permeability (by passive transport) using fluorimetry and confocal microscopy.

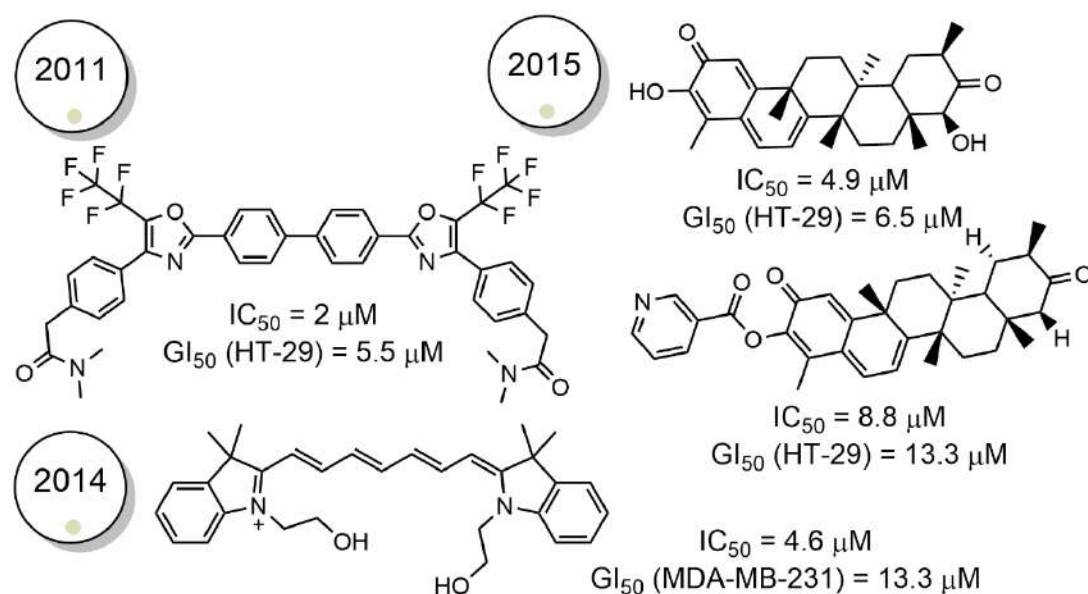


Figure 16. (Left up) Bioxazole derivate, (left down) JAS239 fluorophore chemical structure and (right) natural products derivatives from plants.

3.4. New approaches towards drug design from Academia to Pharma.

Along with the rational design based on the crystal and docking studies of the ChoK, the computational screening of databases took part in the research for newer and more potent inhibitors. The first trial was made in 2011 by the collaboration between the University of Louisville and the Advanced Cancer Therapeutics, LLC company (US).^{56,57} They developed a new potent inhibitor termed CK37 (Figure 17), by a receptor-based computational screening of the ZINC Library. It was smaller than the previous inhibitors and uncharged. However, like its design was done over the in-silico choline pocket template, it was obtained a molecule able to compete with the choline substrate. In addition to the structural adequacy, it was good as antiproliferative affecting other biological pathways (MAPK and PI3K/AKT) involving tumoral growth. All this opened a window of possibilities as the structural prototype was not as limited as thought.

In 2012, Vertex Pharmaceuticals Incorporated (US) carried out a High-throughput screening of 130.000 compounds from their compound collection.⁵⁸ The developed library of compounds showed high potency, in the nanomolar range, as ChoK inhibitors. As so, one of them (Figure 17,

V-11-023907) was used by the Pollard group to study the kinetic mechanism of the ChoK.²⁸ Its crystal structure in complex with enzyme was resolved, showing that the molecule's quinuclidine fragment was attached to the Asp 306 (a key amino acid residue that should be phosphorylated in the ping-pong mechanism) and blocked its action as phosphor-transfer. However, even though their high inhibitory activity, they were not good antiproliferative and promoted only a reversible effect.

All these promising results prompted Serrán-Aguilera *et al.* group, to the in-silico evaluation of the key scaffolds shared among the rationally designed molecules.⁵⁹ The pharmacophoric evaluation had the objective of identifying the key moieties responsible for the antiproliferative and inhibitory activities. For that purpose, 83 HC-3 actives and inactive derivatives were used in the pharmacophore's design. They were docked in the choline binding site and the method was optimized to be able to correlate the activity and the energetic fitness score. Then the Enamine, Chembridge and Life Chemicals virtual libraries of compounds were docked in the catalytic site and compound 10 arise as a new hit (Figure 17). That compound had the pharmacophore characteristics and was able to compete with the Mg-ATP complex and or with the choline.

The Ariad Pharmaceuticals, INC also developed a new hit to lead molecule by fragment-based screening. They first evaluated the most potent structural fragment and studied their biophysical adequacy using ST NMR (Saturation Transfer Nuclear Magnetic Resonance). The remaining fragments were docked in the ChoK crystal and only those who show binding in the choline pocket were able to increase their potency by further modification of the solvent-exposed fragment. It was highlighted the fact that none of the final compounds had a charge, and symmetry of the molecule was not necessary. The diazepine arises as a high-affinity moiety towards the choline groove that could be protonated in the intracellular pH and interact with the catalytic amino acid Asp 306. The final hits were excellent ChoK inhibitors in the nanomolar range and effective antiproliferative in breast cancer cells (Figure 17, comp 67).^{60,61}

Finally, the Nerviano Medical Sciences S.R.L. (IT) company joined the ChoK research synthesizing two libraries. The first one was based on purine and 3-deazapurine derivatives,⁶² whose structure was developed through QSAR studies (Figure 17, comp 114). The carbanucleoside scaffold was obtained by an in-silico analysis of antitumoral drugs and it showed activity in tumoral cells where the ChoK is also overexpressed.⁶³ The second one was based on pyrazoloquinazoline derivatives⁶⁴ as a result of a combinatorial chemistry implementation (Figure 17, comp 39). This group, previously search for new scaffolds able to bind ATPases and kinases because of their role in cellular differentiation, proliferation, and apoptosis regulation.⁶⁵ Due to the multitarget capability of this kind of structure, they also measure the selectivity for ChoK α and ChoK β isomers and obtained potent inhibitors in the nanomolar range.

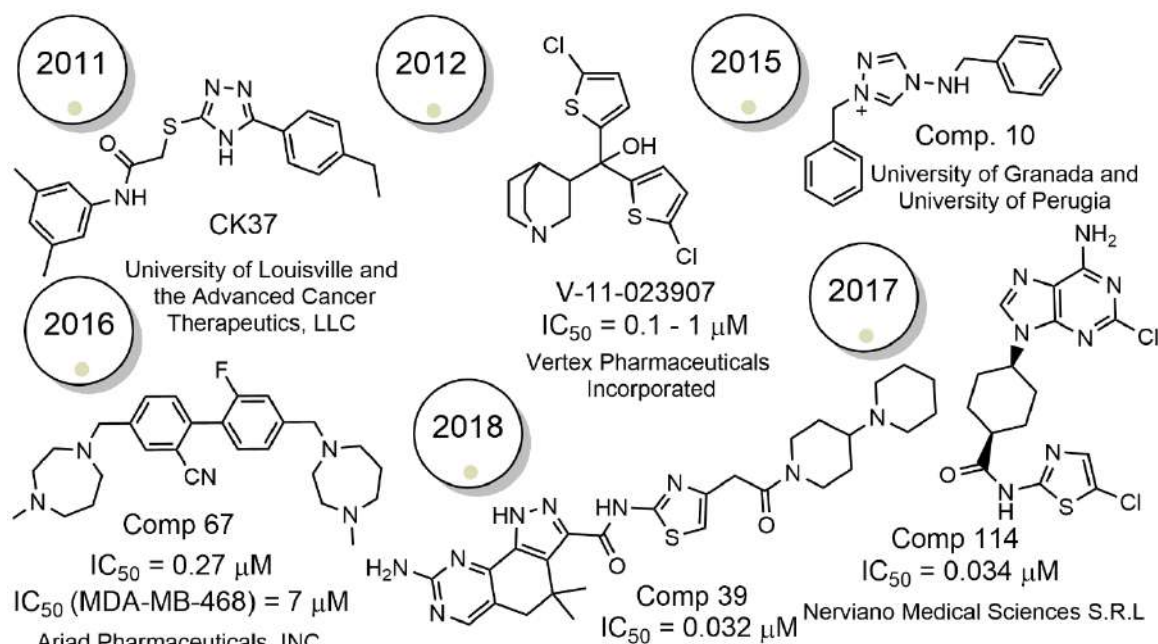


Figure 17. Compounds developed using in-silico methods by Pharmaceuticals Companies and/or in collaboration with academia.

Looking at that extensive inhibitors-timeline, it is possible to appreciate how the increasing interest of the topic and the industry involvement have provided a large number of molecules. More than 1000 ChoK inhibitors have been synthesized up to date. This success resides in the high number of pathologies in which the ChoK is overexpressed or dysfunctional, becoming a wide spectrum therapeutic target.

4. Biological effects of the inhibitors.

Hand to hand in the drug discovery process; it has been also studied how the dysregulation of the phosphocholine metabolisms affects the tumoral cells. Some inhibitors can cause apoptosis in neoplastic cells and a reversible arrest of the cell cycle in the normal ones.

While testing MN58b, it was observed those different modes of action. Rodríguez-González *et al* determined that the imbalance of phosphocholine due to the enzyme inhibition caused the hydrolysis of sphingomyelin (SM) producing phosphocholine and ceramides.³⁷ The lethal metabolite accumulation is responsible for triggering apoptosis and stress in the tumour or cell arrest in normal cells through the ceramides activated effectors.

On the other hand, inhibitors as 10a, also known as EB-3D, cause senescence in tumoral cells. Mariotto *et al*. discovered that this last effect was related to the activation of the AMPK-mTOR pathway. AMPK is the main regulator of energy homeostasis in eukaryotic cells and becomes activated under metabolic stress conditions, which in turn represses the downstream effectors of mTORC1 required for protein synthesis. Moreover, it was still appreciated the lower toxicity towards non-tumoral cells.^{66,67} The suppression of PA also inactivates the MAPK (mitogen-activated protein kinase) and PI3K/AKT (phosphatidylinositol 3-kinase) signalling pathways that lead to tumoral cell survival.⁶⁸

As a result of the cellular deregulation in the lipidic components, it was also noticed endoplasmic and mitochondrial stress without the formation of ROS (reactive oxygen species). The mitochondrial membrane depolarization gives room to the release of cytochrome c, which activates the caspase-3 apoptotic promoter.^{69,70}

The choline kinase inhibitors also sensitized cancer cells towards chemotherapeutics showing synergism even in resistant neoplastic cell lines.

However, the larger size of the latest inhibitors designed to improve the contact in the enzyme catalytic site usually leads to inconsistency between the antiproliferative and inhibitory values. This effect has been finally attributed to their capability to also inhibit the choline transporters. In that way, the biological effect is still the same, as the seize of choline produces the substrate unavailability to be transformed into phosphocholine. There are 4 different types of choline transporters: the high-affinity choline transporters (CHTs), choline transporter-like proteins (CTLs), organic cation transporters (OCTs) and organic cation/carnitine transporters (OCTNs), whose expression levels in tumoral cells can vary.⁴ Some inhibitors as HC-3, EB-3D (10a), EB-3P (10l), Ff-35, ICL-CCIC-0019, T and V among others (Figure 18), showed some choline uptake inhibition after tumoral cell exposure. Nevertheless, it has been determined that they could work following a double mechanism of inhibition: over the transporter and the enzyme, without causing cytotoxicity in normal cells.

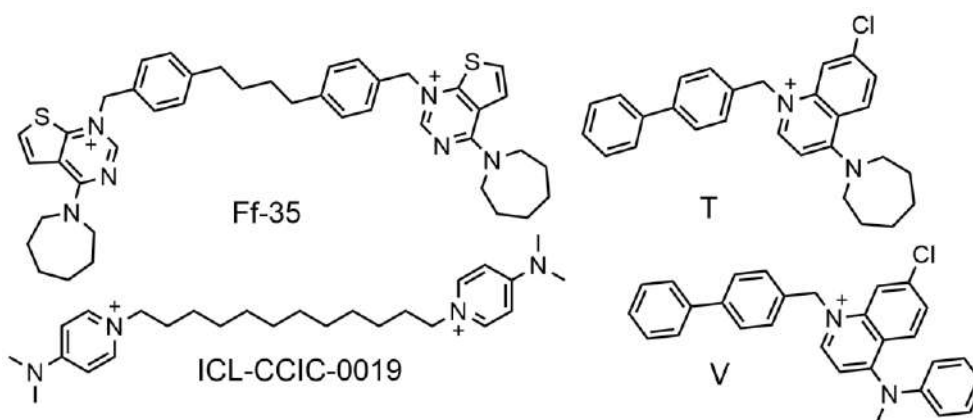


Figure 18. Compounds that can inhibit the choline uptake through the membrane's transporter.

A recent research article, proposed the use of bio-magnetic nanocarriers to couple the ChoK inhibitors as a method to avoid the pass across the membrane transporters of compound Ff-35 and thus be incorporated by endocytosis.⁷¹

Finally, the scaffolding role of the Choline Kinase has been considered as important as its catalytic function. Indeed, the TCD-717-ChoK α crystal showed that the inhibitor is superficially bound in the dimer interface, and not in the choline pocket as was previously supposed. This event modifies the conformation of the enzyme, affecting protein-protein interactions.⁷² Moreover, the depletion of the enzyme by siRNA knockdown produced the cell death by apoptosis while its inhibition causes just a reversible growth effect that disappeared when the drug is removed in most cases.⁷³ In fact, the overexpression of the mutated enzyme catalytically inactive is enough to induce tumorigenesis.⁷⁴ Further evidence in the last years, confirmed that the ChoK bind with the EGFR through the c-Src mediation, which lastly induce DNA synthesis and promote tumour progression.⁷⁵

5. The ChoK α involvement in other pathologies.

Dysregulation of lipid metabolism has also been associated with the ChoK α function in other pathologies and organisms that harm human being health. For example, in rheumatoid arthritis, the hypoxia conditions of this inflammatory disease, also present in cancer environments, suggested the implication of an aberrant ChoK metabolism. Thus, it was determined that the inhibition of ChoK α leads to the attenuation of the MAPK and PI3K/AKT pathways that regulates

synoviocyte function of FLS (fibroblast-like synoviocytes), involved in cartilage destruction, reducing cell migration and inducing apoptosis.⁷⁶

Also, in the HBV (Hepatitis B virus) infection treatment development was studied the metabolic changes in the host cells that could promote the virus replication and expression. As result, it was concluded that the knockdown of the ChoK α , and thus the reduction of PA second messengers, reduces the levels of HBV DNA. In this way, new metabolic targets were determined for the HBV infection, able to stop the virus development.⁷⁷

On the other hand, bacterial pathogens as *Streptococcus pneumoniae* and *Haemophilus influenzae* also express ChoK, which have a well-conserved catalytic site with the HChoK. The enzyme function is involved in the LTA (lipoteichoic acid) synthesis that constituted part of the bacterial cell wall. The chemical inhibition of the enzyme produces a block of the cell division and distortion of the cell barrier that lastly could lead to less adherence to alveolar cells. All this open new opportunities to deal with bacterial resistance, but further studies need to be done to not affect the human microbiome and normal cells proliferation.⁷⁸

However, after cancer, Malaria is the most studied illness in which the ChoK inhibition raised as a promising therapeutical target. Nowadays, Malaria is a hot spot in science and research, as it has been launched the first approved vaccine against Malaria, Sanaria PfSPZ Vaccine, over this year. The vaccine contains radiation-attenuated sporozoites form of the parasite, that is the disease-causing agent. The parasite reaches the liver where develops but is unable to pass through the bloodstream. To avoid a real infection, the vaccine is given in combination with pyrimethamine or chloroquine to kill the parasite in a specific development stage. That promotes sterile immunity in nearly 90% of vaccinated persons. Even if it is a promising step towards malaria eradication, there are still some drawbacks as there are many different strains of the parasite, the need for a drug combination treatment and that parasite production is obtained from live mosquitos which limited the scale-up of the process.^{79,80}

Malaria is a disease caused by the *Plasmodium spp.* parasites (*P. falciparum*, *P. vivax*, *P. malariae* and *P. ovale*), which is transmitted by the bite of the Anopheles mosquito. As expected, the world regions where this mosquito lives are the most beaten by the disease as are Sub-Saharan Africa, South-East Asia, Eastern Mediterranean, Western Pacific, and the Americas. A situation that comprises nearly half of the world population and that gets worse with climate change. In 2020 there were 241 million cases of malaria, being the most fragile population of children under 5 years old.⁸¹

The complex parasite's life cycle and infection have been well studied. First, the parasites enter the human system through the Anopheles mosquito bitten and release through its saliva. The sporozoites cross the skin and enter the bloodstream to arrive at the liver. There, in the hepatocytes, the parasite establishes a parasitophorous vacuole where can replicate asexually. In the next stage of development, the now termed merozoites in the pre-erythrocytic stage are released into the bloodstream. They are able to invade the red cells, within which takes place the second cycle of asexual replication developing from ring stages to trophozoites and then to schizonts. Mature schizonts cause the rupture of the cell blood membrane and become merozoites able to infect new red blood cells (Figure 19).⁸² That is the reason why malaria can cause anaemia and fever episodes related to the parasite blood cell breakout and invasion.

A lot of effort has been done to block the parasite infection and progression, from prevention barriers as insecticides and the use of screens, to the development of antimalarials as artemisinin and chloroquine. However, it is worth noting the resistant development that led to combined therapy usage. This fact justifies the urgent need for new drugs but overall, of new therapeutic targets to fight Malaria without producing resistance.

With this scenario, Vial *et al.* proposed a new strategy based on the different metabolic requirements between the parasite and the host. They realized that parasite replication requires the formation of new lipidic membranes that cover each member of the new progeny.

As the erythrocyte is enucleated and does not have enzymatic machinery to produce the lipidic demand, it is the own parasite metabolism that works using the host starting materials.⁸³

The host-directed therapy (HDT) was based first on the inhibition of the choline and ethanolamine uptake that are precursors of phospholipids.⁸⁴ However, other studies are focused on the inhibition of transporters for salvage purine bases⁸⁵ and glucose⁸⁶, as the parasite is unable to produce them *de novo*.

The lack of phospholipids precursors cause the parasite sexual reproduction,⁸⁷ which means less erythrocytic infection. The formed gametocytes that remain in the bloodstream will lastly disappear from the circulation if not taken up by a mosquito.

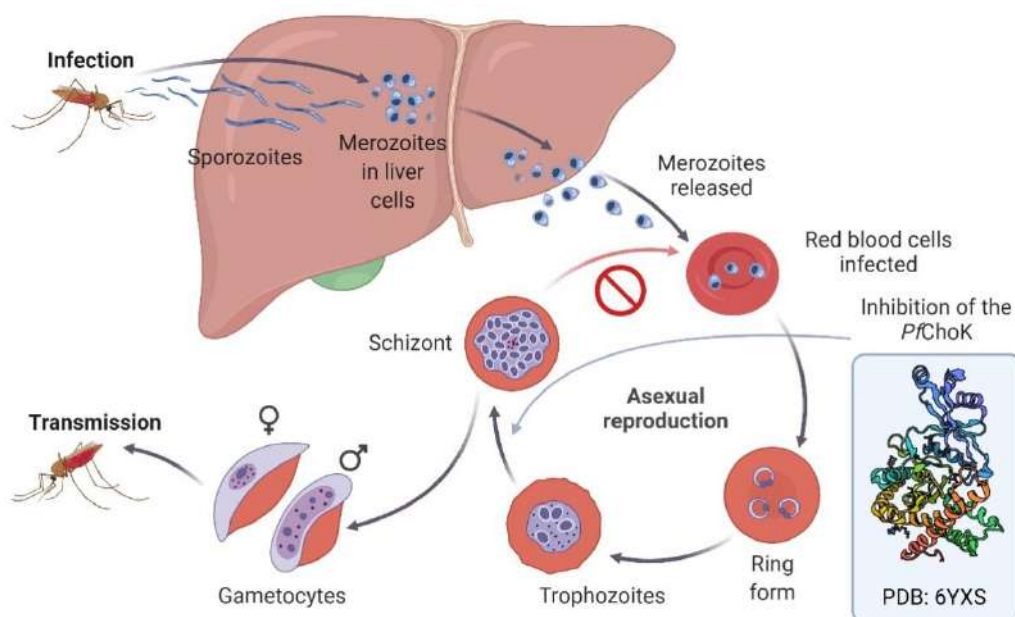


Figure 19. The cycle of infection and reproduction of the *Plasmodium falciparum* parasite. It is also highlighted the replication inhibition step due to the enzymatic inhibition of choline in the parasite.

In line with the foregoing, the *Plasmodium falciparum* Choline Kinase (PfChoK) arise as a promising target to block the parasite infection through enzymatic inhibition. The complete crystallographic structure in complex with Mg^{2+} and ATP as cofactors was recently solved (PDB: 6YXS Apo form and 6YXT ADP bond form).⁸⁸ Its similarity with the *HChoK* supported the use of already developed inhibitors as antimalarials. Zimmerman *et al.* started using the HC-3, MN58b and TCD-717 as antimalarials. They carried out kinetic studies and recognized that the PfChoK has also a ping-pong mechanism of action. As so, while HC-3 and MN58b were competitive with choline, the TCD-717 bind to the phosphorylated-enzyme intermediate by an allosteric pocket and lastly inhibited the choline phosphotransfer.⁸⁹ Most importantly, all of them showed inhibition in resistant strains to chloroquine.

Inhibitors as BR-23 and BR-25 (Figure 20), caused a detriment of phosphatidylethanolamine (PE) biosynthesis as a consequence of the PfChoK inhibition, which is able to use ethanolamine or choline as substrates.⁹⁰ Other asymmetrical ATP-mimicking inhibitors showed good potency at nM concentrations and optimal selectivity (Figure 20).⁹¹ Also, recently (in 2021) bioisosteric molecules with innovative thienopyrimidine heads and linkers of variable length and

bioisosterically decorated were tested but without improving the potency showed by previous inhibitors as 10j (Figure 20, Fg 15).^{92,93}

The described inhibitors used to work in the blood stages of the parasite, delaying the asexual development towards schizonts forms and blocking the intraerythrocytic development. Moreover, it is also thought to have a possible role as choline transporters inhibitors both in the erythrocyte and the parasite membrane.

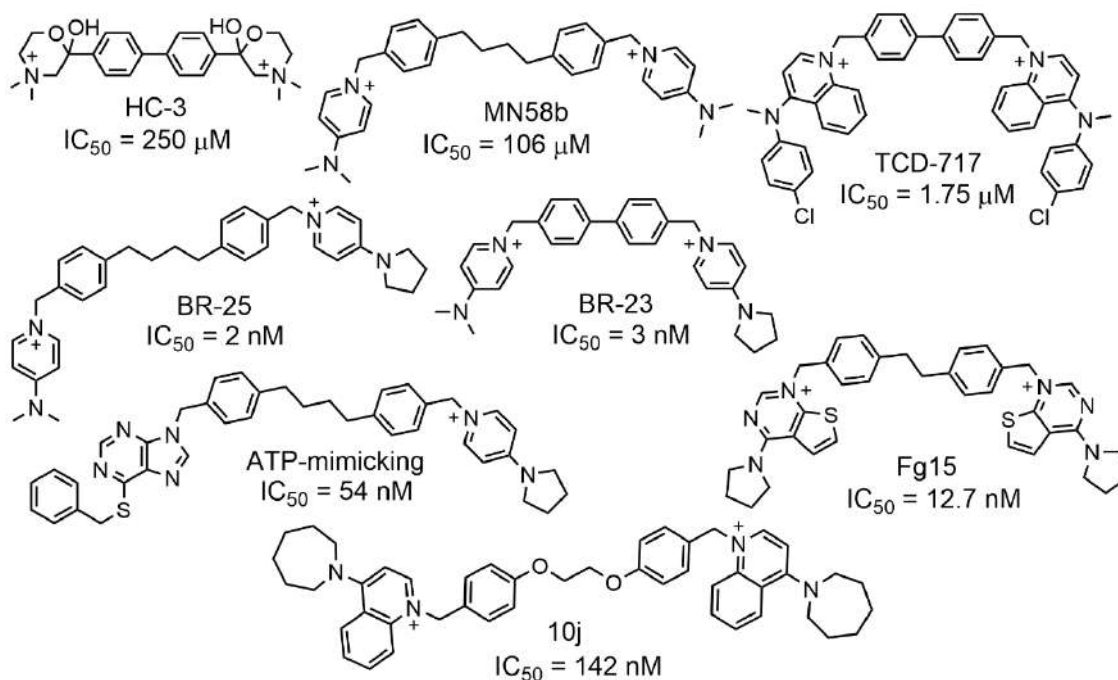


Figure 20. ChoK inhibitors used also as antimalarials.

Vial *et al* rationally designed compounds as actives as G25,⁹⁴ which was used as a hit for further modification (Figure 21). They substituted the quaternary amines for thiazolium rings, a scaffold present in biological molecules and that offer less toxicity.⁹⁵ From this research came up Albitiazolium, which is in phase II of clinical trials (Figure 21). However, the cationic charges are a drawback to allowing oral administration and be further developed as a drug. In fact, Caldarelli *et al.* developed neutral related prodrugs able to get charged after crossing the GI barrier but that resulted to be fewer actives than the parent drug, Albitiazolium.^{96,97}

The presented drugs act over the inhibition of the choline uptake in the parasite within the erythrocyte, accumulating in higher concentration in the infected blood cells in an irreversible way and also interacting with the plasmodial digestive vacuole.⁸⁴ Thus allowing new therapeutic pathways to blockage the parasite asexual reproduction and avoid chemical resistance.

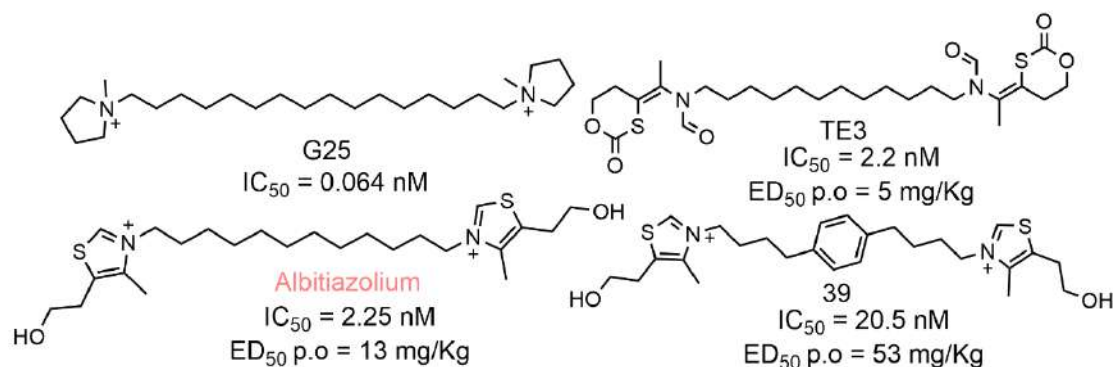


Figure 21. Compounds designed to selectively inhibit PfChoK.

On the left the hit to lead G25 (*up*) and the less toxic derivative Albitiazolium (*down*). On the right, the prodrug TE3 (*up*) was designed to improve the per os (orally) administration. However, it results to get charged in the GI tract and does not develop further. Compound 39 (*down*) is the result of the linker pharmacomodulation.

The synthesis of new molecules with better pharmacodynamics properties is still needed for Malaria eradication. They should guarantee the availability of a scalable synthetic process and an easily and safely administration.

Aims

Over the years, a large variety of ChoK inhibitors have been synthesized and their biological activities tested. Nevertheless, the need for novel and more potent molecules is still a subject of research.

In this Chapter of the thesis, the synthesis of two new libraries of ChoK inhibitors have been studied. In the effort to obtain molecules with better activity keeping the symmetrical and biscationic structure, the introduction of sulphur atoms in the linker to replace carbon or oxygen atoms have been envisaged. Sulphur atoms are able to establish new bonds in the enzyme pocket and improve the compounds solubility. They occupy almost double of the space of a carbon one, so with this change, we are able to design bigger molecules that will occupy a major area.

Furthermore, special attention has been devoted to the synthetic protocol, so that the principles of green chemistry were applied when possible. Such an approach gives an added value to the whole study since the sustainable synthesis of molecules for pharmaceutical use is, nowadays, mandatory in order to define efficient and green protocols.

The biological evaluation of the new inhibitors (enzymatic and antiproliferative assays) has been done in collaboration with Prof. María Paz Carrasco Jiménez of the Department of Biochemistry at the University of Granada.

And finally, in order to assess a correlation between the structure and activity of the synthesized molecules, docking studies have been carried out using the FLAP software in collaboration with Prof. Laura Goracci of the Department of Chemistry at the University of Perugia.

Materials and methods

1. Synthesis of Choline Kinase inhibitors. General conditions.

Chemicals commercially available were purchased from: Sigma-Aldrich, Fluorochem, Acros Organics, Alfa Aesar and VWR Chemicals; and used without further purification unless specified.

Control of reactions progress was performed by thin-layer chromatography (TLC). The used TLC Silica gel 60 F254, 25 Aluminium sheets 20x20 cm purchased by Merck KGaA, are revealed with a UV lamp or by the later coverage on a KMnO₄ stain solution (to see amines and oxidable groups).

Purifications were carried out using flash column chromatography of silica gel (40-63 μm, VWR Chemicals) or aluminium oxide (activated, neutral, Brockmann Activity I) as the stationary phase. On the other hand, organic solvents (hexane or petroleum ether, ethyl acetate, dichloromethane, and ethanol) were used in different volumetric proportions as the mobile phase. However, purification by recrystallization was always preferred becoming a sustainable alternative to the latter, where the final product is precipitated in a solution of acetonitrile or methanol with diethyl ether.

Uncorrected melting points were measured with the Stuart Scientific SMP3 equipment.

Microwave reactions were performed in the Initiator 2.0 microwave synthesizer (Biotage AB, Upsala), which produces controlled radiation of 2.450 GHz.

The ¹H and ¹³C-NMR spectra were recorded at ambient temperature on a BRUKER Avance NEO (400 or 500 MHz) spectrometer at the CIC (Centro de Instrumentación Científica) in the University of Granada. The used deuterated solvents were methanol-*d*₄, chloroform-*d*, DMSO-*d*₆ and deuterium oxide, and the spectra were calibrated using their residual peaks. Chemical shifts (δ) are reported in ppm and coupling constants (*J*) in Hz. The aspect and multiplicity of the reported signals are indicated with the following abbreviation: (s) singlet; (bs) broad singlet; (d) doublet; (dd) doublet of doublets; (t) triplet; (q) quartet; (quint) quintet; (m) multiplet. The spectra were interpreted using MestReNova v14.2.0-26256 of Mestrelab Research S.L.

High-Resolution Mass Spectrometry (HRMS) was conducted using a Waters LCT Premier XE Spectrometer at the University of Granada (CIC).

Elemental analysis was made using a FISONs instrument EA 1108 CHNS, with sulfanilamide as standard and wolframium oxide as comburent.

2. Enzyme-based ChoK activity assays (IC₅₀).

The inhibitory effect of the synthesized compounds was assayed over the HCKα1 purified enzyme, following the procedure previously described.⁴⁹

All the inhibitors were first diluted in DMSO preparing stock solutions of 25 mM. Compounds unable to be dissolved in DMSO (**PL 40**, **PL 46** and **FP 14**) were rejected and not tested. From the DMSO stock, serial dilutions in water were done reaching the concentration of 2.5 mM and then 250 μM. From this final dilution were prepared the test concentrations at 0.2 μM, 1 μM and 5 μM, each of them in duplicate.

In each experiment, DMSO-assays were consistently run in parallel as control and H₂O-assays as blank. DMSO in no case exceeded a concentration of 0.1% in order to avoid unspecific ChoK inhibition.

The purified enzyme HCKα1 was provided by the Latvian Institute of Organic Synthesis & Istituto Italiano di Tecnologia of Milan from Prof. Emilio Parissini, following the reported procedure²⁶. The enzyme was prepared in vials of 10 mg/mL and conserved in aliquots of 1 μL at -80 °C for its

use. For the inhibition assay, the pure enzyme aliquots (1 μ L) are added with 1 mL of Tris-HCl 25 mM mixed with Tris-HCl 25 mM plus 150 mM of NaCl, to adjust the pH at 7.5. From this solution (CK 1/1000), 100 μ L are taken and added together with 900 μ L of Tris 200 mM reaching a final dilution of 1/10000. In this manner, 20 μ L corresponds to 20 ng of HCK α 1 enzyme in agreement with its basal activity.

ChoK activity was assayed by measuring the rate of incorporation of 14 C from [methyl- 14 C] choline (Perkin Elmer, MA, USA) into phosphocholine both in the presence or absence of different inhibitor concentrations. Briefly, the final reaction mixture contained 100 mM Tris (pH 8.5), 10 mM MgCl₂ and 10 mM ATP, and 20 ng of purified ChoK α 1. After the samples were preincubated at 37 °C for 5 min, the reaction was initiated with 1 mM [methyl- 14 C] choline (4500 dpm/nmol) and incubated at 37 °C for 10 min, the final volume being 55 μ L. The assay was stopped by immersing the reaction tubes in boiling water for 3 min. Aliquots of the reaction mixture were applied to the origin of Silica Gel plates (Analtech, NJ, USA) in the presence of phosphocholine (0.1 mg) and choline (0.1 mg) as carriers. The chromatography was developed in methanol/0.6% NaCl/28% NH₄OH in water (50:50:5, v/v/v) as solvent for 2.5 h. Phosphocholine was visualized under exposure to iodine vapour, and the corresponding spot was scraped and transferred to scintillation vials for measurement of radioactivity by a Beckman 6000-TA (Madrid, Spain) liquid-scintillation counter. At least three experiments were performed in all assays.

The inhibitory concentration (IC₅₀ values) is a measure of a compound (drug) concentration needed to inhibit a given biological activity by 50%. It was determined from the percentage activity of the enzymes at different concentrations of synthetic inhibitors by using a sigmoidal dose-response curve (the ED50plus v1.0 software).

3. Computational studies.

Docking analyses were performed using FLAPdock implemented in FLAP 2.0 (Fingerprint for Ligands and Proteins), developed and licensed by Molecular Discovery Ltd.⁹⁸

The crystal structure of human choline kinase alpha in complex with Hemicholinium-3 and ADP (PDB ID: 3G15) was chosen as the template for docking due to its semi-open binding site, and because the catalytic site is conserved in all the enzyme's crystallographic structures with a binding inhibitor. Docking was performed in the catalytic site of chain A because it is the monomer best resolved of the dimeric unit (see Appendix 1 for details).

For each ligand, 25 conformers were automatically generated to take into account flexibility. The ligands were docked in the absence of their counterions and conformations at a min RSM of 0.3 Å were generated. The Molecular probes used to analyse the binding in the catalytic site in terms of GRID MIFs were: H (shape), DRY (hydrophobic interactions), N1 (H-bond donor), O (H-bond acceptor) and NM3 (trimethyl ammonium cation) interactions. The MIFs were generated using a grid resolution of 0.75 Å. The five highest S-score poses of each ligand are analysed and classified according to their probability (see Appendix 2).

The Log P was calculated using <http://www.swissadme.ch/>⁹⁹ as an average of five predictions methods.

Figures were done using PyMOL Molecular Graphics System, Version 2.0 Schrödinger, LLC.

4. Growth inhibition assay (GI₅₀).

All compounds were evaluated for their antiproliferative activity towards the human tumour-cell line MCF-7, of human breast adenocarcinoma and the hepatocellular carcinoma cell line HepG2, supplied by the Cell Bank of the CIC (Centro de Instrumentación Científica) at the University of Granada and from the European Collection of Animal Cell Cultures (Salisbury, UK), respectively.

The MCF-7 cell line was grown in DMEM medium (Gibco, Milan, Italy) and supplemented with 10% fetal bovine serum (FBS) (Invitrogen, Milan, Italy), 115 units/mL of penicillin G (Gibco, Milan, Italy) and 115 µg/mL of streptomycin (Invitrogen, Milan, Italy).

On the other hand, the HepG2 cell line was cultured in MEM containing 10% heat-inactivated FBS from Biowest (Nuaille, France) supplemented with 2 mM L-glutamine, 1% non-essential amino acids, 100 units/mL of penicillin (Gibco, Milan, Italy) and 100 µg/mL streptomycin (Invitrogen, Milan, Italy).

MCF-7 and HepG2 cell lines were tested for mycoplasma contamination every 6 months by the RT-PCR analysis. Individual wells of 96-well tissue-culture microtiter plates were inoculated with 100 µL of complete medium containing 8×10^3 and 10×10^3 cells per well, respectively. The plates were incubated at 37 °C in a humidified 5% CO₂ incubator for 18 h (in MCF-7) and 48 h (in HepG2) before the experiments. After medium removal, 100 µL of fresh medium containing the test compound at different concentrations was added to each well and incubated at 37 °C for 48 h (in MCF-7) and 24h (in HepG2).

Cell viability was assayed by the (3-(4,5-dimethylthiazol-2-yl)-2,5-diphenyltetrazolium bromide test (MTT) as previously described elsewhere¹⁰⁰.

The GI₅₀ is defined as the compound concentration required to inhibit cell proliferation by 50%, in comparison with cells treated with the maximum amount of DMSO (0.25%) and considered as 100% viability.^{51,101}

5. Physico-chemical studies.

UV-visible absorption spectrophotometry and steady-state fluorimetry were carried out using a Lambda 650 UV-visible spectrophotometer (PerkinElmer, Waltham, MA, USA) and a Jasco FP-8300 spectrofluorometer (Jasco, Tokyo, Japan), respectively. The samples were prepared at 25 µM in dioxane and water from a mother solution of 2.5 mM in 1DMSO/9H₂O.

MCF-7 breast adenocarcinoma cells were provided by the Cell Bank of the CIC (Centro de Instrumentación Científica) at the University of Granada. MCF-7 cells were grown in DMEM medium (Gibco, Milan, Italy) and supplemented with 10% fetal bovine serum (FBS) (Invitrogen, Milan, Italy), 115 units/mL of penicillin G (Gibco, Milan, Italy) and 115 µg/mL of streptomycin (Invitrogen, Milan, Italy) in a humidified 5% CO₂ incubator at 37°C. For the FLIM microscopy experiments, cells were seeded onto 25 mm coverslips in 6-well plates at a density of 22.5×10^4 cells/well and an 80% of cellular confluence. For their visualization, the samples were washed three times using phosphate-buffered saline (PBS). The tested compound was added in a 25 µM concentration in PBS from a stock solution of 2.5 mM in 1DMSO/9H₂O.

FLIM images were recorded on a MicroTime 200 fluorescence-lifetime microscope system (PicoQuant) using as excitation source a pulsed diode laser, LDH-375 (PicoQuant), operated at a repetition rate of 20 MHz. The light beam passed through a dichroic mirror (375dcxr, Chroma) and through the oil immersion objective (1.4 NA, 100X) specific to an inverted microscope system (IX-71, Olympus). The fluorescence emitted light was collected back through the objective, filtered by a long-pass filter (405LP, AHF/Chroma), and directed to a 75-µm confocal aperture. The light was transmitted to a 500/40 bandpass filter (Thorlabs) and focused on single-photon avalanche diodes (SPCM-AQR 14, PerkinElmer). The data were collected by a TimeHarp

200 TCSPC module (PicoQuant), and raw fluorescence lifetime images were acquired by a scanner with 512×512-pixel resolution. To obtain the fitted FLIM images, a spatial binning of 2×2 pixels was performed with SymphoTime software, and the matrix data were exported and analysed with the Fiji ImageJ program.

PAINS filters and pharmacodynamics in silico predictions were carried out using the free website (<http://www.swissadme.ch>). It was developed by the SIB Swiss Institute of Bioinformatics using free of charge databases, and algorithms from the literature or developed in-house. It allows for the in-silico prediction of pharmacokinetics (gastrointestinal absorption, brain blood barrier permeability, susceptibility by the Pgp pumping out the cell and cytochrome metabolism), drug-likeness (using the Lipinski rule-of-five but also Ghose, Veber, Egan and Muegge models variation of those rules) and the medicinal chemistry friendliness (as the PAINS and structural alerts implemented by Brenk R. et al¹⁰²) of molecules under an early biological assessment.⁹⁹

6. Figures and Graphics.

Biological representations were designed using the online and free of charge version of Biorender.

Graphics and bar charts were done with the program OriginPro 8.5.

The chemical structures were designed with ChemDraw 20.0.

The cell fluorescence images collected with FLIM were analyzed using the program Fiji-Image J.

Results and discussion.

1. Sustainable Synthesis of Choline Kinase inhibitors

In recent years, the demanding change of chemical processes towards more environmentally friendly transformations that reduce the use of hazardous reagents and solvents has become a priority to accomplish the target of sustainability.

That is especially a concern in the pharmaceutical industry, where the low quantity of APIs production makes difficult the implementation of green processes, becoming one of the most contaminating ones. For that reason, the current “green by design approach” considers the reaction sustainability from the beginning allowing a faster industrial implementation and giving an extra value to the product.

With that philosophy in mind, we carried out the *green* synthesis of two new libraries of Choline Kinase inhibitors. This type of biscationics and symmetrical libraries have demonstrated selectivity towards the choline catalytic site, which constituted an advantage with respect to other kinase inhibitors. Most of them are designed to bind to the ATP pocket common to all this regulatory family of enzymes and thus showing less selectivity.¹⁰³

The rational design behind the synthesis of this new inhibitors is the bioisosteric replacement of C atoms of the linker, in already good inhibitors developed by our group.

For years, it has been optimized the chemical structure's characteristics of size, chemical charge (mono-, bis- or tris-cationic), symmetrical or asymmetrical compounds, and the different polarities of the cationic head. However, we reached an activity plateau, where no improvement was observed when further structural modifications were done, and in addition, SARs were difficult to determine as the inhibitory and antiproliferative values divergence in some cases. This could be caused by the difficulty of those molecules passing through the membrane and reaching the target ChoK. To avoid this drawback, we designed molecules with heteroatoms (N, O and S in the present work) in the linker able to improve the hydrophilic/lipophilic balance and with free electron pairs able to further improve the enzyme affinity.

With respect to the latest bioisosteric diphenoxyethane linker (Figure 15, right), the proposed dithioethane and disulphide linkers enhanced the lipophilicity, are less prone to solvation with structural water in the enzyme, more flexible due to the higher atomic size, and they could protect the inhibitor metabolism by esterases.

There are several examples of drugs where the bioisosteric exchange of oxygen by a sulphur atom improves the activity for which they were designed. We could highlight the case of the monastrol and oxomonastrol, in which the higher nucleophilicity of the S atom seems to be the key to a better anchor over the Mitotic Kinesin Eg5.¹⁰⁴ Its allosteric binding leads to an enzyme conformational change that traps the ATP in the catalytic pocket and avoids the release of ADP to gain the energetic requirements for cellular division, leading to an antiproliferative function.

Also, the bioisosteric change of an hydroxyl group by a sulfhydryl one in cinnamic systems showed enhancement of the antioxidative properties protecting neuroblastoma cells from radicals' damage.¹⁰⁵ Or the glycan replacement of the O-Glycosidic linkage by an S-Glycosidic one, which protects the molecule from enzymatic hydrolysis and reactivity. The bioisosteric change allowed for size adequacy and hydrophobic enhancement for an optimum binding with CR3 and dectin-1 targeting the regulation of phagocytosis.¹⁰⁶

The general structures of the whole inhibitors bearing the new linkers are reported in Figure 22.

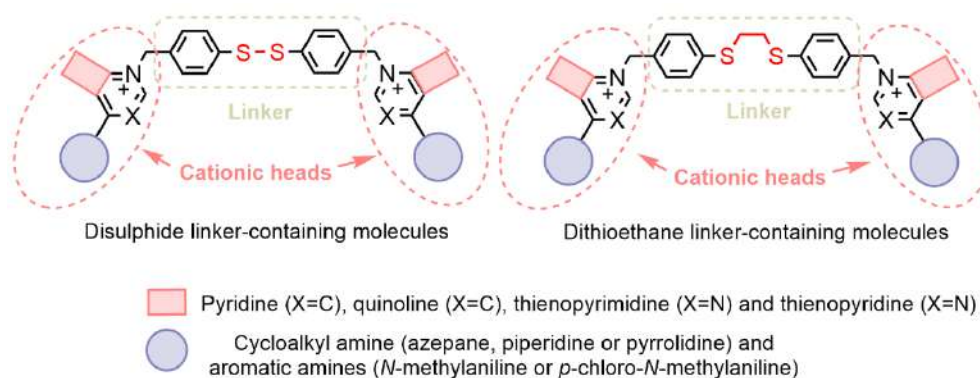


Figure 22. General structure of the new inhibitors.

Concerning the chosen heteroaromatics quaternary amines, they are a representative sample of the most efficient heads. We used pyridines and quinolines that were previously reported to have good inhibitory values due to their size and lipophilicity respectively. The pyridine was small and allowed the inhibitor to easily pass through the membrane giving good inhibition values while, on the other hand, the bigger quinoline showed difficulties to pass the lipidic membrane because of its hindrance, but it could establish more interactions with the choline pocket due to its hydrophobic nature. Furthermore, in the latter case, it was observed the opening of a new binding site when substituted with para-chloro-N-methyl-aniline.⁴⁸

Moreover, we have introduced new isosteric changes in the quinoline ring. As recently reported, thienopyridine and thienopyrimidine are scaffolds with an interesting antitumoral activity while inhibiting multiple enzymes or modulating the activity of receptors.¹⁰⁷ For example, those scaffolds were reported as inhibitors of the FAK (Focal Adhesion Kinase)¹⁰⁸ and the EGFR kinase transmembrane receptor¹⁰⁹, affecting the cellular adhesion, motility, proliferation and survival in neoplastic cells. Thienopyrimidine isomers [2,3-d] and [3,2-d], were used to explore the best spatial arrangement suitability.

The following displayed results are still unpublished, but they will be shortly submitted to a relevant journal in the field due to the results' novelty.

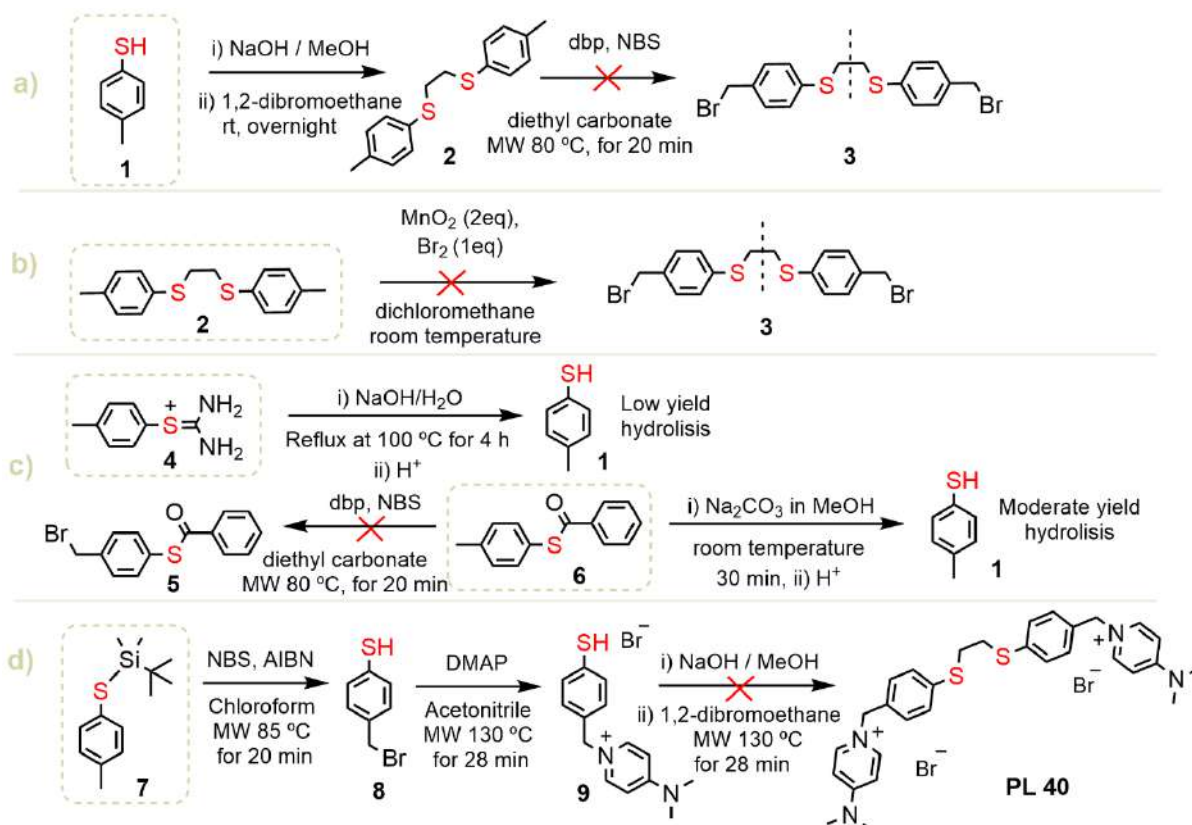
1.2. Optimization of the dithioethane and disulphide linkers.

Similar to the reported synthetic procedure for the diphenoxyethane linker⁵¹, the strategy to assemble the linker and the cationic heads pass through the linker bromide functionalization. As so, the dithioethane synthetic approach was first conducted using the 4-methylbenzylthiol **1** as starting material. First, we carried out the bridge formation and next, the radical bromination with dbp and NBS in the MW¹¹⁰ (Scheme 1, a). However, the thioether group in **2** is more reactive due to the presence of a less electronegative and "larger" (more polarizable) sulphur atom in comparison to the ether. As so, the first is more reactive to the electrophilic attack and the oxidation reactions. Therefore, the radical bromination occurred on the dithioethane bridge **2** yielding a lot of by-products and a crude mixture difficult to purify.

Moreover, it was also tested the bromination of the 1,2-bis(p-tolylthio)ethane **2** at room temperature with bromine and MnO₂¹¹¹ (Scheme 1, b). Even in those soft conditions, we just observed the oxidation of the bridge and its breaking.

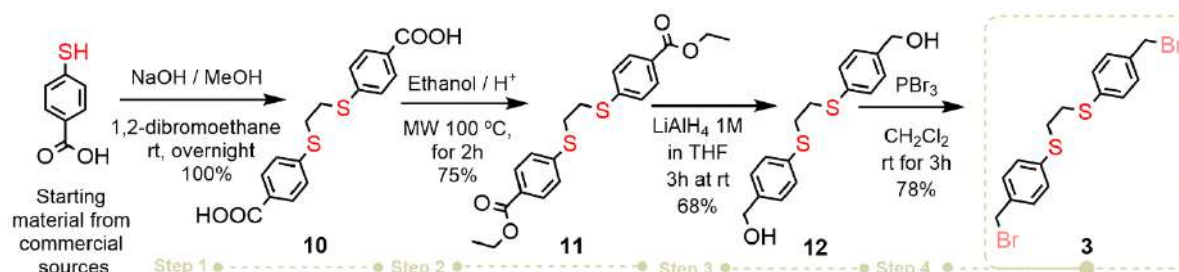
As an alternative pathway, we next tried the protection of the thiol group to allow the 4-methylbenzylthiol **1** to selectively react at the 4-methyl group. We tried to protect it with a thiourea¹¹² **4** and with a benzoyl group¹¹³ **6** (Scheme 1, c). Unfortunately, the hydrolysis of the protecting groups needs strong basic conditions (reflux in a NaOH solution at 100 °C for 4 hours) and did not allow an efficient reconversion to the thiol.

The protection of the 4-methylbenzylthiol **1** with the tert-butyldimethylsilane¹¹⁴ **7** successfully led to the bromide monomer **8** by radical bromination with NBS and AIBN using microwave irradiation (85 °C for 20 min). In addition, we decided to run first the nucleophilic substitution with DMAP, also under microwave irradiation (130 °C for 28 min), and then to form the bridge (Scheme 1, d). However, this last step did not proceed as expected due to the formation of the dimeric disulphide once the thiol was deprotected and preventing the dithioethane formation.



Scheme 1. Attempts for the synthesis of sulphur –containing linkers.

All the reported reactions did not give the desired dibromide linker and also presented several critical aspects from the point of view of the sustainability. The observed reactivity of the thiol group leads us to choose another starting material that could allow the synthesis of the bromo-functionalized linker using greener reaction conditions. It was finally found out the suitability of the 4-mercaptobenzoic acid, which after a series of derivatization steps gives the final product in good yields and in agreement with the *green* requirements. (Scheme 2)

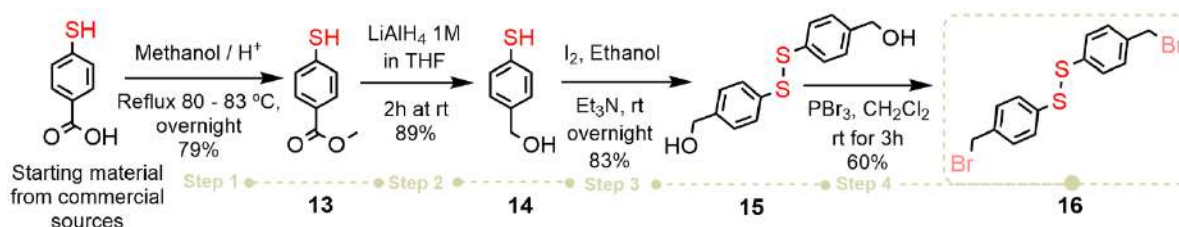


Scheme 2. Dithioethane linker synthetic pathway.

The dithioethane bromide linker **3**, was finally obtained while reacting the 4-mercaptobenzoic acid via the dimeric assembly using 1,2-dibromoethane (0.5 eq) in a basic solution of NaOH (2.4 eq) in methanol (5 mL), to form the bridge in **10**. Then followed the esterification with ethanol using microwave irradiation and sulfuric acid as catalyst. Finally, it took place the reduction to diol with LiAlH₄ (6 eq) and the nucleophilic substitution with PBr₃ (1.3 eq).

The overall chemical yield of the linker synthesis resulted to be of 40%. (For the detailed synthetic protocol see [the Experimental section 1.2](#)).

A similar approach has been applied to the synthesis of the dibromo-disulphide linker as reported in [Scheme 3](#).



Scheme 3. Disulphide linker synthetic pathway.

This time the acid (6.5 mmol) was firstly transformed in the methyl ester **13** by refluxing overnight with methanol (5 mL) and sulfuric acid as the catalyst (2 drops). Then, followed the reduction to alcohol with LiAlH₄ 1M in THF (1.8 eq) under an inert atmosphere for 2 hours at room temperature in THF (4 mL). Next, the dimerization with Iodine (0.5 eq) and triethylamine (0.3 eq) in ethanol (16 mL) and finally, the nucleophilic bromination with PBr₃ (1.3 eq) in dichloromethane (25 mL) for 3 hours at room temperature.

The dibromide linker was obtained with a 60% yield. However, the overall chemical yield of the linker synthesis was of 35%. (For the detailed synthetic protocol see [the Experimental section 1.3](#)).

1.3. Optimization of the final nucleophilic substitution.

The last step of the Choline Kinase inhibitors synthesis, consist of the nucleophilic substitution of the dibromide linker with the corresponding heteroaromatic heads. In literature, this step is carried out in a sealed tube with an aprotic solvent (acetonitrile or 2-butanone), and a stoichiometric quantity of reagents, that were allowed to react under stirring for 3 to 5 days at 100 °C in an oil bath.^{49-51,115-116}

In an attempt to improve the low energetic efficiency of this reaction that follows an S_N2 mechanism, we used other techniques that could shorten the time of heating. We tested the reaction under microwave irradiation, using a Q-tube apparatus (that allows heating at higher pressures than the MW), the autoclave, and also in a sealed tube heated on an oil bath as the reference. We also tested different solvents and solventless reactions, lower times and temperatures, and the use of inert atmosphere to see in which conditions we can still obtain the desired product in good yields while reducing time and energy costs.

We started the optimization process with the 4-pyrrolidinopyridine head because it is commercially available. As said, different methods were employed for heating the reaction (Table 1, entry 1-10), and it was found out that we could push the reaction towards a 53% of conversion just only in 24 hours when no solvent was used (Table 1, entry 10). It was almost as efficient as the literature methodology (Table 1, entry 4) but spent a fifth part of the time.

The use of an argon atmosphere just enhances the conversion in a 9% with respect to an air atmosphere (Table 1, entry 7 vs entry 8).

In the same way, the use of green solvents as the GVL^{117,118} rather than acetonitrile was not suitable because it was difficult to separate from the final product (Table 1, entries 5 and 6). The polar aprotic solvents like acetonitrile and 2-butanone did not speed up the reaction and the substitution seem to be mostly dependent on time (Table 1, entries 3 and 4).

In the dibromide dithioethane linker, the β-carbon attached to the primary halides is very hindrance (a phenyl group), making slower the reaction rate. The difficulty to interact increases when the nucleophilic head is also sterically hindrance and vice versa when they are smaller. This is also reflected in the chemical yields obtained, which are lower in the first and greater in the latter for the same reaction's conditions (Table 1, entries 16 and 18).

Thus, when we tried to apply the Q-tube or the MW methodologies with quinoline-based heads (Table 1, entries 12 and 13), the monosubstituted intermediates were mixed with the main product in the crude mixture, remaining with the final product when the recrystallization purification was performed. The steric hindrance and the higher hydrophobicity of such heads give room to uncompleted reactions. In fact, to avoid the formation of monobromated intermediates of reaction it was added 3 eq of the heteroaromatic head, to push the substitution in both parts of the linker.

The microwave started giving good results with the pyridinic head in the “cooling on” mode that allows continuous heating of the vial increasing the reaction efficiency¹¹⁹ (Table 1, entry 11). Unfortunately, this microwave set-up was no longer available and the alternative “cooling off” mode (Table 1, entries 1 and 12) was inefficient.

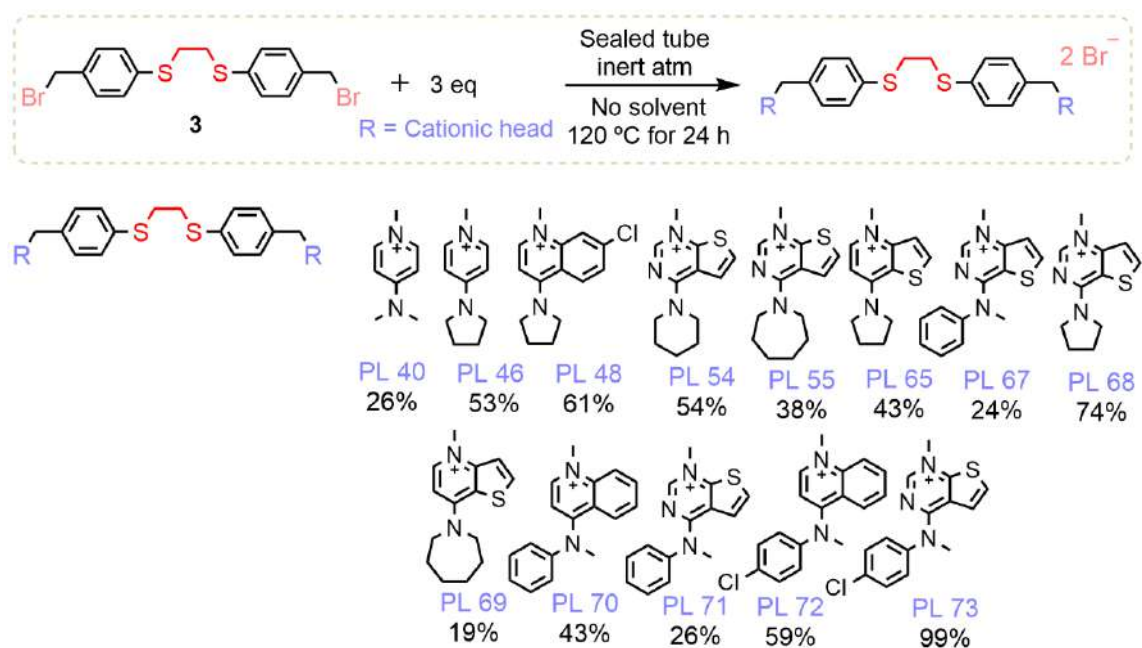
In conclusion, we just found reproducibility and wide applicability with the solventless sealed tube methodology heated over an oil bath for 24 hours at 120 °C and under an inert atmosphere.

Entry	Instrument	Solvent	Atm.	Heating	Time	Yield
1	MW	CH ₃ CN	Air	100 °C	2 h 30 min	9–17 ^c %
2	Autoclave	CH ₃ CN	Air	110 °C	24 h	9%
3	Q-tube	CH ₃ CN	Air	100 °C	2 days	11%
4	Sealed tube	CH ₃ CN	Air	100 °C	5 days	55%
5	Sealed tube	GVL ^a	Air	70 °C	1 day	33%
6	Sealed tube	GVL ^a	Air	150 °C	2 days	37% ^b
7	Sealed tube	no	Argon	100 °C	5 h 30 min	50%
8	Sealed tube	no	Air	120 °C	5 h	41%
9	Sealed tube	no	Air	120 °C	14 h	51%
10	Sealed tube	no	Air	120 °C	24 h	53%
11	MW ^c	CH ₃ CN	Air	85 °C	1 h 30 min	52%
12	MW	2-butanone	Air	140 °C	3 h	9%
13	Q-tube	2-butanone	Air	100 °C	5 days	6%
14	Sealed tube	no	Air	120 °C	24 h	61%
15	Sealed tube	no	Air	120 °C	16 h	40%
16	Sealed tube	no	Air	120 °C	24 h	54%
17	Sealed tube	no	Air	120 °C	15 h	31%
18	Sealed tube	no	Air	120 °C	24 h	38%

Table 1. Optimization of the last synthetic step.

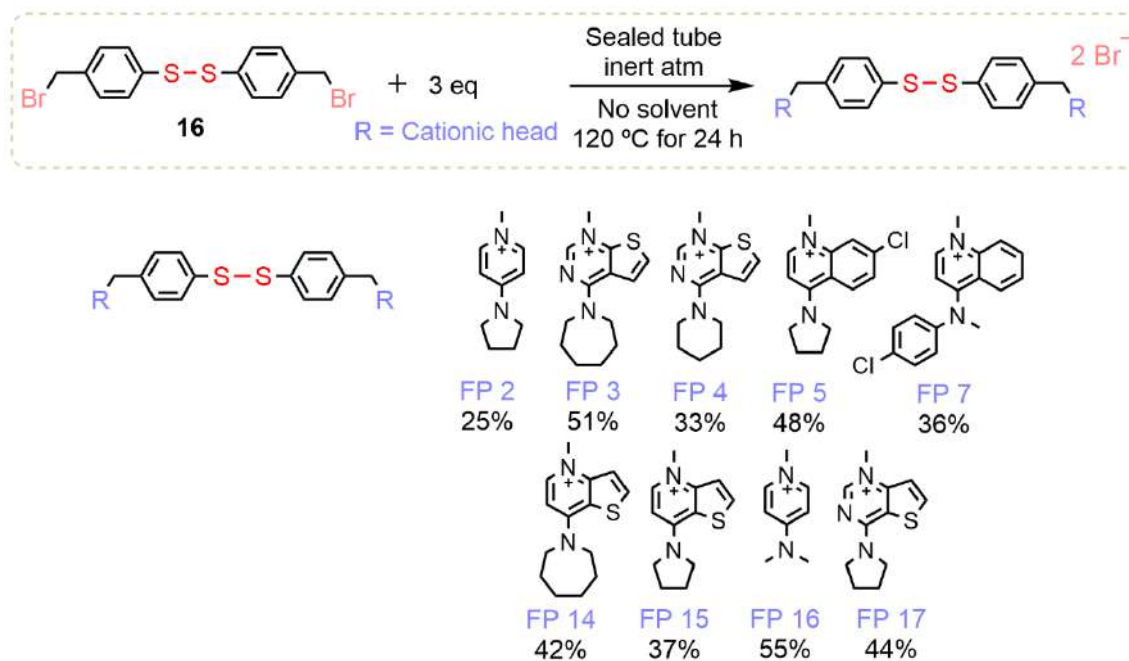
In yellow is highlighted the reported methodology and in green is highlighted the best conditions obtained for each of the studied heads.^a Gamma-valerolactone. ^b Difficult to remove the solvent. ^c Cooling ON mode.

Then, this protocol has been applied to a variety of cationic heads to yield the desired inhibitors as reported in Scheme 4.



Scheme 4. Yields of the final products obtained with the dithioethane linker.

Similarly, the disulphide linker has successfully reacted while using the optimized procedure, allowing the obtention of derivatives with different quaternary amines heads (Scheme 5).



Scheme 5. Yields of the final products obtained with the disulphide linker.

1.4. Green metrics, quantification of sustainability.

Over the years there has been a lot of discussion about the definition of a *green* process. Initially, a green process was defined as the one that follows the Twelve Principles of Green Chemistry, proposed by Anastas and Warner in 1998¹²⁰. Nevertheless, it was still very subjective to compare processes based on them.

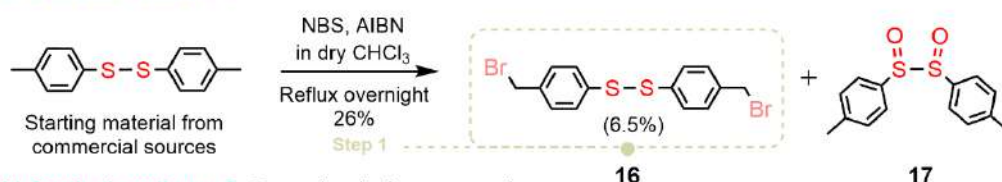
Which is greener, a multi-step reaction with higher yields or another one with lower yields but that avoids the use of toxic solvents? To objectively respond to this question arose the green metrics. Several modes of quantification appeared that could be grouped in those that focus on the maximum transformation of the starting materials (as reflected in the Atom Economy)¹²¹ or those that focus on the quantity of waste generated (as calculated with the E(nvironmental)-factor)¹²². The latter became one of the metrics most used as an E-factor equal to zero means zero waste, being more intuitive to interpret. However, it was not enough because it was not only important the quantity (Kg) but also the nature of that waste and its environmental impact.

Then the problem was the lack of data about the toxic effects of chemicals on human's health and their accumulation in nature. Hopefully, in the era of big data lot of solutions appears based on the massive data collection of known environmental risk, cost, and impact of chemicals. For example, we can point out the software EATOS (Environmental assessment tool for organic synthesis)¹²³ developed by Eissen and Metzger in 2002 or the free webpage EcoScale calculator¹²⁴ developed by van Aken and co-workers in 2006 and used herein.

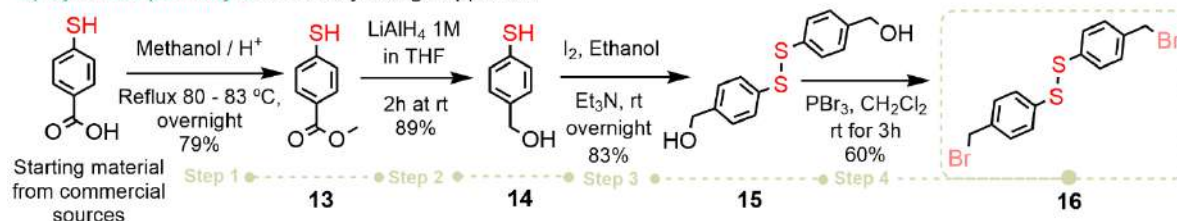
In the first part of the environmental impact assessment, we decided to compare the syntheses of the disulphide linker following both a retrosynthetic methodology and a green by design approach (Scheme 6, a and b) to assess the pros and cons and using some *green metrics* for evaluation. The retrosynthetic process, was usually used with other linkers as the phenoxyethane⁵¹ and the bipyridinic⁵⁰ through a one-step radical bromination of the commercially available starting materials.

We used the green metric E-factor for the measurement of the waste produced and the EcoScale calculator to estimate the environmental impact.

a) Synthetic pathway 1: Retrosynthetic approach



b) Synthetic pathway 2: Green by design approach



Scheme 6. Traditional (a) and proposed sustainable (b) procedure to achieve the brominated disulphide linker.

The traditional retrosynthetic method started from the commercially available p-tolyl disulfide (1eq), that together with NBS (2.04 eq) and AIBN (0.08 eq) in anhydrous chloroform (30 mL) was refluxed during one day under an Argon atmosphere. Then, the crude solvent was removed under pressure and the remaining red oil was extracted with $\text{CH}_2\text{Cl}_2/\text{H}_2\text{O}/\text{brine}$ (x3). The organic phase was dried with Na_2SO_4 , filtered, and removed under pressure. However, the radical bromination is not selective and several subproducts were formed. Thus, the obtained crude

was purified by chromatographic column in silica gel as stationary phase and 9.75 Hex/0.25 EtOAc as mobile phase. The pure product was difficultly isolated and a mixture of the dibromide **16** and the oxidated subproduct 4-methyl-phenyl-disulfoxide **17** was obtained in a 26% yield as a light-yellow solid.¹²⁵

Taking into account that the dibromide linker **16** had a 25% of impurity of an unreactive by-product **17**, the final yield decreases until 6.5% (Scheme 6, a).

The E-factor was calculated for each synthetic step (Scheme 6) as the coefficient between the total mass of waste and the mass of the final product, in mg. The advantage of this metric is that could be easily applied to a multistep process, that we report as *Total* in the bar chart. However, unlike the AE, the E-factor could be calculated just once the reaction is experimentally done and so, is not a good tool for waste prediction. Its strength is that it takes into consideration the use of auxiliary solvents of workup and purification. Solvents have been demonstrated to strongly matter in the environmental damage, waste and cost generated in an industrial process.¹²⁶ That is why we chose to measure the E-factor rather than the Atom Economy. (For a detailed calculation of the E-factor see Experimental section 1.9).

On the other hand, the free software EcoScale calculator (<http://ecoscale.cheminfo.org/calculator>) is based on assigning a range of penalty points to six parameters that can be: the yield, cost, safety/hazards, technical setup, reaction conditions, workup and purification, but also can be included others by the user if needed. The software subtracts points from a total of 100 when conditions are not *green*, establishing the value of a particular synthesis. In that case, lower values mean harmful procedures. The EcoScale value was calculated for each synthetic step reported in Scheme 6. (For a detailed calculation of the EcoScale values see Experimental section 1.10).

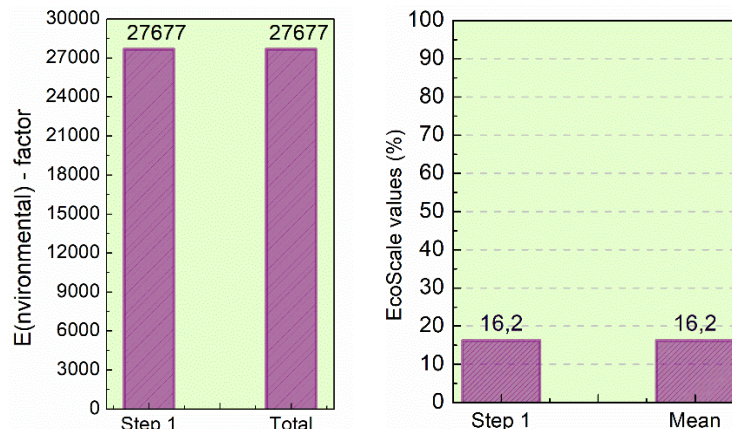


Figure 23. Disulphide linker E-factor (left) and EcoScale value (right) for the retrosynthetic pathway.

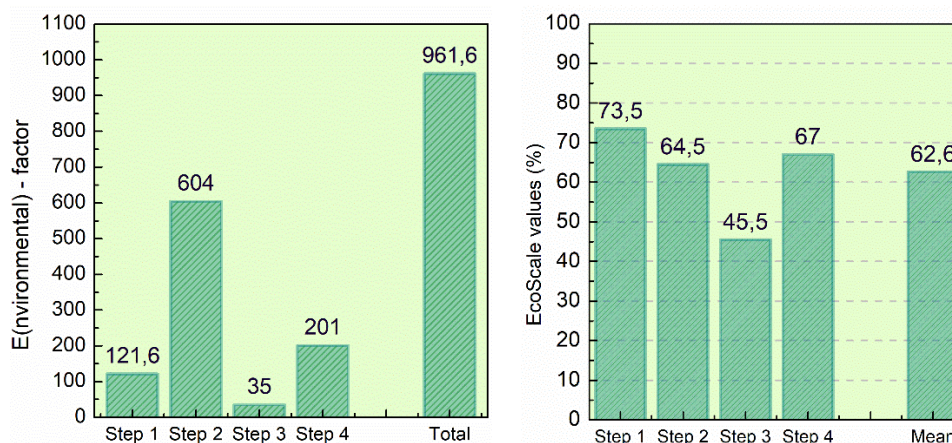


Figure 24. Disulphide linker E-factor (left) and EcoScale value (right) for the green-by-design pathway.

As represented in Figures 23 and 24, it was satisfactory disclosed that the disulphide linker synthetic pathway 2 (Scheme 6, b) produces 29 times less waste than the synthetic pathway 1 (Scheme 6, a), and that there is a 46% improvement in the choice of eco-friendly reagents and reaction conditions.

It can be highlighted the evident contribution that solvents have on synthetic pathway 1 due to the need for chromatographic purification after the radical bromination that produces lots of subproducts (Step 1). The bar chart allows us to quickly recognize which step of the synthesis could be further improved. For example, the synthetic Step 2 in the green by design pathway (Figure 24) produced the biggest quantity of waste of the overall process.

That step corresponds to the reduction from ester to alcohol, which needs acidic solutions to dissolve the lithium salts and their separation of the final product by several extractions with water to clean the organic phase of the aluminium hydroxide and lithium alkoxide rests.

In addition, it could be also pointed out Step 3 of the green procedure, which has the best E-factor but the worst EcoScale value in comparison with the other reaction steps. As so, it could be thought a change in the dimerization step in which instead of iodine, we could use an oxidant catalyst more environmentally benign, as the K-OMS-2. Actually, we tested it using strong reflux conditions (105 °C for 6 hours) with CPME but the reaction was not completed.

As expected, lower E-factor and higher EcoScale values are obtained for the synthetic pathway 2 (961.6 vs 27677 and 62.6 vs 16.2, for the E-factor and EcoScale values in pathways 2 and 1, respectively).

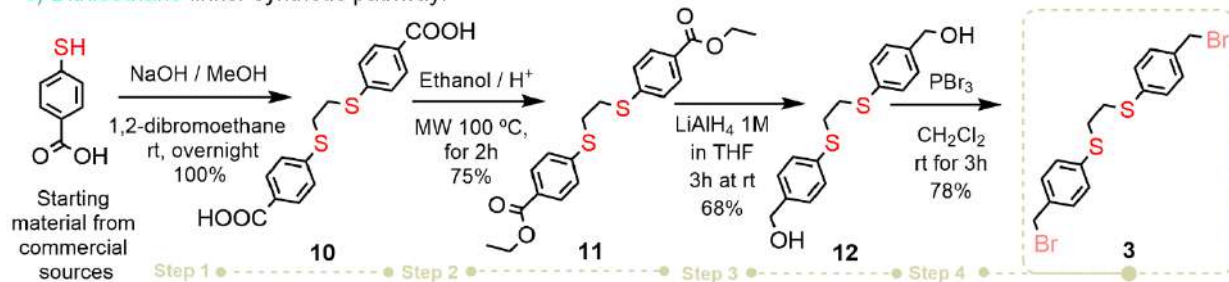
The overall chemical yield for the disulphide linker synthesis is 6.5% in pathway 1 and 35% in pathway 2 (Scheme 6). Therefore, together with an improvement in sustainability, we reach a 28.5% increment of the chemical yield.

In conclusion, longer multi-step synthesis doesn't mean more waste if reactions are selective and there is no need for intermediates purification.

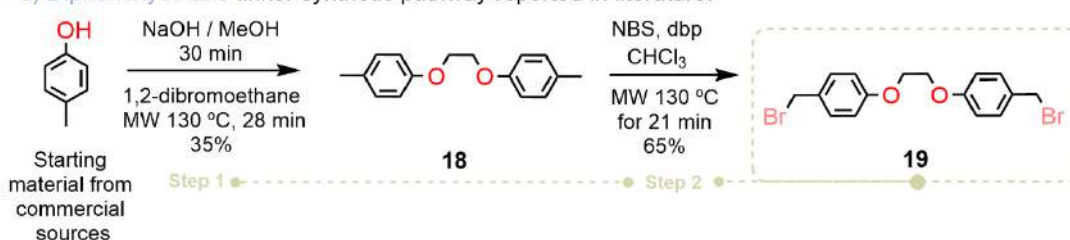
Next, to further evaluate the suggested improvement, we compare the dithioethane synthesis with the synthetic pathway reported in the literature for the homologous linker diphenoxyethane⁵¹, which led to the dibromide derivative **19** in an overall chemical yield of 23% (Scheme 7, d).

From the efficiency point of view, our designed pathway (Scheme 7, c) with an overall yield of 40%, seems to be superior to the reported in the literature. However, the diphenoxyethane linker has less derivatization and intermediates, obtaining the product in two steps while 4 steps are needed for obtaining the dithioethane product.

c) Dithioethane linker synthetic pathway.



d) Diphenoxyethane linker synthetic pathway reported in literature.



Scheme 7. Comparison of the bioisosteric linkers' synthesis.

(c) Dithioethane and (d) diphenoxyethane homologous

Despite that, sustainability also considers the toxicity, the environmental effect of the waste generated and the energy usage so that, we similarly calculated the E-factor and Eco values as reported before.

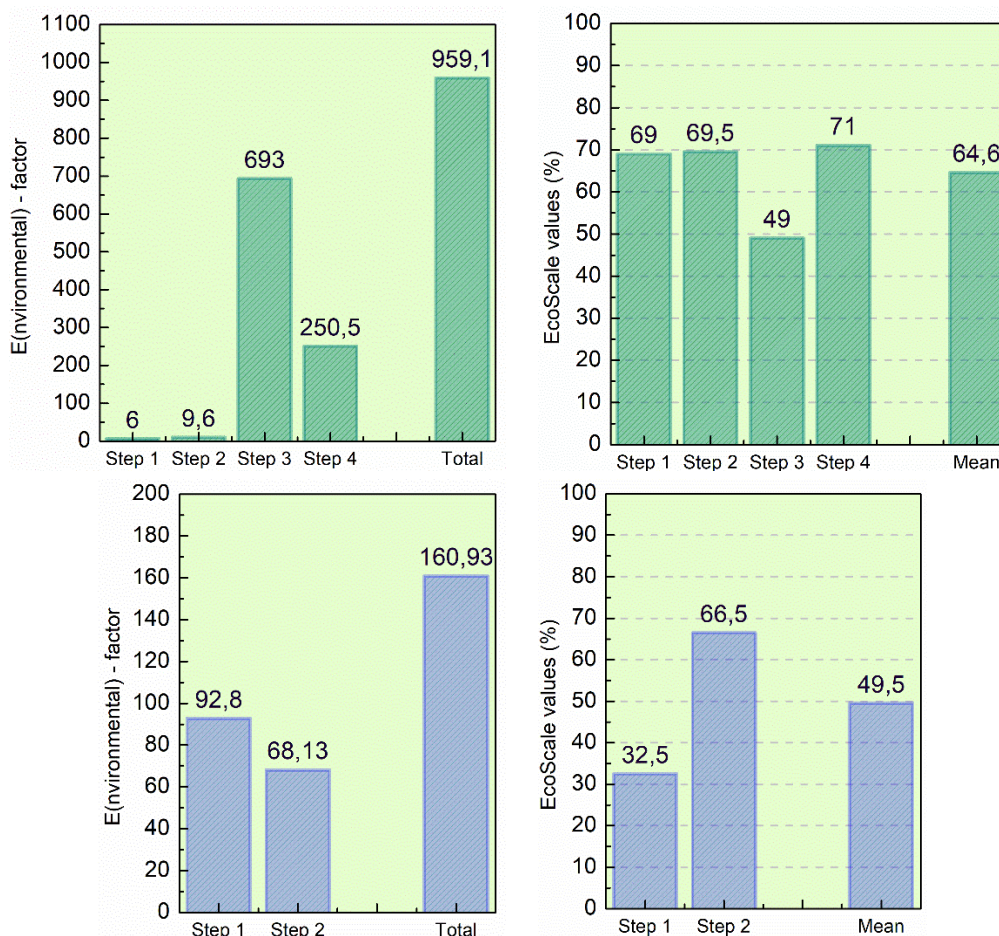


Figure 25. Dithioethane linker (green bar charts) and diphenoxyethane linker (blue bar charts) representation of calculated E-factor (right part) and EcoScale (left part) values for each synthetic step.

The published synthesis of the diphenoxyethane derivatives ⁵¹ has improved using microwave irradiation, which allows for selectivity and obtain the purified products just by precipitation. Thus, this time higher derivatization means more waste and so, our proposed green synthesis produces 6 times more residues than the reported in the literature for its oxygen homologous (Figure 25, right part).

Also, we have to consider the different reactivity of the O and S that limits the synthetic methodologies comparison.

Nevertheless, even with the higher levels of waste produced in the dithioethane synthesis, we get a 15% improvement in the whole environmental impact generated (Figure 25, left part). That percentage makes the difference between an acceptable (EcoScale value > 50) and an inadequate (EcoScale value < 50) reaction, for the dithioethane and diphenoxyethane linkers, respectively.

In conclusion, our synthesis generates more residues for unit of product, but those are less harmful to the environment in comparison with the reported pathway in literature.

2. H ChoK α enzymatic inhibition.

As a mandatory step in drug design, it is necessary to test if the new drugs synthesized are able to effectively improve the predecessor's activity towards the biological target. The *in-vitro* inhibition of the isolated enzyme is a key assay that gives information about the suitability of structural binding without taking into account the biological barriers as the cell membrane permeation.

These experiments were developed in collaboration with Prof. María Paz Carrasco Jiménez of the Department of Biochemistry and Molecular Biology I at the University of Granada during the PhD abroad period.

Compounds were prepared at different concentrations by serial dilutions of a stock in DMSO. The prepared inhibitors together with a buffer solution, cofactors (ATP and Mg^{2+}) and radiolabelled ^{14}C (from methyl) choline, were incubated with the pure enzyme (37 °C for 15 min). After this time, the enzyme was denaturalized immersing the vials in boiling water. The quantity of labelled choline transformed into labelled phosphocholine was determined by the reaction's aliquots separation by chromatography in silica gel plates, and then, their exposure to iodine vapour, to identify the phosphocholine and choline spots. Finally, the phosphocholine in the silica plates was scraped and quantified by the measurement of radioactivity in a liquid-scintillation counter.

Regarding the inhibitory values of the dithioethane library, reported in [Table 2 \(at the top\)](#), we decided to discuss the results classifying the compounds based on the cationic heteroaromatic heads. Starting with the pyridine cationic heads, compounds **PL 40** and **PL 46** showed poor solubility in DMSO and water, so that they were discarded as the results would not be reliable because the concentration homogeneity was not guaranteed.

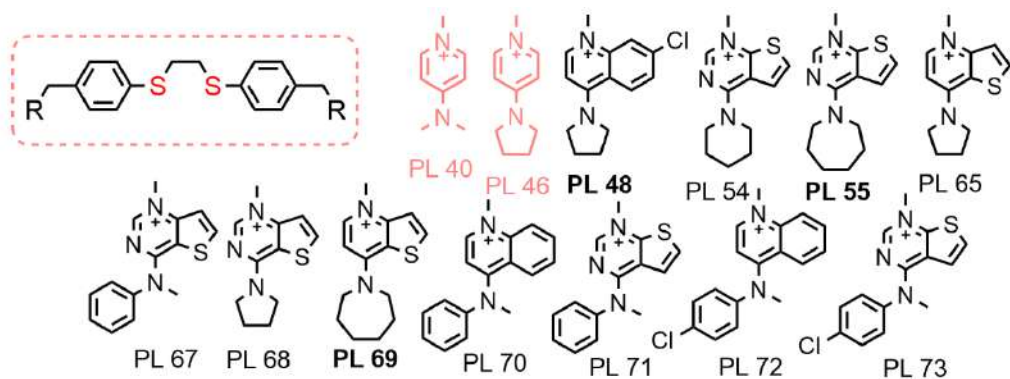
The thieno[2,3-d]pyrimidine cationic head of compounds **PL 54**, **PL 55**, **PL 71** and **PL 73**, shows a wide range of IC_{50} values from 0.66 to 4.37 μM . When the cationic head is substituted by a cycloalkyl amine (**PL 54** IC_{50} = 4.37 μM and **PL 55** IC_{50} = 0.66 μM), the inhibition drastically improves with the size of the ring. On the other hand, when the cationic head is substituted by an aromatic amine (**PL 71** IC_{50} = 1.43 μM and **PL 73** IC_{50} = 0.71 μM), lipophilicity seems to play a key role as the introduction of a chlorine atom double the inhibitory activity (**PL 71** cLog P = 7.07 and **PL 73** cLog P = 8.03).

The thieno[3,2-d]pyrimidine cationic head of compounds **PL 67** and **PL 68**, shows an unexpected behaviour as they are, in general, less potent than their isomers. However, they follow the trend (**PL 68** IC_{50} = 1.35 μM and **PL 67** IC_{50} = 2.6 μM), and the substitution in 4 with a cycloalkyl amine drives to better inhibitory values than with an aromatic amine.

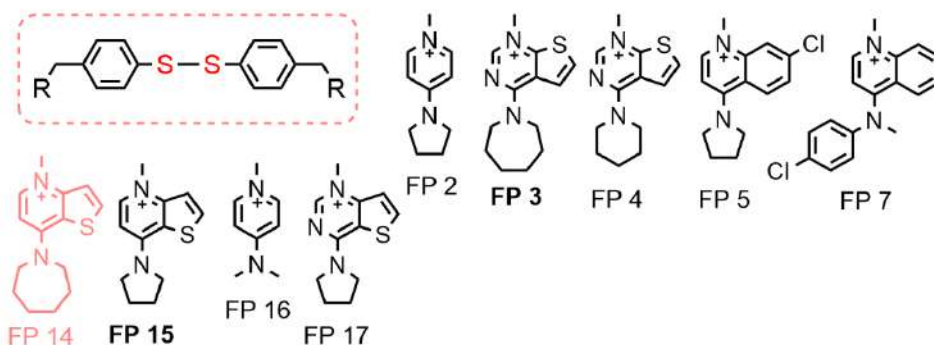
The thieno[3,2-b]pyridine cationic head of compounds **PL 65** IC_{50} = 1.01 μM and **PL 69** IC_{50} = 0.64 μM , shows a higher activity than their isosteric counterparts **PL 68** (IC_{50} = 1.35 μM) and **PL 55** (IC_{50} = 0.66 μM), respectively. The slightly inhibitory improvement is in agreement with an increase of the lipophilic profile due to the absence of the N^3 of the pyrimidine isosteres. The inhibitory activity is in line with the increasing size of the *para*-substituted cycloalkyl amine ring.

Finally, the quinolinic cationic head of compounds **PL 48**, **PL 70** and **PL 72**, shows good inhibitory values in the range of 0.66 to 1.72 μM . In this subfamily of compounds, the substitution with a cycloalkyl amine in **PL 48** gives to higher inhibitory values (IC_{50} = 0.66 μM) as previously noted.

Otherwise, the *para* substitution with an aromatic amine shows less inhibitory potency (**PL 70** IC_{50} = 1.72 μM and **PL 72** IC_{50} = 1.02 μM) but agrees with the lipophilicity values so that the introduction of a chlorine atom in **PL 72** improves the lipophilicity and also the inhibition.



Compound	% Inhibition Human ChoK α 1			IC ₅₀ (μ M)	Mw	*Log P
	0.2 μ M	1 μ M	5 μ M			
PL 40	--	--	--	INSOLUBLE	676.57	3.41
PL 46	--	--	--	INSOLUBLE	728.65	4.12
PL 48	30.54 \pm 3.02	63.39 \pm 2.18	100	0.658 \pm 0.067	897.65	7.07
PL 54	ND	52.65 \pm 4.07	86.48 \pm 2.37	4.373 \pm 0.605	870.84	5.96
PL 55	39.09 \pm 6.94	79.03 \pm 0.98	95.20 \pm 0.14	0.658 \pm 0.079	898.90	6.50
PL 65	ND	57.19 \pm 11.65	90.40 \pm 0.18	1.013 \pm 0.147	840.81	6.06
PL 67	15.23 \pm 4.81	58.44 \pm 0.17	ND	2.595 \pm 0.658	914.86	6.84
PL 68	16.11 \pm 5.62	70.96 \pm 9.56	87.63 \pm 1.51	1.351 \pm 0.041	842.79	5.28
PL 69	4.09 \pm 2.79	66.97 \pm 4.91	97.48 \pm 0.55	0.638 \pm 0.111	896.92	7.12
PL 70	28.52 \pm 4.41	55.67 \pm 1.19	91.96 \pm 0.13	1.723 \pm 0.021	900.84	7.69
PL 71	51.69 \pm 1.02	74.96 \pm 7.55	92.44 \pm 1.37	1.426 \pm 0.270	914.86	7.07
PL 72	66.31 \pm 2.67	87.14 \pm 4.04	97.58 \pm 0.38	1.024 \pm 0.117	969.72	8.7
PL 73	9.92 \pm 0.47	64.38 \pm 0.39	92.43 \pm 0.38	0.709 \pm 0.067	983.74	8.03



Compound	% Inhibition Human ChoK α 1		IC ₅₀ (μ M)	Mw	*Log P
	1 μ M	5 μ M			
FP 2	70.29 \pm 0.34	87.98 \pm 0.66	ND	700.60	3.15
FP 3	88.01 \pm 0.93	96.28 \pm 0.01	ND	870.84	6
FP 4	76.12 \pm 4.08	89.47 \pm 4.55	ND	842.79	5.41
FP 5	54.91 \pm 0.52	87.56 \pm 0.30	ND	869.60	6.39
FP 7	72.97 \pm 6.41	97.28 \pm 0.80	ND	941.67	7.86
FP 14	--	--	INSOLUBLE	868.87	6.64
FP 15	78.96 \pm 2.09	92.23 \pm 0.05	ND	812.76	5.55
FP 16	51.45 \pm 11.75	ND	ND	648.52	2.90
FP 17	65.43 \pm 0.88	86.57 \pm 0.33	ND	814.74	4.79

*Calculated with <http://www.swissadme.ch/> as an average measure of five predictions methods. Table 2. Dithioethane (at the top) and disulphide (at the bottom) libraries' inhibitory activity and cLog P. Insoluble molecules are coloured in red.

To sum up, best results are obtained with compounds **PL 55** (thieno[2,3-d] pyrimidine family), **PL 69** (thieno[3,2-b] pyridine family) and **PL 48** (quinolinic family) with an IC₅₀ in the low μM range (from 0.64 to 0.66 μM). As a common feature, we can highlight the presence of a cycloalkyl amine at 4 position, being the azepane the most suitable one.

As a general trend, it is possible to point out that the aromatic amine (*N*-methyl aniline) and its derivatives are worse substituents at the *para* position of the cationic head than the cycloalkyl amines (pyrrolidine, piperidine or azepane). The activity of the cycloalkyl amines substituents improves with the size of the ring (azepane > piperidine > pyrrolidine), and in the aromatic amines with the increased lipophilicity.

Regarding the disulphide library of compounds, the inhibitory values also reported in [Table 2 \(at the bottom\)](#), were discussed following the previous classification.

This time, the pyridine family was able to be tested. Compounds **FP 2** and **FP 16** (70.29% and 51.45% of inhibition at 1 μM, respectively) show better inhibition when a cyclic amine (pyrrolidine) rather than an aliphatic one is used as the *para* substituent.

The thieno[2,3-d] pyrimidine cationic head of compounds **FP 4** and **FP 3** (76.12 % and 88.01% of inhibition at 1 μM, respectively), shows an increase of activity while the cycloalkyl amine ring size does (from piperidine to azepane).

The thieno[3,2-d] pyrimidine cationic head of compound **FP 17** shows a 65.43% of inhibition at 1 μM. It is an isomer of the previously mentioned family and in comparison to them; the inhibitory activity is lower due to the smaller cycloalkyl amine (pyrrolidine). Also, the cationic head lacks binding affinity as is noticed in the dithioethane library counterparts (**PL 67** and **PL 68**).

The thieno[3,2-b] pyridine cationic head of compound **FP 15**, with a 78.96% of inhibition at 1 μM, is substituted at the *para* position by the cycloalkyl amine pyrrolidine. The compound **FP 14** with the cycloalkyl amine azepane, was insoluble and thus, unable to be tested. As previously noted, this family shows better results than its isoster **FP 17** that is less lipophilic.

Finally, the quinolinic cationic head of compounds **FP 5** and **FP 7** (with 54.91% and 72.97% of inhibition at 1 μM, respectively), show a cycloalkyl amine (pyrrolidine) and an aromatic amine as a substituent, respectively. However, contrary to the dithioethane library, the aromatic amine in **FP 7**, is a better substituent for the enzymatic inhibition. Although these compounds' family are the most lipophilic of this series, they are not the most actives.

The best inhibitory activity was achieved with compounds **FP 3** (thieno[2,3-d]pyrimidine family) and **FP 15** (thieno[3,2-b]pyridine family). We can highlight the presence of a cycloalkyl amine at 4 position in both of them, bigger (azepane) when the cationic head is more polar (in **FP 3**) and smaller (pyrrolidine) when it is more lipophilic as in **FP 15**.

In general terms, the disulphide library shows greater inhibition when the cycloalkyl amine ring of the *para* substituent increase in size. The thieno[3,2-d] pyrimidine is the worst cationic head while the isomer thieno[2,3-d] pyrimidine is the best. Quinolinic derivatives, however, are more actives when are substituted in *para* position with aromatics amines.

Both libraries concur with the lead compound chemical structure. The most actives compounds **PL 55** and **FP 3** agree on the structural features that give room to high inhibitory potency in both series.

The dithioethane library is, however, more lipophilic than the disulphide one due to the linker nature, and the antiproliferative assays in tumour-cell lines would be essential to emphasize one library to the other.

Comparing the homologous inhibitors in both libraries (Figure 26), it is a remarkable fact that at 5 μM the % of ChoK inhibition is almost equivalent inside each pair of homologous.

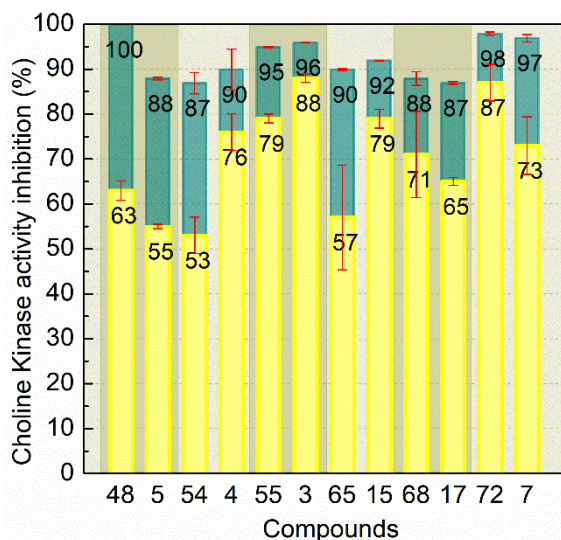


Figure 26. Comparison between the dithioethane and disulphide library's homologous inhibitors. In yellow is represented the inhibitory activity at 1 μM and in teal the inhibitory activity at 5 μM .

Nevertheless, when they are tested at 1 μM , the % of ChoK inhibition is higher in the disulphide library. The exceptions to this trend are compounds **PL 72**, **PL 48** and **PL 68** from the quinolinic and thieno[3,2-d]pyrimidine families, respectively. For compounds **PL 72** and **PL 68**, it could be proposed an allosteric binding due to the disagreement between their physicochemical properties and the inhibition rate in comparison with the rest of the group.

For example, the more lipophilic quinolinic family show less inhibitory activity while in the other families an increase of lipophilicity is translated into a better inhibition.

In the thieno[3,2-d]pyrimidine family, however, the sulphur arrangement gives room to a loss of activity, which

may be caused for a lost interaction inside the catalytic side or an allosteric and less effective binding.

To conclude, we would like to compare the inhibition rate of the previously synthesized bioisosteres with the aim of analysing the improvements achieved with the proposed linker.

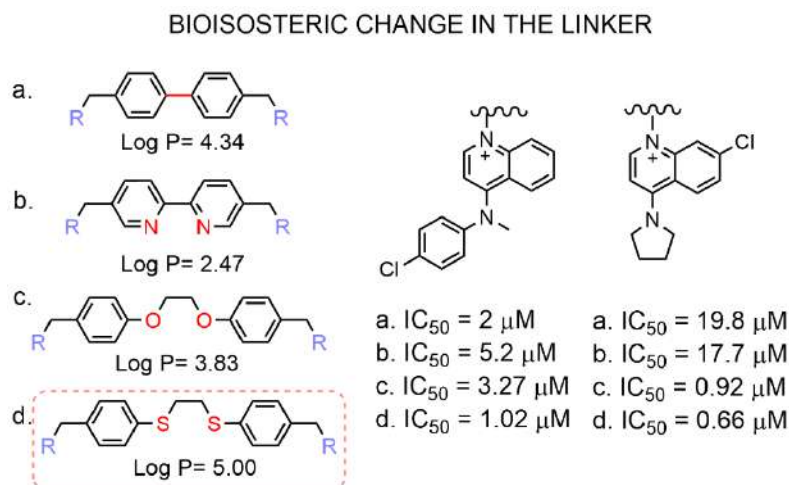


Figure 27. Effect of the linker bioisosteric exchange in the inhibitory activity towards the ChoK.

For that purpose, we have chosen two substituents present in all the discussed libraries. As reported in the Figure 27, starting with the general scaffold of **HC-3** with the biphenyl linker ³⁶, several modifications have been proposed to increase the inhibitory activity passing through bipyridinic ⁵⁰, diphenoxyethane ⁵¹ and our proposed dithioethane linker.

All of them are symmetrical and biscationic compounds and, with respect to the IC_{50} values, it is observed a remarkable improvement when using our designed linker (Figure 27, d). The key to success resides in the hydrophilic/lipophilic equilibrium and the sulphur free-electrons pairs, that can further interact in the catalytic site.

3. Modelling compound-protein interactions.

Computational studies are gaining importance nowadays as most accurate algorithms have been developed and easier to handle software are at the service of little expertise public.

In collaboration with Prof. Laura Goracci of the Department of Chemistry, Biology and Biotechnology at the University of Perugia, preliminary computational studies have been performed using *Flapdock*, with the aim of gaining information on the potential binding mode of synthesized compounds of interest over the enzyme catalytic pocket and hypothesizing how their binding interactions relate to the in vitro inhibitory activity.

In this study, the FLAPdock module in the FLAP (Fingerprints for Ligands and Proteins) software was used. Briefly, FLAPdock is an algorithm for flexible fragment-based docking based on GRID Molecular Interaction Fields (MIFs) similarities,^{127,128} combined with classical energetics.¹²⁹ Indeed, the docking option in Flap divides the ligand into fragments and dock them in the target, basing on the affinity between their molecular interaction fields. In this manner, the most suitable conformation is adopted for the first fragment and consecutively until the whole molecule is docked. Then, the predicted poses are scored according to the MIFs similarity and dissimilarity, and the energetic terms (internal and external Lennard-Jones terms and Electrostatic terms).¹³⁰

Although FLAPdock allows to use the WaterFLAP waters to guide the docking, in this preliminary study structural waters were not considered in docking. In addition, during GRID MIFs generation the flexibility of aminoacidic residues is taken into account, but the backbone is maintained fixed. Therefore, the backbone of the catalytic pocket as in the crystal structure of human choline kinase alpha in complex with **HC-3** and ADP (PDB ID: 3G15) was used as a rigid entity in docking, possibly limiting the interaction towards the new ligands especially if very different from the X-ray ligand.

We assumed that binding occurs in the choline catalytic pocket without considering possible allosteric interactions. In the enzyme pocket, apart from choline coexist the Mg atoms and ADP cofactors, in a more deeply cage (ATP binding site) that is opened and intercommunicated with the catalytic pocket. For that reason, we decided to maintain the Mg atoms attacked when doing the docking studies (see the [Experimental section 1.11](#) for details).

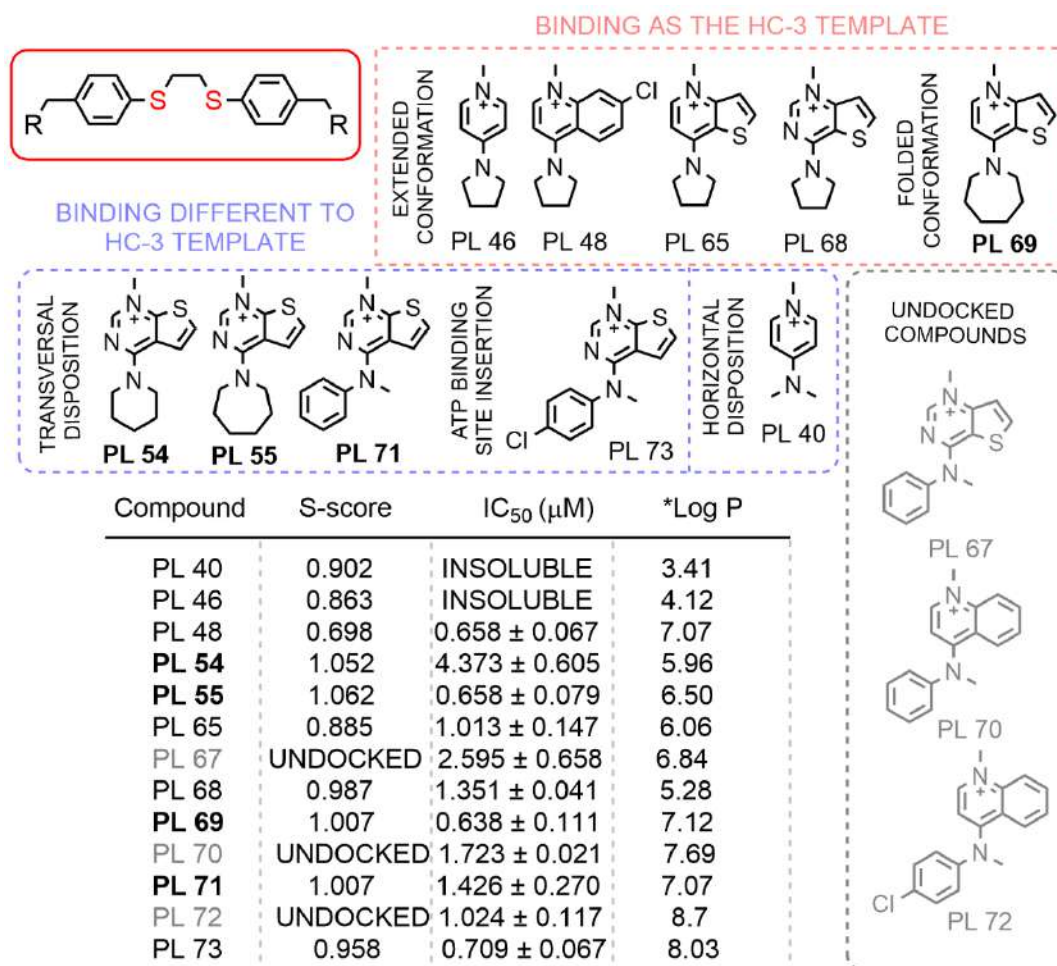
In an effort to mimic the biological events, we determine that docking an empty cavity without cofactors could lead to an erroneous model. Considering that in the inhibitory assays it is used ATP and Mg over the Km concentration, it could be thought that the active enzyme is phosphorylated. For that reason, in the following study, the most vicinal Mg atoms are considered in terms of spatial volume and interaction with the library of compounds.

Several examples about Flapdock applications on ligand-protein interactions are available, proving its reliability as a docking method.^{129,131-132}

3.2 Dithioethane library of compounds.

The library of compounds with the dithioethane linker will be first discussed. It is composed of biscationic symmetrical molecules that occupy the whole choline-binding site and, in most cases, shown one half of the molecule exposed to the solvent.

A general overview of the compound's classification according to its mode of binding and the values herein discussed are reported below (Table 3).



* Calculated using <http://www.swissadme.ch/> as an average of five predictions methods.

Table 3. Classification of the dithioethane library binding mode and reported S-score, IC₅₀ and cLog P values for comparison.

Compounds **PL 46**, **PL 48**, **PL 65** and **PL 68** are docked in the catalytic pocket in the same way as the template inhibitor **HC-3**. They adopted an extended conformation that points the half of the ligand outside the pocket. In the outer fragment, no binding or slightly interaction with the residues of the enzyme surface was observed.

This group of ligands get well inserted in the deep hydrophobic cavity of the choline pocket, as the **HC-3** template does. They established π - π stacking and cation- π interactions with residues Trp 420, Trp 423, Tyr 333, Tyr 354, Try 440 and Phe 435.

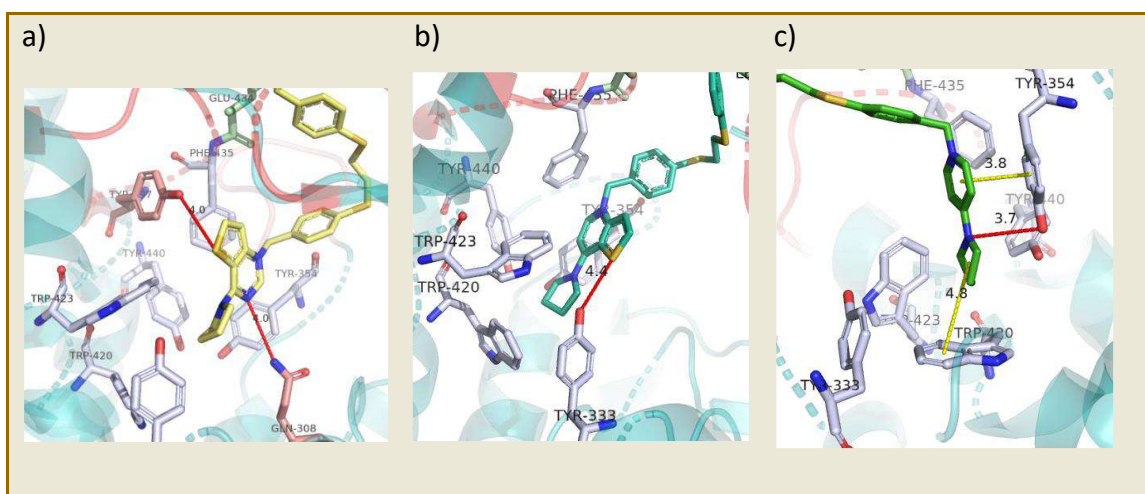
At the bottom of such cavity, there is a cationic acceptor region as shown by the NM3 probe (see Experimental part section 1.11), to which all heads stay anchored due to the cationic charge resonance. This part of the pocket is enriched by acidic residues (Asp 306 and Glu 349) that are deprotonated at physiological pH, and as so negatively charged.

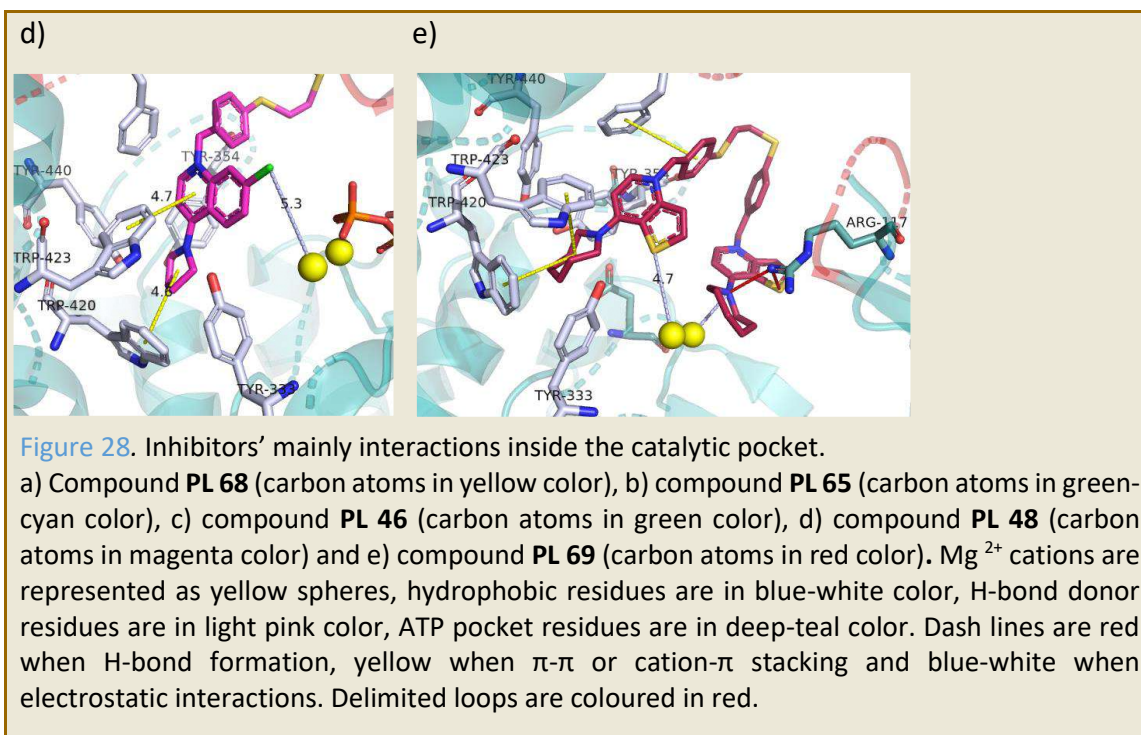
From this group, compound **PL 68** is the one with a higher *S*-score (0.987). The 4-(1-pyrrolidinyl) thienopyrimidine moiety overlaps well with two H-bond donors MIFs of the enzyme, at the sulphur and the N³ atom of the thienopyrimidine, that could correspond to interactions with Tyr 437 and, Tyr 354 or Gln 308, respectively (Figure 28, a). For that reason, it could be more stabilized in the catalytic site than its isoster **PL 65** (*S*-score: 0.885) with the 4-(1-pyrrolidinyl) thienopyridine moiety (Figure 28, b). However, this fact seems not to be relevant in the biological media. Compound **PL 65** has an IC₅₀= 1.01 μM and a cLog P= 6.06, while **PL 68** has an IC₅₀= 1.35 μM and a cLog P= 5.28. The lipophilicity plays a bigger role than the H-Bond formation in the pocket binding.

Regarding compound **PL 46**, it is mainly stabilized by π-π and cation-π hydrophobic interactions with the catalytic site as previously reported and could form an H-bond with the Tyr 354 (*S*-score: 0.863; cLog P= 4.12) (Figure 28, c). However, it was insoluble, and its inhibitory activity couldn't be tested.

Finally, compound **PL 48** is also well inserted in the choline hydrophobic cage. The pose obtained exposes the chlorine atom of the 7-chloroquinoline moiety towards the Mg ions and the ADP (at 5 Å of distance) (Figure 28, d). The *S*-score with a value of 0.698, is the lowest of the group but however, it shows the highest IC₅₀= 0.66 μM. This disagreement could be explained due to the presence of a hindrance group (the chlorine) near to the Mg atoms, that could displace the attached coordination water, destabilizing their binding to the enzyme. Another hypothesis is the formation of a complex with the Mg cations, blocking the phosphor-transfer. The cLog P=7.07 is the highest of this series, which seems to be the key for the best anchor in the binding site and thus the best inhibition.

The linker dithioethane can adopt an anti or synclinal conformation. It confers to the compounds' second half a wide range of interactions in the inter-loop environment (**Loop 1** between sheet β1 and β2 in the N-terminal domain, **Loop 9** between helix α9 and α10 in the C-terminal domain and **Loop 8** between sheet β11 and β12 in the C-terminal domain), adopting different orientations in each pose. As a common feature, the outer cationic heads do not interact much and are exposed to the solvent getting oriented towards the Glu 357 or Glu 434 negatively charged residues. However, the phenyl groups attached to the linker can still make hydrophobic interactions with Leu 120 (loop 1), Ile 433 (loop 9) or Phe 361 (loop 8).





Compound **PL 69** constituted a subgroup in this classification, because it deeply interacts with the hydrophobic catalytic cage as **HC-3** but presents a folded conformation (Figure 28, e). This disposition allows further interactions of the second cationic head in the pocket which is also captured in the S-score value of 1.007. The flexibility of the linker allows this synclinal conformation that is also observed in compound **PL 65**. Nevertheless, the probability of **PL 65** to adopt a folded conformation is lower than the extended one (see Appendix 2).

Compound **PL 69** is also an isoster of **PL 65**. The introduction of azepane instead of pyrrolidine as the cycloalkyl amine moiety has a significant influence on the inhibition behaviour. As previously pointed out, the increase of lipophilicity is again related to a greater inhibition. For **PL 69**, the cLog P is equal to 7.12 while for **PL 65** it is equal to 6.06, showing IC_{50} values of 0.64 μM and 1.01 μM , respectively.

This enhancement of the inhibitory activity could be explained as the consequence of the orientation of the second cationic head towards a new anionic enriched region. The cationic charge is stabilized by Glu 309, Asp 353 and Arg 117 residues. The last one is an essential residue for the anchoring of the β -phosphate of the ATP to the enzyme and could form an H-Bond with the tertiary amine azepane. Moreover, the cycloalkyl amine is introduced in the ATP pocket causing steric hindrance and ousting the stabilization water from the Mg atoms surroundings. This moiety is also stabilized by hydrophobic residues, as Leu 124 and Ile 329. (Figure 28, e)

The rest of this library's compounds **PL 54**, **PL 55**, **PL 71** and **PL 73** are not docked as the template inhibitor **HC-3**. These compounds are quite outside of the hydrophobic cage of the choline-binding site, where there is interaction just with the cycloalkyl amine in **PL 54** and **PL 55**, and the aniline moiety in **PL 71**. All of them have an extended conformation and expose half of the molecule to the solvent.

Compounds **PL 54**, **PL 55** and **PL 71** are similarly anchored to the catalytic site while their different inhibition values should be derived from the cLog P values and the further stabilization of the molecule in the enzyme surface. In all three, the bound cationic head is very close to the Mg atoms and repulsion between the cationic charges can cause instability. There is still π - π stacking with Trp 420, Trp 423 and interaction with the residue Tyr 333 which is faced towards

the tertiary amines. The inner cationic heads occupy the space where the transferred phosphate should be placed. The thieno[2,3-d] pyrimidine group in these compounds, can also be stabilized by H-bond interactions between the pyrimidine N³ atom and the Gln 308 residue (Figure 29, f, g and h).

Compound **PL 55** has the best S-score value 1.062 of the three; a cLog P= 6.5 and an IC₅₀= 0.66 μ M. Compound **PL 54** follows with an S-score: 1.052, a cLog P= 5.96 and an IC₅₀= 4.37 μ M. Finally, compound **PL 71** has an S-score of 1.007, a cLog P= 7.07 and an IC₅₀= 1.43 μ M.

In this case activity and lipophilicity are not correlated. The most lipophilic molecule **PL 71** is not the most active; furthermore, it could be stabilized in the outer by weak interactions with Arg 117, Ile 433, Leu 120, Glu 434 and Phe 361 (Figure 29, h). In comparison, compound **PL 54** only interacts in the outer space with Glu 434 and Phe 361 (Figure 29, f) while compound **PL 55** in addition to Glu 434 and Phe 361 also interacts with Ile 433 (Figure 29, g). Incomprehensibly, compound **PL 55** is more active than **PL 71** even if the latter interact better and closer with the enzyme.

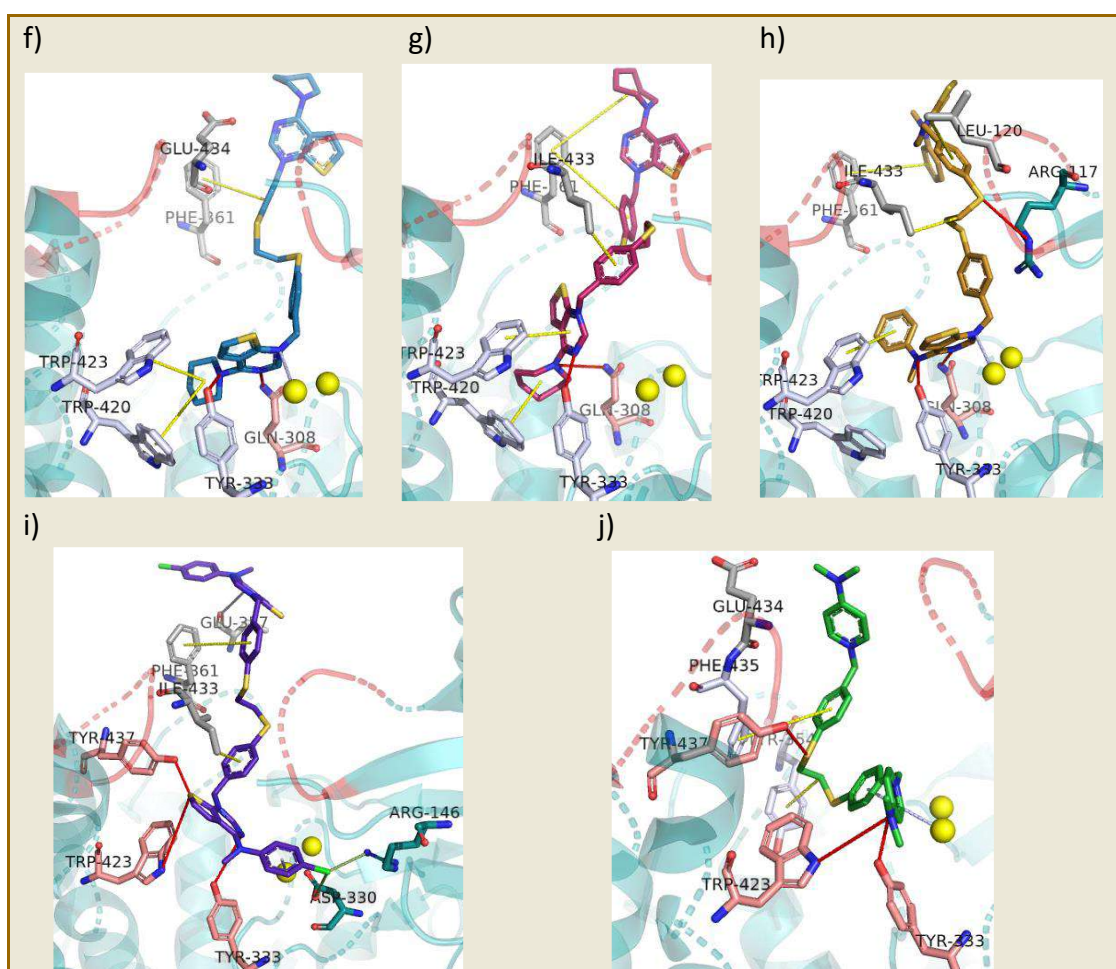


Figure 29. Inhibitors' mainly interactions inside the catalytic pocket.

f) Compound **PL 54** (carbon atoms in blue color), g) compound **PL 55** (carbon atoms in dark-pink color), h) compound **PL 71** (carbon atoms in yellow-orange color), i) compound **PL 73** (carbon atoms in purple color) and j) compound **PL 40** (carbon atoms in green color). Mg²⁺ cations are represented as yellow spheres, hydrophobic residues are in blue-white color, H-bond donor residues are in light pink color, ATP pocket residues are in deep-teal color and surface residues are in grey color. Dash lines are red when H-bond formation, yellow when

π - π or cation- π stacking, green when Cl-X interactions and blue-white when electrostatic interactions. Delimited loops 1 and 9 are coloured in red.

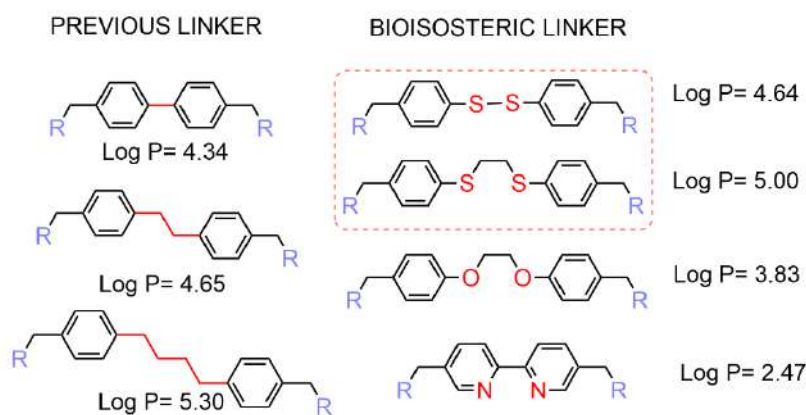
By the docking visualization, this behaviour could be attributed to the perpendicular disposition of the aniline ring and the cycloalkyl amine of **PL 71** and **PL 54**, respectively, in the hydrophobic cage regarding compound **PL 55**. However, further research needs to be done to clarify if compound **PL 71** interacts with another cavity of the enzyme not considered in our study.

On the other hand, compound **PL 73** is discussed separately because of its unique mode of binding. This molecule has the cationic head inserted in the ATP binding site, leading to steric hindrance in the Mg surroundings. The *para* chlorine is oriented towards the Arg 146, competing with the ADP phosphate oxygens to bind. In addition, interacts with Tyr 333, Trp 423, Tyr 437 (H-bond interactions), Ile 433, Phe 361 (hydrophobic interactions), Glu 357 (electrostatic interaction) and Arg 146 or Asp 330 (Cl bond) residues (Figure 29, i). It shows an S-score of 0.958, which value is lower than the obtained for its counterpart compound **PL 71**, due to the loss interaction with the hydrophobic cage in the choline pocket. It has a cLog P= 8.03 and an IC₅₀= 0.71 μ M, exhibiting 2-fold more inhibitory activity than compound **PL 71** just by the addition of chlorine in the *para* position.

The last inhibitor of this series is compound **PL 40**, with the smaller and most polar cationic head (dimethylamine) which is reflected in the cLog P value of 3.41. Due to its polar nature, it is not inserted in the hydrophobic cage but for the linker, which adopts a gauche conformation addressing the cationic heads outside the pocket which is also captured in the low S-score value of 0.902. Compound **PL 40** interacts with Tyr 333, Tyr 354, Tyr 437 (H-bond interactions), Trp 423, Tyr 354, Phe 435 (hydrophobic interactions) and Glu 434 (electrostatic interactions) (Figure 29, j). However, due to the insolubility in DMSO its inhibitory activity was not determined.

To sum up, it is highlight that the inhibitors that show the highest S-score values (**PL 55**, **PL 54**, **PL 71**, **PL 69**), and as so best fit in the pocket are those interfering with the Mg atoms. It is remarkable that to synthesized better inhibitors we need to match the phospho-transfer region rather than occupy the whole hydrophobic cage of choline. With this strategy, we could design molecules able to stay in the pocket even in the closed enzyme conformation.

We also realized that interactions with the sulphur atoms in the dithioethane linker slightly improve the binding by interactions with the amine backbone functions of residues in the inter-loop region but gives the necessary compound's flexibility to get inserted in the pocket. In addition, this linker shows a good balance between lipophilicity and solubility (Scheme 8).



Scheme 8. (Left part) cLog P of the linkers mainly used as part of the Choline Kinase inhibitors. (Right part) Bioisosteric changes in the linker.

The linker cLog P in decreasing order: diphenylbutane > bis(phenylthio) ethane > diphenylethane > diphenyldisulfane > bipyridine > diphenoxyethane > bipyridine.

Regarding the cationic heads, the [2,3-d] thienopyrimidine group successfully interacts through H-bond formation with the enzyme residues. This head becomes a hit to further research in comparison with pyridine and quinoline derivatives that show less binding with the enzyme.

For compounds **PL 70** and **PL 72**, quinolinic derivatives unable to be docked in the catalytic pocket (**Figure 30, left part**), is proposed a similar mode of binding than to the inhibitor TCD-717, in the inter-dimer region of the enzyme.⁷²

The same happens to compound **PL 67**, an isoster of compound **PL 71** (**Figure 30, right part**). It was not able to be docked even if it occupies the same volume as **PL 71**. The differences in the dipolar moment between them could justify the lack of an optimal binding with the enzyme in **PL 67**. This different dipolar moment is particularly important when the thienopyrimidine scaffold is substituted in 4 by an *N*-methylaniline.

When it is substituted by a cycloalkyl amine, there is almost no difference in the inhibition activity (see **Table 3, PL 68 vs PL 65 or PL 55 vs PL 69**).

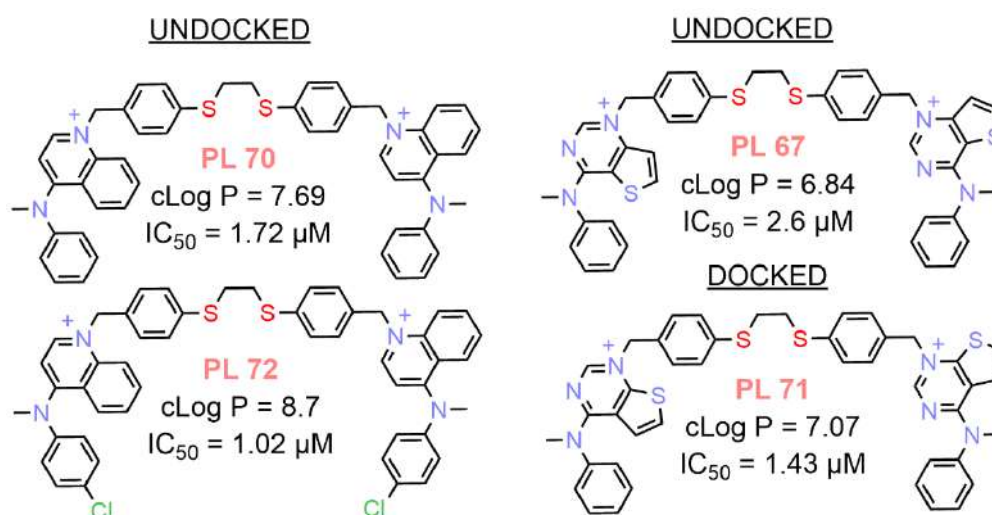
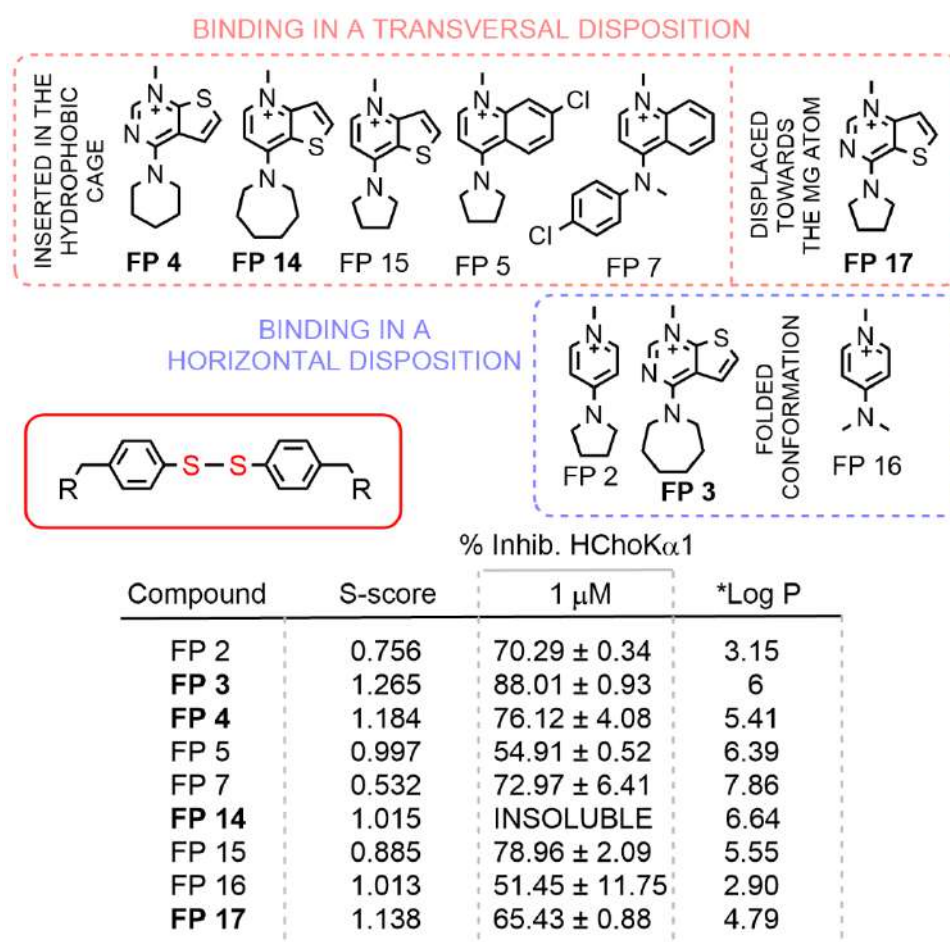


Figure 30. Undocked compounds **70**, **72** and **67**. Compound **71**, an isoster of **67**, can be docked and is also doubly active than **67**.

3.3 Disulphide library of compounds.

On the other hand, the second library of compounds is characterized by a disulphide linker. This time, the molecules can be classified by those that mainly bind the enzyme in an extended conformation transversally to the catalytic pocket and those that adopt a horizontal disposition regarding the catalytic site.

For clarity of reading, a general overview of the compound's classification according to its mode of binding and the values herein discussed are reported below (Table 4).



*Calculated using <http://www.swissadme.ch/> as an average of five predictions methods.

Table 4. Classification of the disulphide library binding mode and reported S-score, IC₅₀ and cLog P values for comparison.

The first group is composed of compounds: **FP 4**, **FP 17**, **FP 14**, **FP 5**, **FP 15**, and **FP 7**, which mostly constituted this library. As previously noted, the extended conformation leaves one half of the molecule exposed to the solvent, slightly interacting with the pocket's surface residues.

From this group, compounds that contain the thienopyrimidine or thienopyridine moiety as cationic head show the highest S-score values.

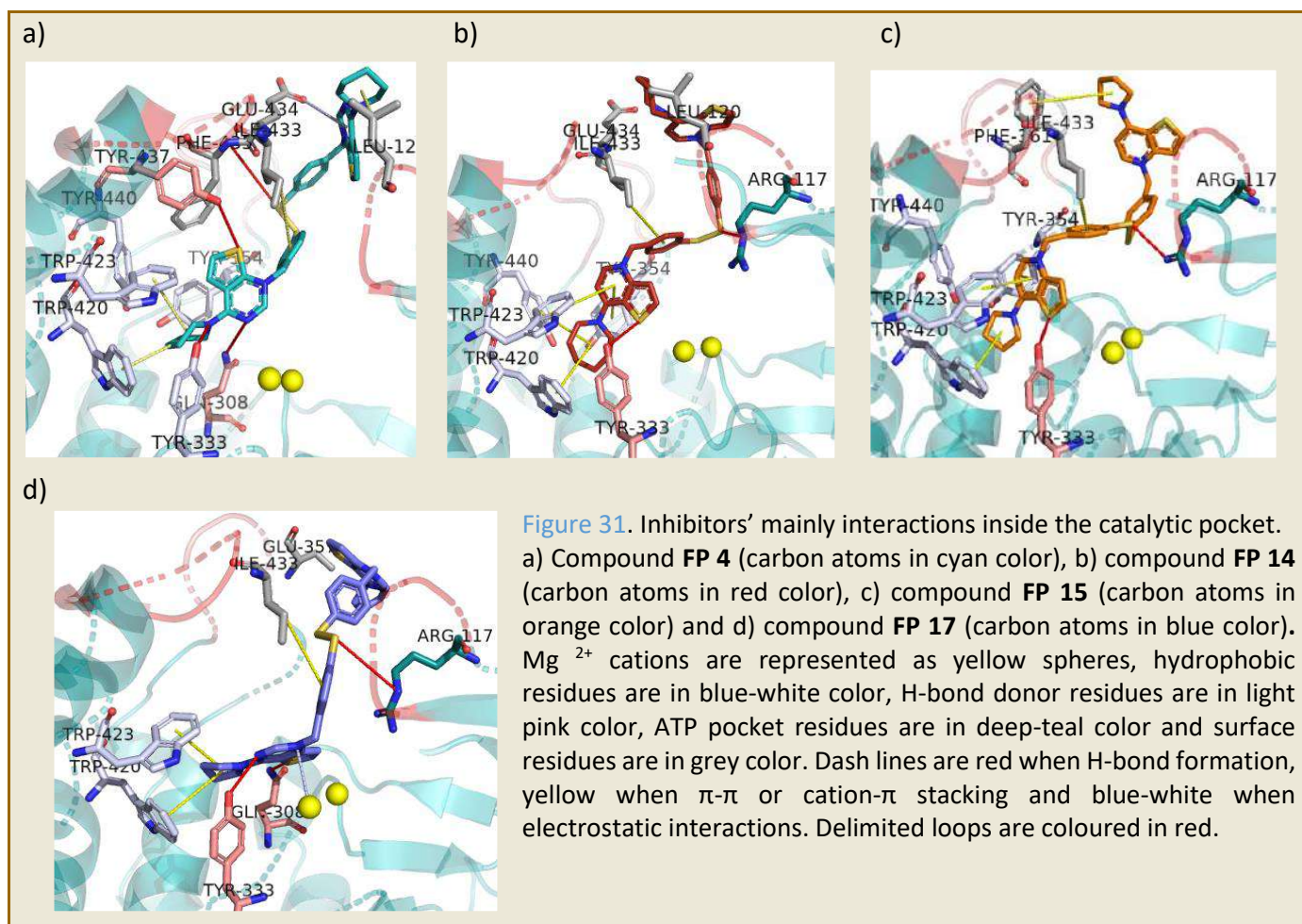
Starting with them, compounds **FP 4**, **FP 14** and **FP 15** show an optimal insertion of the cationic heads in the hydrophobic cage. There are π - π and cation- π stacking with residues Trp 420, Trp 423, Phe 435, Tyr 440, Tyr 354, and Tyr 333 (Figure 31, a, b and c). Compound **FP 4** with a thienopyrimidine group can establish more H-bond interactions in the pocket than compounds **FP 14** and **FP 15** with a thienopyridine group, which is written on the S-score values.

FP 4 interacts with Tyr 437 at the sulphur and with Gln 308 at the N³ atom of the thienopyrimidine moiety (Figure 31, a), while **FP 14** and **FP 15** only show an interaction between the Tyr 333 and the sulphur of the thiophene group (Figure 31, b and c).

As said, **FP 4**, **FP 15** and **FP 14** show decreasing S-score values of 1.184, 1.015 and 0.885, respectively. Also, in these compounds, the linker's phenyl ring establishes hydrophobic interaction with Ile 433 and the disulphide group could interact with the amine backbone function in Arg 117 (**FP 14** and **FP 15**) or Phe 435 (**FP 4**). The cationic head expose to the solvent is oriented towards Glu 434 and the cycloalkyl amine interacts with Leu 120 in **FP 4** and **FP 14** (Figure 31, a and b), and with Phe 361 in **FP 15** (Figure 31, c).

The last compound included in this subgroup is **FP 17**. It is an isoster of **FP 15**, with a pyrimidine group instead of pyridine. In fact, as well as in **FP 4** (which also has the pyrimidine moiety), the S-score is higher than the counterparts **FP 15** and **FP 14**, with a value of 1.138.

However, **FP 17** shows a different mode of binding. Only its pyrrolidine moiety interacts with the choline hydrophobic cage residues Trp 423 and Trp 420. The rest of the cationic head is displaced towards the Mg atoms, seated in a region surrounded by several negatively charged residues as Glu 332, Asp 330 and Asp 306. H-bond interactions are observed between Tyr 333 and Gln 308 with the N³ and the sulphur atom of the thienopyrimidine moiety, respectively. The phenyl linker and the disulphide group interact with Ile 433 and the amine backbone function of Arg 117, while the outer cationic head is oriented towards the Glu 357 residue (Figure 31, d).



However, the best Similarity-Scores do not come with the best inhibitory activity. To a large extent, it seems to depend on the compound's lipophilicity.

The thienopyrimidine cationic heads show less inhibition than the thienopyridine, being the size of the cycloalkyl amine ring that determines the different activity between them.

Compound **FP 4**, with a piperidine ring, has a cLog P= 5.41 and inhibits the enzyme a 76.12% at 1 μM , while compound **FP 17** its isomer with a pyrrolidine ring has a cLog P=4.79 and inhibits the enzyme a 65.43% at 1 μM .

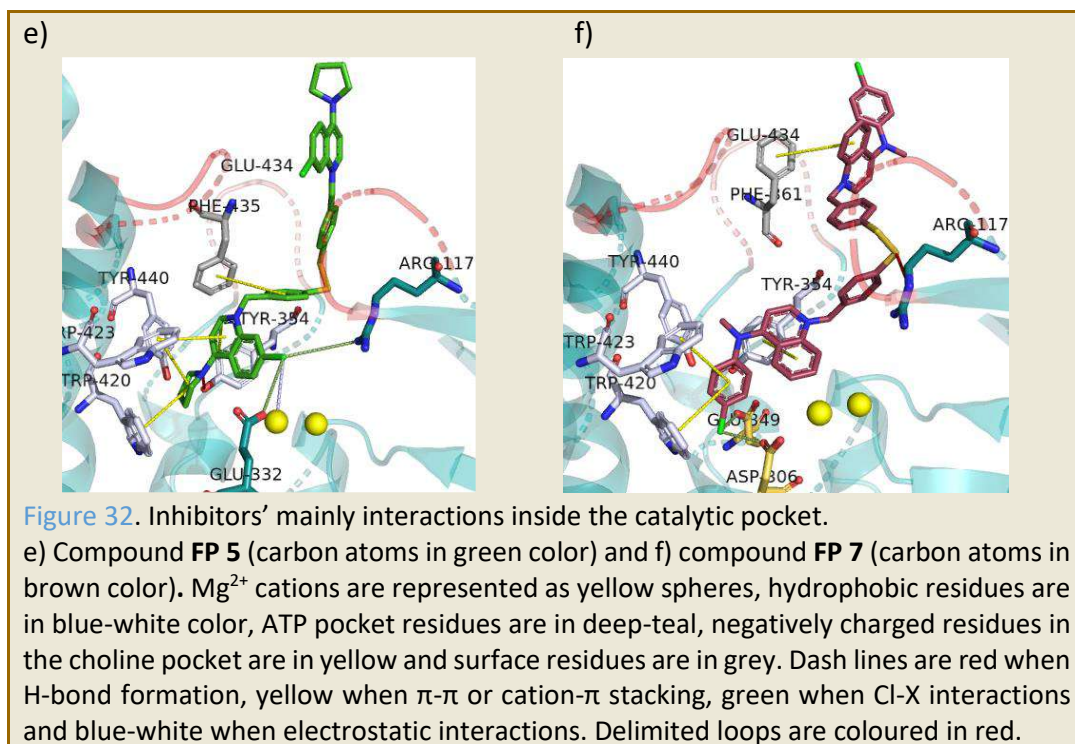
Compound **FP 15**, the isoster of **FP 17**, with the thienopyridine moiety has a cLog P= 5.55 and inhibits the enzyme a 78.96% at 1 μM . Its counterpart **FP 14**, with an azepane group at 4 position, has a cLog P=6.64 but was insoluble and its inhibition was not able to be tested.

The last compounds comprised in this classification are **FP 5** and **FP 7** (Figure 32, e and f). These compounds have quinolinic cationic heads substituted in 4 position by a cycloalkyl amine in **FP 5** and an aniline derivative in **FP 7**. In general, the S-score values are lower than in the previously discussed compounds, but they present more lipophilic structures. Compound **FP 5** has an S-score= 0.997 and a cLog P=6.39, and compound **FP 7** has an S-score= 0.532 and a cLog P=7.86.

Both of them are well inserted in the hydrophobic cage of the catalytic site. There are hydrophobic and π - π interactions with Trp 420, Trp 423, Tyr 354 and Tyr 440. The chlorine at the *para* position in **FP 7** could establish a Cl-O bonding with Glu 349 or Asp 306, which play a key role in the phospho-transfer enzymatic activity (Figure 32, f). On the other hand, the chlorine at 7 position of the quinolinic ring in **FP 5**, is oriented towards the Mg atoms and could create hindrance avoiding the stabilization of the cofactors and slightly interacting with Arg 117 or Glu 332 (Figure 32, e).

The linker's phenyl and disulphide groups are mostly stabilized in **FP 5**, by means of Phe 435 and the amine backbone function of the Glu 434 residue, respectively (Figure 32, e). Otherwise, the disulphide group in **FP 7** could interact with the amine backbone function of the Arg 117 residue (Figure 32, f). In both inhibitors, the exposed part to the solvent is oriented towards Glu 434 and Phe 361.

Compound **FP 5** seems to fit best the pocket because it interacts closer with the hydrophobic residues, also around the linker, showing a higher S-score value. However, it is not reflected in the inhibitory activity. Compound **FP 5** inhibits the enzyme a 54.91% at 1 μM while compound **FP 7** inhibits the enzyme a 72.97% at 1 μM , according to the cLog P values.



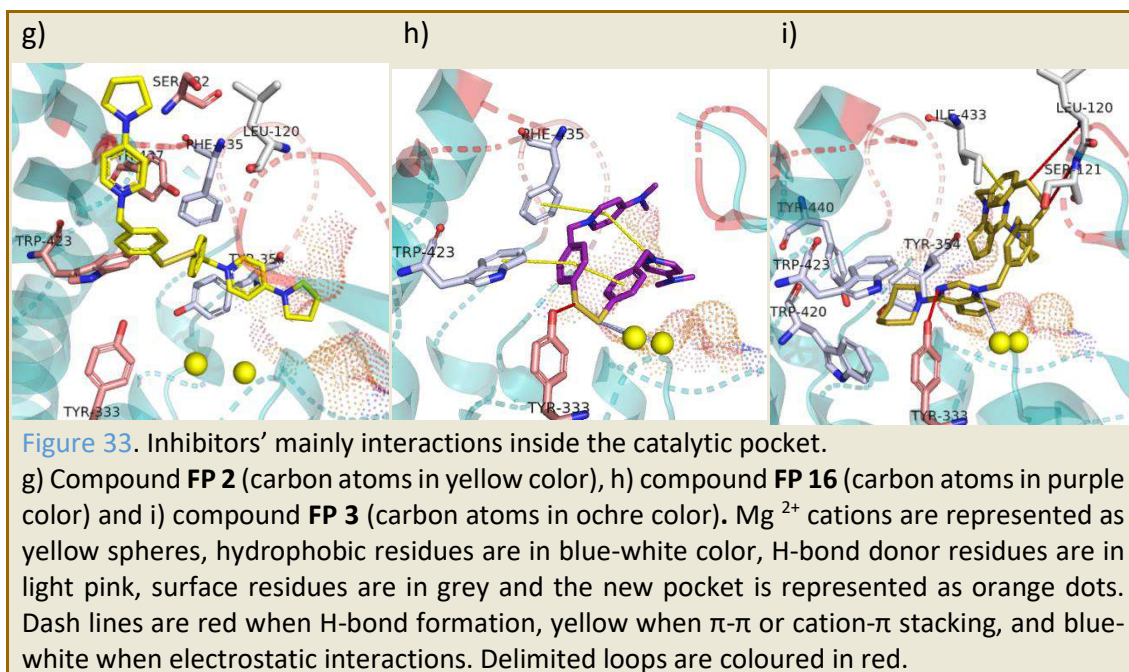
Finally, we discuss the compounds of this library that mainly bind the enzyme in a folded conformation or cross horizontally the pocket. To this group belong compounds: **FP 3**, **FP 16** and **FP 2** (Figure 33, i, h and g).

Compounds **FP 16** and **FP 2** have a pyridine cationic head substituted in *para* position by an aliphatic (dimethylamino) and a cyclic (pyrrolidine) tertiary amine, respectively. Both are smaller and more polar than the previously reported inhibitors, with cLog P values of 2.90 for **FP 16** and 3.15 for **FP 2**. Due to the hydrophilicity of these compounds, they are not well anchored to the hydrophobic cage of the choline-binding site and adopt two different conformations.

Compound **FP 2** crosses the pocket horizontally. It is not inserted in the hydrophobic cage, but there are π - π and cation- π interactions with Phe 435 and Tyr 354 residues. The disulphide linker is stabilized by H-bond interaction with Tyr 437, Tyr 333 and Trp 423 residues. One half of the molecule is out of the pocket and interacts with the inter-loop residues as Leu 120 (hydrophobic interaction), Ser 432 and Ser 431 (H-bond formation). The other symmetrical half is inserted in a new cavity closer to the ATP binding site. This cavity is enriched by polar and negatively charged amino acids like Ser 355, Arg 213, Asp 215, Asp 353 and Glu 309, where the cationic moiety is stabilized (Figure 33, g).

On the other hand, compound **FP 16** is folded over itself. The disulphide linker forms an H-bond with Tyr 333 and is exposed towards the Mg atoms, with who could be coordinated blocking the phosphate group transfer to the Asp 306. In addition, this compound is deep introduced in the catalytic pocket establishing π - π interactions with Trp 423 and Phe 435 and intramolecular π - π and cation- π interactions between the compound's phenyl and pyridine moieties. Both cationic heads are oriented towards the new polar cavity (Figure 33, h).

Compound **FP 16** has an S-score value higher than **FP 2**, 1.013 and 0.754, respectively. It could be due to the fact that **FP 16** is completely inserted in the pocket while **FP 2** has one cationic head exposed to the solvent. However, the opposite trend is observed regarding inhibitory activity. Compound **FP 16** inhibits the enzyme a 51.45% at 1 μM while compound **FP 2** inhibits the enzyme a 70.29% at 1 μM , in agreement with the increasing compound's lipophilicity.



Finally, compound **FP 3** is disposed horizontally to the pocket as **FP 2** does. This molecule has the thienopyrimidine cationic head substituted in 4 by an azepane group. Only the azepane group is deep inserted in the hydrophobic choline pocket establishing interactions with Trp 420, Trp 423, Tyr 354 and Tyr 440, while the thienopyrimidine group is oriented towards the Mg atoms causing hindrance and the cofactors destabilization. The N^3 atom of the pyrimidine moiety can also form an H-bond with Tyr 333. The disulphide linker in a synclinal conformation interacts with the amine backbone functions of Leu 120 and Ser 121, and the phenyl group interacts with Ile 433. The second cationic head is inserted in the new cavity enriched with polar and negatively charged amino acids (Figure 33, i).

Compound **FP 3** has the higher S-score of the library, with a value of 1.265. As previously discussed, the thienopyrimidine derivatives (**FP 4** and **FP 17**) are expected to have a good Similarity value due to the greater interaction with the pocket. In addition, it is the hit to lead of this library with an enzymatic inhibition of 88.01% at $1 \mu M$ and a cLog P=6.

The molecules with higher S-score values: **FP 3**, **FP 4**, **FP 17** and **FP 14**, show a hindrance cycloalkyl amine at the 4-position in the thieno- pyrimidine or pyridine cationic head.

The thieno[2,3-d] pyrimidine is the best cationic head, showing better anchor to the pocket when is substituted at 4-position with most lipophilic cycloalkyl amines (azepane > piperidine > pyrrolidine).

It could be highlighted the fact that in this library, the inhibitor proximity to the Mg and the ATP pocket is not associated with the inhibitory potency, as an example, compound **FP 17**.

The shorten disulphide linker does not play a key role in the binding except for **FP 16**, which is able to closely interact with the Mg atoms due to the small cationic heads. However, the insertion of sulphur atoms in the linker that are less polar but more nucleophilic than the former oxygen-containing bioisosteres, give room to a good lipophilic-hydrophilic balance (Scheme 8, cLog P calculations).

It is also noted that the quinolinic inhibitor **FP 7** has a low S-score value and a high inhibitory activity. These conflicting results could be due to the fact that the inhibitor interacts with an allosteric pocket, not considered in the present study.

3.4 Comparison between library's homologous and discussion.

Based on the poses mainly adopted by the compounds of the two libraries, it is possible to conclude that:

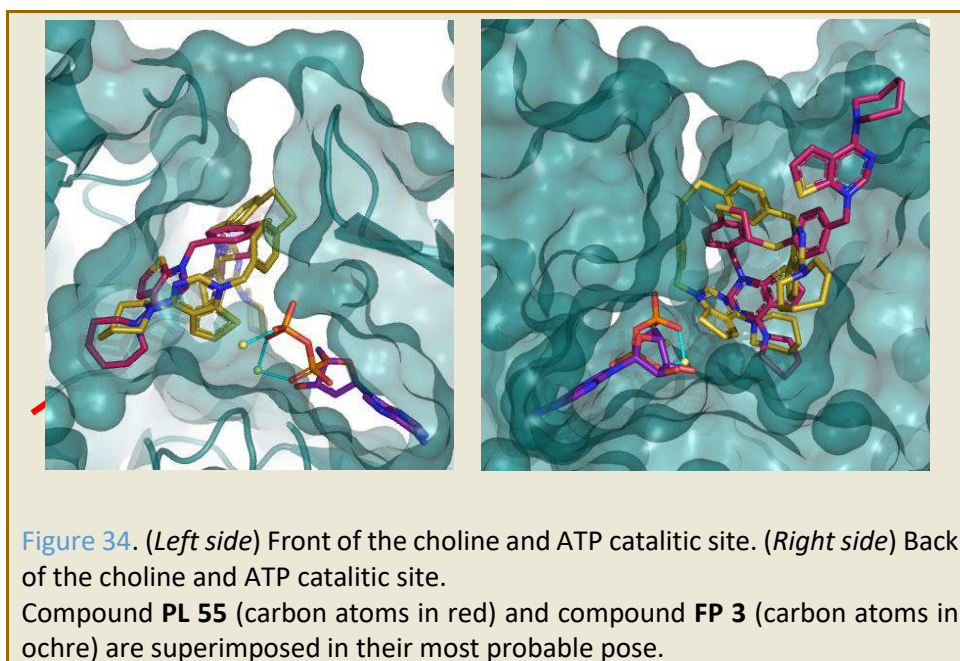
-Best S-scores correspond to compounds: **PL 55** (dithioethane liker) and **FP 3** (disulphide linker). Both of them have as cationic head the 4-(1-azepanyl) thieno[2,3-d]pyrimidine, which shows a deep insertion in the choline hydrophobic cage.

-The dithioethane linker show similar inhibition values to the disulphide one. However, the biggest length and flexibility of the linker allows the azepane moiety to interact deeply in the choline binding site ([Figure 34, left side](#)), and on the other hand, to mostly expose the second cationic head to the solvent ([Figure 34, right side](#)). This fact gives room to a lower S-score in comparison with its most rigid disulphide homologous.

-Regarding the cationic heads, they generally show the same activity order in both libraries. The thienopyrimidines > thienopyridine > pyridine. Also, increasing the activity when hindrance tertiary amines are used in 4 position: azepane > piperidine > pyrrolidine. On the contrary, quinolinic heads show low similarity to the catalytic site but higher inhibitory values. For that reason, it is thought that they could bind in an allosteric pocket of the enzyme.

-The higher activity of the dithioethane linker library is also attributed to the hindrance or the caused instability in the enzyme's cofactors as reported by Estévez-Braun *et al*⁵³, in which the most active TPQ natural product formed a cluster with Mg^{2+} , and thus supporting our results.

The possible coordination with the Mg^{2+} atoms is also supported by studies conducted with other metallo-based proteins that use Zn^{2+} cofactors as in the β -lactamases, in which the best inhibitors are binding to the Zn atom.¹³¹



4. Antiproliferative activity.

The last step in this early stage of drug design, consisted of testing the in-vitro antiproliferative activity, of both libraries **PL** and **FP**, over the human tumour-cell line MCF-7 of human breast adenocarcinoma and the hepatocellular carcinoma cell line HepG2, respectively. The experiments were done by Prof. María Paz Carrasco Jiménez of the Department of Biochemistry and Molecular Biology I at the University of Granada.

This study, shed light on the pharmacodynamic properties of the inhibitors and their ability to reach the target. The chosen cells lines MCF-7 and HepG2 were selected as an example among the proto-oncogene Ras active tumour cells.

The tested compounds were prepared at different concentrations by serial dilutions of a stock solution in DMSO. Once the tumoral cells were incubated and achieved an adequate population, the medium was replaced by a fresh one in which the inhibitor is dissolved at different concentrations. The antiproliferative effect of the tested compounds was evaluated by the MTT assay using a cell-number-based standard curve, that quantified the cell viability by the colorimetric detection spectrophotometrically.

Regarding the MCF-7 antiproliferative values of the dithioethane library, reported in [Table 5](#) (*at the top*), we can point out that the family of compounds **PL 54**, **PL 55**, **PL 71** and **PL 73** with the thieno[2,3-d] pyrimidine cationic head show the best antiproliferative results.

When this cationic head is substituted in 4 position by a cycloalkyl amine as in compounds **PL 54** (piperidine) and **PL 55** (azepane), it was observed slightly better growth-inhibitory values in **PL 54** ($GI_{50} = 1.215 \mu\text{M}$) rather than in **PL 55** ($GI_{50} = 1.465 \mu\text{M}$). This trend was unexpected as compound **PL 55** was almost 7-fold most active regarding the inhibition in the isolated enzyme ($IC_{50} = 4.373 \mu\text{M}$ for **PL 54**, and an $IC_{50} = 0.658 \mu\text{M}$ for **PL 55**). For that reason, it is thought that compound **PL 54** could exhibit an off-target effect when tested over the MCF-7 tumoral cell line so that its high antiproliferative activity could be a consequence of the unspecific inhibition of overexpressed enzymes involved in the cell death pathways.

However, when the cationic head is substituted in 4 position with an aromatic amine, compounds **PL 71** (*N*-methyl aniline group) and **PL 73** (*p*-chloro-*N*-methyl aniline group), there is a high loss of activity. Compounds **PL 71** and **PL 73** showed a GI_{50} of 3.944 and 2.373 μM , respectively.

These results agree with the $c\text{Log P}$ values. Compound **PL 73** ($c\text{Log P} = 8.3$) showing better antiproliferative activity than its counterpart **PL 71** ($c\text{Log P} = 7.07$). Both are good ChoK inhibitors ($IC_{50} = 1.426 \mu\text{M}$ for **PL 71**, and an $IC_{50} = 0.709 \mu\text{M}$ for **PL 73**) but on the tumoral cell, they could interact with other overexpressed targets as kinases structurally similar to the ChoK due to the lack of an IC_{50} and GI_{50} correlation.

The isomeric thieno[3,2-d] pyrimidine cationic head of compounds **PL 67** and **PL 68**, shows the worse antiproliferative values of the dithioethane library.

Compound **PL 67** with an aromatic amine (*N*-methyl aniline) as substituent in 4 position, has a $GI_{50} = 9.121 \mu\text{M}$ and an $IC_{50} = 2.595 \mu\text{M}$, while compound **PL 68** with a cycloalkyl amine (pyrrolidine) shows a $GI_{50} = 4.337 \mu\text{M}$ and an $IC_{50} = 1.357 \mu\text{M}$. This cationic head leads to poor binding to the enzyme but also has an unspecific effect on tumoral cells.

The thieno[3,2-b] pyridine cationic head of compounds **PL 65** and **PL 69** (with a GI_{50} of 3.113 μM and 2.122 μM , respectively), showed a higher antiproliferative activity than the latter family of compounds.

When compound **PL 65** is compared with its isosteric counterpart, compound **PL 68**, it can be observed an improvement in the inhibitory and antiproliferative activity. Moreover, the activity is still increased when as substituent at 4 position there is a bigger cycloalkyl amine azepane

(compound **PL 69**) rather than the pyrrolidine in compound **PL 65**. Even if the raise lipophilicity agrees with a greater cell growth inhibition, those values are low in comparison to their high inhibitory activity over the *in-vitro* enzyme (an IC_{50} of 1.013 μ M for compound **PL 65** and 0.638 μ M for compound **PL 69**).

This fact could be attributed to a lack of selectivity for the ChoK or the inability to reach the target, working as membrane transporters inhibitors.

Finally, from the quinolinic family **PL 48**, **PL 70** and **PL 72**, the derivative called **PL 48** was chosen to be also tested over the neoplastic cell line HepG2, allowing the comparison between libraries.

This inhibitor is substituted in 7 by a chlorine atom and in 4 position by a cycloalkyl amine (pyrrolidine), showing GI_{50} = 1.34 μ M that correlates well with the high enzymatic inhibition IC_{50} = 0.658 μ M.

When the quinolinic cationic head is substituted in 4 position by an aromatic amine, compounds **PL 70** and **PL 72**, the antiproliferative values fall drastically. Compound **PL 70**, with an *N*-methyl aniline group, shows a GI_{50} = 4.732 μ M, while compound **PL 72** with a *p*-chloro-*N*-methyl aniline substituent shows a GI_{50} = 3.692 μ M. They were moderate inhibitors of the ChoK enzyme (IC_{50} = 1.723 μ M for **PL 70**, and an IC_{50} = 1.024 μ M for **PL 72**), but when tested over the cell they could have problems passing through the plasmatic membrane affecting their activity because of the inability to reach the target.

As reported in the thieno[2,3-d] pyrimidine family (**PL 71** and **PL 73**) and the thieno[3,2-d] pyrimidine derivative **PL 67**, when aromatics amines are used as substituent the growth inhibition could be correlated to an off-target effect.

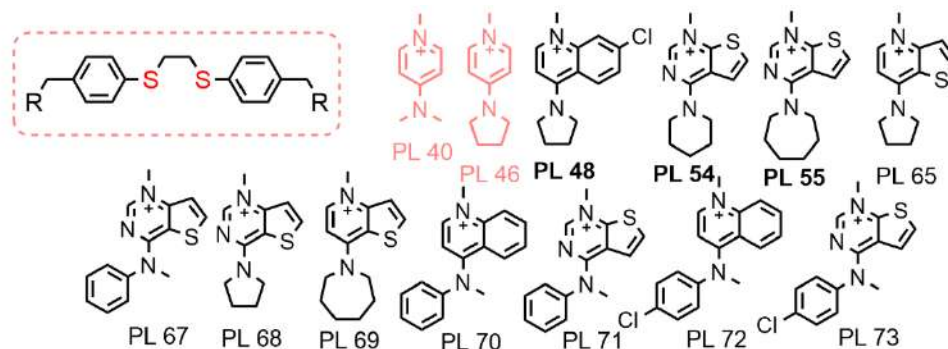
Lipophilicity plays a key role in potency improvement but, as reported for inhibitors **PL 70** and **PL 72**, bulky structures could show a low pharmacodynamic profile.

To sum up, we can highlight compounds **PL 48**, **PL 54** and **PL 55** as the best antiproliferative inhibitors in the MCF-7 cell line. Of them, just compounds **PL 48** and **PL 55** showed a suitable correlation with the inhibitory activity over the ChoK. In general, the most promising cationic heads are the thieno[2,3-d] pyrimidine and the 7-chloro quinoline substituted at 4-position with a cycloalkyl amine rather than an aromatic amine. The bigger ring of the cycloalkyl amine the better the selectivity for the target and the correlation towards cell growth and enzymatic inhibition.

Regarding the antiproliferative values of the disulphide library towards the HepG2 cell line, reported in [Table 5 \(at the bottom\)](#), we can underline compound **FP 17**, which has the best antiproliferative outcome of this series. This compound is the only one of this series with a thieno[3,2-d] pyrimidine cationic head and is substituted in 4 position by the pyrrolidine cycloalkyl amine.

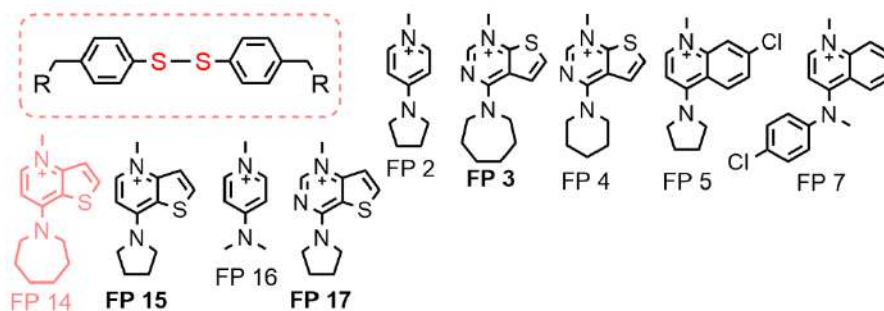
However, even if this derivative has a good antiproliferative activity, GI_{50} = 26.476 μ M, when tested over the isolated enzyme at 1 μ M there was only a 65.43% of enzymatic inhibition. So that, such a growth inhibitory value could be due to an off-target effect over other tumoral overexpressed enzymes or even caused by an unknown role in the mechanisms of cellular death.

After it, the family of compounds with better antiproliferative values correspond to the thieno[2,3-d] pyrimidine cationic head substituted in 4 position by a cycloalkyl amine. Belonging to this group are the inhibitors **FP 3** and **FP 4**.



Antiproliferative activity
(MCF-7) 48 h

Compound	% Inhibition HChok α 1		IC ₅₀ (μ M)	Mw	*Log P	
	GI ₅₀ (μ M)	1 μ M				5 μ M
PL 40	INSOLUBLE	--	--	INSOLUBLE	676.57	3.41
PL 46	INSOLUBLE	--	--	INSOLUBLE	728.65	4.12
PL 48	1.34 \pm 0.4806	3.39 \pm 2.18	100	0.658 \pm 0.067	897.65	7.07
PL 54	1.215 \pm 0.028	52.65 \pm 4.07	86.48 \pm 2.37	4.373 \pm 0.605	870.84	5.96
PL 55	1.465 \pm 0.232	79.03 \pm 0.98	95.20 \pm 0.14	0.658 \pm 0.079	898.90	6.50
PL 65	3.113 \pm 0.277	57.19 \pm 11.65	90.40 \pm 0.18	1.013 \pm 0.147	840.81	6.06
PL 67	9.121 \pm 0.678	58.44 \pm 0.17	ND	2.595 \pm 0.658	914.86	6.84
PL 68	4.337 \pm 0.478	70.96 \pm 9.56	87.63 \pm 1.51	1.351 \pm 0.041	842.79	5.28
PL 69	2.122 \pm 0.218	66.97 \pm 4.91	97.48 \pm 0.55	0.638 \pm 0.111	896.92	7.12
PL 70	4.732 \pm 0.183	55.67 \pm 1.19	91.96 \pm 0.13	1.723 \pm 0.021	900.84	7.69
PL 71	3.944 \pm 0.050	74.96 \pm 7.55	92.44 \pm 1.37	1.426 \pm 0.270	914.86	7.07
PL 72	3.692 \pm 0.022	87.14 \pm 4.04	97.58 \pm 0.38	1.024 \pm 0.117	969.72	8.7
PL 73	2.373 \pm 0.219	64.38 \pm 0.39	92.43 \pm 0.38	0.709 \pm 0.067	983.74	8.03



**Antiproliferative activity

Compound	% Inhibition HChok α 1		IC ₅₀ (μ M)	Mw	*Log P	
	GI ₅₀ (μ M)	1 μ M				5 μ M
FP 2	53.601 \pm 1.699	70.29 \pm 0.34	87.98 \pm 0.66	ND	700.60	3.15
FP 3	26.831 \pm 1.077	88.01 \pm 0.93	96.28 \pm 0.01	ND	870.84	6
FP 4	37.905 \pm 0.556	76.12 \pm 4.08	89.47 \pm 4.55	ND	842.79	5.41
FP 5	81.993 \pm 3.178	54.91 \pm 0.52	87.56 \pm 0.30	ND	869.60	6.39
FP 7	38.706 \pm 1.383	72.97 \pm 6.41	97.28 \pm 0.80	ND	941.67	7.86
FP 14	INSOLUBLE	--	--	INSOLUBLE	868.87	6.64
FP 15	29.335 \pm 1.923	78.96 \pm 2.09	92.23 \pm 0.05	ND	812.76	5.55
FP 16	36.561 \pm 0.814	51.45 \pm 11.75	ND	ND	648.52	2.90
FP 17	26.476 \pm 1.761	65.43 \pm 0.88	86.57 \pm 0.33	ND	814.74	4.79
PL 48	12.837 \pm 2.428	63.39 \pm 2.18	100	0.658 \pm 0.067	897.65	7.07

**Antiproliferative activity tested at 5 μ M. * Calculated with <http://www.swissadme.ch/as> as an average measure of five predictions methods.

Table 5. Dithioethane (at the top) and disulphide (at the bottom) libraries' antiproliferative activity. Insoluble molecules are coloured in red.

Compound **FP 3** is substituted with an azepane showing a GI₅₀ = 26.831 μ M and an inhibitory activity over the enzyme at 1 μ M of 88.01%, while compound **FP 4** substituted with piperidine,

shows a $GI_{50} = 37.905 \mu\text{M}$ and an inhibitory activity over the enzyme at $1 \mu\text{M}$ of 76.12%. In this group, there is a good correlation between the GI_{50} and the percentage of inhibition, being compounds more selective towards the ChoK. Also, there is a drop-in activity when the cycloalkyl amine size is reduced from the azepane to the piperidine, highlighting how lipophilicity is gaining relevance in this cationic head family.

Next, the thieno[3,2-b] pyridine cationic head of compound **FP 15**, substituted in 4 position by a cycloalkyl amine (pyrrolidine), shows a $GI_{50} = 29.335 \mu\text{M}$ and an inhibitory activity over the enzyme at $1 \mu\text{M}$ of 78.96%. This compound is an isomer of the top series' compound **FP 17**. So that, it is bringing out the fact that even if **FP 15** has a lower antiproliferative activity than its counterpart **FP 17**, the first shows 1-fold more inhibitory potency at the same concentration of $1 \mu\text{M}$. As so, **FP 15** is expected to have an antiproliferative activity owing to a higher interaction with the cytosolic enzyme ChoK.

On the other hand, compound **FP 14** that also belongs to this group, was unable to be tested due to solubility problems in the DMSO stock solution.

The pyridine cationic head of compounds **FP 16** and **FP 2**, disclose a low antiproliferative efficiency and inhibitory selectivity. Compound **FP 16** is substituted in *para* position by an aliphatic dimethyl amine, showing a $GI_{50} = 36.561 \mu\text{M}$ and an inhibitory activity over the enzyme of 51.45% at $1 \mu\text{M}$. On the other hand, compound **FP 2**, which is substituted in *para* position by a cycloalkyl amine (pyrrolidine), shows a $GI_{50} = 53.601 \mu\text{M}$ and an inhibitory activity over the enzyme of 70.29% at $1 \mu\text{M}$. The cationic head of this family is the most polar of this series, which could be the cause of low permeability through the cell membrane and thus less antiproliferative values.

The quinolinic cationic head of compounds **FP 5** and **FP 7**, show very different behaviour depending on the substitution in the 4 position.

Compound **FP 5**, with a cycloalkyl amine (pyrrolidine), shows a $GI_{50} = 81.993 \mu\text{M}$, which is the worst value of this series, while compound **FP 7** with an aromatic amine (*p*-chloro-*N*-methyl aniline) show a $GI_{50} = 38.706 \mu\text{M}$. In fact, compound **FP 7** has a better relationship between the GI_{50} and the inhibition of the enzyme (a 72.97% at $1 \mu\text{M}$). However, compound **FP 5** with a 54.91% of ChoK inhibition at $1 \mu\text{M}$, seems not able to reach the target in the tumoral cell line.

Contrary to the pyridine family, this is the most lipophilic group but, none of them presents good antiproliferative values. It must be achieved a hydrophobic-hydrophilic balance, because although higher lipophilic inhibitors are able to establish more hydrophobic interactions in the isolated enzyme and show better IC_{50} values, they could be very bulky to pass the cell membrane, giving room to fewer antiproliferative results.

To sum up, compounds **FP 17**, **FP 3** and **FP 15** have the best antiproliferative activity in this library, with GI_{50} values between $26.476 \mu\text{M}$ and $29.335 \mu\text{M}$. However, just compounds **FP 3** and **FP 15** show a good correlation with the ChoK inhibitory values and so could justify their activity by the effect over the ChoK enzyme. From a general point of view, the most suitable cationic heads are the thieno[2,3-d] pyrimidine and the thieno[3,2-b] pyridine, substituted in 4 position by a cycloalkyl amine. A general trend was also observed when increasing the size of the cycloalkyl amine, from piperidine to azepane, which lead to a higher antiproliferative potency. Only the quinolinic heads show preference toward the aromatic amines.

Moreover, the most polar and lipophilic heads belonging to the pyridine and quinoline families respectively, showed the worst antiproliferative values due to their poor pharmacodynamics properties.

A comparison between libraries could not be done as the period of treatment (48 h vs 24 h) and the cell line chosen for the antiproliferative assay, were different.

Only compound **PL 48** from the dithioethane linker library was tested on the same tumoral cell line (HepG2 for 24 hours) as the disulphide linker inhibitors. In comparison with them, compound **PL 48** highlights with a GI_{50} = 12.837 μ M, in concordance with its inhibitory activity, which was also very high (IC_{50} = 0.658 μ M).

Interestingly, it was possible to determine the higher activity of the compound **PL 48**, with a dithioethane linker, when compared with its disulphide homologous **FP 5** that almost did not show an antiproliferative effect (GI_{50} = 81.993 μ M).

In a general overview, the dithioethane library shows higher antiproliferative activity than the disulphide one. The lower effect of the disulphide library over the cells could be due to the sulphur bond breakage, leading to the formation of two thiol derivatives. This could happen by the action of the glutathione reductase enzyme that regulates the intracellular oxidative stress, as observed with the pro-drug Romidepsin¹³³.

We must also consider the fact that the antiproliferative activity has been only assay in two cell lines and that these results could vary when testing the libraries on other Ras activated tumoral cells lines as HeLa from human cervical cancer or HT-29 from human colorectal adenocarcinoma, commonly used in ChoK studies.

Differences among tumoral-cell lines could lead to differences in cell membrane composition and permeability, in the presence or absence of overexpressed enzymes as kinases, and in activated apoptotic pathways with which our inhibitors could interact.

Further studies must be done to see if the permeability in other tumoral-cell lines leads to higher activity for those compounds with low MCF-7 and HepG2 antiproliferative values.

5. Inhibitor's physical-chemistry properties in the PL library.

As we have already observed in previously synthesized inhibitors, and also noted in the introduction, the characteristics of size and charge in our compounds, make them able to act as membrane transporters inhibitors as well (all of them show $M_w > 500$). However, the effect observed in the in-vitro antiproliferative assays is the same as if they were inhibiting the enzyme. If the choline uptake is reduced, the ChoK production of phosphocholine would also diminish due to the substrate shortage.

To shed light on the possible uptake inhibition mechanism of our library, we tested if some of the synthesized compounds emitted fluorescence. In this way, they could be followed by FLIM (Fluorescence-Lifetime Imaging Microscopy), and quickly determine if they accumulate in the plasmatic membrane, in the cytosolic or in both cellular regions. FLIM is a well-noted technique able to collect the emission of biosensing fluorophores (as pH¹³⁴, polarity^{135,136} and viscosity¹³⁷ sensors) but also could measure the fluorescence lifetime as a quantitative parameter of the signal, independently of the fluorophore concentration. In the present study, we did not analyze the decay lifetimes of the tracking inhibitor because of the qualitative purpose of the measure (yes/no answer).

Of the entire PL library, compounds **PL 68** and **PL 54** mostly showed fluorescence emission when observed under the UV lamp (in the UVB region (280 nm – 315 nm)). As so, in collaboration with the Ph.D student Laura Espinar Barranco of the Physical-Chemistry Department in the Faculty of Pharmacy at the University of Granada, we studied their use as fluorophores and their capability to be followed inside the cell and determine where are accumulated.

5.2 Absorbance and fluorescence spectra.

Even if compounds **PL 67**, **PL 55** and **PL 65** also showed fluorescence, we selected compounds **PL 68** (green yellowish emitted light) and **PL 54** (blue emitted light) due to their brightness and different colour to be tested as tracking probes.

We first determined the absorption spectra in both water and dioxane solutions. The selection of a polar and a non-polar solvent environment could mimic the different cellular environments, as the cytosol and the plasmatic membrane, respectively.

To examine our compounds behaviour as fluorophores, we collect the absorption spectra in which intensity maximum is established the wavelength for fluorescence excitation and then, recorded the fluorescence emission.

As we can see in [Figure 35](#), both compounds **PL 68** and **PL 54** show a decrement in intensity when are dissolved in water. In dioxane, the intensity increased but was not achieve a maximum in the selected wavelength range. For that reason, the fluorescence emission was collected using the water absorbance maximum for excitation (310 nm in **PL 68** and 303 nm in **PL 54**).

The different behaviour depending on the solvent used, highlights the solvatochromism of this type of inhibitors.¹³⁸ When we used dioxane, the absorption band is blue-shifted in comparison with the water one. The latter is a media that, in addition, seems to quench the intensity outcome of our compounds. There are a lot of factors that govern such a polarity dependence, as could be the different hydrogen bonding, preferential solvation, rigidity of the local environment, intermolecular electron and proton transfer or probe-probe interactions as examples.

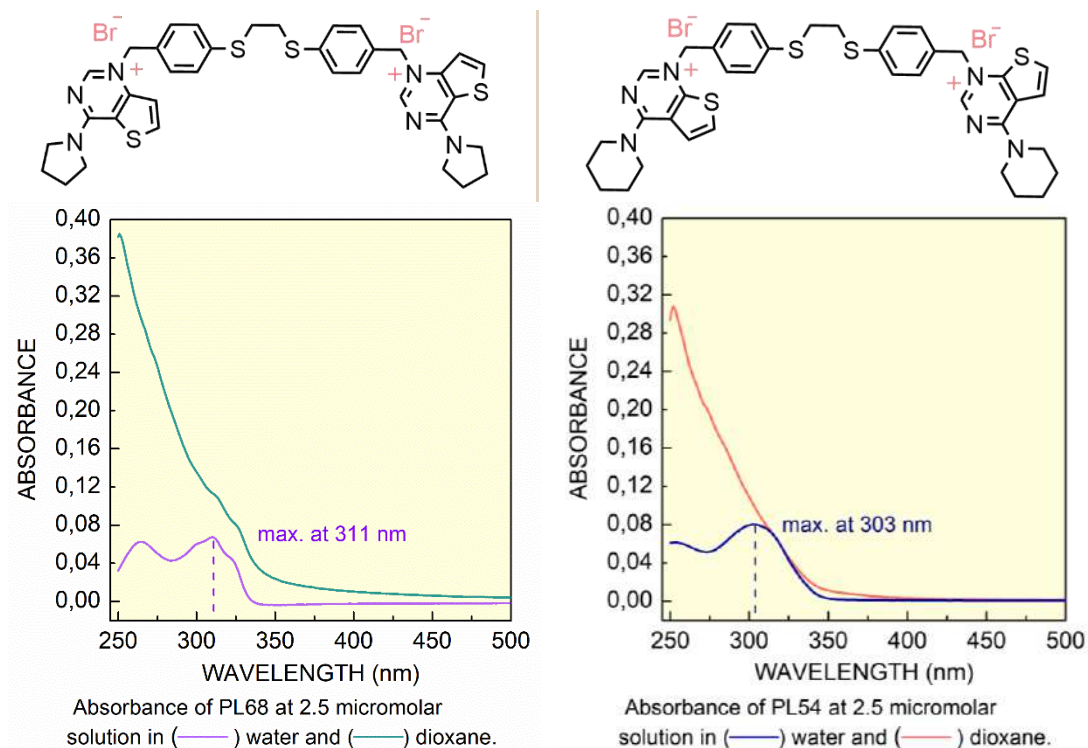


Figure 35. Absorption spectra of compound **PL 68** left and **PL 54** right.

It is displayed the water and dioxane absorbance superimposed for each studied inhibitor.

The polarity of the solvent did not only affect the molecular ground state, as we can see when obtaining the absorption spectra but, also affects the excited state as observed in the emission one (Figure 36 and 37).

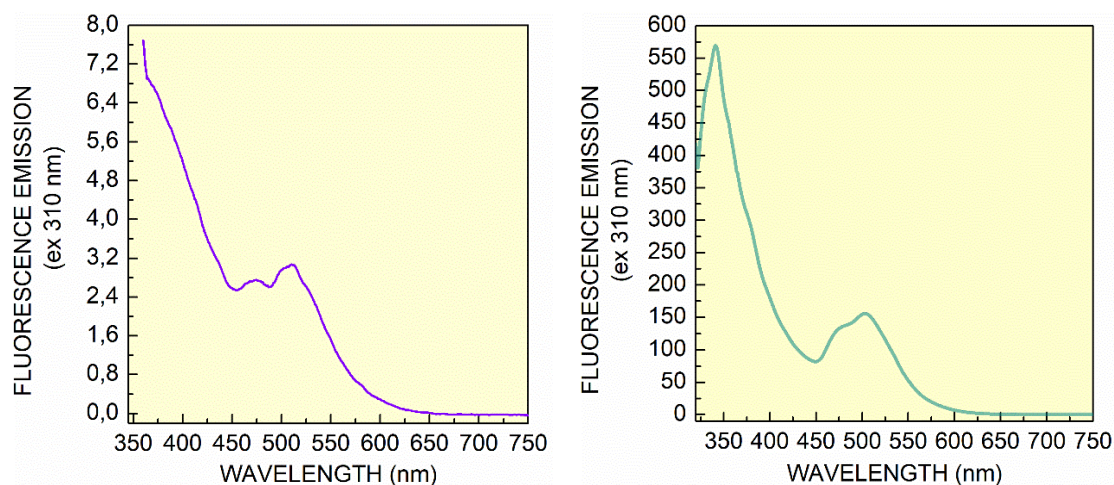


Figure 36. Fluorescence emission spectra of compound **PL 68** dissolved in water (left) and dioxane (right) using the maximum absorption in water, 310 nm for excitation.

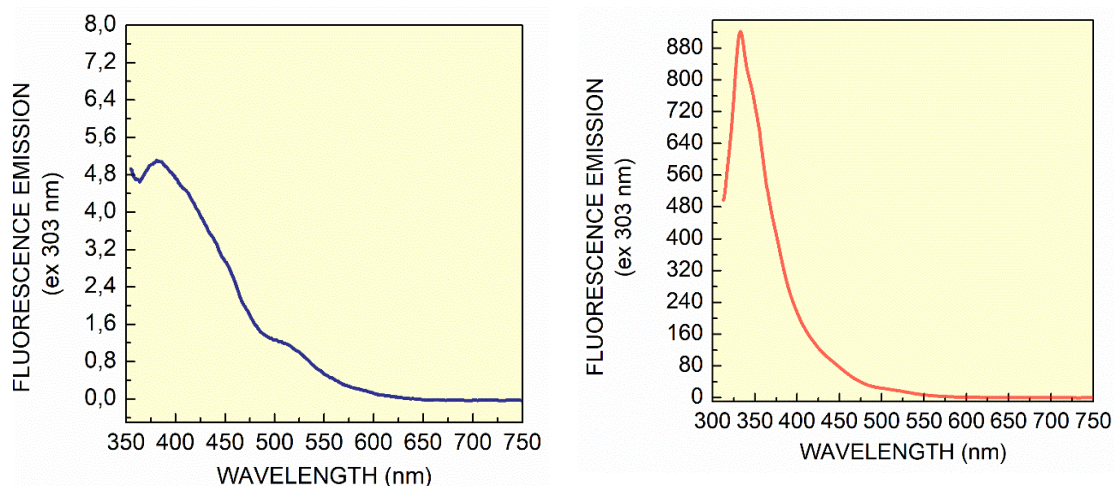


Figure 37. Fluorescence emission spectra of compound **PL 54** dissolved in water (*left*) and dioxane (*right*) using the maximum absorption in water, 303 nm for excitation.

As the fluorescence emission was so low in water compared with dioxane, we could expect a reduction in the intensity when the molecule would be in more polar regions of the cell. The dual bands of emission mainly observed in **PL 68** (Figure 36, *right part*), could be due to the chemical structure in which the cationic heads and the linker are bounded by weak interactions allowing an energetic exchange.

However, to be able to successfully excite the molecule in a cellular environment, we further explored the dioxane spectra. We collected the absorption spectra in dioxane from the fluorescence spectra, as its absorption maxima were not recorded in the spectrometer wavelength range used in none of the studied compounds.

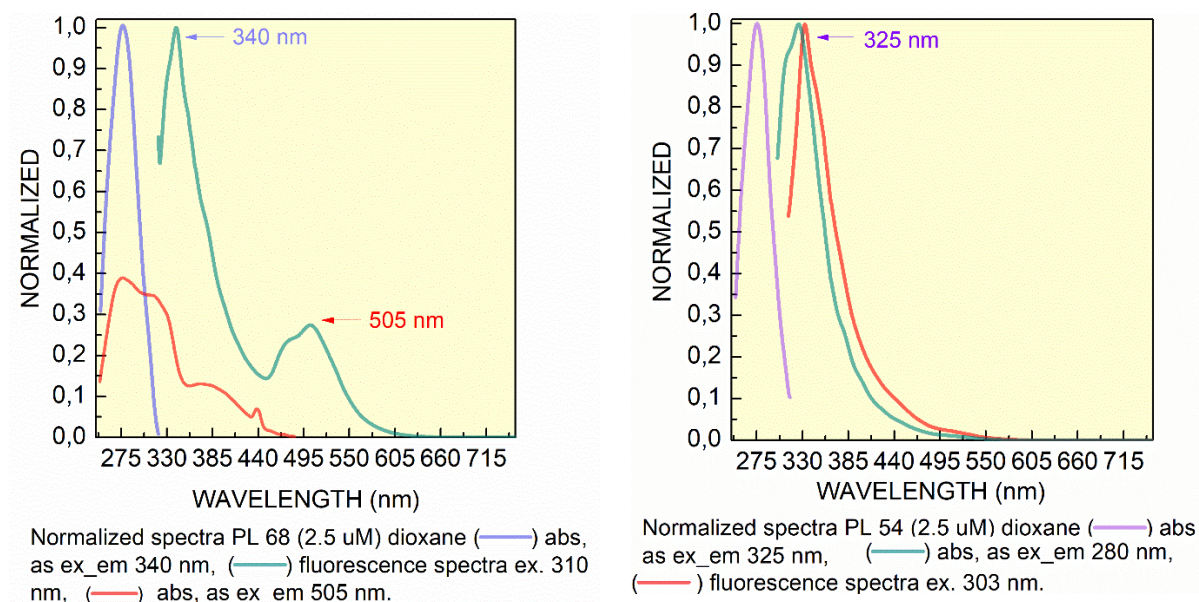


Figure 38. Absorption spectra recovered from the emission maximums for compounds **PL 68** (*left*) and **PL 54** (*right*).

We collected the excitation spectra at the peaks of fluorescence emission. In this way, we are able to see the “absorption” that give room to these bands and what is more, we can evaluate if the available laser wavelength in FLIM is able to work in a region of maximal absorption. From compound **PL 68**, we collected the excitation spectra when the emission was 340 nm and 505

nm (Figure 38, left part). The first absorption band (from 340 nm) was so energetic to be used with cells, while the second one (from 505 nm) even if of lower intensity allows using the 375 nm laser to excite the compound in confocal microscopy, even if not in its absorption maximum (Figure 39, left part).

On the other hand, for compound **PL 54** we recorded the excitation spectra when the emission was 325 nm. The collected “absorption peak”, was also blue-shifted and so energetic to be used (Figure 38, right part). At this point, we determined the excitation spectra when the emission was 280 nm which corresponds to a lower emission region but that gives an absorption inside the laser excitable wavelength (Figure 39, right part). There are no lasers of all the wavelengths available in the laboratory and the one we could use (at 375 nm) is already very energetic so that the biological sample is exposed to a lot of energy during the measure.

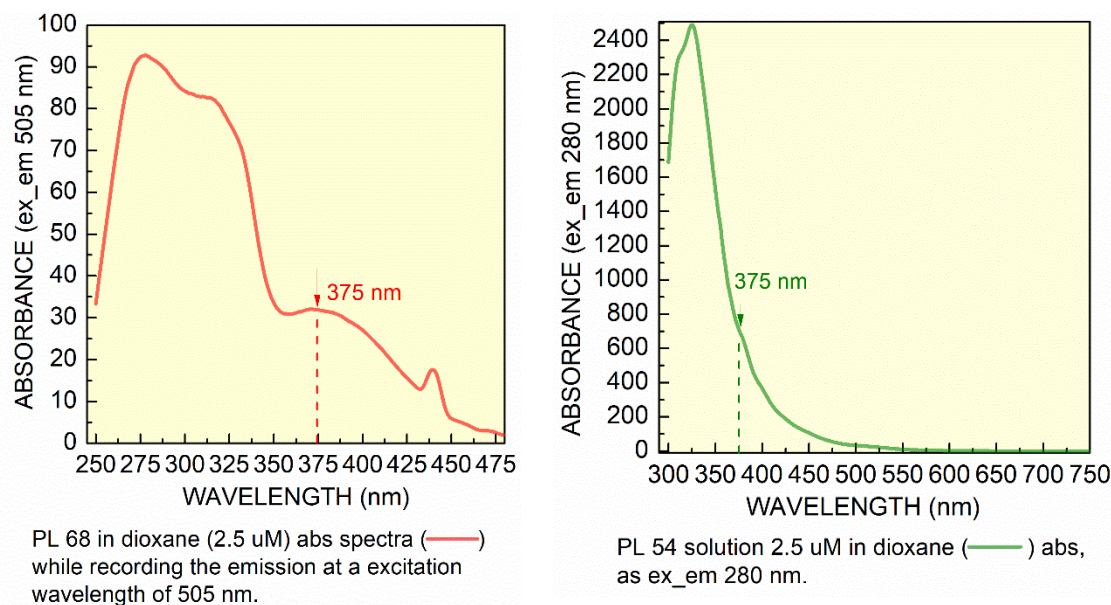


Figure 39. Absorption spectra in dioxane of **PL 68** (left) and **PL 54** (right) with the laser employed in FLIM (375 nm) excite region indicated.

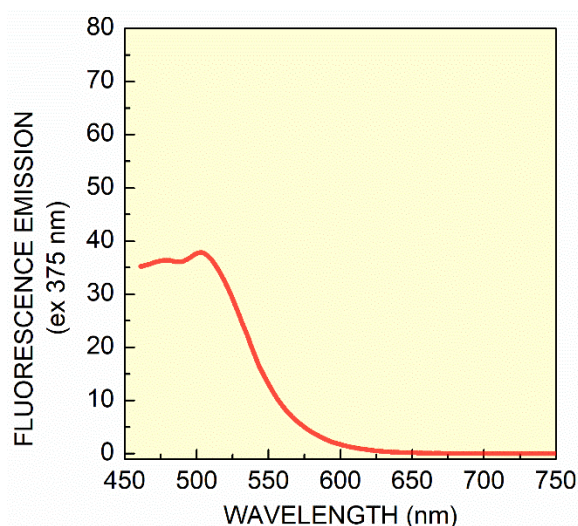


Figure 40. Compound **PL 68** fluorescence emission spectra when excited at 375 nm (same wavelength of the used laser in FLIM).

Given that the excitable part of the **PL 54** spectra is almost the tail of the absorption band (Figure 39, right part), it could lead to an unspecific fluorescence signal not owned to our compound but from other biological components.

Finally, we decided to use the compound **PL 68** for further in vitro assays and collected its fluorescence emission spectra when excited at 375 nm. The obtained spectra (Figure 40) showed low intensity, but it was enough to allow the recognition of the molecule inside the biological media.

The chosen compound showed absorption in the low UV spectra that could lead to cell damage and photobleaching. However, our purpose was not the implementation of those inhibitors as dyes

but to be able to see them in the cells over a short time and confirm their antiproliferative effect due to an enzymatic inhibition.

5.3 FLIM bioimaging on MCF-7 cells.

For the in-vitro evaluation, we used the cell line MCF-7 of breast adenocarcinoma. This type of neoplastic cell has been previously used in Choline Kinase inhibition and for testing its antiproliferative activity. They are Ras-activated cells and present overexpression of our target enzyme, ChoK.

The cells were grown in 25 mm coverslips for their visualization in the confocal microscopy lens. The cell medium was removed, and PBS (990 μ L) was added. The autofluorescence of the cells was measured as an average of different recorded cells. Then, 10 μ L of **PL 68** from a 2.5 mM stock solution, was added to the cell medium with a final concentration of 25 μ M. Images of the same cell were taken over time to see the compound accumulation. To those images have been subtracted the autofluorescence so that the collected signal is only due to our molecule.

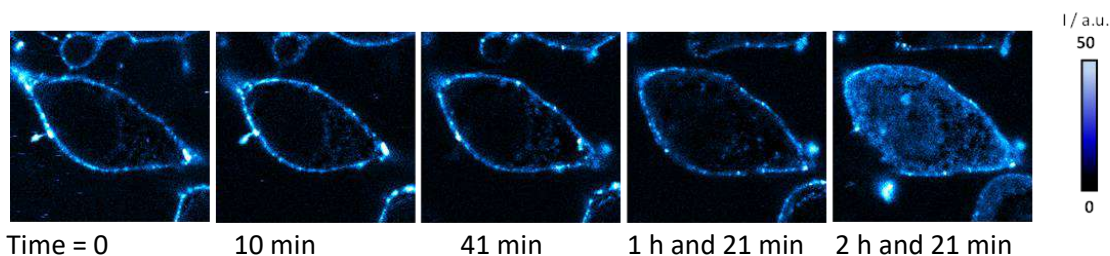


Figure 41. **PL 68** distribution on MCF-7 cells over the time.

As we can see in [Figure 41](#), firstly the inhibitor is accumulated in the plasmatic membrane. However, the compound is able to pass through it and reach the cytosol where the intensity is lower (more blue than white), as we previously observed in the fluorescence emission spectra done in water and dioxane.

To further analyse the intensity change, we took the same section in all the analysed images and recorded their intensity profile. It turned out that when the section went through the cell membrane, the collected intensity showed the highest peaks at the beginning and the end of the graphic. In the latter image ([Figure 42, image 5](#)), those intense peaks were also observed in the middle part of the graphic, which corresponds with the section crossing the cytosol and justified the proper entrance of **PL 68** in the cell.

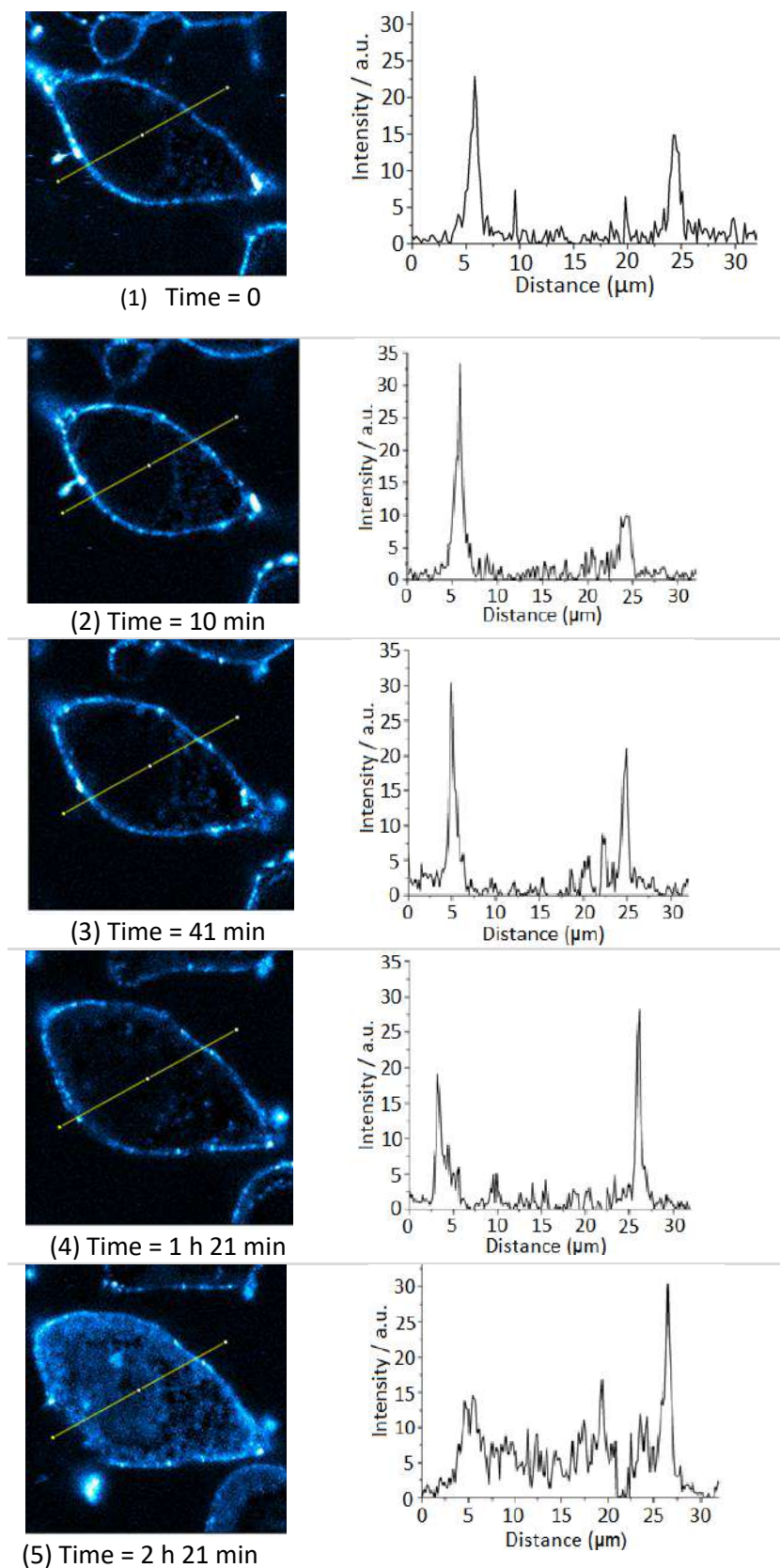


Figure 42. Intensity profile of PL 68 in the cross-section of the cell over time.

Finally, as the inhibitor is able to passively cross the membrane, we wanted to measure the amount of it that was able to enter and the proportion that remains in the membrane. In this

manner, we could determine if it is the enzyme inhibition, the choline uptake inhibition, or both mechanism that leads to the in-vitro antiproliferative effect.

In this attempt to quantify the inhibitor present in the cytosol, we selected the same cytosolic section in all the collected images and determined its average intensity value (Figure 43).

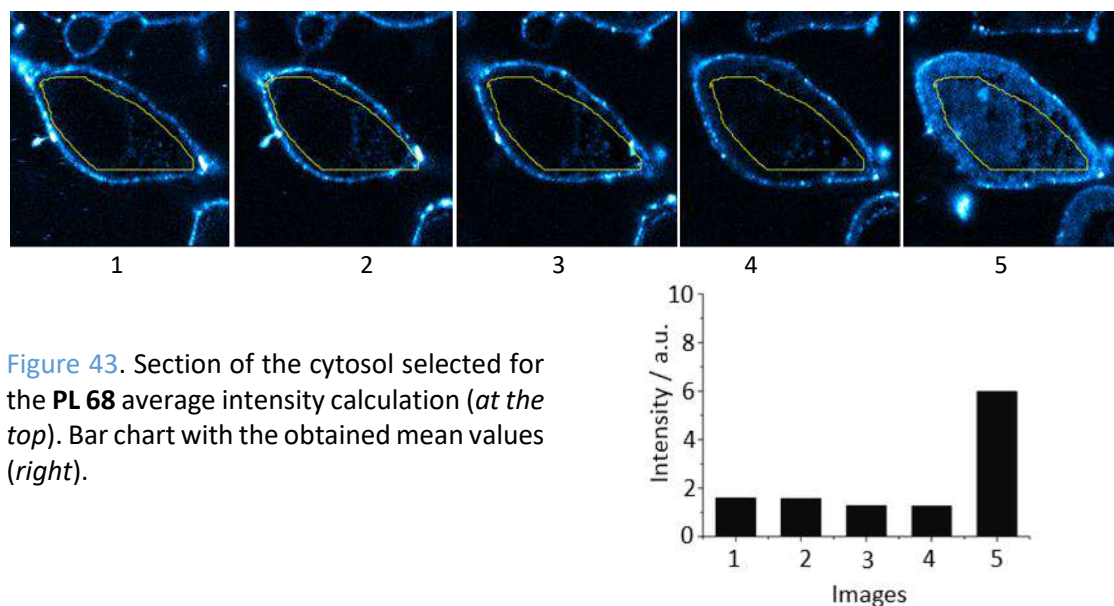


Figure 43. Section of the cytosol selected for the PL 68 average intensity calculation (at the top). Bar chart with the obtained mean values (right).

The mean intensity values represented in the bar chart (Figure 43, right part), allowed for clear visualization of the entrance of the inhibitor inside the cell. However, it was not possible to quantify the percentage of the compound inside and outside the cell, as we need to consider that with time part of the inhibitor could be washed out. The compound concentration inside the cell cannot be determined only with the fluorescence intensity. Nevertheless, we could confirm that there is a dual mechanism of action with which our inhibitors are able to reduce the phosphocholine contents in neoplastic cells.

5.4 In silico PAINS and pharmacodynamics assays.

Recently, PAINS (Pan Assays Interference Structures)¹³⁹ have been underlined as the major cause of High Throughput Screening (HTS) development failure.

It consists of structural moieties of drugs that could lead to a potent biological response that does not correspond to the target but to an off-target cytotoxic effect. Characteristics such as metal aggregation, chemical decomposition, protein reactivity and fluorescence are typically found in these kinds of structures.¹⁴⁰ Given the fluorescent properties of the synthesized compounds, we evaluated the medicinal chemistry suitability using the in-silico screening tool available in the free website (<http://www.swissadme.ch>) and developed by the SIB Swiss Institute of Bioinformatics.⁹⁹

The structures are drawn in the molecular sketcher or inserted in the SMILES format, and the compound's fragments are filtered through chemical libraries of compounds that are known to be unstable, reactive, toxic, or prone to interfere with biological assays. In this way, it could be recognized those undesirable patterns early in medicinal chemistry synthesis and evaluation. Compounds containing fragments as quinones, catechols, rhodanines or curcumins are among the 400 structural classes of well-known PAINS.¹³⁹ However, it is not an exclusion condition as there are commercial drugs that contain some of those groups, for example, antimalarials.

Compound	PAINS	Structural alert ^a	Compound	PAINS	Structural alert ^a
PL 40	NO	Quaternary N	PL 72	NO	Quaternary N
PL 46	NO	Quaternary N	PL 73	NO	Quaternary N
PL 48	NO	Quaternary N	FP 2	NO	Quaternary N and disulphide
PL 54	NO	Quaternary N	FP 3	NO	Quaternary N and disulphide
PL 55	NO	Quaternary N	FP 4	NO	Quaternary N and disulphide
PL 65	NO	Quaternary N	FP 5	NO	Quaternary N and disulphide
PL 67	NO	Quaternary N	FP 7	NO	Quaternary N and disulphide
PL 68	NO	Quaternary N	FP 14	NO	Quaternary N and disulphide
PL 69	NO	Quaternary N	FP 15	NO	Quaternary N and disulphide
PL 70	NO	Quaternary N	FP 16	NO	Quaternary N and disulphide
PL 71	NO	Quaternary N	FP 17	NO	Quaternary N and disulphide

Table 6. Structural alert and PAINS of the synthesized libraries.

^aImplemented by Brenk *et al*¹⁰². In green, we have highlighted compounds that are predicted to have good gastrointestinal absorption, in orange those with BBB (blood-brain-barrier) permeability and in grey those with low absorption and permeability.

As we can observe in Table 6, the main structural alert of our library of compounds is the quaternary nitrogen because it makes the molecule more reactive and could also behave as a surfactant agent. However, it is necessary for the inhibitor's selectivity and binding in the choline pocket. In the disulphide library, it was also emphasized the disulphide bond lability, which could suffer from breakage by the glutathione reductase or by radical species, for example. Nevertheless, apart from the eventual metabolism of the disulfide library, there are no fragments on the proposed inhibitors able to create considerable interferences in the biological outcome.

We further used the ADME predicted tool to preliminary evaluate the pharmacodynamic of our inhibitors. Most of them are absorbed in the gastrointestinal tract (Table 6, green colour) or shows poor solubility (Table 6, grey colour). Only compounds **PL 48**, **PL 70** and **FP 5** (Table 6, orange colour) showed BBB permeability which is an undesirable effect due to the capability to inhibit the acetylcholinesterase of previous inhibitors as **HC-3**, which gave room to cytotoxicity and respiratory paralysis.³¹

This useful information, even if from in-silico predictions, could guide the research towards the further modification of those compounds with low absorption or high BBB permeation, towards a safer absorption profile.

Conclusions

Following the philosophy of a green by design approach, we have synthesized two new libraries of ChoK inhibitors following the principles of Green Chemistry. The **PL library** was based on the dithioethane linker and composed of 13 inhibitors while the **FP library** was based on a disulphide linker and composed of 9 inhibitors.

The “greenness” assessment of such syntheses has been analyzed using green metrics such as the E-factor and EcoScale.

From the inhibitory point of view, the disulphide library (**FP**) seems to be more active than the dithioethane one (**PL**). However, **FP** compounds are more susceptible to being metabolized in cells.

Both linkers improved their activity when are assembled with the cationic heads [2,3-d] thienopyrimidine and thieno[3,2-b] pyridine substituted in 4 position with bigger cycloalkyl amines (azepane > piperidine > pyrrolidine). Compounds **PL 55** and **FP 3** arising as the hit to lead.

Docking assays correlate the **PL** library inhibitory activity to the interaction with the Mg atoms in the catalytic site, while the smaller **FP** linker was more rigid and showed higher S-scores due to the better interaction in the choline pocket and the less exposed cationic heads. Surprisingly, compound **FP 16** showed an unprecedented mode of binding in which both sulfur atoms are coordinated with the Mg cofactors.

Antiproliferative assays in MCF-7 and HepG2 tumoral cell lines determined that the dithioethane linker is superior to the disulphide in the biological media.

The molecules with the thieno[2,3-d] pyrimidine head showed growth inhibition values in accordance with their inhibitory activity over the enzyme, while the thieno[3,2-d] pyrimidine and the quinolinic ones seem to interact with off-target apoptotic pathways or to have permeability problems. The thieno[3,2-b] pyridine family was efficient inhibiting the enzyme but showed low antiproliferative activity. This fact could be due to their possible interaction with the choline membrane transporters.

Lastly, the pyridinic family was too polar, showing both low inhibitory and antiproliferative values as well as solubility problems in the **PL** library.

The best antiproliferative **PL** library showed slightly fluorescence in some inhibitors. As so, we could determine if the inhibitors accumulation in the neoplastic cells' membrane could be the reason for the uncorrelated inhibitory and antiproliferative profile in some compounds.

FLIM analysis showed that a dual mechanism coexists in this library of compounds. Thus, they could be more efficient towards different cancer cell lines as their function could be independent of their membrane permeability.

Finally, as fluorescence is a characteristic of molecules with PAINS, we carried out an in-silico evaluation of the possible interference structures of our libraries. In fact, the cationic charge, and the disulphide bond were detected as undesirable features. However, while the cationic charge is a necessary feature for the choline-binding site selectivity, the disulphide bond could effectively be broken and metabolized in cells.

Moreover, the predicted pharmacodynamics showed low GI absorption for the hit to lead compounds **PL 55** and **FP 3**. For that reason, further studies could be done to improve the ADME properties and design new inhibitors that could effectively displace the Mg²⁺ cofactors or bind to them to inhibit the enzymatic catalytic reaction.

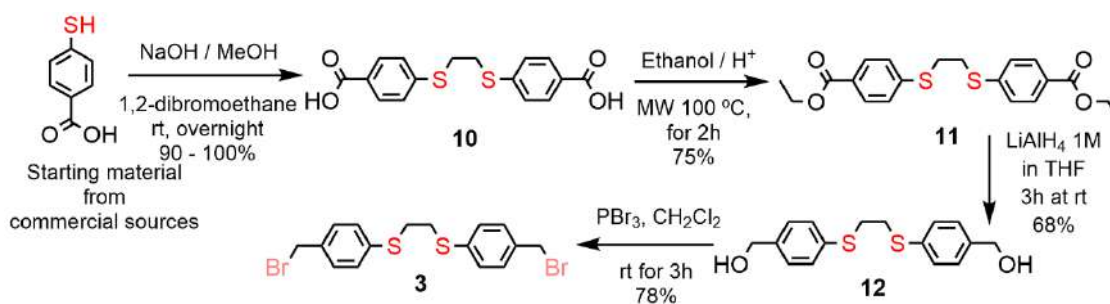
Experimental part

1. Synthesized compounds characterization: ^1H and ^{13}C NMR spectra, HRMS or Elemental Analysis, and melting point.

Reactions have been followed by TLC (Thin Layer Chromatography) and also, stained with KMnO_4 when the heads were synthesized to observe unreacted cyclic amines. The final compounds NMR signals have been unequivocally assigned by means of the bidimensional NMR experiments HSQC and HMBC of compounds **PL 54** and **FP 16**, of general structure. Methyl, methylene, tertiary, and quaternary carbons were well determined by ^{13}C -NMR and DEPT-135 spectra. High-Resolution Mass Spectrometry and or elemental analysis together with the melting point complete the characterization of both intermediates and final products.

1.2 Procedure for the synthesis of the dithioethane linker:

The synthesis of the dithioethane linker was done through a series of intermediates that allow achieving the desired product without the need for purification steps and with high yields. The synthetic strategy adopted is outlined in [Scheme 9](#).



Scheme 9. Dithioethane linker synthesis.

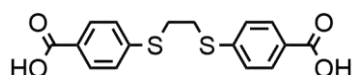
First, compound **10** was synthesized from the commercially available starting material 4-mercaptobenzoic acid. In a flame-dried round-bottom flask was charged sequentially a stir bar, NaOH (435.8 mg, 10.89 mmol, 2.4 eq) and methanol (5 mL for each 4.5 mmol of starting material). After stirring for 20 min at room temperature, 1,2-dibromoethane (195.6 μL , 2.27 mmol, 0.5 eq) and the thiol 4-mercaptobenzoic acid (700 mg, 4.54 mmol, 1 eq) were added to the solution.¹⁴¹ After stirring overnight, the volatiles were removed at 50 °C under reduced pressure. The obtained light-yellow solid was washed with HCl 2N and filtered in a Buchner. The final product **10** is obtained in a 100% yield (1.52 g, 4.54 mmol) after dried under vacuum.

Compound **10** (200 mg, 0.6 mmol, 1 eq) was loaded in a microwave tube with ethanol (2 mL for each 200 mg of comp. **10**) and sulphuric acid as the catalyst (1 drop for each 100 mg of comp. **10**). The reaction was left for 2 hours at 100 °C and then cooled down under an ice bath. A white solid precipitated was recovered in a funnel of porous filter and dried well under vacuum, obtaining **11** in a 75% yield (175.9 mg, 0.45 mmol).

Next, in an oven-dried two neck-flask and under a nitrogen atmosphere was added the magnetic stir, compound **11** (322 mg, 0.825 mmol, 1 eq) and dry THF (18 mL for each 400 mg of comp. **11**). When the solution was homogeneous, the flask was surrounded with an ice/water bath and, when it was 0 °C, a solution of LiAlH₄ 1M in THF (4.95 mL, 4.95 mmol, 6 eq) was added dropwise. After the addition, the reaction was stirred at room temperature for 3 hours and then, quenched with HCl 2N and some methanol. The crude solution was left stirring overnight open to air and extracted with EtOAc/H₂O (x3), dried with Na₂SO₄, filtered, and the solvent removed under reduced pressure, obtaining **12** in a 68% yield (171.9 mg, 0.56 mmol).¹⁴² Improving the reaction was also possible using DIBAL 1M in Toluene (5 mL, 5 mmol, 6 eq) instead of the more

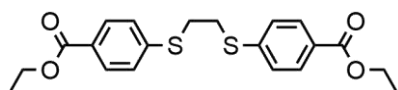
reactive LiAlH_4 , that in the same conditions and after 24 hours of reaction provide compound **12** in a 64% yield (161 mg, 0.53 mmol).

Finally, to the diol **12** (217 mg, 0.708 mmol, 1 eq) in dichloromethane (7 mL for each 200 mg of comp. **12**), was added PBr_3 (87.4 μL , 0.921 mmol, 1.3 eq) at 0 °C and the resulting yellowish solution was stirred at room temperature for 3 hours. Then, the reaction mixture was quenched with a saturated NaHCO_3 solution and stirred at room temperature for an additional 30 min. The resulting white suspension was extracted with CH_2Cl_2 (x3), and the combined extracts were dried over Na_2SO_4 and evaporated in vacuo to give **3** in a 78% yield (239.2 mg, 0.55 mmol).¹⁴³ In a closer approach towards a *green* procedure, it was possible to use diethyl ether (3 mL for each 0.13 mmol of comp. **12**) as reaction media running the reaction at room temperature for 1 day and extracting it with EtOAc (x3). Compound **3** was thus obtained at a 59% yield (33 mg, 0.07 mmol) without further purification.¹⁴⁴



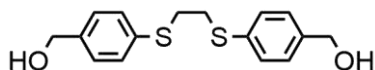
4,4'-(ethane-1,2-diylbis(sulfanediyl))dibenzoic acid (10). The product was obtained without further purification as a light-yellow solid, (1.52 g, 4.54 mmol), yield: 100%, melting point:

307.8 °C. ¹H-NMR (400 MHz, DMSO): δ 7.84 (d, J = 8.4 Hz, 4H, Ar-S), 7.37 (d, J = 8.4 Hz, 4H, Ar-C), 3.30 (s, 4H, S-(CH₂)₂-S). ¹³C-NMR (101 MHz, DMSO-*d*₆): δ 129.93 (4C, -CH-, Ar-C), 126.83 (4C, -CH-, Ar-S), 46.45 (2C, -CH₂-, S-(CH₂)₂-S). The sample was insoluble at high concentrations and quaternary carbons were unable to be recorded in the JMOD-13C. **ES- HRMS** (m/z) [M]: calculated for C₁₆H₁₃O₄S₂: 333.0255, found: 333.0232.



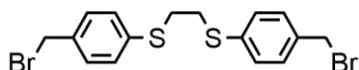
Diethyl 4,4'-(ethane-1,2-diylbis(sulfanediyl))dibenzoate (11). The product was obtained without further purification as a white solid, (175.9 mg, 0.45 mmol), yield:

75%, melting point: 98.5 °C. ¹H-NMR (500 MHz, DMSO): δ 7.86 (d, J = 8.5 Hz, 4H, Ar-S), 7.42 (d, J = 8.5 Hz, 4H, Ar-C), 4.30 (q, J = 7.1 Hz, 4H, -CH₂-), 3.34 (s, 4H, S-(CH₂)₂-S), 1.31 (t, J = 7.1 Hz, 6H, -CH₃). ¹³C-NMR (101 MHz, DMSO-*d*₆): δ 165.34 (2C, -C-), 142.57 (2C, -C-), 129.71 (4C, -CH-, Ar-C), 126.79 (4C, -CH-, Ar-S), 126.72 (2C, -C-), 60.69 (2C, -CH₂-, -CH₂-CH₃), 30.51 (2C, -CH₂-, S-(CH₂)₂-S), 14.18 (2C, -CH₃-, -CH₂-CH₃). **ES+ HRMS** (m/z) [M+Na]⁺: calculated for C₂₀H₂₂O₄S₂Na: 413.0857, found: 413.0835.



((Ethane-1,2-diylbis(sulfanediyl))bis(4,1-phenylene)) dimethanol (12). The product was obtained without

further purification as a white solid, (171.9 mg, 0.56 mmol), yield: 68%, melting point: 241.7 °C. ¹H-NMR (500 MHz, DMSO): δ 7.27 (d, J = 8.9 Hz, 4H, Ar-S), 7.26 (d, J = 9.0 Hz, 4H, Ar-C), 5.19 (bs, 2H, -OH), 4.46 (s, 4H, -CH₂-), 3.09 (s, 4H, S-(CH₂)₂-S). ¹³C-NMR (101 MHz, DMSO-*d*₆): δ 140.99 (2C, -C-), 132.85 (2C, -C-), 129.11 (4C, -CH-, Ar-C), 127.35 (4C, -CH-, Ar-S), 62.46 (2C, -CH₂-, CH₂-OH), 32.56 (2C, -CH₂-, S-(CH₂)₂-S). **ES- HRMS** (m/z) [M+CHOOH]⁺: calculated for C₁₇H₁₉O₄S₂: 351.0725, found: 351.0728.



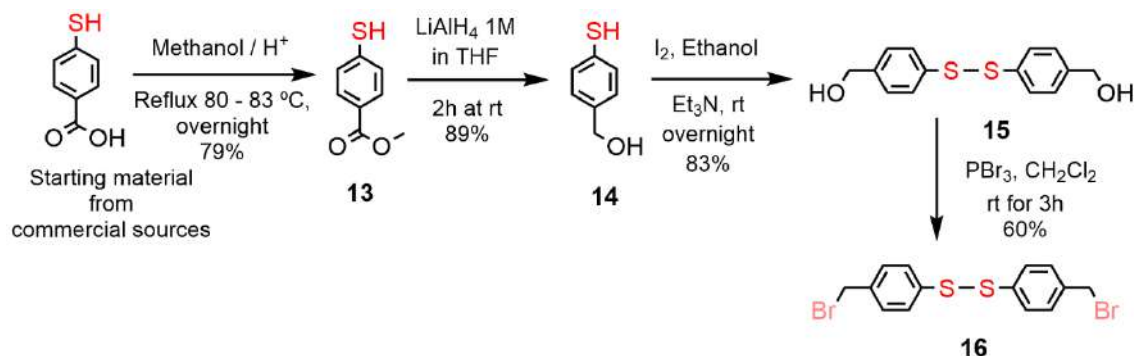
1,2-bis((4-(bromomethyl)phenyl)thio)ethane (3). The product was obtained without further purification as a

white solid, (239.2 mg, 0.55 mmol), yield: 78%, melting point: 138.6 °C. ¹H-NMR (400 MHz, DMSO): δ 7.39 (d, J = 8.4 Hz, 4H, Ar-S), 7.28 (d, J = 8.4 Hz, 4H, Ar-C), 4.69 (s, 4H, -CH₂-), 3.18 (s, 4H, S-(CH₂)₂-S). ¹³C-NMR (101 MHz, DMSO-*d*₆): δ 135.82 (2C, -C-), 135.70 (2C, -C-), 130.12 (4C, -CH-, Ar-C), 128.47 (4C, -CH-, Ar-S), 34.26 (2C, -CH₂-, CH₂-Br), 31.73 (2C, -CH₂-, S-(CH₂)₂-S). **ES+ HRMS** (m/z) [M+H]⁺: calculated for C₁₆H₁₇S₂Br₂: 430.9138, found: 430.9140.

1.3 Procedure for the synthesis of the disulphide linker.

The disulphide linker synthesis has been improved based on the last developed procedure for the dithioethane linker. Similarly, we started the synthesis with the commercially available 4-mercaptobenzoic acid.

The synthetic strategy adopted is following described in [Scheme 10](#).



Scheme 10. The disulphide linker synthetic pathway.

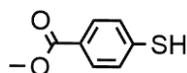
To a solution of 4-mercaptobenzoic acid (1 gr, 6.5 mmol, 1 eq) in methanol (5 mL for each 6.5 mmol of 4-mercaptobenzoic acid) was added catalytic sulfuric acid (2 drops for each 6.5 mmol of 4-mercaptobenzoic acid) and then refluxed at 80 °C – 83 °C overnight. Once finished, the methanol was distilled off in vacuo and the residue was diluted with EtOAc. Then, it was extracted twice with water, followed by a 10% aq. sodium bicarbonate solution. The organic layer was dried over Na₂SO₄ and concentrated in vacuo to obtain the product **13** in a 79% yield (861.9 mg, 5.12 mmol).¹⁴⁵ We also tried to optimize this step by reducing the heating time using the microwave irradiation (30 min at 70 °C), but together with the desired product, it was also observed substitution in the free thiol group and unreacted starting material, giving room to a 59% yield (161.6 mg, 0.96 mmol) after chromatographic purification in silica gel flash with a polarity of 9.75 CH₂Cl₂/ 0.25 MeOH.

Next, follows the reduction to alcohol using the same procedure as used for comp. **12**. In an oven-dried two neck-flask and under a nitrogen atmosphere was added the magnetic stir, compound **13** (100 mg, 0.59 mmol, 1 eq) and dry THF (4 mL for each 100 mg of comp. **13**). When the reaction is a homogeneous solution, we add dropwise the LiAlH₄ 1M in THF (1.07 mL, 1.07 mmol, 1.8 eq) with the flask under an ice/water bath. After the addition, the reaction is left at room temperature for 2 hours. Then, it is quenched with HCl 2N and some methanol. The crude solution was left stirring still one hour and a half open to air and extracted with EtOAc/H₂O (x3), dried with Na₂SO₄, filtered, and the solvent removed under reduced pressure, obtaining **14** in an 89% yield (73.6 mg, 0.52 mmol).^{142,146}

The dimerization step took place adding the comp. **14** (758 mg, 5.4 mmol, 1eq) and iodine (686.4 mg, 2.704 mmol, 0.5 eq) to a solution of ethanol (10 mL for each 470 mg of comp. **14**). Then, triethylamine (226.1 μL, 1.62 mmol, 0.3 eq) was added, and the solution was left overnight to react. Excess iodine was removed by reduction with an aq. solution 10% of sodium thiosulfate. The solvent was removed under vacuum and the product precipitated with HCl 2N. Compound **15** was collected after filtration under pressure and dried up under vacuum, in an 83% yield (623.8 mg, 2.24 mmol).¹⁴⁷

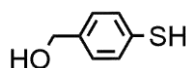
Finally, the bromination was carried out as for the dithioethane linker. To the diol **15** (689.5 mg, 2.48 mmol, 1eq) in a solution of dichloromethane (7.5 mL for each 200 mg of comp. **15**), was added PBr₃ (306 μL, 3.22 mmol, 1.3 eq) at 0 °C and the resulting orangish solution was stirred at room temperature for 3 hours. Then, the reaction mixture was quenched with a sat. solution in NaHCO₃ and stirred at room temperature for an additional 30 min. Next, it was extracted with

$\text{CH}_2\text{Cl}_2/\text{H}_2\text{O}$ (x3) and the organic phase dried with Na_2SO_4 and evaporated in vacuo to give compound **16** in a 60% yield (601.4 mg, 1.49 mmol).¹⁴³



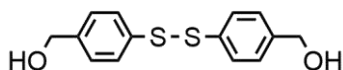
Methyl 4-mercaptobenzoate (13). The product was obtained without further purification as white-yellow solid, (861.9 mg, 5.12 mmol), yield: 79%, melting point: 55.9 °C. ¹**H-NMR** (400

MHz, CDCl_3): δ 7.88 (d, J = 8.6 Hz, 2H, Ar-C), 7.28 (d, J = 8.7 Hz, 2H, Ar-S), 3.89 (s, 3H, $-\text{CH}_3$), 3.60 (s, 1H, $-\text{SH}$). **ES- HRMS** (m/z) [M]: calculated for $\text{C}_8\text{H}_7\text{O}_2\text{S}$: 167.0167, found: 167.0159. The characterized product is in accordance with the literature.¹⁴⁸



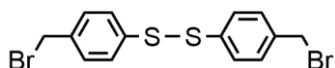
(4-mercaptophenyl) methanol (14). The product was obtained without further purification as a white solid, (73.6 mg, 0.52

mmol), yield: 89%, melting point: 51.1 °C. ¹**H-NMR** (400 MHz, CDCl_3): δ 7.27 (d, J = 8.5 Hz, 2H, Ar-S), 7.24 (d, J = 8.5 Hz, 2H, Ar-C), 4.64 (s, 2H, $-\text{CH}_2-$), 3.45 (s, 1H, $-\text{SH}$). **ES- HRMS** (m/z) [M]: calculated for $\text{C}_7\text{H}_7\text{OS}$: 139.0218, found: 139.0213. The characterized product is in accordance with the literature.¹⁴⁹



(Disulfanediylbis(4,1-phenylene)) dimethanol (15). The product was obtained without further purification as a brown-

yellow solid, (623.8 mg, 2.24 mmol), yield: 83%, melting point: 110.1 °C – 110.3 °C. ¹**H-NMR** (400 MHz, CDCl_3): δ 7.49 (d, J = 8.5 Hz, 4H, Ar-S), 7.30 (d, J = 8.8 Hz, 4H, Ar-C), 4.66 (s, 4H, $-\text{CH}_2-$). **ES- HRMS** (m/z) [M+Cl]: calculated for $\text{C}_{14}\text{H}_{14}\text{O}_2\text{S}_2\text{Cl}$: 313.0124, found: 313.0128. The characterized product is in accordance with the literature.¹⁵⁰



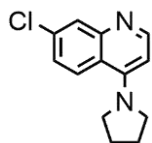
1,2-bis(4-(bromomethyl) phenyl) disulfane (16). The product was obtained without further purification as a light-yellow

solid, (601.4 mg, 1.49 mmol), yield: 60%, melting point: 90 °C. ¹**H-NMR** (400 MHz, CDCl_3): δ 7.45 (d, J = 8.6 Hz, 4H, Ar-S), 7.33 (d, J = 8.5 Hz, 4H, Ar-C), 4.46 (s, 4H, $-\text{CH}_2-$). **ES- HRMS** (m/z) [M+HCl]: calculated for $\text{C}_{14}\text{H}_{13}\text{Br}_2\text{ClS}_2$: 437.8500, found: 437.2452. Elemental analysis: theoretical C: 41.60%, H: 2.99%, S: 15.86%, Br: 39.54%; found C: 46.75%, H: 4.22%, N: 0.12%, S: 14.41%, Br: 39%. The characterized product is in accordance with the literature.¹⁵¹

1.4 Procedure for the synthesis of the heads.

Regarding the heteroaromatic heads, only the DMAP (*p*-dimethylamino pyridine) and the 4-pyrrolidine pyridine were commercially available from Sigma Aldrich. The rest of the chosen heads were synthesized from previously reported procedures or adapting them to a greener methodology when possible.

Compound **20** was synthesized adapting the classical reported procedure that uses reflux conditions¹¹⁶ to the microwave *greener* methodology. To a microwave reaction tube was added 4,7-dichloroquinoline (600 mg, 3.03 mmol, 1 eq) and pyrrolidine (252.8 μL , 3.03 mmol, 1 eq). The reaction was set at 100 °C for 1 hour and a half and when the mixture was cooled to room temperature, neutralized with NaOH 1N and extracted with $\text{CH}_2\text{Cl}_2/\text{H}_2\text{O}$ (x3). The combined organic layers were dried with Na_2SO_4 and concentrated in vacuo.

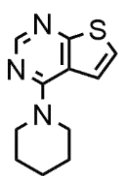


7-chloro-4-(pyrrolidin-1-yl) quinoline (20). The crude product was purified by silica gel column chromatography (9.75 $\text{CH}_2\text{Cl}_2/0.25$ MeOH) obtaining the tittle product as a brown solid, (244.8 mg, 1.05 mmol), yield: 34%, melting point: 92.4 °C. ¹**H-NMR** (400 MHz, Chloroform-*d*): δ 8.44 (d, J = 5.5 Hz, 1H, H-2quin),

8.12 (d, J = 9.2 Hz, 1H, H-8quin), 7.92 (d, J = 2.2 Hz, 1H, H-5quin), 7.24 (dd, J = 9.2, 2.3 Hz, 1H, H-6quin), 6.40 (d, J = 5.5 Hz, 1H, H-3quin), 3.68 – 3.62 (m, 4H, H-2,5pyrr), 2.07 – 2.02 (m, 4H, H-

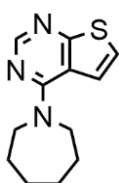
3,4-pyrr). **ES+ HRMS** (m/z) [M+H]⁺: calculated for C₁₃H₁₄N₂Cl: 233.0846, found: 233.0860. The characterized product is in accordance with the literature.¹¹⁶

Compounds **21** and **22** were synthesized following both the same procedure. In a microwave tube was added 4-chlorothieno[2,3-d] pyrimidine (200 mg, 1.17 mmol, 1 eq), the corresponding cyclic amine piperidine or azepane (126.5 μ L of piperidine or 145 μ L of azepane, 1.29 mmol, 1.1 eq) and DIPEA (245 μ L, 1.41 mmol, 1.2 eq). To this mixture is added isopropanol (2 mL for each 100 mg of 4-chlorothieno[2,3-d] pyrimidine) under an ice bath because the reaction is exothermic. The sealed tube was introduced in the microwave at 130°C for 15 min and once cooled down, extracted with EtOAc/H₂O (x3). The organic layers were dried with Na₂SO₄ and concentrated in vacuo. The crude product was purified stirring at room temperature in Hexane, while the impurities remain insoluble.



4-(piperidin-1-yl)thieno[2,3-d]pyrimidine (21). The product was obtained without further purification as a yellow-brown solid, (218 mg, 0.99 mmol), yield: 85%, melting point: 49.6 °C. **¹H-NMR** (400 MHz, Methanol-*d*₄): δ 8.32 (s, 1H, H-2thienop), 7.50 (d, *J* = 6.2 Hz, 1H, H-6thienop), 7.46 (d, *J* = 6.0 Hz, 1H, H-5thienop), 3.94 – 3.82 (m, 4H, H-2,6piper), 1.83 – 1.62 (m, 6H, H-3,4,5piper). **ES+ HRMS** (m/z) [M+H]⁺: calculated for C₁₁H₁₄N₃S: 220.0908, found: 220.0898.

The characterized product is in accordance with the literature.^{152,153}



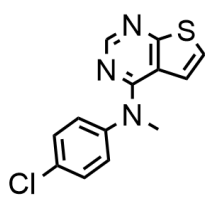
4-(azepan-1-yl)thieno[2,3-d] pyrimidine (22). The product was obtained without further purification as a yellow solid, (245 mg, 1.05 mmol), yield: 90%, melting point: 69.8 °C. **¹H-NMR** (400 MHz, Methanol-*d*₄): δ 8.29 (s, 1H, H-2thienop), 7.56 (d, *J* = 6.2 Hz, 1H, H-6thienop), 7.41 (d, *J* = 6.2 Hz, 1H, H-5thienop), 3.97 (t, *J* = 6.0 Hz, 4H, H-2,7azep), 1.97 – 1.82 (m, 4H, H-3,6azep), 1.66 – 1.53 (m, 4H, H-4,5azep). **ES+ HRMS** (m/z) [M+H]⁺: calculated for C₁₂H₁₆N₃S: 234.1065, found: 234.1042. The characterized product is in accordance with the literature.¹⁵²

The characterized product is in accordance with the literature.¹⁵²

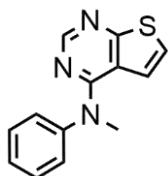
On the other hand, when using an aromatic amine as substituent in the para position, the synthesis of **23** and **24** were done differently from their cyclic amine counterparts. This time, to a solution of 4-chlorothieno[2,3-d] pyrimidine (300 mg, 1.76 mmol, 1 eq) and *N*-methylaniline or 4-chloro-*N*-methylaniline (228.6 μ L of *N*-methylaniline or 255.5 μ L of 4-chloro-*N*-methylaniline, 2.11 mmol, 1.2 eq) in isopropanol (5 mL for each 250 mg of 4-chlorothieno[2,3-d] pyrimidine) is added 3 drops of HCl concentrated and it is mixed under stirring for 24 hours (comp. **24**) and 4 hours (comp. **23**) at room temperature. Once the reaction is completed, the product is precipitated in the flask with diethyl ether and stirred for an additional 15 min. The product is finally filtered under vacuum and washed with more Et₂O.

In an attempt to reproduce the reaction using the microwave, compound **24** was also synthesized with another procedure following described. In a microwave reaction vessel was introduced 4-chlorothieno[2,3-d] pyrimidine (170 mg, 0.99 mmol, 1 eq), *N*-methylaniline (130 μ L, 1.19 mmol, 1.2 eq) and triethylamine (166 μ L, 1.19 mmol, 1.2 eq) in methanol (2 mL for each 170 mg of 4-chlorothieno[2,3-d] pyrimidine). Seal the reaction vessel and irradiate at 100°C for 10-12 min at a maximum power of 80 W. Control the reaction by TLC, and after completion evaporate the solvent and wash the crude product with cold methanol. However, it was necessary to further purify the crude product with a chromatographic column in silica gel and gradually increase the polarity from 9 Hex/1 EtOAc to 1 Hex/1 EtOAc. It was obtained a 52% yield (125.9 mg, 0.5 mmol) of comp. **24**.¹⁵⁴

***N*-(4-chlorophenyl)-*N*-methylthieno[2,3-d] pyrimidin-4-amine (23)**. The product was obtained without further purification as a light-green solid, (194 mg, 0.7 mmol), yield: 40%, melting point: 150.9 °C - 153 °C; (183 °C dc). **¹H-NMR** (400 MHz, Chloroform-*d*): δ 8.73 (s, 1H, H-2thienop), 7.59

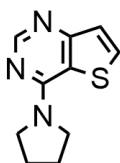


(d, $J = 8.6$ Hz, 2H, H-3,5anil), 7.33 (d, $J = 8.6$ Hz, 2H, H-2,6anil), 7.21 (d, $J = 6.0$ Hz, 1H, H-6thienop), 5.64 (d, $J = 5.7$ Hz, 1H, H-5thienop), 3.80 (s, 3H, N-CH₃). ¹³C-NMR (126 MHz, Chloroform-*d*): δ 145.83 (1C, -CH-, C-2thienop), 141.66 (2C, -C-), 136.19 (1C, -C-), 131.32 (2C, -CH-, C-3,5anil), 128.58 (2C, -CH-, C-2,6anil), 125.27 (1C, -CH-, C-6thienop), 121.24 (1C, -CH-, C-5thienop), 117.12 (2C, -C-), 42.50 (1C, -CH₃, N-CH₃). **ES+ HRMS** (m/z) [M+H]⁺: calculated for C₁₃H₁₁N₃SCl: 276.0362, found: 276.0343.

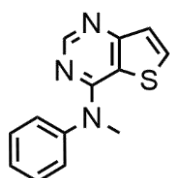


N-methyl-*N*-phenylthieno[2,3-*d*]pyrimidin-4-amine (**24**). The product was obtained without further purification as a light-pink solid, (237 mg, 0.98 mmol), yield: 56%, melting point: 132.9 °C. ¹H-NMR (500 MHz, Methanol-*d*₄): δ 8.49 (s, 1H, H-2thienop), 7.56 – 7.51 (m, 2H, H-2,6anil), 7.50 – 7.46 (m, 1H, H-4anil), 7.36 (dd, $J = 8.3, 1.3$ Hz, 2H, H-3,5anil), 7.06 (d, $J = 6.2$ Hz, 1H, H-6thienop), 5.59 (d, $J = 6.2$ Hz, 1H, H-5thienop), 3.62 (s, 3H, N-CH₃). ¹³C-NMR (101 MHz, Methanol-*d*₄): δ 147.88 (1C, -CH-, C-2thienop), 144.72 (2C, -C-), 132.05 (2C, -CH-, C-2,6anil), 131.24 (1C, -CH-, C-4anil), 128.30 (2C, -CH-, C-3,5anil), 124.88 (1C, -CH-, C-6thienop), 123.22 (1C, -CH-, C-5thienop), 118.49 (2C, -C-), 42.44 (1C, -CH₃, N-CH₃). **ES+ HRMS** (m/z) [M+H]⁺: calculated for C₁₃H₁₂N₃S: 242.0752, found: 242.0751.

For the synthesis of compounds **25** and **26** with the 4-chlorothieno[3,2-*d*]pyrimidine moiety, it was followed the same procedure as in the previously describe 4-chlorothieno[2,3-*d*]pyrimidine counterparts, for cyclic and aromatic amines, using the pyrrolidine and the *N*-methylaniline respectively.



4-(pyrrolidin-1-yl)thieno[3,2-*d*]pyrimidine (**25**). The product was obtained without further purification as a yellow solid, (139.3 mg, 0.67 mmol), yield: 58%, melting point: 144.9 °C. ¹H-NMR (500 MHz, Methanol-*d*₄): δ 8.31 (s, 1H, H-2thienop), 8.01 (d, $J = 5.5$ Hz, 1H, H-6thienop), 7.32 (d, $J = 5.6$ Hz, 1H, H-7thienop), 3.89 (bs, 4H, H-2,5pyrr), 2.09 (bs, 4H, H-3,4pyrr). **ES+ HRMS** (m/z) [M+H]⁺: calculated for C₁₀H₁₂N₃S: 206.0752, found: 206.0739. The characterized product is in accordance with the literature.^{152,155}

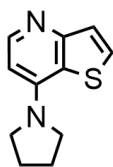


N-methyl-*N*-phenylthieno[3,2-*d*]pyrimidin-4-amine (**26**). The product was obtained without further purification as a yellow solid, (408 mg, 1.69 mmol) yield: 96%, melting point: 239.6 °C. ¹H-NMR (400 MHz, Methanol-*d*₄): δ 8.88 (s, 1H, H-2thienop), 8.17 (d, $J = 5.6$ Hz, 1H, H-6thienop), 7.70 – 7.63 (m, 3H, H-2,4,6anil), 7.60 – 7.57 (m, 2H, H-3,5anil), 7.40 (d, $J = 5.6$ Hz, 1H, H-7thienop), 3.82 (s, 3H, N-CH₃). ¹³C-NMR (101 MHz, Methanol-*d*₄): δ 159.76 (1C, -C-), 149.16 (1C, -CH-, C-2thienop), 147.86 (1C, -C-), 142.59 (1C, -C-), 141.64 (1C, -CH-, C-6thienop), 132.02 (1C, -CH-, C-7thienop), 131.76 (2C, -CH-, C-2,6anil), 130.02 (2C, -CH-, C-3,5anil), 117.93 (1C, -CH-, C-4anil), 117.46 (1C, -C-), 41.56 (1C, -CH₃, N-CH₃). **ES+ HRMS** (m/z) [M+H]⁺: calculated for C₁₃H₁₂N₃S: 242.0752, found: 242.0748.

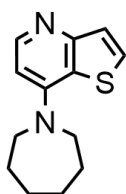
Compounds **27** and **28**, with the thieno[3,2-*b*]pyridine moiety, were first synthesized using the microwave irradiation as a heating source. However, the cyclic amine azepane in comp. **28** showed low reaction yield so that it was finally synthesized using the traditional reflux methodology for longer times.

For compound **27**, in a microwave tube was added 7-chlorothieno[3,2-*b*]pyridine (200 mg, 1.18 mmol, 1 eq) and pyrrolidine (295 μ L, 3.5 mmol, 3 eq). To the sealed tube was injected an inert atmosphere of Argon and then, was introduced in the microwave at 180 °C for 15 min with stirring. Once finished, it was extracted with CH₂Cl₂/H₂O (x3) and the organic layers dried with Na₂SO₄, filtered, and evaporated under reduced pressure with the rotavapor.

For compound **28**, in a flask was added 7-chloro-thieno[3,2-*b*]pyridine (400 mg, 2.36 mmol, 1 eq) and azepane (1.86 mL, 16.5 mmol, 7 eq) with a magnetic stir. The mixture is refluxed under Argon atmosphere at 110 °C for 24 hours. After this time, the reaction is cooled down at room temperature and neutralized with NaOH 1 N. The crude product was extracted with CH₂Cl₂/H₂O (x2) and once with brine. The organic phase is dried with Na₂SO₄, filtered, and evaporated under reduced pressure.

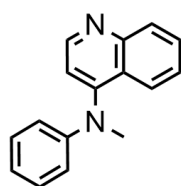


7-(pyrrolidin-1-yl)thieno[3,2-*b*]pyridine (27). The product was obtained after chromatographic column purification in silica gel and a mobile phase of 9.5 CH₂Cl₂/ 1 MeOH, as a light-brown solid, (149 mg, 0.73 mmol), yield: 62%, melting point: 76.5 °C. ¹H-NMR (500 MHz, Methanol-*d*₄): δ 8.09 (d, *J* = 5.9 Hz, 1H, H-2thienop), 7.81 (d, *J* = 5.6 Hz, 1H, H-6thienop), 7.33 (d, *J* = 5.6 Hz, 1H, H-7thienop), 6.32 (d, *J* = 5.9 Hz, 1H, H-3thienop), 3.78 (t, *J* = 6.7 Hz, 4H, H-2,5pyrr), 2.09 (quint, *J* = 3.3 Hz, 4H, H-3,4pyrr). **ES+ HRMS** (m/z) [M+H]⁺: calculated for C₁₁H₁₃N₂S: 205.0799, found: 205.0779. The characterized product is in accordance with the literature.¹⁵²

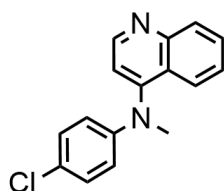


7-(azepan-1-yl)thieno[3,2-*b*]pyridine (28). The product was obtained after chromatographic column purification in silica gel and a polarity of 9.5 CH₂Cl₂/ 1 MeOH, as a dark-brown oil, (219.2 mg, 0.94 mmol), yield: 40%. ¹H-NMR (400 MHz, Chloroform-*d*): δ 8.27 (d, *J* = 5.8 Hz, 1H, H-2thienop), 7.58 (d, *J* = 5.6 Hz, 1H, H-6thienop), 7.48 (d, *J* = 5.6 Hz, 1H, H-7thienop), 6.40 (d, *J* = 5.8 Hz, 1H, H-3thienop), 3.78 (t, *J* = 6.0 Hz, 4H, H-2,7azep), 1.95 – 1.88 (m, 4H, H-3,6azep), 1.64 – 1.58 (m, 4H, H-4,5azep). **ES+ HRMS** (m/z) [M+H]⁺: calculated for C₁₃H₁₇N₂S: 233.1112, found: 233.1104. The characterized product is in accordance with the literature.¹⁵²

Finally, for the quinolinic heads **29** and **30**, we used the same methodology. In a microwave reaction vessel was introduced 4-hydroxyquinoline (100 mg, 0.69 mmol, 1 eq) and phosphoryl trichloride (321 μL, 3.44 mmol, 5 eq), and were irradiated at 150 °C for 30 min. Then, to the sealed tube was added the aromatic amine *N*-methylaniline or 4-chloro-*N*-methylaniline (224 μL for the *N*-methyl aniline or 250.3 μL for the *p*-chloro-*N*-methyl aniline, 2.07 mmol, 3 eq) and irradiated at 180 °C for 8 min. Once the reaction is finished, follows the neutralization with NaOH and extraction with CH₂Cl₂/H₂O (x3). The organic phase is dried with Na₂SO₄, filtered, and evaporated under reduced pressure.¹⁵⁶



***N*-methyl-*N*-phenylquinolin-4-amine (29)**. The product was obtained after column chromatographic purification in silica gel with a polarity of 9.5CH₂Cl₂/ 0.5MeOH, as a light-brown oil, (105.1 mg, 0.45 mmol), yield: 65%. ¹H-NMR (400 MHz, Chloroform-*d*): δ 8.74 (d, *J* = 5.0 Hz, 1H, H-2quin), 8.01 (d, *J* = 8.7 Hz, 1H, H-8quin), 7.62 (dd, *J* = 8.5, 1.0 Hz, 1H, H-5quin), 7.53 (ddd, *J* = 8.4, 6.9, 1.4 Hz, 1H, H-7quin), 7.22 (ddd, *J* = 8.4, 6.9, 1.3 Hz, 1H, H-6quin), 7.18 – 7.12 (m, 2H, H-2,6anil), 7.04 (d, *J* = 5.0 Hz, 1H, H-3quin), 6.87 (dt, *J* = 7.4, 1.0 Hz, 1H, H-4anil), 6.80 (dd, *J* = 8.7, 1.0 Hz, 2H, H-3,5anil), 3.39 (s, 3H, N-CH₃). **ES+ HRMS** (m/z) [M+H]⁺: calculated for C₁₆H₁₅N₂: 235.1235, found: 235.1224. The characterized product is in accordance with the literature.^{116,157}

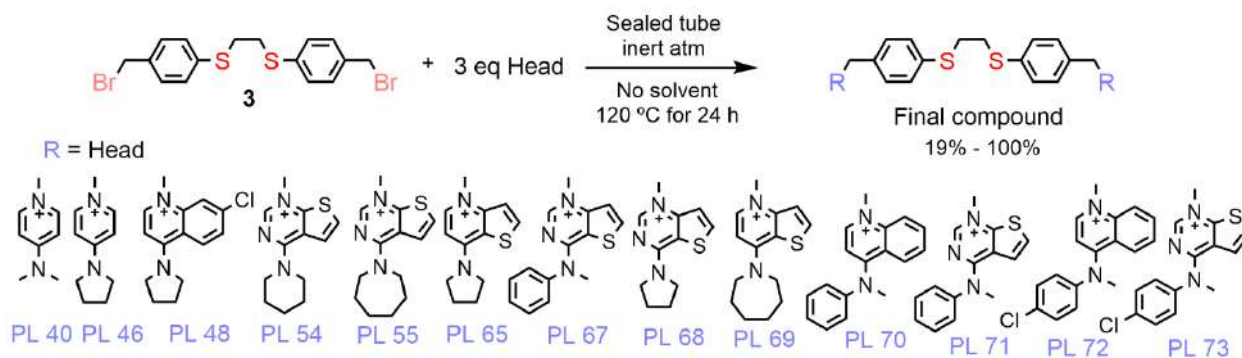


***N*-(4-chlorophenyl)-*N*-methylquinolin-4-amine (30)**. The product was obtained after column chromatographic purification in silica gel with a polarity of 9.5CH₂Cl₂/ 0.5MeOH, as a yellow oil, (111 mg, 0.41 mmol), yield: 60%. ¹H-NMR (400 MHz, Methanol-*d*₄): δ 8.75 (d, *J* = 5.1 Hz, 1H, H-2quin), 7.98 (d, *J* = 8.0 Hz, 1H, H-8quin), 7.69 – 7.64 (m, 2H, H-6,7quin), 7.35 (td, *J* = 7.7, 1.4 Hz, 1H, H-5quin), 7.28 (d, *J* = 5.1 Hz, 1H, H-3quin), 7.22 (d, *J* = 9.0 Hz, 2H, H-3,5anil), 6.89 (d, *J* = 9.0 Hz, 2H, H-2,6anil), 3.50 (s, 3H, N-CH₃). **ES+ HRMS**

(m/z) [M+H]⁺: calculated for C₁₆H₁₄N₂Cl: 269.0846, found: 269.0846. The characterized product is in accordance with the literature.¹¹⁶

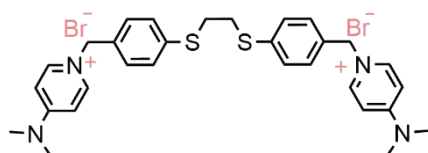
1.5 General procedure A for the synthesis of the dithioethane final products.

The assembly of the final compounds is obtained through a one-step reaction successfully applied to the whole chemical library. The synthetic strategy adopted is outlined in Scheme 11.



Scheme 11. Assembly of the dithioethane library's final compounds.

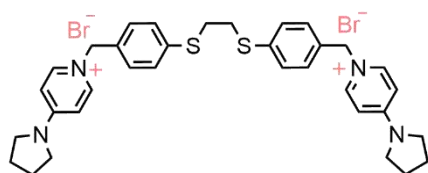
In an oven-dried reaction tube and under a nitrogen atmosphere, was introduced sequentially the magnetic stir, the dibromide linker **3** (100 mg, 0.23 mmol, 1 eq) and an excess of the corresponding head (0.69 mmol, 3 eq). The reaction was sealed and carried out without solvent for 24 hours at a temperature of 120 °C in an oil bath. Then, the crude product is dissolved in a minimum quantity of methanol and precipitated adding diethyl ether. The final product is obtained after filtration under vacuum and several washes with EtOAc and Et₂O to remove the excess head and monosubstituted products. Further purification with a chromatography column was needed in the quinolinium derivatives as specified below. It was obtained diverse chemical yields - from 19% to a quantitative 100% - depending on the hindrance of the cationic heads.



1,1'-(((ethane-1,2-diylbis(sulfanediy))bis(4,1-phenylene))bis(methylene))bis(4-(dimethylamino)pyridin-1-ium) bromide (**PL 40**).

Following the general procedure A, furnished **PL 40** as a light-pink solid, (40.4 mg, 0.06 mmol), yield: 26% after

stirring 3 hours at rt on acetonitrile and precipitation with diethyl ether, melting point: 267.4 °C - 269 °C; (281 °C dc). ¹H-NMR (400 MHz, Deuterium Oxide): δ 7.94 (d, J = 7.4 Hz, 4H, H-2,6pyrid), 7.10 (d, J = 8.2 Hz, 4H, Ar-S), 6.86 (d, J = 7.8 Hz, 4H, Ar-C), 6.65 (d, J = 7.3 Hz, 4H, H-3,5pyrid), 5.12 (s, 4H, CH₂-N⁺), 3.04 (s, 12H, N-CH₃), 2.78 (s, 4H, S-(CH₂)₂-S). ¹³C-NMR (101 MHz, Deuterium Oxide): δ 156.07 (2C, -C-), 141.02 (4C, -CH-, C-2,6pyrid), 136.37 (2C, -C-), 132.77 (2C, -C-), 129.09 (4C, -CH-, Ar-C), 128.74 (4C, -CH-, Ar-S), 107.75 (4C, -CH-, C-3,5pyrid), 59.96 (2C, -CH₂-, CH₂-N⁺), 39.43 (4C, -CH₃-, N-CH₃), 31.53 (2C, -CH₂-, S-(CH₂)₂-S). **ES+ HRMS** (m/z) [M]²⁺: calculated for C₃₀H₃₆N₄S₂: 516.2381, found: 516.2366.

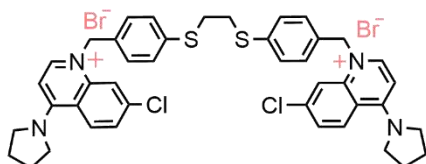


1,1'-(((ethane-1,2-diylbis(sulfanediy))bis(4,1-phenylene))bis(methylene))bis(4-(pyrrolidin-1-yl)pyridin-1-ium) bromide (**PL 46**).

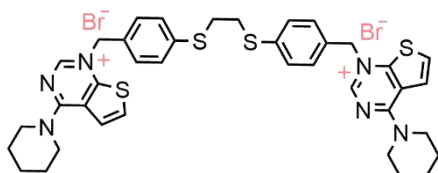
Following the general procedure A, furnished **PL 46** as a light-yellow solid, (91.9 mg, 0.13 mmol), yield: 53% after stirring

overnight in acetonitrile at 40 °C and precipitation with diethyl ether, melting point: 98 °C; (109 °C dc). ¹H-NMR (400 MHz, Deuterium Oxide): δ 7.90 (d, J = 7.6 Hz, 4H, H-2,6pyrid), 7.03 (d, J = 8.7

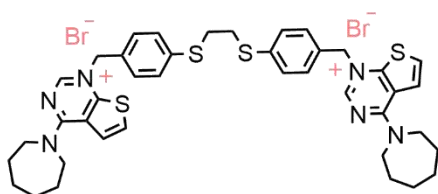
Hz, 4H, Ar-S), 6.85 (d, $J = 8.6$ Hz, 4H, Ar-C), 6.54 (d, $J = 7.8$ Hz, 4H, H-3,5pyrid), 5.09 (s, 4H, $\text{CH}_2\text{-N}^+$), 3.41 – 3.22 (m, 8H, H-2,5pyrr), 2.79 (s, 4H, S-(CH_2)₂-S), 2.10 – 1.89 (m, 8H, H-3,4pyrr). **¹³C-NMR** (151 MHz, Deuterium Oxide): δ 153.24 (2C, -C-), 140.87 (4C, -CH-, C-2,6pyrid), 136.30 (2C, -C-), 132.93 (2C, -C-), 128.99 (4C, -CH-, Ar-C), 128.68 (4C, -CH-, Ar-S), 108.34 (4C, -CH-, C-3,5pyrid), 59.99 (2C, - CH_2 -, $\text{CH}_2\text{-N}^+$), 48.40 (4C, - CH_2 -, C-2,5pyrr), 31.50 (2C, - CH_2 -, S-(CH_2)₂-S), 24.70 (4C, - CH_2 -, C-3,4pyrr). **ES+ HRMS** (m/z) [M]²⁺: calculated for C₃₄H₄₀N₄S₂: 568.2694, found: 568.2692.



1,1'-(((ethane-1,2-diylbis(sulfanediy))bis(4,1-phenylene))bis(methylene))bis(7-chloro-4-(pyrrolidin-1-yl)quinolin-1-ium) bromide (**PL 48**). Following the general procedure A, furnished **PL 48** as a white solid, (126.7 mg, 0.14 mmol), yield: 61% after a first recrystallization in $\text{CH}_2\text{Cl}_2/\text{Et}_2\text{O}$ and a final recrystallization from a solution of CH_3CN (at 40 °C stirred for 2 hours) and precipitation with Et_2O , melting point: 210 °C. **¹H-NMR** (500 MHz, Methanol- d_4): δ 8.61 (d, $J = 9.3$ Hz, 2H, H-8quin), 8.50 (d, $J = 7.8$ Hz, 2H, H-2quin), 7.95 (d, $J = 2.0$ Hz, 2H, H-5quin), 7.64 (dd, $J = 9.2, 2.2$ Hz, 2H, H-6quin), 7.32 (d, $J = 8.6$ Hz, 4H, Ar-S), 7.21 (d, $J = 8.6$ Hz, 4H, Ar-C), 6.89 (d, $J = 7.7$ Hz, 2H, H-3quin), 5.74 (s, 4H, $\text{CH}_2\text{-N}^+$), 4.41 – 3.66 (m, 8H, H-2,5pyrr), 3.09 (s, 4H, S-(CH_2)₂-S), 2.18 (bs, 8H, H-3,4pyrr). **¹³C-NMR** (101 MHz, Methanol- d_4): δ 157.13 (2C, -C-), 146.27 (2C, -CH-, C-8quin), 141.60 (2C, -C-), 141.02 (2C, -C-), 137.86 (2C, -C-), 133.91 (2C, -C-), 131.20 (2C, -CH-, C-2quin), 131.10 (4C, -CH-, Ar-C), 128.67 (4C, -CH-, Ar-S), 126.92 (2C, -CH-, C-5quin), 119.30 (2C, -C-), 118.78 (2C, -CH-, C-6quin), 103.89 (2C, -CH-, C-3quin), 58.12 (2C, - CH_2 -, $\text{CH}_2\text{-N}^+$), 53.67 (4C, - CH_2 -, C-2,5pyrr), 33.74 (2C, - CH_2 -, S-(CH_2)₂-S), 26.87 (4C, - CH_2 -, C-3,4pyrr). **ES+ HRMS** (m/z) [M]²⁺: calculated for C₄₂H₄₂N₄S₂Cl₂: 736.2228, found: 736.2252.

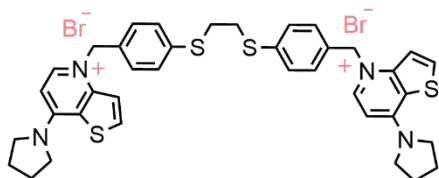


1,1'-(((ethane-1,2-diylbis(sulfanediy))bis(4,1-phenylene))bis(methylene))bis(4-(piperidin-1-yl)thieno[2,3-d]pyrimidin-1-ium) bromide (**PL 54**). Following the general procedure A, furnished **PL 54** as a white-beige solid, (54.5 mg, 0.06 mmol), yield: 54% after stirring overnight in CH_3CN at 40 °C and recrystallization with Et_2O , melting point: 208.9 °C; (221.4 °C dc). **¹H-NMR** (500 MHz, Methanol- d_4): δ 8.89 (s, 2H, H-2thienop), 7.80 (d, $J = 6.0$ Hz, 2H, H-6thienop), 7.74 (d, $J = 6.0$ Hz, 2H, H-5thienop), 7.41 (d, $J = 8.5$ Hz, 4H, Ar-S), 7.37 (d, $J = 8.5$ Hz, 4H, Ar-C), 5.61 (s, 4H, $\text{CH}_2\text{-N}^+$), 4.31 – 4.11 (m, 8H, H-2,6pip), 3.14 (s, 4H, S-(CH_2)₂-S), 1.86 (bs, 12H, H-3,4,5pip). **¹³C-NMR** (126 MHz, Methanol- d_4): δ 157.41 (2C, -C-), 156.19 (2C, -C-), 149.60 (2C, -CH-, C-2thienop), 138.97 (2C, -C-), 131.36 (2C, -C-), 130.72 (4C, -CH-, Ar-C), 130.31 (4C, -CH-, Ar-S), 125.01 (2C, -CH-, C-6thienop), 124.47 (2C, -CH-, C-5thienop), 117.69 (2C, -C-), 58.29 (2C, - CH_2 -, $\text{CH}_2\text{-N}^+$), 51.62 (4C, - CH_2 -, C-2,6pip), 33.51 (2C, - CH_2 -, S-(CH_2)₂-S), 27.37 (2C, - CH_2 -, C-3or5pip), 26.98 (2C, - CH_2 -, C-3or5pip), 24.79 (2C, - CH_2 -, C-4pip). **ES+ HRMS** (m/z) [M]²⁺: calculated for C₃₈H₄₂N₆S₄: 710.2354, found: 710.2367.



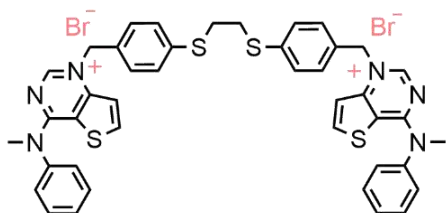
1,1'-(((ethane-1,2-diylbis(sulfanediy))bis(4,1-phenylene))bis(methylene))bis(4-(azepan-1-yl)thieno[2,3-d]pyrimidin-1-ium) bromide (**PL 55**). Following the general procedure A, furnished **PL 55** as a white solid, (79 mg, 0.09 mmol), yield: 38% after stirring overnight in CH_3CN at rt and recrystallization with Et_2O , melting point: 172 °C. **¹H-NMR** (500 MHz, Methanol- d_4): δ 8.91 (s, 2H, H-2thienop), 7.82 (d, $J = 6.0$ Hz, 2H, H-6thienop), 7.73 (d, $J = 6.0$ Hz, 2H, H-5thienop), 7.41 (d, $J = 8.4$ Hz, 4H, Ar-S), 7.37 (d, $J = 8.4$ Hz, 4H, Ar-C), 5.62 (s, 4H, $\text{CH}_2\text{-N}^+$), 4.20 (t, $J = 5.9$ Hz, 4H, H-2or7azep), 4.16 (t, $J = 5.9$ Hz, 4H, H-2or7azep), 3.14 (s, 4H, S-(CH_2)₂-S), 2.03 (quint, $J = 5.7$ Hz, 4H, H-3or6azep),

1.97 (quint, $J = 5.8$ Hz, 4H, H-3or6azep), 1.69 (bs, 8H, H-4,5azep). $^{13}\text{C-NMR}$ (126 MHz, Methanol- d_4): δ 158.07 (2C, -C-), 155.94 (2C, -C-), 149.47 (2C, -CH-, C-2thienop), 139.04 (2C, -C-), 131.27 (2C, -C-), 130.72 (4C, -CH-, Ar-C), 130.28 (4C, -CH-, Ar-S), 125.13 (2C, -CH-, C-6thienop), 124.74 (2C, -CH-, C-5thienop), 117.84 (2C, -C-), 58.34 (2C, -CH $_2$ -, CH $_2$ -N $^+$), 53.00 (2C, -CH $_2$ -, C-2or7azep), 51.76 (2C, -CH $_2$ -, C-2or7azep), 33.50 (2C, -CH $_2$ -, S-(CH $_2$) $_2$ -S), 28.79 (2C, -CH $_2$ -, C-3or6azep), 27.90 (2C, -CH $_2$ -, C-3or6azep), 27.81 (2C, -CH $_2$ -, C-4or5azep), 27.59 (2C, -CH $_2$ -, C-4or5azep). **ES+ HRMS** (m/z) $[\text{M}]^{2+}$: calculated for $\text{C}_{40}\text{H}_{46}\text{N}_6\text{S}_4$: 738.2667, found: 738.2687.



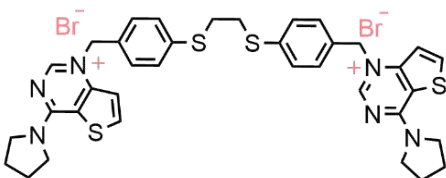
1,1'-(((ethane-1,2-diylbis(sulfanediy))bis(4,1-phenylene))bis(methylene))bis(7-(pyrrolidin-1-yl)thieno[3,2-b]pyridin-4-ium) bromide (**PL 65**). Following the general procedure A, furnished **PL 65** as a light-yellow solid, (84.5 mg, 0.1 mmol), yield: 43% after stirring overnight in CH_3CN at 40 °C and

recrystallization with Et_2O , melting point: 219 °C – 220 °C. $^1\text{H-NMR}$ (500 MHz, Methanol- d_4): δ 8.32 (d, $J = 7.5$ Hz, 2H, H-2thienop), 8.30 (d, $J = 5.8$ Hz, 2H, H-6thienop), 7.61 (d, $J = 5.9$ Hz, 2H, H-7thienop), 7.33 (d, $J = 8.4$ Hz, 4H, Ar-S), 7.23 (d, $J = 8.4$ Hz, 4H, Ar-C), 6.74 (d, $J = 7.4$ Hz, 2H, H-3thienop), 5.65 (s, 4H, CH $_2$ -N $^+$), 4.28 (bs, 4H, H-2or5pyrr), 3.73 (bs, 4H, H-2or5pyrr), 3.10 (s, 4H, S-(CH $_2$) $_2$ -S), 2.26 - 2.11 (m, 8H, H-3,4pyrr). $^{13}\text{C-NMR}$ (126 MHz, Methanol- d_4): δ 153.55 (2C, -C-), 147.31 (2C, -C-), 143.05 (2C, -CH-, C-2thienop), 138.06 (2C, -C-), 137.51 (2C, -CH-, C-6thienop), 134.01 (2C, -C-), 130.93 (4C, -CH-, Ar-C), 129.08 (4C, -CH-, Ar-S), 122.28 (2C, -C-), 118.65 (2C, -CH-, C-7thienop), 103.39 (2C, -CH-, C-3thienop), 59.13 (2C, -CH $_2$ -, CH $_2$ -N $^+$), 52.13 (4C, -CH $_2$ -, C-2,5pyrr), 33.68 (2C, -CH $_2$ -, S-(CH $_2$) $_2$ -S), 27.26 (2C, -CH $_2$ -, C-3or4pyrr), 25.55 (2C, -CH $_2$ -, C-3or4pyrr). **ES+ HRMS** (m/z) $[\text{M}]^{2+}$: calculated for $\text{C}_{38}\text{H}_{40}\text{N}_4\text{S}_4$: 680.2136, found: 680.2154.



*1,1'-(((ethane-1,2-diylbis(sulfanediy))bis(4,1-phenylene))bis(methylene))bis(4-(methyl(phenyl)amino)thieno[3,2-d]pyrimidin-1-ium) bromide (**PL 67**). Following the modified procedure A, furnished **PL 67** as a yellow solid, (51.6 mg, 0.06 mmol), yield: 24% after chromatographic

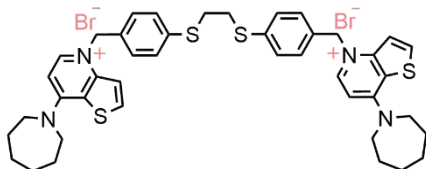
column purification in 9.5 $\text{CH}_2\text{Cl}_2/0.5$ MeOH (gradually increasing the polarity), melting point: 281.3 °C dc. $^1\text{H-NMR}$ (500 MHz, Methanol- d_4): δ 9.13 (s, 2H, H-2thienop), 8.14 (d, $J = 5.7$ Hz, 2H, H-6thienop), 7.70 – 7.63 (m, 6H, H-3,4,5anil), 7.60 (d, $J = 7.3$ Hz, 4H, H-2,6anil), 7.49 (d, $J = 5.7$ Hz, 2H, H-7thienop), 7.36 (d, $J = 8.8$ Hz, 4H, Ar-S), 7.34 (d, $J = 8.5$ Hz, 4H, Ar-C), 5.74 (s, 4H, CH $_2$ -N $^+$), 3.84 (s, 6H, N-CH $_3$), 3.11 (s, 4H, S-(CH $_2$) $_2$ -S). $^{13}\text{C-NMR}$ (126 MHz, Methanol- d_4): δ 166.37 (2C, -C-), 151.67 (2C, -CH-, C-2thienop), 142.40 (2C, -C-), 141.78 (2C, -CH-, C-6thienop), 138.32 (2C, -C-), 133.21 (2C, -C-), 133.11 (2C, -C-), 132.16 (2C, -CH-, C-4anilina), 131.86 (4C, -CH-, C-2,6anil), 130.93 (4C, -CH-, Ar-C), 129.98 (4C, -CH-, C-3,5anil), 129.50 (4C, -CH-, Ar-S), 118.34 (2C, -C-), 117.95 (2C, -CH-, C-7thienop), 56.87 (2C, -CH $_2$ -, CH $_2$ -N $^+$), 41.80 (2C, -CH $_3$, N-CH $_3$), 33.62 (2C, -CH $_2$ -, S-(CH $_2$) $_2$ -S). **ES+ HRMS** (m/z) $[\text{M}]^{2+}$: calculated for $\text{C}_{42}\text{H}_{38}\text{N}_6\text{S}_4$: 754.2041, found: 754.1989.



*1,1'-(((ethane-1,2-diylbis(sulfanediy))bis(4,1-phenylene))bis(methylene))bis(4-(pyrrolidin-1-yl)thieno[3,2-d]pyrimidin-1-ium) bromide (**PL 68**). Following the modified procedure A, furnished **PL 68** as a yellow solid, (215 mg, 0.3 mmol), yield: 74% after stirring overnight in CH_3CN at 40 °C and recrystallization with Et_2O , melting point: 238 °C; (248.8

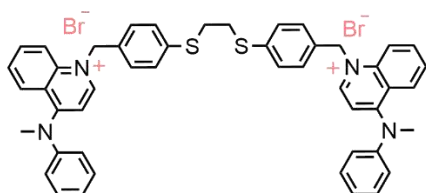
¹ Those final products with (*), were synthesized using dry acetonitrile as solvent (2mL for each 300 mg of reactive) at 90°C for 72 hours.

°C dc). **¹H-NMR** (400 MHz, Methanol-*d*₄): δ 8.86 (s, 2H, H-2thienop), 8.44 (d, *J* = 5.6 Hz, 2H, H-6thienop), 7.58 (d, *J* = 5.6 Hz, 2H, H-7thienop), 7.33 (s, 8H, Ar-S, Ar-C), 5.65 (s, 4H, CH₂-N⁺), 4.20 (t, *J* = 6.8 Hz, 4H, H-2or5pyrr), 4.00 (t, *J* = 6.8 Hz, 4H, H-2or5pyrr), 3.10 (s, 4H, S-(CH₂)₂-S), 2.27 (quint, *J* = 6.9 Hz, 4H, H-3or4pyrr), 2.11 (quint, *J* = 6.9 Hz, 4H, H-3or4pyrr). **¹³C-NMR** (101 MHz, Methanol-*d*₄): δ 156.72 (2C, -C-), 151.27 (2C, -CH-, C-2thienop), 147.55 (2C, -C-), 140.19 (2C, -CH-, C-6thienop), 138.25 (2C, -C-), 133.26 (2C, -C-), 130.94 (4C, -CH-, Ar-C), 129.38 (4C, -CH-, Ar-S), 118.59 (2C, -CH-, C-7thienop), 118.26 (2C, -C-), 56.44 (2C, -CH₂-, CH₂-N⁺), 51.70 (2C, -CH₂-, C-2or5pyrr), 50.74 (2C, -CH₂-, C-2or5pyrr), 33.66 (2C, -CH₂-, S-(CH₂)₂-S), 27.21 (2C, -CH₂-, C-3or4pyrr), 25.05 (2C, -CH₂-, C-3or4pyrr). **ES+ HRMS** (*m/z*) [*M*]²⁺: calculated for C₃₆H₃₈N₆S₄: 682.2041, found: 682.2001.



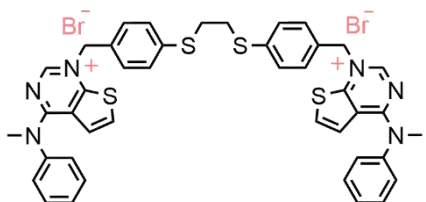
1,1'-(((ethane-1,2-diylbis(sulfanediy))bis(4,1-phenylene))bis(methylene))bis(7-(azepan-1-yl)thieno[3,2-b]pyridin-4-ium) bromide (**PL 69**). Following the general procedure A, furnished **PL 69** as a brown solid, (39.9 mg, 0.04 mmol), yield: 19% after a

first recrystallization in CH₂Cl₂/Et₂O and a final recrystallization while stirring it in CH₃CN at 40 °C overnight and precipitation with Et₂O, melting point: 197 °C – 200 °C. **¹H-NMR** (500 MHz, Methanol-*d*₄): δ 8.37 (d, *J* = 7.6 Hz, 2H, H-2thienop), 8.31 (d, *J* = 5.9 Hz, 2H, H-6thienop), 7.65 (d, *J* = 5.9 Hz, 2H, H-7thienop), 7.33 (d, *J* = 8.4 Hz, 4H, Ar-S), 7.25 (d, *J* = 8.4 Hz, 4H, Ar-C), 6.97 (d, *J* = 7.6 Hz, 2H, H-3thienop), 5.69 (s, 4H, CH₂-N⁺), 4.17 – 3.98 (m, 8H, H-2,7azep), 3.10 (s, 4H, S-(CH₂)₂-S), 2.05 – 1.96 (m, 8H, H-3,6azep), 1.72 – 1.63 (m, 8H, H-4,5azep). **¹³C-NMR** (101 MHz, Methanol-*d*₄): δ 155.62 (2C, -C-), 147.95 (2C, -C-), 143.10 (2C, -CH-, C-2thienop), 138.13 (2C, -C-), 137.41 (2C, -CH-, C-6thienop), 133.88 (2C, -C-), 130.97 (4C, -CH-, Ar-C), 129.18 (4C, -CH-, Ar-S), 120.87 (2C, -C-), 118.79 (2C, -CH-, C-7thienop), 103.21 (2C, -CH-, C-3thienop), 59.32 (2C, -CH₂-, CH₂-N⁺), 53.83 (4C, -CH₂-, C-2,7azep), 33.70 (2C, -CH₂-, S-(CH₂)₂-S), 27.53 (8C, -CH₂-, C-3,4,5,6azep). **ES+ HRMS** (*m/z*) [*M*]²⁺: calculated for C₄₂H₄₈N₄S₄: 736.2762, found: 736.2737.



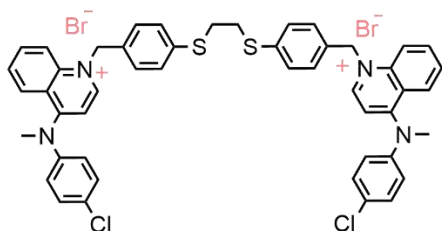
1,1'-(((ethane-1,2-diylbis(sulfanediy))bis(4,1-phenylene))bis(methylene))bis(4-(methyl(phenyl)amino)quinolin-1-ium) bromide (**PL 70**). Following the general procedure A, furnished **PL 70** as an orange solid, (91.3 mg, 0.1 mmol), yield: 43% after chromatographic column purification in 9.5 CH₂Cl₂/0.5

MeOH (gradually increasing the polarity), melting point: 183 °C; (314.9 °C dc). **¹H-NMR** (400 MHz, Methanol-*d*₄): δ 8.89 (d, *J* = 7.4 Hz, 2H, H-2quin), 8.03 (d, *J* = 8.6 Hz, 2H, H-8quin), 7.76 (ddd, *J* = 8.7, 7.1, 1.5 Hz, 2H, H-7quin), 7.59 (dd, *J* = 8.8, 1.1 Hz, 2H, H-6quin), 7.54 – 7.48 (m, 4H, H-2,6anil), 7.46 – 7.41 (m, 2H, H-5quin), 7.40 – 7.32 (m, 10H, Ar-S, Ar-C, H-3quin), 7.29 – 7.25 (m, 6H, H-3,4,5anil), 5.92 (s, 4H, CH₂-N⁺), 3.82 (s, 6H, N-CH₃), 3.10 (s, 4H, S-(CH₂)₂-S). **¹³C-NMR** (101 MHz, Methanol-*d*₄): δ 160.02 (2C, -C-), 149.25 (2C, -C-), 148.02 (2C, -CH-, C-2quin), 140.80 (2C, -C-), 137.99 (2C, -C-), 134.76 (2C, -CH-, C-8quin), 133.87 (2C, -C-), 131.92 (4C, -CH-, Ar-C), 131.05 (4C, -CH-, Ar-S), 129.49 (2C, -CH-, C-7quin), 129.38 (2C, -CH-, C-6quin), 128.81 (4C, -CH-, C-2,6anil), 127.01 (2C, -CH-, C-5quin), 126.92 (4C, -CH-, C-3,5anil), 121.39 (2C, -C-), 120.09 (2C, -CH-, C-3quin), 106.95 (2C, -CH-, C-4anil), 59.02 (2C, -CH₂-, CH₂-N⁺), 45.98 (2C, -CH₃, N-CH₃), 33.73 (2C, -CH₂-, S-(CH₂)₂-S). **ES+ HRMS** (*m/z*) [*M*]²⁺: calculated for C₄₈H₄₄N₄S₂: 740.3007, found: 740.2996.



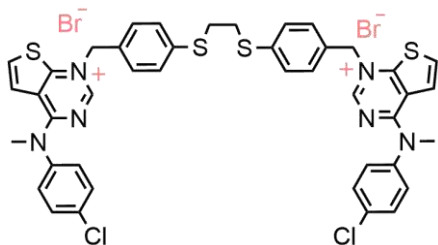
1,1'-(((ethane-1,2-diylbis(sulfanediy))bis(4,1-phenylene))bis(methylene))bis(4-(methyl(phenyl)amino)thieno[2,3-d]pyrimidin-1-ium) bromide (**PL 71**). Following the general procedure A, furnished **PL 71** as a light-green solid, (55.4 mg, 0.06 mmol), yield: 26% after chromatographic column

purification in 9.5 CH₂Cl₂/0.5 MeOH (gradually increasing the polarity), melting point: 165 °C; (175 °C dc). **¹H-NMR** (400 MHz, Methanol-d₄): δ 9.16 (s, 2H, H-2thienop), 7.66 – 7.63 (m, 6H, H-2,6anil, H-6thienop), 7.55 – 7.51 (m, 4H, H-3,5anil), 7.44 (d, J = 8.4 Hz, 4H, Ar-S), 7.39 – 7.33 (m, 6H, Ar-C, H-4anil), 5.70 (s, 4H, CH₂-N⁺), 5.53 (d, J = 5.6 Hz, 2H, H-5thienop), 3.85 (s, 6H, N-CH₃), 3.14 (s, 4H, S-(CH₂)₂-S). **¹³C-NMR** (101 MHz, Methanol-d₄): δ 158.45 (2C, -C-), 155.82 (2C, -C-), 150.52 (2C, -CH-, C-2thienop), 144.48 (2C, -C-), 139.08 (2C, -C-), 132.11 (4C, -CH-, C-2,6anil), 131.34 (2C, -CH-, C-6thienop), 131.13 (2C, -C-), 130.75 (4C, -CH-, Ar-C), 130.42 (4C, -CH-, Ar-S), 128.22 (4C, -CH-, C-3,5anil), 125.03 (2C, -CH-, C-4anil), 123.84 (2C, -CH-, C-5thienop), 119.09 (2C, -C-), 58.80 (2C, -CH₂-, CH₂-N⁺), 42.59 (2C, -CH₃, N-CH₃), 33.52 (2C, -CH₂-, S-(CH₂)₂-S). **ES+ HRMS** (m/z) [M]²⁺: calculated for C₄₂H₃₈N₆S₄: 754.2041, found: 754.2098.



1,1'-(((ethane-1,2-diylbis(sulfanediy))bis(4,1-phenylene))bis(methylene))bis(4-((4-chlorophenyl)(methyl)amino)quinolin-1-ium) bromide (**PL 72**). Following the general procedure A, furnished **PL 72** as an orange solid, (82.3 mg, 0.08 mmol), yield: 59% after chromatographic column purification in 9.5 CH₂Cl₂/0.5 MeOH (gradually

increasing the polarity), melting point: 193.1 °C; (200 °C dc). **¹H-NMR** (400 MHz, Methanol-d₄): δ 8.92 (d, J = 7.4 Hz, 2H, H-2quin), 8.07 (d, J = 8.9 Hz, 2H, H-8quin), 7.80 (t, J = 7.9 Hz, 2H, H-6or7quin), 7.65 (d, J = 8.7 Hz, 2H, H-5quin), 7.50 (d, J = 8.7 Hz, 4H, H-3,5anil), 7.41 – 7.32 (m, 12H, H-3quin, H-6or7quin, Ar-S, H-2,6anil), 7.27 (d, J = 8.3 Hz, 4H, Ar-C), 5.94 (s, 4H, CH₂-N⁺), 3.80 (s, 6H, N-CH₃), 3.11 (s, 4H, S-(CH₂)₂-S). **¹³C-NMR** (101 MHz, Methanol-d₄): δ 160.16 (2C, -C-), 148.25 (2C, -CH-, C-2quin), 147.94 (2C, -C-), 140.83 (2C, -C-), 138.08 (2C, -C-), 134.94 (2C, -CH-, C-8quin), 134.82 (2C, -C-), 133.75 (2C, -C-), 131.90 (4C, -CH-, C-3,5anil), 131.00 (4C, -CH-, C-2,6anil), 129.25 (2C, -CH-, C-7quin), 128.85 (4C, -CH-, Ar-C), 128.49 (4C, -CH-, Ar-S), 127.37 (2C, -CH-, C-6quin), 121.52 (2C, -C-), 120.25 (2C, -CH-, C-5quin), 107.55 (2C, -CH-, C-3quin), 59.16 (2C, -CH₂-, CH₂-N⁺), 45.75 (2C, -CH₃, N-CH₃), 33.70 (2C, -CH₂-, S-(CH₂)₂-S). **ES+ HRMS** (m/z) [M]²⁺: calculated for C₄₈H₄₂N₄S₂Cl₂: 808.2228, found: 808.2255.

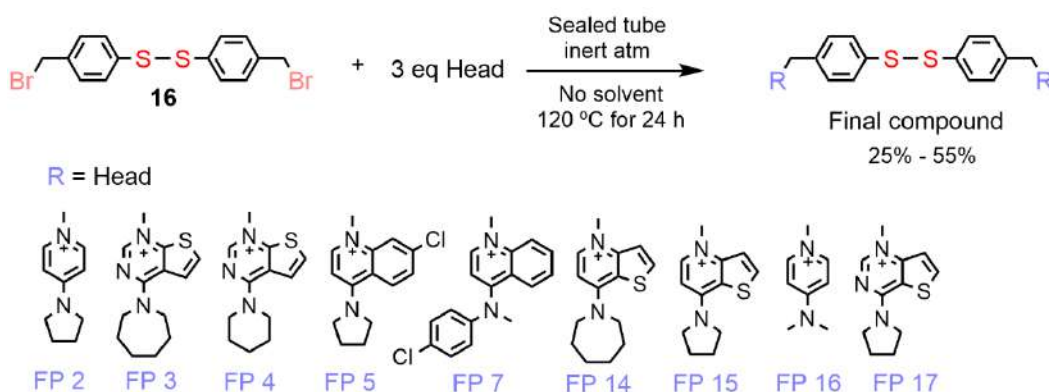


*1,1'-(((ethane-1,2-diylbis(sulfanediy))bis(4,1-phenylene))bis(methylene))bis(4-((4-chlorophenyl)(methyl)amino)thieno[2,3-d]pyrimidin-1-ium) bromide (**PL 73**). Following the modified procedure A, furnished **PL 73** as a pink-violet solid, (228 mg, 0.23 mmol), yield: 100%, melting point: 197 °C. **¹H-NMR** (400 MHz, Methanol-d₄): δ 9.17 (s, 2H, H-

2thienop), 7.66 (d, J = 8.6 Hz, 4H, H-3,5anil), 7.54 (d, J = 8.6 Hz, 4H, H-2,6anil), 7.44 (d, J = 8.4 Hz, 6H, H-6thienop, Ar-S), 7.37 (d, J = 8.4 Hz, 4H, Ar-C), 5.71 (s, 6H, H-5thienop, CH₂-N⁺), 3.83 (s, 6H, N-CH₃), 3.15 (s, 4H, S-(CH₂)₂-S). **¹³C-NMR** (101 MHz, Methanol-d₄): δ 158.54 (2C, -C-), 156.04 (2C, -C-), 150.50 (2C, -CH-, C-2thienop), 143.14 (2C, -C-), 139.16 (2C, -C-), 137.05 (2C, -C-), 132.21 (4C, -CH-, C-3,5anil), 131.03 (2C, -C-), 130.70 (4C, -CH-, Ar-C), 130.43 (4C, -CH-, Ar-S), 130.01 (4C, -CH-, C-2,6anil), 125.53 (2C, -CH-, C-7thienop), 123.68 (2C, -CH-, C-6thienop), 119.12 (2C, -C-), 58.87 (2C, -CH₂-, CH₂-N⁺), 42.60 (2C, -CH₃, N-CH₃), 33.48 (2C, -CH₂-, S-(CH₂)₂-S). **ES+ HRMS** (m/z) [M]²⁺: calculated for C₄₂H₃₆N₆S₄Cl₂: 822.1261, found: 822.1247.

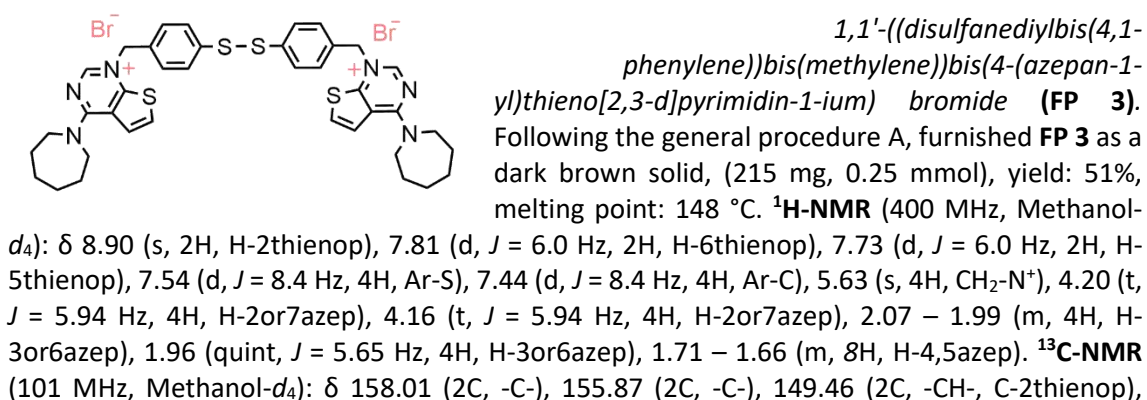
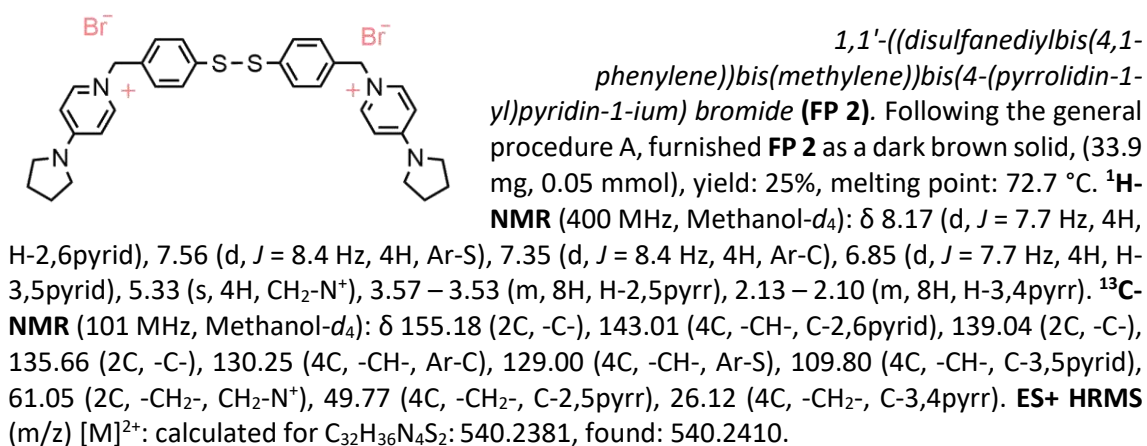
1.6 General procedure A for the synthesis of the disulphide final products.

The assembly of the linker and heads of the disulphide library was done using the optimized reaction conditions as reported before. The reaction is outlined in [Scheme 12](#).

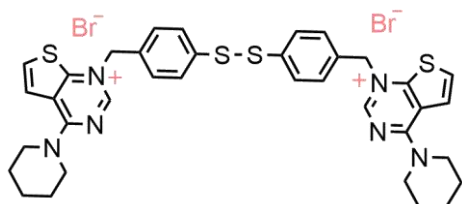


Scheme 12. Assembly of the disulphide library's final compounds.

This final step consists of the bromide linker (**16**) substitution with the corresponding 4-substituted aromatic amines by an S_N2 mechanism. The reaction takes place in an oven-dry sealed tube and under a nitrogen atmosphere, where is added **16** (100 mg, 0.25 mmol, 1 eq) and an excess of the corresponding head (0.69 mmol, 3 eq) with a magnetic stir. The reaction was sealed and carried out without solvent for 24 hours at a temperature of 120 °C in an oil bath. Then, the crude product is dissolved in a minimum quantity of methanol and precipitated adding diethyl ether. It was purified from the intermediates of reaction by several washes with ethyl acetate and diethyl ether. There were obtained different chemical yields - from 25% to 55% - depending on the cationic head hindrance. The products were dried under vacuum with phosphorus pentoxide before their characterization.



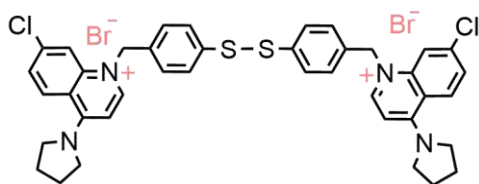
139.35 (2C, -C-), 132.78 (2C, -C-), 130.44 (4C, -CH-, Ar-C), 128.91 (4C, -CH-, Ar-S), 125.15 (2C, -CH-, C-6thienop), 124.77 (2C, -CH-, C-5thienop), 117.80 (2C, -C-), 58.15 (2C, -CH₂-, CH₂-N⁺), 53.01 (2C, -CH₂-, C-2or7azep), 51.76 (2C, -CH₂-, C-2or7azep), 28.78 (2C, -CH₂-, C-3or6azep), 27.88 (2C, -CH₂-, C-3or6azep), 27.80 (2C, -CH₂-, C-4or5azep), 27.59 (2C, -CH₂-, C-4or5azep). **ES⁺ HRMS** (m/z) [M]²⁺: calculated for C₃₈H₄₂N₆S₄: 710.2354, found: 710.2368.



1,1'-((disulfaneyldiylbis(4,1-phenylene))bis(methylene))bis(4-(piperidin-1-yl)thieno[2,3-d]pyrimidin-1-ium) bromide (FP 4).

Following the general procedure A, furnished **FP 4** as a brown solid, (152 mg, 0.18 mmol), yield: 33%, melting point: 131 °C, (169.1°C dc). **¹H-NMR** (400

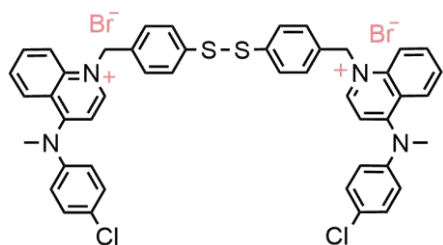
MHz, Methanol-*d*₄): δ 8.86 (s, 2H, H-2thienop), 8.42 (d, *J* = 5.8 Hz, 2H, H-6thienop), 7.56 (d, *J* = 5.8 Hz, 2H, H-5thienop), 7.51 (d, *J* = 8.4 Hz, 4H, Ar-S), 7.35 (d, *J* = 8.3 Hz, 4H, Ar-C), 5.67 (s, 4H, CH₂-N⁺), 4.34 – 4.18 (m, 8H, H-2,6pip), 1.86 (bs, 12H, H-3,4,5pip). **¹³C-NMR** (101 MHz, Methanol-*d*₄): δ 157.23 (2C, -C-), 150.91 (2C, -CH-, C-2thienop), 148.83 (2C, -C-), 139.65 (2C, -CH-, C-6thienop), 138.81 (2C, -C-), 134.60 (2C, -C-), 129.53 (4C, -CH-, Ar-C), 129.02 (4C, -CH-, Ar-S), 118.84 (2C, -CH-, C-5thienop), 116.48 (2C, -C-), 56.34 (2C, -CH₂-, CH₂-N⁺), 51.55 (4C, -CH₂-, C-2,6pip), 27.68 (2C, -CH₂-, C-3or5pip), 27.05 (2C, -CH₂-, C-3or5pip), 24.86 (2C, -CH₂-, C-4pip). **ES⁺ HRMS** (m/z) [M]²⁺: calculated for C₃₆H₃₈N₆S₄: 682.2041, found: 682.2097.



1,1'-((disulfaneyldiylbis(4,1-phenylene))bis(methylene))bis(7-chloro-4-(pyrrolidin-1-yl)quinolin-1-ium) bromide (FP 5).

Following the general procedure A, furnished **FP 5** as a brown solid, (162 mg, 0.19 mmol), yield: 48%, melting point: 207 °C, (215 °C dc). **¹H-NMR** (400 MHz, Methanol-*d*₄): δ 8.60 (d, *J* = 9.2 Hz, 2H, H-8quin), 8.47

(d, *J* = 7.7 Hz, 2H, H-2quin), 7.90 (d, *J* = 2.0 Hz, 2H, H-5quin), 7.63 (dd, *J* = 9.2, 2.0 Hz, 2H, H-6quin), 7.49 (d, *J* = 8.3 Hz, 4H, Ar-S), 7.22 (d, *J* = 8.3 Hz, 4H, Ar-C), 6.88 (d, *J* = 7.7 Hz, 2H, H-3quin), 5.73 (s, 4H, CH₂-N⁺), 4.29 – 3.83 (m, 8H, H-2,5pyrr), 2.18 (bs, 8H, H-3,4pyrr). **¹³C-NMR** (126 MHz, Methanol-*d*₄): δ 157.12 (2C, -C-), 146.29 (2C, -CH-, C-8quin), 141.53 (2C, -C-), 141.00 (2C, -C-), 138.51 (2C, -C-), 135.35 (2C, -C-), 131.25 (2C, -CH-, C-2quin), 129.23 (4C, -CH-, Ar-C), 128.76 (4C, -CH-, Ar-S), 126.91 (2C, -CH-, C-5quin), 119.28 (2C, -C-), 118.68 (2C, -CH-, C-6quin), 103.94 (2C, -CH-, C-3quin), 57.90 (2C, -CH₂-, CH₂-N⁺), 56.24 (2C, -CH₂-, C-2or5pyrr), 54.42 (2C, -CH₂-, C-2or5pyrr), 27.77 (2C, -CH₂-, C-3or4pyrr), 25.13 (2C, -CH₂-, C-3or4pyrr). **ES⁺ HRMS** (m/z) [M]²⁺: calculated for C₄₀H₃₈N₄S₂Cl₂: 708.1915, found: 708.1910.

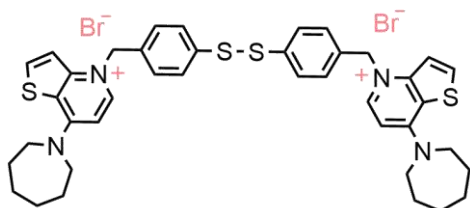


1,1'-((disulfaneyldiylbis(4,1-phenylene))bis(methylene))bis(4-((4-chlorophenyl)(methyl)amino)quinolin-1-ium) bromide (FP 7).

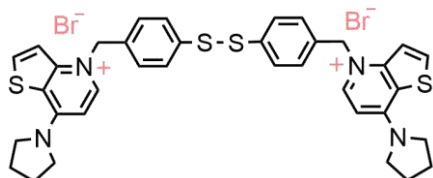
Following the general procedure A, furnished **FP 7** as a yellow solid, (197 mg, 0.21 mmol), yield: 36%, melting point: 210 °C. **¹H-NMR** (400 MHz, Methanol-*d*₄): δ 8.89 (d, *J* = 7.4 Hz, 2H, H-2quin), 8.01

(d, *J* = 8.9 Hz, 2H, H-8quin), 7.84 – 7.77 (m, 2H, H-6or7quin), 7.65 (d, *J* = 8.6 Hz, 2H, H-5quin), 7.53 – 7.49 (m, 8H, H-3,5anil, H-3quin, H-6or7quin), 7.37 (d, *J* = 8.6 Hz, 8H, H-2,6anil, Ar-S), 7.28 (d, *J* = 8.3 Hz, 4H, Ar-C), 5.93 (s, 4H, CH₂-N⁺), 3.80 (s, 6H, N-CH₃). **¹³C-NMR** (101 MHz, Methanol-*d*₄): δ 160.13 (2C, -C-), 148.31 (2C, -CH-, C-2quin), 147.90 (2C, -C-), 140.75 (2C, -C-), 138.63 (2C, -C-), 135.13 (2C, -C-), 134.95 (2C, -CH-, C-7quin), 134.78 (2C, -C-), 131.88 (4C, -CH-, C-3,5anil), 129.25 (2C, -CH-, C-8quin), 129.09 (4C, -CH-, Ar-C), 128.96 (4C, -CH-, Ar-S), 128.51 (4C, -CH-, C-2,6anil), 127.33 (2C, -CH-, C-6quin), 121.46 (2C, -C-),

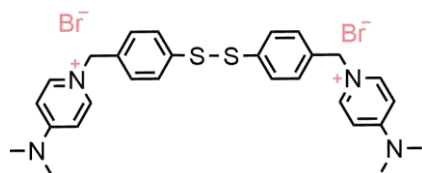
120.17 (2C, -CH-, C-5quin), 107.60 (2C, -CH-, C-3quin), 58.98 (2C, -CH₂-, CH₂-N⁺), 45.80 (2C, -CH₃, N-CH₃). **ES+ HRMS** (m/z) [M]²⁺: calculated for C₄₆H₃₈N₄S₂Cl₂: 780.1915, found: 780.1901.



4,4'-((disulfanediy)bis(4,1-phenylene))bis(methylene))bis(7-(azepan-1-yl)thieno[3,2-b]pyridin-4-ium) bromide (FP 14). Following the general procedure A, furnished **FP 14** as a white solid, (119.4 mg, 0.14 mmol), yield: 42%, melting point: 207 °C. **¹H-NMR** (400 MHz, Methanol-*d*₄): δ 8.34 (d, *J* = 7.6 Hz, 2H, H-2thienop), 8.30 (d, *J* = 5.9 Hz, 2H, H-6thienop), 7.60 (d, *J* = 5.9 Hz, 2H, H-7thienop), 7.51 (d, *J* = 8.4 Hz, 4H, Ar-S), 7.26 (d, *J* = 8.3 Hz, 4H, Ar-C), 6.96 (d, *J* = 7.6 Hz, 2H, H-3thienop), 5.68 (s, 4H, CH₂-N⁺), 4.09 (bs, 8H, H-2,7azep), 2.01 (bs, 8H, H-3,6azep), 1.69 (quint, *J* = 3.0 Hz, 8H, H-4,5azep). **¹³C-NMR** (101 MHz, Methanol-*d*₄): δ 155.59 (2C, -C-), 147.86 (2C, -C-), 143.14 (2C, -CH-, C-2thienop), 138.66 (2C, -C-), 137.48 (2C, -CH-, C-6thienop), 135.28 (2C, -C-), 129.33 (4C, -CH-, Ar-C), 129.02 (4C, -CH-, Ar-S), 120.84 (2C, -C-), 118.76 (2C, -CH-, C-7thienop), 103.29 (2C, -CH-, C-3thienop), 59.13 (2C, -CH₂-, CH₂-N⁺), 53.83 (4C, -CH₂-, C-2,7azep), 27.54 (8C, -CH₂-, C-3,4,5,6azep). **ES+ HRMS** (m/z) [M]²⁺: calculated for C₄₀H₄₄N₄S₄: 708.2449, found: 708.2435.

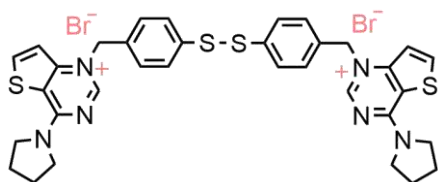


4,4'-((disulfanediy)bis(4,1-phenylene))bis(methylene))bis(7-(pyrrolidin-1-yl)thieno[3,2-b]pyridin-4-ium) bromide (FP 15). Following the general procedure A, furnished **FP 15** as a grey solid, (93.7 mg, 0.12 mmol), yield: 37%, melting point: 204.2 °C. **¹H-NMR** (600 MHz, DMSO-*d*₆): δ 8.59 (d, *J* = 7.4 Hz, 2H, H-2thienop), 8.50 (d, *J* = 5.8 Hz, 2H, H-6thienop), 7.74 (d, *J* = 5.8 Hz, 2H, H-7thienop), 7.49 (d, *J* = 8.3 Hz, 4H, Ar-S), 7.31 (d, *J* = 8.4 Hz, 4H, Ar-C), 6.80 (d, *J* = 7.4 Hz, 2H, H-3thienop), 5.74 (s, 4H, CH₂-N⁺), 4.15 (bs, 4H, H-2or5pyrr), 3.65 (bs, 4H, H-2or5pyrr), 2.16 – 1.99 (m, 8H, H-3,4pyrr). **¹³C-NMR** (151 MHz, DMSO-*d*₆): δ 151.32 (2C, -C-), 145.39 (2C, -C-), 142.14 (2C, -CH-, C-2thienop), 137.09 (2C, -CH-, C-6thienop), 135.83 (2C, -C-), 134.83 (2C, -C-), 128.30 (4C, -CH-, Ar-C), 127.50 (4C, -CH-, Ar-S), 120.02 (2C, -C-), 117.79 (2C, -CH-, C-7thienop), 102.41 (2C, -CH-, C-3thienop), 56.73 (2C, -CH₂-, CH₂-N⁺), 50.90 (2C, -CH₂-, C-2or5pyrr), 50.44 (2C, -CH₂-, C-2or5pyrr), 25.87 (2C, -CH₂-, C-3or4pyrr), 24.06 (2C, -CH₂-, C-3or4pyrr). **ES+ HRMS** (m/z) [M]²⁺: calculated for C₃₆H₃₆N₄S₄: 652.1823, found: 652.1761.



1,1'-((disulfanediy)bis(4,1-phenylene))bis(methylene))bis(4-(dimethylamino)pyridin-1-ium) bromide (FP 16). Following the general procedure A, furnished **FP 16** as a dark brown solid, (204 mg, 0.31 mmol), yield: 55%, melting point: 123.6 °C. **¹H-NMR** (400 MHz, Methanol-*d*₄): δ 8.20 (d, *J* = 7.8 Hz, 4H, H-2,6pyrid), 7.56 (d, *J* = 8.4 Hz, 4H, Ar-S), 7.35 (d, *J* = 8.4 Hz, 4H, Ar-C), 7.00 (d, *J* = 7.9 Hz, 4H, H-3,5pyrid), 5.35 (s, 4H, CH₂-N⁺), 3.25 (s, 12H, N-CH₃). **¹³C-NMR** (101 MHz, Methanol-*d*₄): δ 158.00 (2C, -C-), 143.10 (4C, -CH-, C-2,6pyrid), 139.04 (2C, -C-), 135.55 (2C, -C-), 130.32 (4C, -CH-, Ar-C), 128.99 (4C, -CH-, Ar-S), 109.22 (4C, -CH-, C-3,5pyrid), 61.00 (2C, -CH₂-, CH₂-N⁺), 40.43 (4C, -CH₃-, N-CH₃). **ES+ HRMS** (m/z) [M]²⁺: calculated for C₂₈H₃₂N₄S₂: 488.2068, found: 488.2086.

1,1'-((disulfanediy)bis(4,1-phenylene))bis(methylene))bis(4-(pyrrolidin-1-yl)thieno[3,2-d]pyrimidin-1-ium) bromide (FP 17). Following the general procedure A, furnished **FP 17** as a brown solid, (163.8 mg, 0.2 mmol), yield: 44%, melting point: 261 °C, (268°C dc). **¹H-NMR** (500 MHz, Methanol-*d*₄): δ 8.84 (s, 2H, H-2thienop), 8.43 (d, *J* = 5.8 Hz, 2H, H-6thienop), 7.54 (d, *J* =



5.7 Hz, 2H, H-7thienop), 7.49 (d, $J = 8.6$ Hz, 4H, Ar-S), 7.34 (d, $J = 8.6$ Hz, 4H, Ar-C), 5.65 (s, 4H, CH₂-N⁺), 4.19 (t, $J = 7.0$ Hz, 4H, H-2or5pyrr), 3.99 (t, $J = 7.0$ Hz, 4H, H-2or5pyrr), 2.26 (quint, $J = 6.9$ Hz, 4H, H-3or4pyrr), 2.11 (quint, $J = 6.9$ Hz, 4H, H-3or4pyrr). ¹³C-NMR (126 MHz, Methanol-d₄): δ 156.66 (2C, -C-), 151.28 (2C, -CH-, C-2thienop), 147.45 (2C, -C-), 140.24 (2C, -CH-, C-6thienop), 138.79 (2C, -C-), 134.65 (2C, -C-), 129.48 (4C, -CH-, Ar-C), 128.98 (4C, -CH-, Ar-S), 118.49 (2C, -CH-, C-7thienop), 118.23 (2C, -C-), 56.23 (2C, -CH₂-, CH₂-N⁺), 51.71 (2C, -CH₂-, C-2or5pyrr), 50.74 (2C, -CH₂-, C-2or5pyrr), 27.22 (2C, -CH₂-, C-3or4pyrr), 25.06 (2C, -CH₂-, C-3or4pyrr). **ES+ HRMS** (m/z) [M]²⁺: calculated for C₃₄H₃₄N₆S₄: 654.1728, found: 654.1744.

1.7 Bidimensional spectra HMBC and HSQC of Compound **FP 16**.

Two-dimensional NMR experiments were conducted to unequivocally assign the signals of proton and ¹³-carbon NMR spectra. Obviously, as the cationic head changes from one to another compound of the same library, we just could not clearly identify the linker through all of them. The HMBC spectra was divided into two zones, the aromatic (zone 1, Figure 44) and aliphatic (zone 2, Figure 45) regions, to facilitate the carbon-proton correlation visualization. The deuterated solvent used was methanol. The HSQC was also reported (Figure 46).

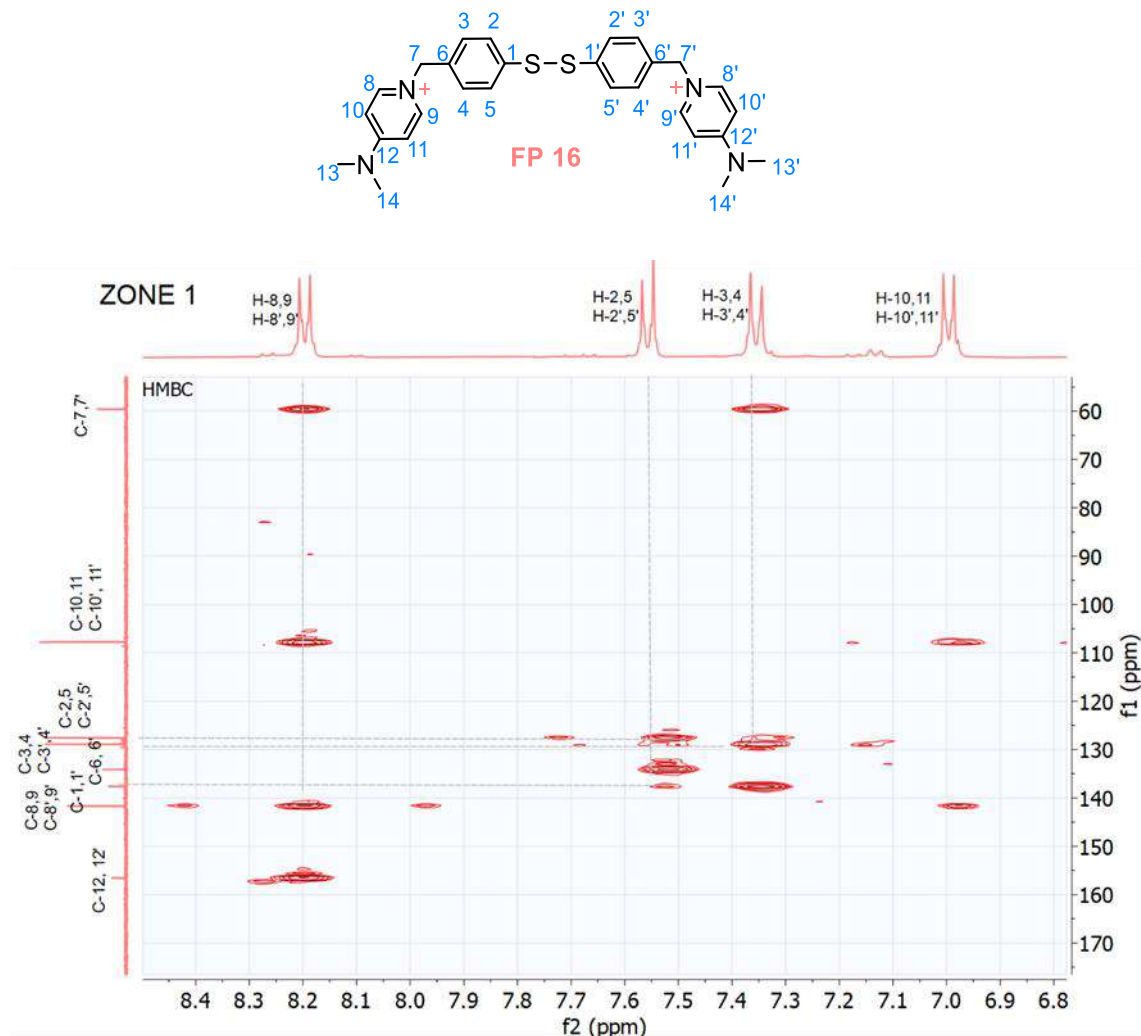


Figure 44. Broadening of the aromatic region of the **FP 16** HMBC spectra.

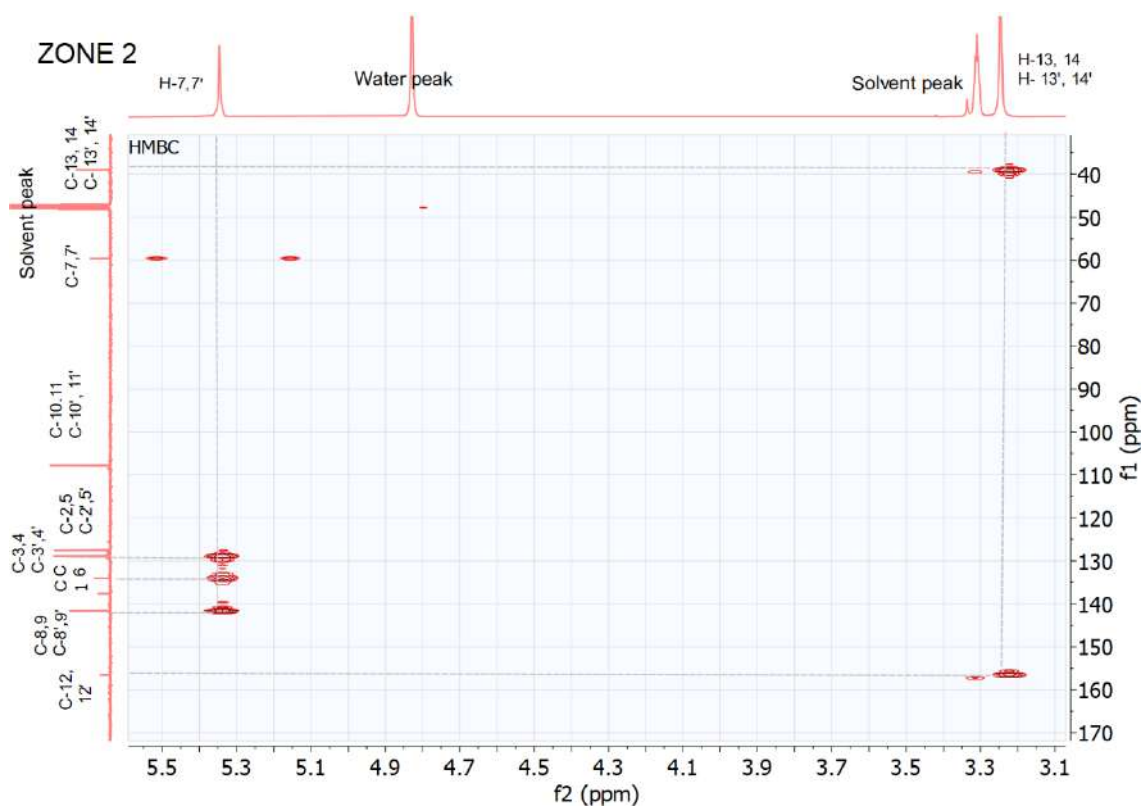


Figure 45. Broadening of the aliphatic region of the FP 16 HMBC spectra.

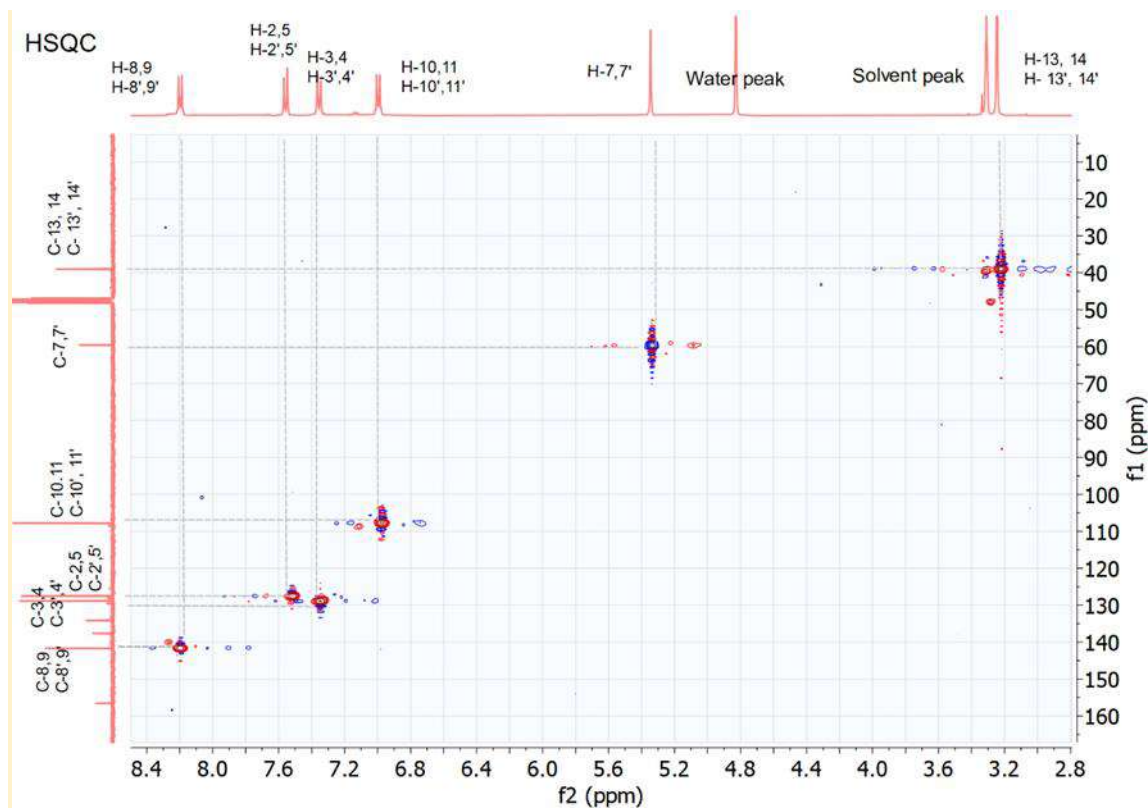


Figure 46. HSQC spectra of compound FP 16.

1.8 Bidimensional spectra HMBC of Compound **PL 54**.

Similarly, we conducted two-dimensional HMBC for the correct assignment of the ^1H and ^{13}C signals of the linker in the PL library. We divided the whole spectra in two main regions, the aromatic (zone 1, Figure 47) and the aliphatic (zone 2, Figure 48).

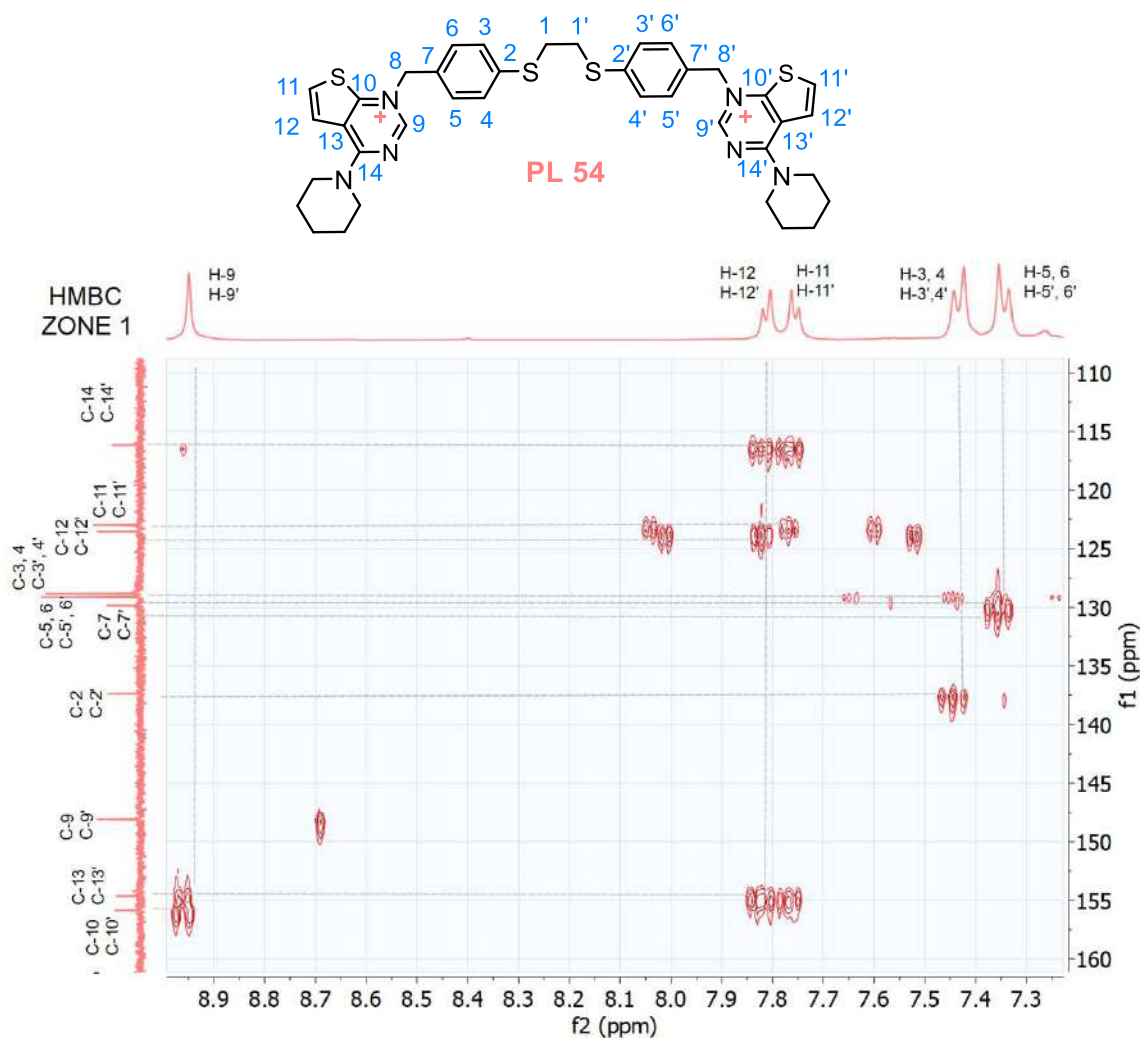


Figure 47. Broadening of the aromatic region of the **PL 54** HMBC spectra.

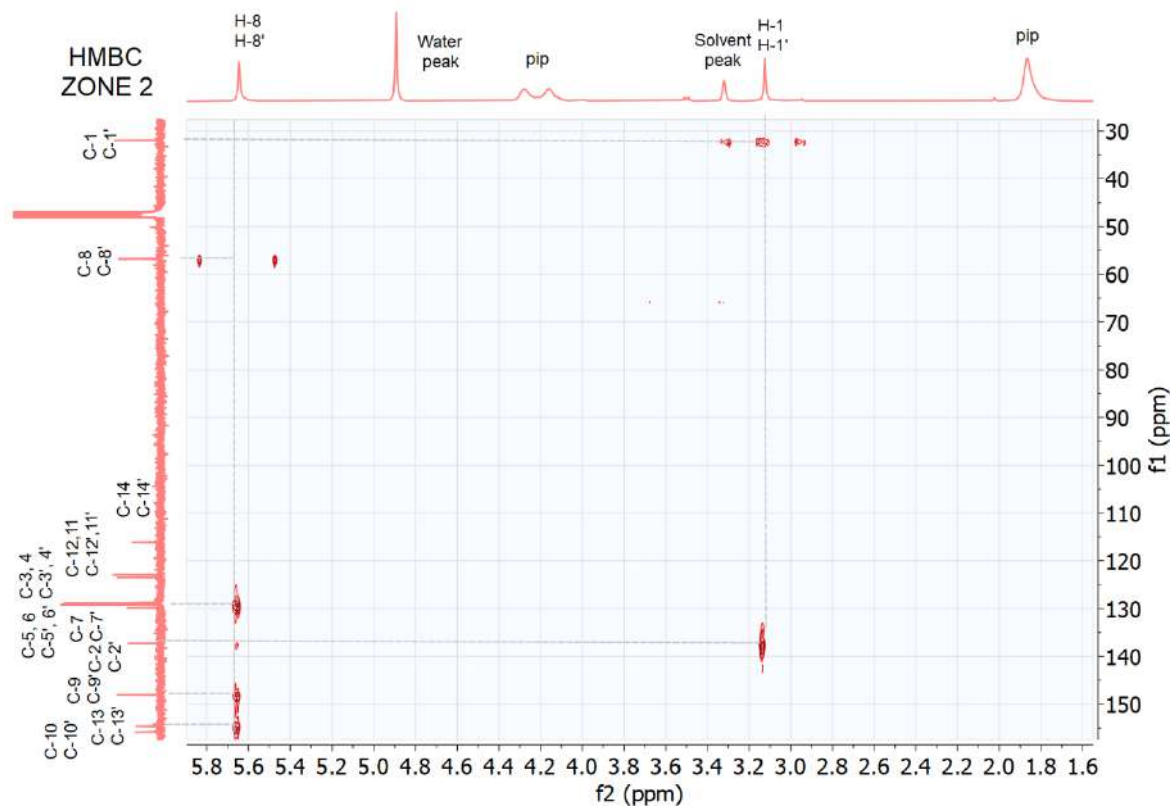


Figure 48. Broadening of the aliphatic region of the **PL 54** HMBC spectra.

1.9. Green metrics calculation.

The E-factor was born to measure the quantity of waste generated by different industrial sectors¹⁵⁸, but it can be also applied to a laboratory scale (mg). The simple (s) E-factor does not consider water used in the process. The reason is that it would increase too much the calculated values to be easily handled. However, the fact that water was not included in the metric result in inconsistency as chemical processes that use a huge amount of water as media could give room to greenest values than others in which water is recirculated, and the need for pre-treatment is included in waste. That is the reason why the known as complete (c) E-factor was proposed. We also considered in our calculation the water used in liquid-liquid extractions and quenching of reactions, in an attempt to obtain accurate results.¹⁵⁹

The values represented in Figure 23, 24 and 25, were calculated following the Equation 1:

$$E - factor = \frac{Kg \text{ of waste including water}}{Kg \text{ of product}}$$

$$= \frac{\text{Amount of reactants and aux. solvents (Kg)} - \text{amount of the final product (Kg)}}{\text{amount of the final product (Kg)}}$$

Equation 1. E-factor calculation.

1.9.2. E-factor of the disulphide linker synthetic pathway.

For the traditional retrosynthetic method 1, we obtained:

Total amount of reactants and solvents: 500 mg (p-tolyl disulfide) + 736.8 mg (NBS) + 26.6 mg (AIBN) + 44700 mg (chloroform) + 33250 (CH₂Cl₂) + 75000 mg (water and brine) + 1276860 mg (hexane) + 45000 mg (EtOAc) = 1476073.4 mg
Amount of final product: 53.33 mg (6.5% yield)

$$E\text{-factor}_{STEP 1} = (1476073.4 - 53.33) / 53.33 = \mathbf{27677}$$

For the green synthetic pathway 2 of the disulphide linker, we calculated:

Step 1: Esterification with methanol.

Total amount of reactants and solvents: 1000 mg (4-mercaptobenzoic acid) + 3959 mg (MeOH) + 183 mg (sulfuric acid) + 22500 mg (EtOAc) + 50000 mg (water) + 28000 mg (10% aq. NaHCO₃) = 105642 mg
Amount of final product: 861.9 mg (79% yield)

$$E\text{-factor}_{STEP 1} = (105642 - 861.9) / 861.9 = \mathbf{121.6}$$

Step 2: Reduction to alcohol.

Total amount of reactants and solvents: 100 mg (methyl 4-mercaptobenzoate) + 3560 mg (THF) + 968.4 mg (LiAlH₄ 1M in THF) + 396 mg (quenching MeOH) + 512 mg (quenching HCl 2N) + 9000 mg (EtOAc) + 30000 mg (water) = 44536.4 mg
Amount of final product: 73.6 mg (89% yield)

$$E\text{-factor}_{STEP 2} = (44536.4 - 73.6) / 73.6 = \mathbf{604}$$

Step 3: Dimerization.

Total amount of reactants and solvents: 758 mg (4-mercaptobenzyl alcohol) + 686.4 mg (iodine) + 12624 mg (ethanol) + 164 mg (triethylamine) + 3201 mg (Na₂S₂O₃) + 5110 (HCl 2N) = 22543.4 mg

Amount of final product: 623.8 mg (83% yield)

$$E\text{-factor}_{\text{STEP 3}} = (22543.4 - 623.8) / 623.8 = 35$$

Step 4: Nucleophilic bromination.

Total amount of reactants and solvents: 689.5 mg (comp. **16**) + 34580 (CH₂Cl₂) + 872 mg (PBr₃) + 10480 mg (NaHCO₃) + 75000 mg (water) = 121621.5 mg

Amount of final product: 601.4 mg (60% yield)

$$E\text{-factor}_{\text{STEP 4}} = (121621.5 - 601.4) / 601.4 = 201$$

$$\text{Total E-factor}_{\text{STEP 1 TO 4}} = 121.6 + 604 + 35 + 201 = 961.6$$

1.9.3. E-factor of the dithioethane linker synthetic pathway.

Step 1: Dimerization and ethane bridge formation.

Total amount of reactants and solvents: 435.8 mg (NaOH) + 3959 mg (MeOH) + 424.5 mg (1,2-dibromoethane) + 700 mg (4-mercaptobenzoic acid) + 5110 mg (HCl 2N) = 10629.3 mg

Amount of final product: 1520 mg (100% yield)

$$E\text{-factor}_{\text{STEP 1}} = (10629.3 - 1520) / 1520 = 6$$

Step 2: Esterification using the microwave.

Total amount of reactants and solvents: 200 mg (comp. **10**) + 1578 mg (ethanol) + 91.5 mg (sulfuric acid) = 1869.5 mg

Amount of final product: 175.9 mg (75% yield)

$$E\text{-factor}_{\text{STEP 2}} = (1869.5 - 175.9) / 175.9 = 9.6$$

Step 3: Reduction to alcohol.

Total amount of reactants and solvents: 322 mg (comp. **11**) + 13350 mg (THF) + 4479.75 mg (LiAlH₄) + 1583.6 mg (methanol) + 2044 mg (HCl 2N) + 22500 mg (EtOAc) + 75000 mg (water) = 119279.35 mg

Amount of final product: 171.9 mg (68% yield)

$$E\text{-factor}_{\text{STEP 3}} = (119279.35 - 171.9) / 171.9 = 693$$

Step 4: Nucleophilic bromination.

Total amount of reactants and solvents: 217 mg (comp. **12**) + 9310 mg (CH₂Cl₂) + 249.09 mg (PBr₃) + 10480 mg (NaHCO₃) + 39900 mg (CH₂Cl₂) = 60156.09 mg

Amount of final product: 239.2 mg (78% yield)

$$E\text{-factor}_{\text{STEP 4}} = (60156.09 - 239.2) / 239.2 = 250.5$$

$$\text{Total E-factor}_{\text{STEP 1 TO 4}} = 6 + 9.6 + 693 + 250.5 = 959.1$$

1.9.4. E-factor of the diphenoxyethane linker synthetic pathway.

The following procedure was taken from the literature.⁵¹

First, to a solution of 0.4 g of NaOH in 5 mL of EtOH was added 1 g of 4-methoxyphenol. The mixture was stirred for 30 min at room temperature and afterwards, 0.4 mL of 1,2-dibromoethane was added before microwave irradiation at 140 °C for 28 min. The reaction was quenched by cooling (ice/water bath) and by the addition of 25 mL distilled water. The solid was filtered and washed twice with water H₂O (2 x 2 mL) and EtOH (1 x 2 mL), dried to vacuum to

furnish a white solid identified as *1,2-bis(p-ethylphenoxy) ethane* in a 35% yield (392.14 mg, 1.62 mmol).

Total amount of reactants and solvents: 400 mg (NaOH) + 3945 mg (ethanol) + 1000 mg (4-methoxyphenol) + 868 mg (1,2-dibromoethane) + 29000 mg (distilled water) + 1578 mg (ethanol wash) = 36791 mg

Amount of final product: 392.14 mg (35% yield)

$$E\text{-factor}_{\text{STEP 1}} = (36791 - 392.14) / 392.14 = \mathbf{92.8}$$

Then, to a solution of *1,2-bis(p-ethylphenoxy) ethane* (0.1 g, 25 mmol) in chloroform (3 mL) was added a mixture of dibenzoyl peroxide (0.5 mg, 2 mmol) and NBS (9.08 mg, 51 mmol). The mixture was purged with argon before microwave irradiation at 120 °C, 21 min. The precipitate was filtered and washed twice with diethyl ether (2 x 2 mL) and dried under vacuum to give *1,2-bis(4-(bromomethyl)phenoxy) ethane* as a yellow solid in a 65% yield (107.33 mg, 0.27 mmol).

Total amount of reactants and solvents: 100 mg (*1,2-bis(p-ethylphenoxy) ethane*) + 4470 mg (chloroform) + 0.5 mg (dbp) + 9.08 mg (NBS) + 2840 mg (diethyl ether) = 7419.6 mg

Amount of final product: 107.33 mg (65% yield)

$$E\text{-factor}_{\text{STEP 2}} = (7419.6 - 107.33) / 107.33 = \mathbf{68.13}$$

$$\mathbf{\text{Total E-factor}_{\text{STEP 1 AND 2}} = 92.8 + 68.13 = 160.93}$$

1.10. Calculation with EcoScale.

The free software EcoScale was developed as a tool for the evaluation of the chemical reaction's conditions on a laboratory scale. It is based on the ChemExper database, which contains currently more than 10 million chemicals together with their Material Safety Data Sheet information. There are assessed six main characteristics of a chemical reaction which are ranked as:

1. Yield, that punishes with $(100 - \text{yield})/2$ points;
2. The price of the reaction components to produce 10 mmol of the final product (0 points if <10\$, -3 points if it costs between 10\$ and 50\$ or -5 points if costs >50\$);
3. The safety is based on the risk phrases, where N (dangerous for the environment), T (toxic) and F (highly flammable) count as -5 points while E (explosive) and T+ and F+ (extremely toxic and flammable, respectively) count as -10 points;
4. Technical setup as a meaning of the extra glassware or equipment needed to carry out the reaction (i.e. the use of an addition funnel counts -1 points, introduce an inert atmosphere counts as -1 and the use of an autoclave count for -3 points);
5. Temperature and time, where cooling is punished more (-4 or -5) than heating (from -1 to -3 points);
6. Workup and purification, being the chromatographic column the costliest (-10 point) and purification by crystallization the cheaper (-1 point). All the reaction treatments' that involve the use of solvents are also punished (from -2 to -3).

The intrinsic subjectivity of the chosen reaction's characteristics and the penalty points for them assigned could be discussed.¹²⁴ However, in our study the calculation was done using the default criteria for each reaction step in [Scheme 6](#) and [7](#), to objectively compare them. The only modification introduced by us, was to not subtract points in **4**. due to the use of microwave because it was considered as a green technique and just consider the time of heating in **5**.

Using a 0 to 100 scale, we can classify the reactions conditions as: excellent when the value is > 75, acceptable when it is > 50 and inadequate when < 50.

The final EcoScale value is simply a subtraction of the penalty points to the maximum value of 100 (Equation 2).

$$\text{EcoScale} = 100 - \text{sum of individual penalties}$$

Equation 2. EcoScale calculation.

Then, for the comparison between the disulphide linker retrosynthetic and green-by-design pathway, we calculated the EcoScale value of each step and the overall reaction value as the average of them (Table 7 and 8).

Synthetic pathway 1: Step 1. Bromination.		Penalty points
1. Yield: 6.5%		-46.8
2. p-Tolyl disulfide (2.03 mmol, 500 mg)		-5
N-Bromosuccinimide (4.14 mmol, 736.8 mg)		-5
AIBN (0.162 mmol, 26.6 mg)		-5
Chloroform (371.9 mmol, 30 mL)		-5
3. Safety		0
4. Reflux under Argon atmosphere		-1
5. 100 °C for 24 hours (Heating > 1h)		-3
6. Cooling to room temperature		0
Removal of Chloroform		0
Extraction with dichloromethane/water		-3
Drying over Na ₂ SO ₄ and filter		0
Removal of dichloromethane		0
Column chromatographic purification		-10
EcoScale:		16.25

Table 7. Summary of the EcoScale values calculation for the synthetic pathway 1.

Synthetic pathway 2: Step 1. Esterification.		Penalty points	Step 2. Reduction to alcohol.		Penalty points
1. Yield: 79%		-10.5	1. Yield: 89%		-5.5
2. 4-mercaptobenzoic acid (6.5 mmol, 1 gr)		0	2. Methyl 4-mercaptobenzoate (0.59 mmol, 100 mg)		0
Methanol (123.4 mmol, 5 mL)		0	LiAlH ₄ 1M in THF (1.07 mmol, 1.07 mL)		0
Sulfuric acid (1.9 mmol, 0.1 mL)		0	Tetrahydrofuran (48.8 mmol, 4 mL)		0
3. Methanol (T, F)		-10	3. LiAlH ₄ (F+)		-15
4. Reflux (Common set-up)		0	Tetrahydrofuran (F)		-5
5. 90 °C for 24 hours (Heating > 1h)		-3	4. Dropwise addition of LiAlH ₄		-1
6. Cooling		0	Inert atmosphere of Argon		-1
Dilution with EtOAc		0	5. Cooling to 0 °C while the addition takes place		-4
Washing with water and brine		-3	Room temperature for 2 hours		-1
Drying over Na ₂ SO ₄ and filter		0	6. Quenching with HCl/MeOH		0
Removal of EtOAc		0	Dilution with EtOAc		0
EcoScale:		73.5	Liquid extraction with water		-3
			Drying over Na ₂ SO ₄ and filter		0
			Removal of EtOAc		0
			EcoScale:		64.5

Next, the EcoScale value was also calculated for the homologous dithioethane (Table 9) and diphenoxyethane (Table 10) linkers to assess the sustainable value of the suggested synthesis.

Step 3. Dimerization.	Penalty points	Step 4. Bromination.	Penalty points
1. Yield: 83%	-8.5	1. Yield: 60%	-20
2. 4-Mercaptobenzyl alcohol (5.4 mmol, 758 mg)	-5	2. 4,4'-Disulfanediybis(4,1-phenylene)dimethanol (2.48 mmol, 689 mg)	0
Iodine (2.704 mmol, 686.4 mg)	0	Phosphorus tribromide (3.22 mmol, 0.3 mL)	0
Triethylamine (1.62 mmol, 0.225 mL)	0	Dichloromethane (390 mmol, 25 mL)	0
Ethanol (274.4 mmol, 16 mL)	-5	3. *Dichloromethane (T)	-5
3. Iodine (F, N, T)	-15	4. Common glassware, stirring	0
Triethylamine (F, T)	-10	5. Cooling to 0 °C while the addition takes place	-4
Ethanol (F, T)	-10	Room temperature for 3 hours	-1
4. Common glassware, stirring	0	6. Quenching with sat. NaHCO ₃	0
5. Room temperature overnight	-1	Extraction with water	-3
6. Quenching with HCl/Na ₂ S ₂ O ₃	0	Drying over Na ₂ SO ₄ and filter	0
Precipitated filtration	0	Removal of dichloromethane	0
EcoScale:	45.5	EcoScale:	67

Table 8. Summary of the EcoScale values calculation for the synthetic pathway 2.

Dithioethane synthetic pathway:			
Step 1. Dimerization.	Penalty points	Step 2. Esterification.	Penalty points
1. Yield: 100%	0	1. Yield: 75%	-12.5
2. 4-Mercaptobenzoic acid (4.54 mmol, 700 mg)	0	2. 4,4'-(ethane-1,2-diylbis(sulfanediy)) dibenzoic acid (0.6 mmol, 200 mg)	-5
Sodium hydroxide (10.89 mmol, 435.6 mg)	0	Ethanol (34.3 mmol, 2 mL)	0
Methanol (123.4 mmol, 5 mL)	0	Sulfuric acid (1.87 mmol, 0.1 mL)	0
1,2-Dibromoethane (2.27 mmol, 0.196 mL)	0	3. Ethanol (F, T)	-10
3. Sodium hydroxide (F, T)	-10	4. Sealed microwave vessel	0
Methanol (F, T)	-10	5. Irradiation at 100 °C for 2 hours	-3
1,2-Dibromoethane (N, T)	-10	6. Cooling to room temperature	0
4. Common glassware, stirring	0	Filtration	0
5. Room temperature overnight	-1	EcoScale:	69.5
6. Removal of MeOH	0		
Addition of HCl 2N	0		
Filtration	0		
EcoScale:	69		
Step 3. Reduction to alcohol.	Penalty points	Step 4. Bromination.	Penalty points
1. Yield: 68%	-16	1. Yield: 78%	-11
2. Diethyl 4,4'-(ethane-1,2- diylbis(sulfanediy))dibenzoate (0.825 mmol, 322 mg)	-5	2. ((Ethane-1,2-diylbis(sulfanediy))bis(4,1- phenylene))dimethanol (0.708 mmol, 217 mg)	-5
LiAlH ₄ 1M in THF (4.95 mmol, 4.95 mL)	0	Phosphorus tribromide (0.921 mmol, 0.087 mL)	0
Tetrahydrofuran (219.6 mmol, 18 mL)	0	Dichloromethane (109.2 mmol, 7 mL)	0
3. LiAlH ₄ 1M in THF (F+)	-15	3. *Dichloromethane (T)	-5
Tetrahydrofuran (F)	-5	4. Common glassware, stirring	0
4. Dropwise addition of LiAlH ₄	-1	5. Cooling to 0 °C while the addition takes place	-4
Inert atmosphere of Argon	-1	Room temperature for 3 hours	-1
5. Cooling to 0 °C while the addition takes place	-4	6. Quenching with sat. NaHCO ₃	0
Room temperature for 3 hours	-1	Extraction with water	-3
6. Quenching with HCl 2 N/MeOH	0	Drying over Na ₂ SO ₄ and filter	0
Extraction with EtOAc/H ₂ O	-3	Removal of dichloromethane	0
Drying over Na ₂ SO ₄ and filter	0	EcoScale:	71
Removal of EtOAc	0		
EcoScale:	49		

*Was not considered as a penalty by the software, but we did.

Table 9. Summary of the EcoScale values calculation for the dithioethane linker synthetic pathway.

Diphenoxyethane synthetic pathway:

Step 1. Dimerization.

	Penalty points
1. Yield: 35%	-32.5
2. 4-Methoxyphenol (8.06 mmol, 1 gr)	0
Sodium hydroxide (10 mmol, 400 mg)	0
Ethanol (85.74 mmol, 5 mL)	0
1,2-Dibromoethane (4.63 mmol, 0.4 mL)	0
3. Sodium hydroxide (F,T)	-10
Ethanol (F, T)	-10
1,2-Dibromoethane (N, T)	-10
4. Common glassware, stirring	0
5. Stirring at rt for 30 min	0
MW irradiation 140 °C for 28 min	-2
6. Cooling to room temperature	0
Quenching with ice/water	0
Filtration and washing with H ₂ O and EtOH	-3
Drying under vacuum	0
EcoScale:	32.5

Step 2. Bromination.

	Penalty points
1. Yield: 65%	-17.5
2. 1,2-bis(p-tolyloxy)ethane (0.25 mmol, 100 mg)	0
Chloroform (37.19 mmol, 3 mL)	0
Dibenzoyl peroxide (0.02 mmol, 5 mg)	0
N-Bromosuccinimide (0.5 mmol, 90 mg)	0
3. Dibenzoyl peroxide (E)	-10
4. Common glassware, stirring	0
Purge the system with Argon	-1
5. MW irradiation at 120 °C, 21 min	-2
6. Cooling to room temperature	0
Filtration of the precipitate	0
Several washes with Et ₂ O	-3
EcoScale:	66.5

Table 10. Summary of the EcoScale values calculation for the diphenoxyethane synthetic pathway.

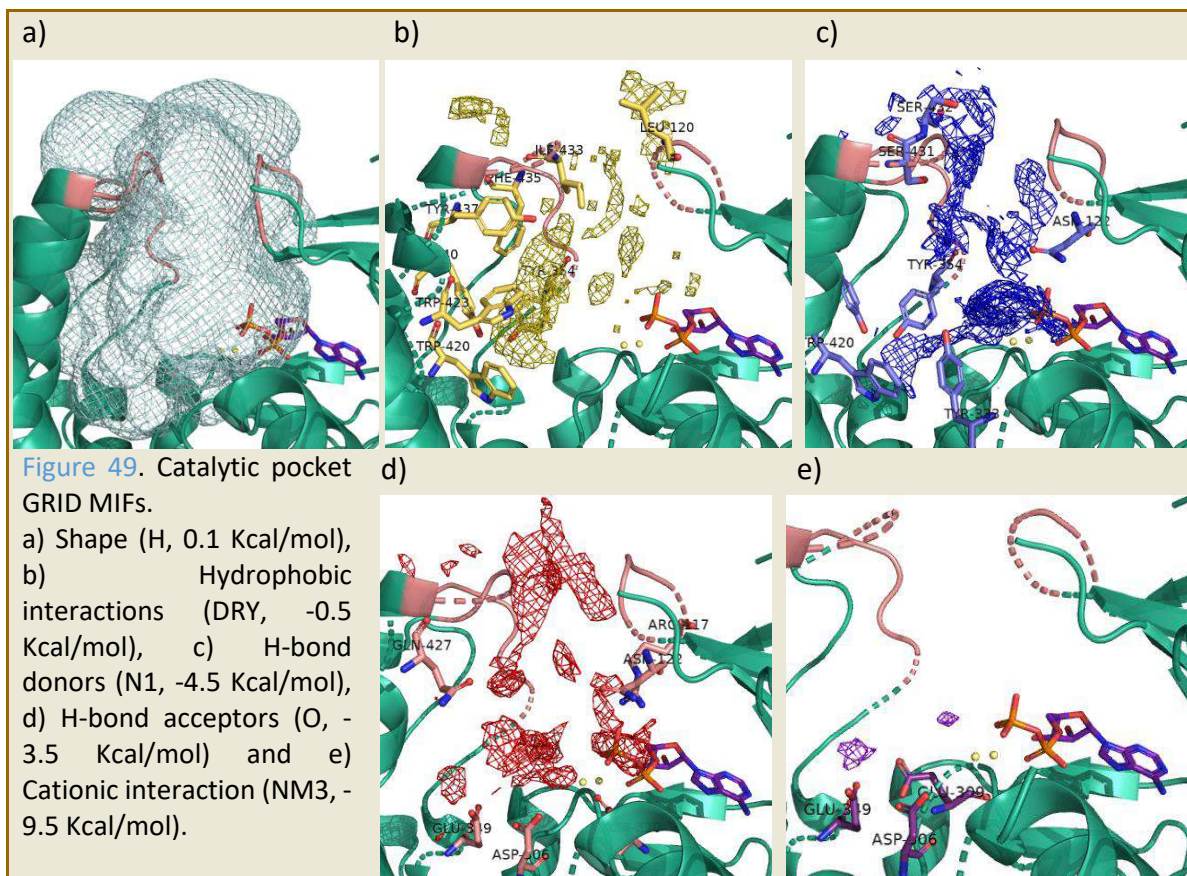
1.11. Crystallographic enzyme and search of pockets.

The crystallographic structure used in this study was downloaded directly from the protein data bank (PDB ID: 3G15, with a resolution of 1.7 Å) and corresponds with the semi-open conformation of the Human Choline Kinase α 1 in complex with **HC-3**, ADP, and two Mg^{+2} atoms. The protein structure was loaded into FLAP and processed by the FLAP default basic filters for PDB files, that remove artefacts but metal ions and cofactors.

Then, the next step consisted of the search of the catalytic pocket. For that purpose, it was used the FLAPsite algorithm⁹⁸ that automatically identifies the cavities in the 3D structure. It was possible to maintain some objects in the enzyme 3D structure as the magnesium (II) atoms and the ADP. In this way, the software will take into account the occupied space and it will search for pockets around. The rest of the parameters were left as default: sensitivity as 6 and erosion as 2.

However, when loaded the crystallographic ligand **HC-3** there was a fragment that remained uncovered by the pocket. As the catalytic site is surrounded by three loops, some of their border residues were tested to be merged with the default pocket and totally covered the ligand. From all the tested conditions, the best pocket was designed around the residue Phe 361, using an extension of 6 and a thickness of 7. Those parameters refer to the volumetric extension and the proximity to amino acid chains, respectively. The choose amino acid residue was particularly oriented towards the catalytic cavity (see Appendix 1).

Finally, the pocket MIFs were generated using the probes: H (shape), DRY (hydrophobic), N1 (hydrogen bond donor), O (hydrogen bond acceptor) and NM3 (trimethyl ammonium cation), all of them at their standard energy values (Figure 49, a, b, c, d and e respectively). MIFs are an excellent tool to identify and study the interactions and affinity between the ligands and the catalytic pocket.



Analysing the molecular interaction fields, it is possible to recognize that: (Figure 49, a) the pocket shape is big enough to involve the ligands and is contained among three bordering loops; (Figure 49, b) that the hydrophobic interactions are favoured in the deep choline site due to residues Tyr 354, Tyr 440, Trp 420, Trp 423; (Figure 49, c and d) that the pocket has a hydrogen bond acceptor rather than donor character, overall nearly to the Mg atoms; and (Figure 49, e) that the cationic charged moieties are well anchored due to the negative nature of residues at the bottom of the catalytic site (Asp 306 and Glu 349).

1.12. Validation of the model.

To dock the compounds in FLAP it was first necessary to optimize some parameters. With the default values, which consists of a radius around the pocket of 2 Å and middle-high accuracy, nine molecules from a total of twenty-two were unable to be docked. The radius around the pocket of 2 Å seems not big enough to harbour almost half of the synthesized ligands.

When the radius around the pocket was increased to 3 Å and used the middle-low accuracy, the number of undocked molecules was reduced so that only three of them were unable to dock the pocket. The parameters used in Models A and B can reproduce the binding mode of the crystallographic ligand **HC-3** so that we can rely on the model to study the docking of our library (Table 11).

Even if lengthening the radius around the pocket diminishes the S-score and the Glob P values with respect to the default model, Model B is enriched over the correct pose of the crystallographic ligand (Table 11, 80% in Model B versus 40% in Model A) and allows the evaluation of most inhibitors.

Compounds **PL 72**, **PL 70** and **PL 67** were unable to dock. They are particularly hindrance, having as cationic heads quinolinium and thieno[3,2-d] pyrimidinium moieties substituted at the 4 position by *N*-methylaniline or *p*-chloro-*N*-methylaniline groups.

The synthesized molecules are larger than the crystallographic ligand in almost double the size. That means that they are docked in a limited catalytic site, in which the enzyme conformation and the residues orientation are favoured towards the **HC-3** ligand, assuming the limitation that it confers to our study.

Compound	S-score	H	O	N1	DRY	GlobP	GlobSum	POSI	POSI norm	Etot
MODEL (A) HC-3 as default	1.047	0.978	0.419	0.653	0.513	0.367	1.197	54.489	0.132	0.094
MODEL (B) HC-3	1.03	0.992	0.34	0.594	0.501	0.348	1.207	46.666	0.113	0.13

Scores obtained for **HC-3** in the two models. It is only reported the best value out of five solutions given.

MODEL A: HC-3 as default (2 Å and middle-high accuracy)	Probability of each pose (%)	40% Correct	60% Incorrect
MODEL B: HC-3 (3 Å and middle-low accuracy)	Probability of each pose (%)	80% Correct	20% Incorrect

Table 11. Model A and B scores (up table), and probabilities of getting the correct (carbon atoms in pink color) or incorrect (carbon atoms in blue color) pose for the crystallographic ligand **HC-3** (carbon atoms in yellow color).



**NEW GREEN
PROCESSES FOR
INTERESTING
PHARMACEUTICAL
SCAFFOLDS**

Chapter 2

Introduction

1. Towards sustainability of processes.

For many years, the standard focus of synthetic procedures has been the production of molecules able to perform a designed function but lacking in their impact assessment over the environment. Their possible bioaccumulation in the biosphere and the reactivity on natural conditions of humidity, light, or metals exposure has not been considered in the design procedure most of the time.¹⁶⁰

Since the publication of the Twelve Principles of Green Chemistry in 1998 by Anastas and Warner, Green Chemistry has developed as a new branch of chemistry. New processes are proposed to obtain molecules with the same performance but also paying attention to waste reduction or by-products revaluation. Thus, it is needed to rewrite the way chemistry processes are done to supply the demands of the present without compromising the future. Models as the one shown in Figure 50, remark how the transition from linear to circularity must be addressed.

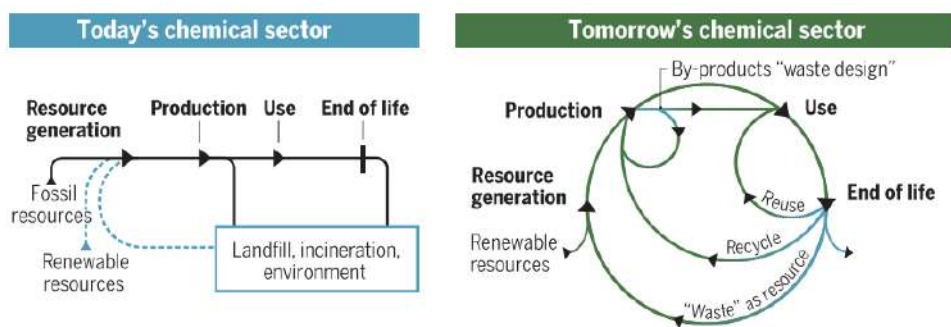


Figure 50. The development of processes able to match both chemical performance and generate harmless by-products and waste for reuse.

The figure is taken from the reference *Science* 2020, 367, 397–400.

Indeed, the preferred use of bio-based starting materials and solvents instead of those obtained from petroleum cracking has been proposed. Lignocellulosic biomass^{161,162}, fermentation products and algae hydrotreating¹⁶³ have claimed the attention as an alternative source of fuel without causing competition with food production (vegetable oil, sugar cane or corn).

In addition, non-persistent materials and solvents are desirable to accomplish the target of biodegradability. Recent advances in this direction are the synthesis of biopolymers from renewable sources and also benign to the environment as the poly(limonene carbonate) (PLimC) from the citrics' peel¹⁶⁴, or the development of insecticides as Spinosad that are harmless to mammals and could be degraded in nature within days¹⁶⁵.

However, the evaluation of the waste generated by industries of different sectors pointed out the pharmaceutical industry as the most polluting.¹⁵⁸ The implementation of green measures in this sector is highly challenging due to the use of multistep processes, low volume of production and the need for regulatory approval for new methods in the synthesis of APIs. For that reason, it is mandatory for academia the development of new technologies and green-by-design molecules in drug development and synthesis, so that a green transition to industry could be easier.

2. Flow implementation in processes.

The current trend in drug discovery and development, are automatic processes that will work at a higher speed than the traditional reactions in batch, giving to the scientific community fast results that can guide the research in the right direction. One of these technologies is the reactions in flow, conducted inside tubing or microchannels, that present a high potential for industrial use.¹⁶⁶ The flow technology main advantages are:

- a) fast mixing: in a flow microreactor, mixing takes place by molecular diffusion so that a concentration gradient can be avoided;
- b) high surface-to-volume ratio: the microstructure of microreactors allows for a very rapid heat transfer enabling fast cooling, heating and, hence, precise temperature control;
- c) safety: because of the high efficiency in heat exchange, avoids accumulation of unstable intermediates, and the possibility of dealing with hazardous reagents and gases that can be safely prepared and consumed, otherwise problematic on scale;
- d) economy: due to lower manufacturing and operating costs, reduced workup procedures, use of less raw materials and solvents and reduced waste;
- e) improved yields and selectivity.

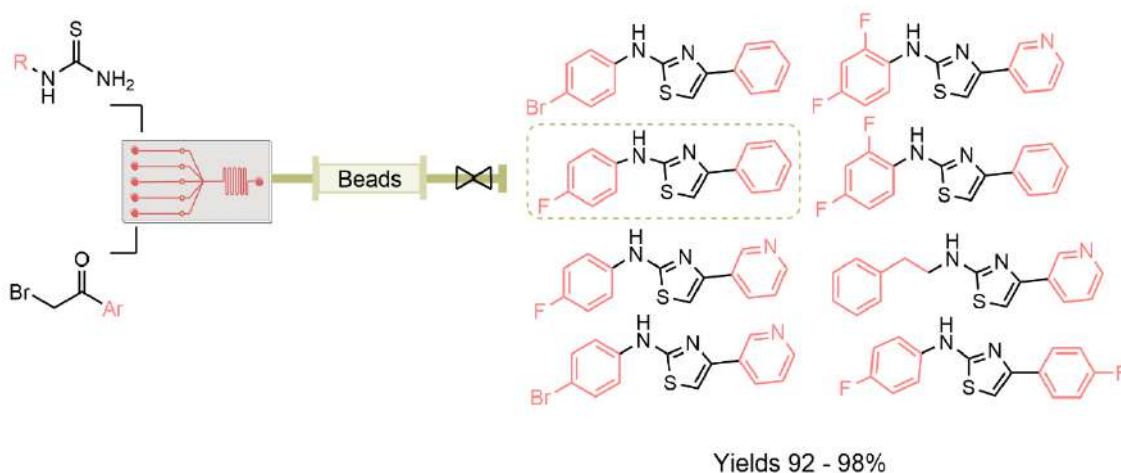
Another advantage is the possibility of connecting instruments in-line for analysis, like detectors or elements for purification and phase separators. The options are countless.

The symbiotic combination between this technology and greener chemical processes will open a new pathway to synthesize molecules that obey the Twelve Principles of Green Chemistry and that will give room to competitive alternatives in the industry.

In fact, the application of this technique to the synthesis of chemical libraries of compounds¹⁶⁷ has allowed a faster screening of functional groups in biological active scaffolds, speeding the hit to lead process.

To cite one example, we could highlight the research developed by Alam *et al*¹⁶⁸, which made a screening of small molecules able to mimic the Humanin peptide agonist binding to the gp130 receptor. Those molecules could promote neuronal protection from amyloid-beta (A β)-related toxicity and thus become drugs candidates for Alzheimer's disease.

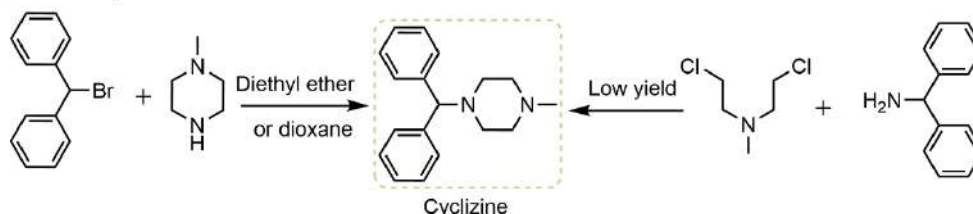
Alam's group¹⁶⁸ successfully synthesized a series of 2-aminothiazoles molecules through Hantzsch condensation using 2-bromo-1-phenylethan-1-one (and its derivatives) and 1-(4-bromophenyl) thiourea (and its derivatives) (Scheme 13). The reaction was performed in a microfluidic reactor that provided higher yields, minimum reaction optimization, selectivity, and faster outcomes (within minutes). These characteristics are important to establish SARs that could lead the research.



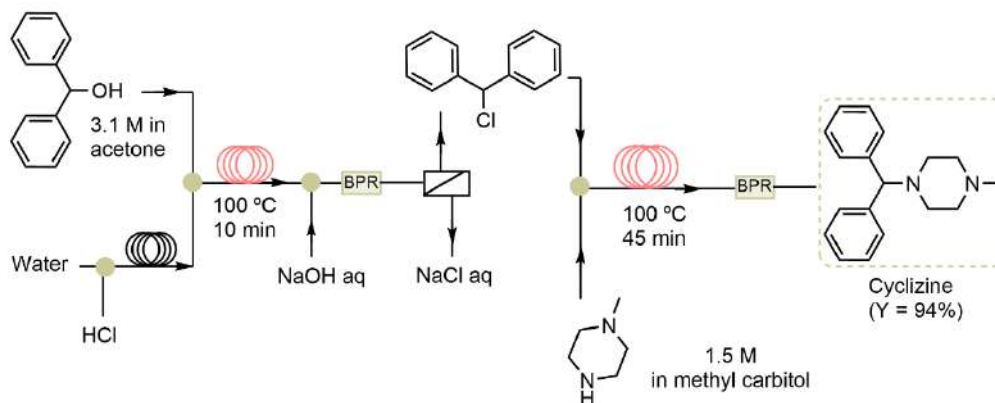
Scheme 13. Microfluidic flow protocol example for the synthesis of chemical libraries.

Examples of the implementation of green chemistry in the synthesis of APIs are well-reviewed in reference ¹⁶⁹. As an example of the green chemistry transition in flow, we could mention the synthetic development of Cyclizine, an anti-sickness and antihistaminic medicine (**Scheme 14**). The patented procedure of its synthesis (**Scheme 14, a**) relies on halogenated starting materials, low yields and stoichiometric waste productions.¹⁷⁰ However, in 2016 Noel *et al* proposed the use of a flow system in which diphenylmethanol is halogenated in line (with HCl), while the excess of acid is neutralized and separated by liquid-liquid extraction from the chlorinated product (**Scheme 14, b**). Etheral solvents (dioxane and diethyl ether) were replaced by acetone and water, enhancing the efficiency of chlorination due to the best solubility of HCl as well as accomplishing the green approach. The last step consisted of the nucleophilic substitution with methyl piperazine that gave room to the synthesis of the final product in high yields.¹⁷¹

a) Patented procedures.



b) Flow methodology implementation.



Scheme 14. Transformation of traditional on batch (*a*) towards the in-flow (*b*) synthesis of Cyclizine. The scheme was taken from ref ¹⁶⁹.

However, despite the above-presented advantages of flow systems in comparison to batch, they are still designed as linear processes. Waste generated from solvents and additives needs to be minimized and/or recirculated in the process.

3. Heterogeneous catalyst in green chemistry.

A step towards sustainability consists in the use of catalytic reactions in flow that can allow the use of mild conditions due to the reduction of the activation energy. The employed catalyst must be supported in alumina, charcoal, polymers¹⁷² or be heterogenous itself (metal organic frameworks-MOF) to avoid leaching in the final product and cytotoxicity problems.

Heterogeneous catalysts are also highly desirable from the sustainable point of view because of their chemical selectivity and reusability. However, precious metals such as Pd and Pt or Cu, mainly used in coupling reactions could increase the price of the process due to the resource's shortage and politics governing their extraction and distribution.

Manganese arises among the transition metals series as an interesting alternative. It is the twelfth most abundant element in the earth crust, exists in a wide range of oxidation states from -3 to +7, exhibiting diverse coordination geometries and reactivities.

The compatibility with biological systems as enzymatic cofactor and plants requirements for growth ensure its low toxicity for the environment.¹⁷³

Of particularly interest are the heterogeneous Mn-based OMS (Octahedral Molecular Sieve) catalysts, first developed by Suib *et al*^{174,175}. Those materials based on Mn oxide units, were synthesized in several morphology, shape and porosity types. Different synthetic methodologies (sol-gel¹⁷⁶, high-temperature¹⁷⁷, hydrothermal¹⁷⁸, microwave¹⁷⁹, solvent-free¹⁸⁰, reflux¹⁷⁵ and sonochemical¹⁸¹) lead to different catalytic electronic properties and doping cavities with Na⁺, Fe⁺³ among others or H⁺ (by ion exchange)¹⁸² improved their potential as a selective oxidative catalysts. The catalytic properties of those materials were related to the redox cycling of the different oxidation states in which the Mn is found (+2, +3 and +4) and the availability of Lewis acid sites.

OMS-1, OMS-2, OMS-5 and OMS-6 refers to the order of its discovery and distinguish the different material tunnel size 3 x 3, 2 x 2, 2 x 4 and 2 x 3, respectively.¹⁸³

From all of them, cryptomelane-type OMS-2 showed a greater catalytic potential of oxidation without the formation of over-oxidated by-products. It contains a one-dimensional tunnel structure formed by 2 x 2 edge shared MnO₆ octahedra. The composition of K-OMS-2 is KMn₈O₁₆ · nH₂O and the tunnels have dimensions of 4.6 x 4.6 Å. The average oxidation state of Mn in K-OMS-2 is ~ 3.8 due to the presence of Mn⁴⁺, Mn³⁺, and Mn²⁺ ions in the framework.¹⁸⁴ The K⁺ ions in the solution acts as a template to construct the correct tunnel structure and balance the charge of the system.

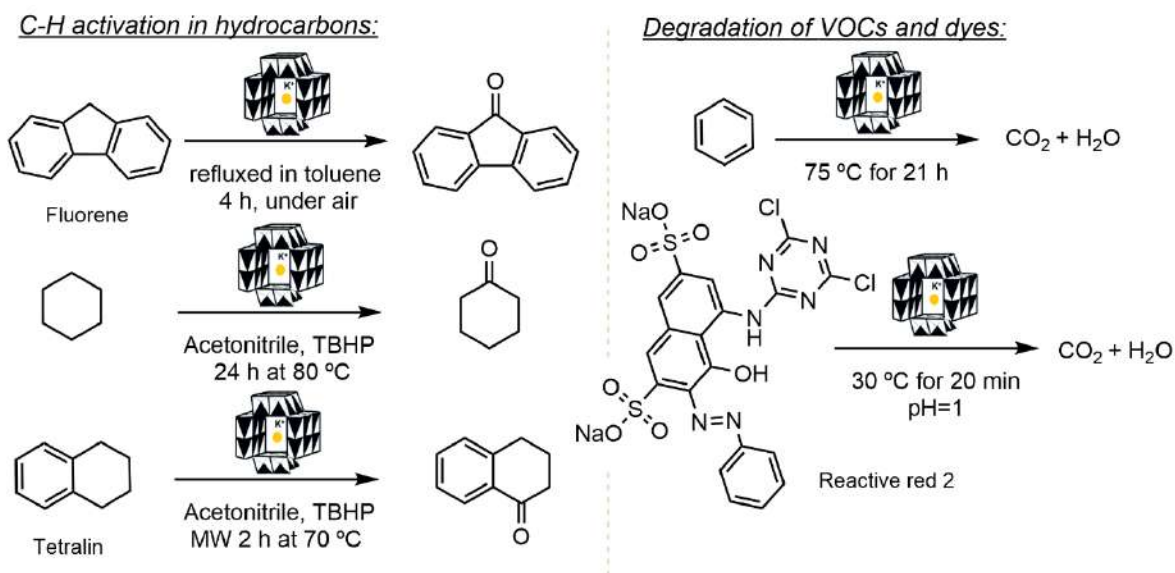
Its catalytic potential has been widely explored (Scheme 15). It was successfully used for the oxidation of inert C-H bonds of hydrocarbons as the fluorene conversion to 9-fluorenone under air¹⁸⁵, the tetralin oxidation to tetralone with TBHP¹⁸⁶, the cyclohexane transformation to cyclohexanone with TBHP¹⁸⁷, and oxidative decomposition reactions of benzene¹⁸⁸ and organic dyes from sewage¹⁸⁹.

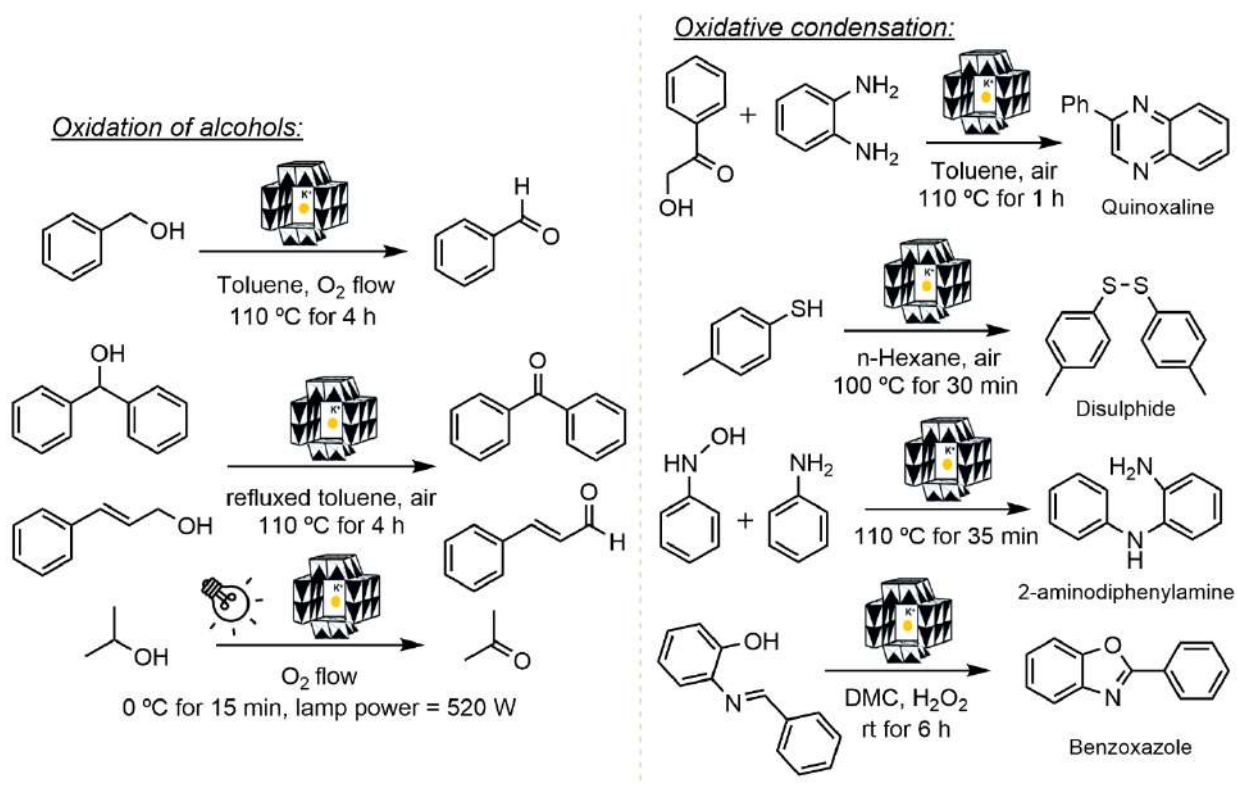
More efficiently it converts allylic and benzylic primary and secondary alcohols to the corresponding aldehydes or ketones^{190,191}, and the 2-propanol through photocatalyzed oxidation to acetone¹⁹².

Other applications consist of the one-pot synthesis of quinoxaline building blocks from the condensation of hydroxy ketones and diamines ¹⁹³, the oxidative dimerization of aliphatic and aromatic thiols to disulphides ¹⁹⁴, the enhancement in selectivity for *ortho*-aminodiphenylamine from the condensation of phenylhydroxylamine with aniline under acidic conditions ¹⁹⁵, or the *green* oxidative cyclization of thio/phenolic imines for the synthesis of benzoxazoles or benzothiazoles ¹⁹⁶.

For that reason, the oxidation versatility of the OMS-2, which could be modulated by the methodology of its synthesis, the amount of Lewis acid sites, and the doping with other metals, has opened a world of possibilities for heterogeneous catalyst implementation.

The reusability, low leaching and sustainable conditions afforded with OMS-2 catalysts proved the growing interest in the development of new transformations.





Scheme 15. Examples of the OMS-2 oxidation applications.

As observed air or an oxygen source in combination with sacrificial oxidants (as TBHP or H_2O_2) considered green additives for the process, are necessary to replace the lost lattice oxygen content and maintain the OMS-2 crystal structure.¹⁹⁷

Apart from the catalytic properties, those materials have found wide applicability in lithium-ion batteries as energy storage materials¹⁹⁸, as membranes for filtration¹⁹⁹ and as chemical sensors²⁰⁰, to cite some examples.

It is highly desirable to search flow synthesis applications that implemented these reusable materials in line, which could be a step ahead in the transition of processes towards circularity.

Aims

In the second Chapter of the thesis, we were interested in the development of greener processes for the synthesis of pharmaceutical scaffolds.

With that purpose, we studied the implementation of the heterogeneous catalyst K-OMS-2 in C-H activation/dimerization and oxidation reactions. The abundance of Mn and the heterogeneity of OMS materials made of this catalyst an interesting choice for cheaper, and reusable catalytic systems.

The first part, consist of the optimization of green conditions adequate for the catalyst use in a flow system in collaboration with Prof. Luigi Vaccaro and Dr. Francesco Ferlin of the Department of Chemistry at the University of Perugia. The proposed green process is a convenient alternative to enzymatic reactions performed by peroxidases, showing robustness, selectivity, low leaching, high yields, and reusability.

In the second part, we focus on the oxidative potential of K-OMS-2 to synthesize isoquinolinones under green conditions. Its potential as a chemical synthon justified the research of new procedures that provide it in a sustainable manner.

Materials and methods

General conditions of synthesis.

In the first part, the catalytic reactions in batch were carried out in pre-dried 10 mL vials adapted with rubber septum when the gas atmosphere was used, while in the second part we used sealed vials warmed in a holey metal plaque. Chemicals were obtained from commercial sources and were used without further purification unless noted otherwise. Yields refer to isolated compounds, estimated to be > 95% pure as determined by $^1\text{H-NMR}$.

TLC plates were purchased from Merck, TLC Silica gel 60 F254 with detection under UV light at 254 nm. Chromatography separations were carried out on Merck Geduran[®] Silica 60 (0.040–0.063 mm, 70–230 mesh ASTM) or Aluminium oxide (activated, neutral, Brockmann Activity I).

GLC analyses were performed by using Hewlett-Packard HP 5890 SERIES II equipped with a capillary column DB5MS (30 m, 0.32 mm), a FID detector and helium as a gas carrier.

GC-EIMS analyses were carried out by using a Hewlett-Packard HP 6890N Network GC system /5975 Mass Selective Detector equipped with an electron impact ionizer at 70 eV.

NMR spectra in solution were recorded on a Bruker DRX-ADVANCE 400 MHz (^1H at 400 MHz and ^{13}C at 100.6 MHz).

Elemental analysis of manganese content was carried out using an Agilent 4210 MP-AES instrument.

Melting points were collected on a Barloworld Scientific Stewart SMP3 micro melting point apparatus and are uncorrected.

All IR spectra were recorded on a Bruker FT-IR Alpha device.

The XRD patterns were collected on a PANalytical X'PERT PRO diffractometer, PW3050 goniometer, equipped with an X'Celerator detector by using the $\text{CuK}\alpha$ radiation.

High-resolution Transmission Electron Microscopy (HRTEM) was conducted on a JEOL JEM-2100F system electron microscope to observe the morphology and structure of the samples.

Results and discussion

1. Green flow chemistry applied to pharmaceutical scaffolds.

The present project was based on the sustainable synthesis of pharmaceutical molecules of interest constituted by a phenoxazinone or phenazine scaffold, as they have different uses as antibiotics or in chemotherapy. It was reported in the literature the synthesis of those building blocks using enzymes as laccases or the phenoxazinone synthase that are multicopper oxidases purified from plants, fungi, or bacteria.²⁰¹ Bruyneel *et al*, successfully demonstrated the versatility of substrates that laccases could transform by oxidation and C-H/C-O homo- or hetero- cross-coupling giving the desired phenoxazinones and phenazines.²⁰² However, the selectivity of the enzymatic catalytic site is a drawback for some substrates that are unable to bind. Also, the pH strongly affected the enzymatic redox activity and the substrates susceptibility for oxidation.^{203,204}

Other synthetic methodologies consist of mimicking the nature function of oxidases and peroxidases, as the Laccase and the Horseradish peroxidase (HRP)²⁰⁵, using inorganic catalysts. For example, copper²⁰⁶ and iron metal complexes^{207,208}, diselenide catalysts²⁰⁹, ferromagnetic nanoparticles²¹⁰ and or nanozymes²¹¹ have been used for oxidation and C-H activation of aminophenol. Those synthetic alternatives are more robust, but still present drawbacks as the use of homogeneous catalysts, non-reusable systems, and the need for ligands and adjuvant reagents.

In our approach to green methodologies, we focus our attention on a heterogeneous catalyst able to be recovered and reactivated. The OMS (Octahedral Molecular Sieves) materials attracted our interest due to their oxidative properties thanks to their octahedral pore shape and morphology constituted of Mn metal centres. Particularly, the K-OMS (potassium-containing OMS) is composed of manganese oxide tunnels with a cryptomelane-type morphology in which the K⁺ cation is accommodated. This type of catalyst has already been used in a plethora of oxidation reactions, as is shown in the introduction, that together with its high stability and well-noted synthesis in the literature, prompted us to its implementation for the C-H oxidation/dimerization reaction of *o*-aminophenol and its derivatives using a flow system. This part of the chapter was successfully published in the journal *Green Chemistry* **2020**, *22*, 397-403 under the title "Waste minimized synthesis of pharmaceutically active compounds via heterogeneous manganese catalysed C-H oxidation in flow."

At first, we carried out the synthesis of K-OMS that is reported in the literature (see [experimental part A. 2.](#)). The catalyst was isolated by size exclusion filtration, and MP-AES analysis of the resulting material was performed, founding a manganese loading of 62% w/w. The average manganese oxidation state was calculated to be 3.8 and the crystal cryptomelane tunnel structure of the K-OMS-prepared was confirmed by XRD spectroscopy in accordance with the literature.²¹²

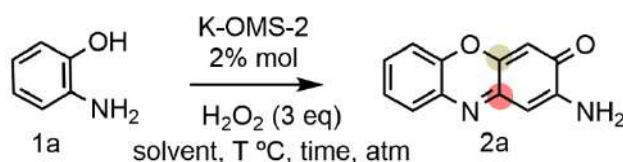
Then, the reaction was tested in batch to optimize the reaction medium and temperature as well as the influence of oxygen in the process.

1.2 Optimization of the batch reaction conditions.

Before moving to the flow system, we evaluate which parameters affected the reaction outcome in batch. For that purpose, we used the commercially available 2-aminophenol as the case study. Previously attempts in batch were also performed by the Vaccaro's group and they showed excellent conversion results using ethanol as reaction media.²¹³ In our study, we go further and select a set of *green* solvents to be tested as reaction media.

As the synthetic strategy is based on oxidative conditions, we focused our attention on the possible use of cyclopentyl methyl ether (CPME) as a solvent, due to its low tendency to generate peroxides compared to a classical ethereal solvent. In addition, CPME has a relatively high boiling point (106 °C) and low toxicity profile, and it is prepared from easily accessible C-5 raw materials derived from furfural or from bio-based adipic acid, which could avoid its future petrochemical-based production.¹⁶¹

Other green solvents tested were: the biomass-derived gamma-valerolactone (GVL)²¹⁴ and 2-MeTHF¹⁶², and the naphtha derivatives tert-amyl methyl ether (TAME) and methyl tert-butyl ether (MTBE), that are still more environmentally friendly in comparison with some of the classic ethereal solvents as THF or 1,4-dioxane. However, in the optimal conditions obtained with the CPME, they gave a lower conversion of 2-aminophenoxazin-3-one (Table 12, from entry 9 to 12).



Entry	Solvent	Gas (1bar)	Temperature	Time (h)	Conversion ^a (%)
1	CPME	O ₂	27 °C	2	42
2	CPME	O ₂	37 °C	2	68
3	CPME	O ₂	50 °C	2	82
4	CPME	O ₂	50 °C	3	> 99
5	CPME	Air ^b	50 °C	3	62
6	CPME	N ₂	50 °C	2	30
7	CPME	Air	50 °C	2	66
8	CPME	Argon	50 °C	2	32
9	2-MeTHF	O ₂	50 °C	3	80
10	GVL	O ₂	50 °C	3	29
11	TAME	O ₂	50 °C	3	72
12	MTBE	O ₂	50 °C	3	78

Reaction conditions: **1a** (1 mmol), solvent 4 mL (0.25 M), (3 mmol, 3 eq) of H₂O₂, KOMS-2 (2% mol) and a gas balloon, temperature and time as specified in the table.

^a The conversion was measured by GLC analyses using samples of pure compounds as a reference. ^b In a closed vial.

Table 12. Screening of the parameters in batch.

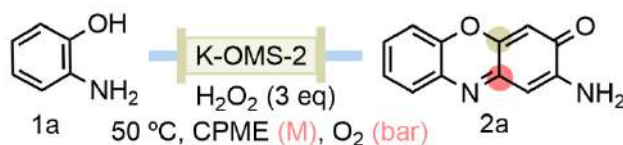
Also, in the previous batch analysis, it was highlighted the role of oxidants as molecular oxygen but also of the hydrogen peroxide usage in the reaction development. In the absence of catalyst, the rate of autoxidation in the presence of both oxidants was of 12 %²¹³, which justified their influence in the catalyst rather than in the substrate oxidation. Both oxidants and the temperature, play a key role in the reaction development. The inert atmosphere allowed the conversion in a 30% (Table 12, entry 6 and 8) while air transformed **1a** in a 66% and 62%, respectively (Table 12, entry 7 and 5). The temperature also increased the conversion rate from a 42% at 27°C to an 82% at 50°C (Table 12, entries 1 and 3). Finally, changing from 2 to 3 hours of reaction we obtained a quantitative conversion.

The optimized conditions consist of the use of CPME as solvent, hydrogen peroxide as sacrificial oxidant and an oxygen atmosphere at 50 °C for 3 hours.

1.3 Flow system implementation and optimized conditions.

With these preliminary results in batch, we designed and assembled the flow system that is constituted by three main elements: (I) an oxygen line acting as driving force to push the reaction mixture through the reactor system, (II) a reagent reservoir in which the line tube is introduced below the solvent level to push the reaction mixture of the starting material dissolved in CPME and hydrogen peroxide under stirring, (III) a PTFE tube (15 cm length) acting as reactor at a constant temperature of 50 °C in which the catalyst K-OMS-2 (70 mg) was safely packed with inert crystal balls, and finally (IV) the collector test tube.

Then, we optimized the operating pressure in order to obtain a shorter residence time, but enough to have full conversion. Thus, varying the inlet pressure of oxygen and the back pressure regulator (BPR) inserted between the reactor and the collector, we could measure the residence time and the percentage of product conversion by GLC analysis. As a result of the best heat transfer and reaction mixture in the flow system, it was allowed to reduce the reaction time from 3 hours in batch (Table 12, entry 4) to 30 min in flow (Table 13, entry 5).



Entry	O ₂ (bar)	BPR	Residence time	Conversion ^a (%)
1	1	5 psi	10 min	85
2	2	5 psi	7 min	80
3	3	45 psi	15 min	90
4	4	45 psi	12 min	88
5	5	75 psi	30 min	97

Entry	[Aminophenol]	Conversion ^a (%)	Yield
6	0.25 M	97	97%
7	0.50 M	> 99	> 99%
8	1 M	> 99	92%
9	1.5 M	> 99	87%

Reaction conditions: 1a (1 mmol), CPME, (3 mmol, 3 eq) of H₂O₂, KOMS-2 (70 mg, 62% Mn loading), 50 °C, O₂ pressure and concentration (M) as specified in the table.

^a The conversion was measured by GLC analyses using samples of pure compounds as a reference.

Table 13. Screening of oxygen pressure and concentration in flow.

Limits were found in the concentration of starting material used. In fact, higher concentrations caused precipitation of the product and therefore the reactor blocking, as well as the poisoning of the catalyst. Even if higher concentrated solutions of the substrate are desirable, as less solvent is employed and less waste is produced, we observed that in solutions of up to 0.5 M concentration, part of the product precipitated in the reactor. Consequently, it was necessary the use of larger amounts of solvent to dissolve it and clean the system.

Moving from 0.25 M to 0.50 M, the process efficiency increased (Table 13, entry 6 and 7), while at higher concentrations the outcome was less satisfactory (Table 13, entry 8 and 9). The need to preheat the reservoir to ensure solubility and the amount of solvent to clean the system (4 mL x 4 of CPME) pointed out the limits of the system to afford concentrations up to 0.5 M.

Optimal conditions were therefore obtained when a solution of 0.5 M of the substrate in CPME at 50 °C and 5 bar of oxygen using a 75 psi back pressure was allowed to react.

1.4 Plausible catalytic mechanism.

Based on the literature and the obtained results, we have proposed a plausible mechanism for the K-OMS-2 mediated oxidative process (Figure 51). Initially, hydrogen peroxide induces the formation of the electrophilic species quinone-iminium ion (II) which readily reacts with an additional 2-aminophenol molecule via 1,4-addition (*Michael addition*) to form p-quinone imine (III). This key intermediate undergoes a manganese insertion (VI) followed by reductive elimination to give the corresponding 2-aminophenoxazin-3-one. The oxidative capacity of the catalyst can be recovered due to the continuous O₂ supply and the added H₂O₂ to the system, maintaining the optimal mixed-manganese oxide network. To give further evidence, XRD and HRTEM analysis for the fresh and used catalyst were done, showing the integrity of the three-dimensional structure, and highlighting its appropriate reusability without loss of efficiency (See experimental part A. 6.).

This mechanism agrees with the general mechanism found in metal catalysis in which a C-H/C-O bond is assembled, along with the formation of organometallic intermediates as (IV) that finally led to the product by reductive elimination.^{207,215-216}

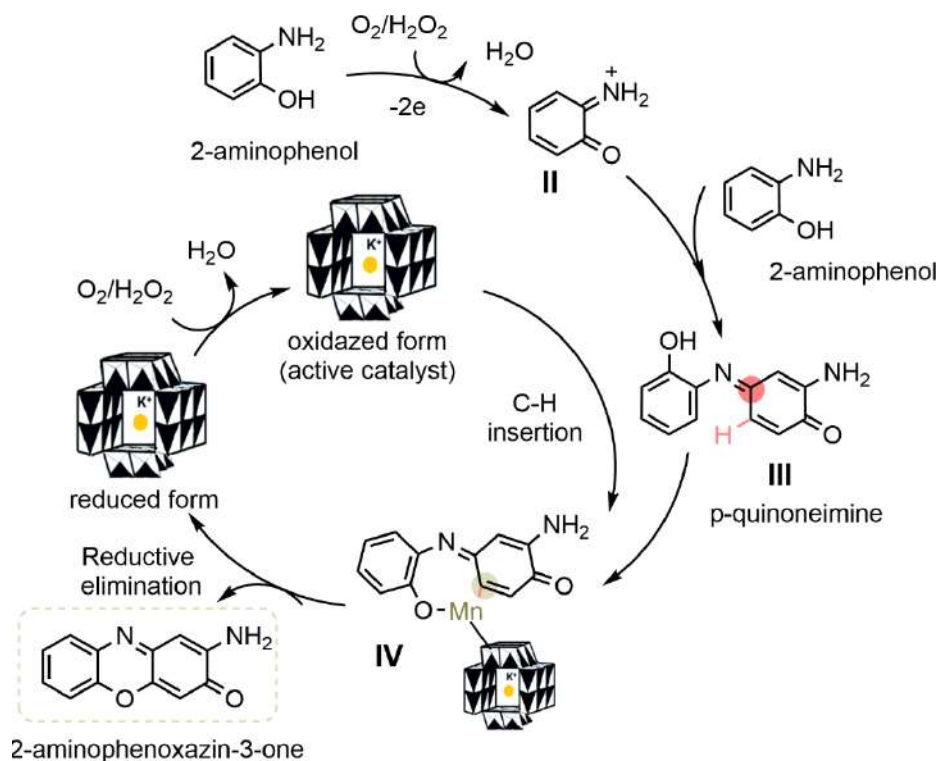
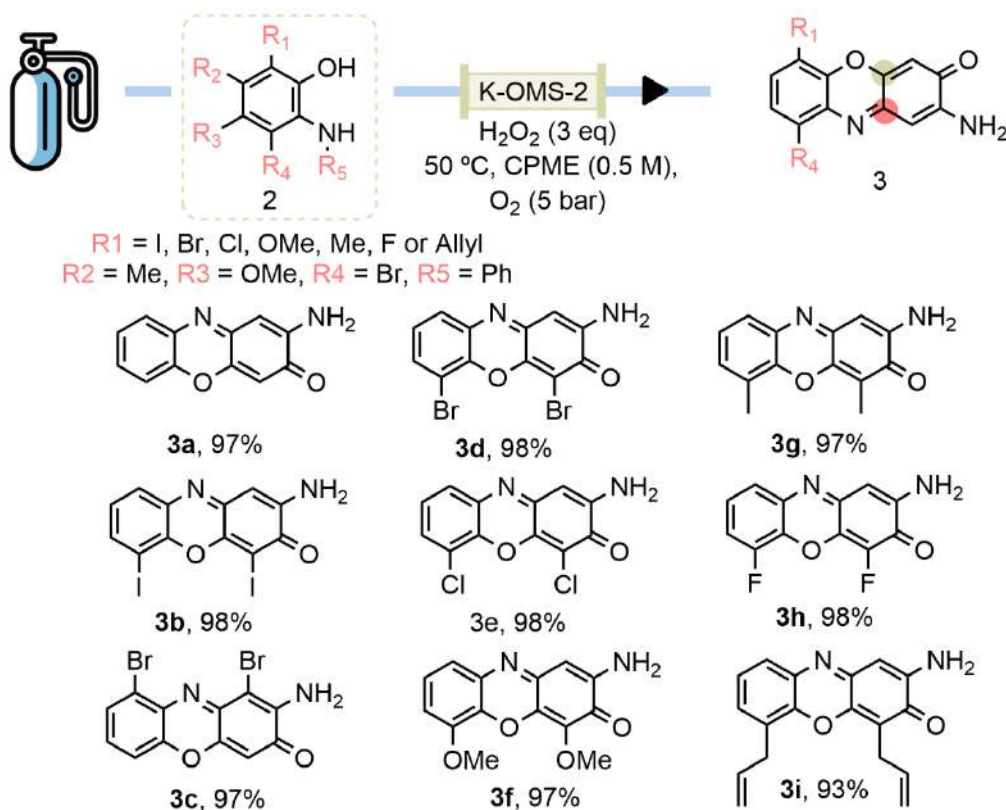


Figure 51. Plausible catalytic mechanism.

1.5 Flow system regioselectivity and versatility.

We next further investigated the scope of the flow system using a variety of substituted 2-aminophenols (**2a** to **2l**) (for its synthesis see experimental part A. 1.). In most of the studied cases, we found that our flow conditions were very efficient leading to the synthesis of the corresponding products in high yields without the detection of any side products. However, only substrates substituted in **R1** and **R4** were allowed to react (Scheme 16). Substrates **2j** and **2k**, **R2** and **R3** substituted, were unable to react because the **R3** position is necessary to form the p-quinone imine (intermediate of reaction) in **2k** and the inability to eliminate the **R2**-substituent in the C-H coupling reaction of **2j**, necessary to lead the final cyclization.



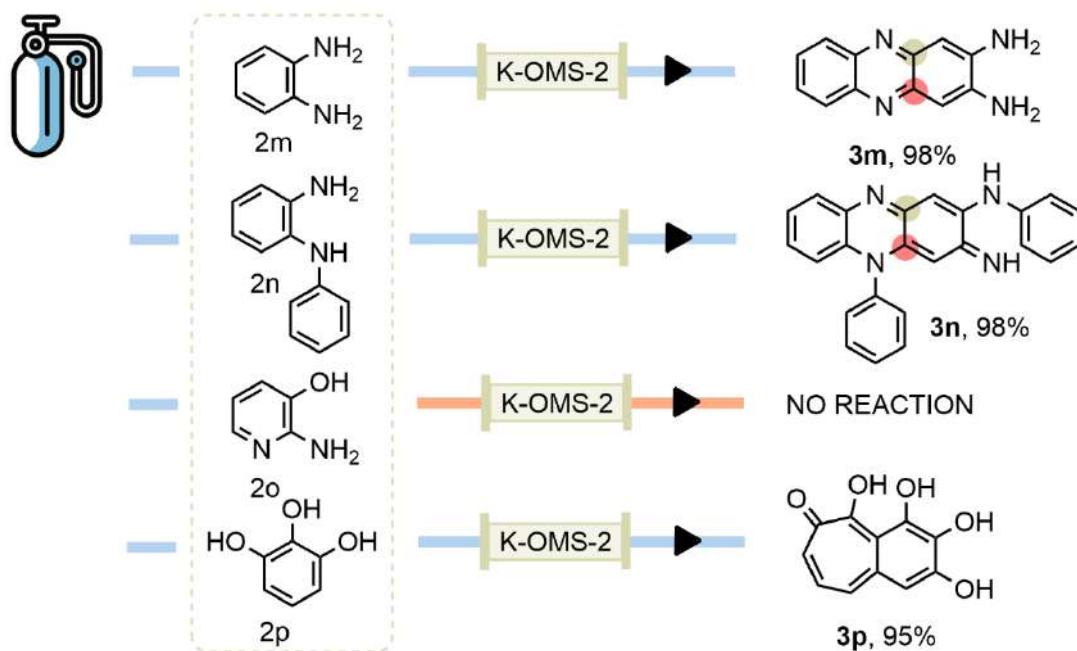
Scheme 16. Substrates scope using substituted aminophenols.

The simplified starting material structure **2** is substituted only in one position in each assay. If the substitution is **R1** = OMe, the rest of positions **R 2,3,4,5** = H.

Remarkably, the presence of halogen atoms in the core structure constituted an excellent starting point to get complex structures with antibiotic or anti-tumour properties.

With the goal to test the enzyme mimicking capability of the K-OXS-2 catalyst, we used substrates that are commonly transformed by the HRP (Horseradish peroxidase) enzyme. To this end, we used other heterocyclic scaffolds as the synthesized o-phenylenediamine derivatives (**2m**, **2n**) and 2-aminopyridin-3-ol (**2o**) (see experimental part A. 1.). Successfully our system quantitatively transforms compounds **2m** and **2n**. However, the most nucleophile pyridine scaffold (**2o**) was unable to react (Scheme 17).

The fact that **2n** but not **2l** (**R5** aminophenol substituted) reacts, could be due to the higher nucleophilicity of the NH rather than the OH group that is able to attack the para position of the imine group. All the substrates tested, showed high regioselectivity so that the nucleophilic 1,4 addition of aminophenols takes place in the imine β -carbon independently of the electron-withdrawing or electron-donating nature of the **R** group.



Reaction conditions: H_2O_2 (3 eq), 50 °C, CPME (0.5 M), O_2 (5 bar)

Scheme 17. Enzymatic substrates of HRP.

Finally, it was also tested the HRP naturally oxidized substrate pyrogallol, available from commercial sources (Scheme 17, **2p**). We found out that our catalytic system was able to effectively convert the pyrogallol to purpurogallin²¹⁸ in excellent yields, supporting its capability to replace enzymatic-catalysed reactions.

1.6 Big scale reaction and metal leaching.

To ensure the competitiveness of the flow system we carried out the conversion of 50 mmol of the substrates (**2a** to **2i**, **2m**, **2n** and **2p**) adding sequentially 2 mmol in 4 mL of CPME (0.5 M solutions) to avoid the poisoning of the catalyst and recharging the reservoir when empty. The product was recovered at a constant rate in the collector with a 98% - 99% yield after the solvent removal under reduced pressure (see experimental part A. 5.).

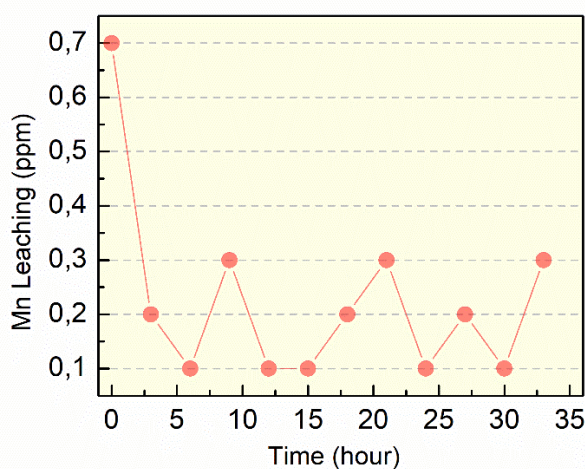


Figure 52. Manganese leaching in flow.

Interestingly, the obtained products could be also isolated by simply precipitation under cooling, and the solvent can be reused by the system.

The metal leaching was also periodically measured during the flow procedure to determine the stability and efficiency of the packed heterogeneous catalyst. After an initial release of the metal of 0.7 ppm, it was stabilized around 0.17 ppm, so that the product is minimally contaminated by the metal and there is no need for additional purification steps (Figure 52).

1.7 Green metrics comparison for batch and flow processes.

In an attempt to highlight the beneficial effect of the flow system in comparison with the optimized conditions in batch, we calculated several green metrics for both systems with and without the recirculation of solvent. We analysed the E-factor, the Atom Economy (AE) and the Turnover Number and Frequency (TON and TOF) of the catalyst.

The E-factor is a measure of the waste generated by a chemical process. For that reason, values closer to zero are desirable when evaluating a reaction.

There is a considerable improvement in the E-factor value with the flow system implementation in comparison to the batch process. In addition, the recovery and recirculation of the solvent decrease the environmental values to 6 kg of waste per kg of product in batch and 4 kg of waste per kg of product in flow (Figure 53).

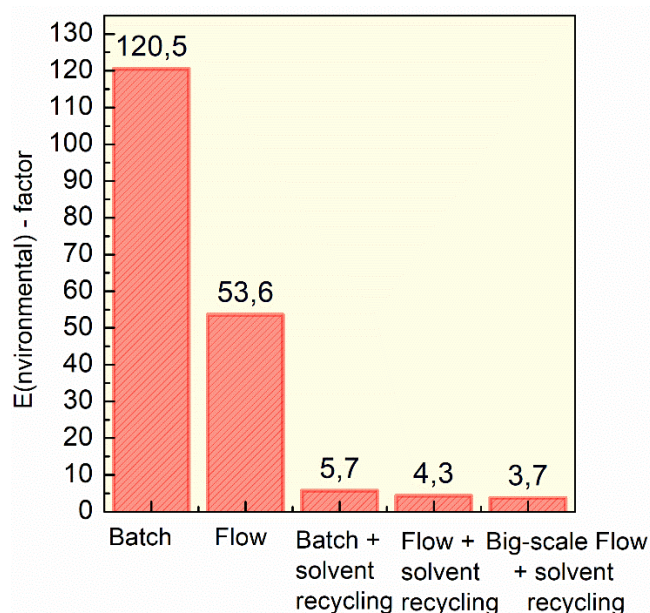


Figure 53. E-factor of flow and batch procedures, with and without the recirculation of solvents.

When was evaluated the big-scale flow procedure, we get an E-factor of **3.7**, which turned out to be a very competitive process, even after a longer usage, in comparison to synthetic procedures found in the literature (*ACS Sustainable Chem. Eng.*, 2019, 74, 4414-4419 and *Tetrahedron Letters*, 2015, 56, 6104–6107), which shows **92** and **418** E-factor values, respectively (See experimental part A. 7.).

On the other hand, the AE defines the conversion efficacy of the reactants into products. Our reaction showed an AE of 97%, which means that a 97% of the reactant's atoms were incorporated into the product. This fact is in accordance with the formal loss of two hydrogen atoms during the oxidative C-H coupling.

Finally, we evaluated the catalyst performance by calculating the Turnover Number and Turnover Frequency (TON and TOF) for both, the batch and flow processes (see experimental part A. 7.).

Considering the use of 2 mol % of K-OMS-2 in batch and the 0.8 mmol of catalyst packed in flow, we obtained a $\text{TON}_{\text{BATCH}} = 50$ and a $\text{TON}_{\text{FLOW}} = 1.6$, which refers to the conversion per unit of catalyst. If we take into account the conversion per unit of time, $\text{TOF}_{\text{BATCH}} = 16.6 \text{ h}^{-1}$ and $\text{TOF}_{\text{FLOW}} = 3.2 \text{ h}^{-1}$. However, the possibility to apply the flow at a continuous rate as in the big-scale process (for 25 hours), enhanced the TON outcome to **80**.

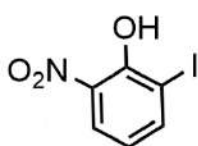
In conclusion, those results support the superiority of our catalytic system in comparison to enzymatic reactions. It has shown to be more robust in terms of temperature and solvent usage, and what is more important, reusable due to the use of an oxygen stream that preserves the catalyst active form allowing an on-flow regeneration.

Experimental part A: Green flow chemistry process

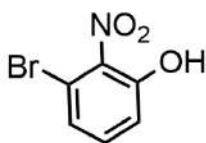
1. Synthesis and characterization of the starting materials.

The *ortho*-aminophenols used as starting materials were obtained by the nitration and the consecutive reduction to amine of the substituted phenolic derivatives. Only the *2-aminophenol* used for the synthesis of **3a** was commercially available.

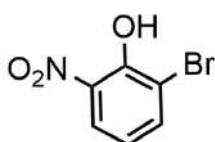
The nitration procedure was taken from the literature.²¹⁹ The corresponding 1-substituted phenol (10.1 mmol, 1eq) was dissolved in acetic acid (23 mL, 0.38 mmol, 0.037 eq) and water (2.3 mL, 0.13 mmol, 0.013 eq). After cooling at 5 °C in an ice/water bath, fuming HNO₃ (0.5 mL, 0.008 mmol) in acetic acid (4.5 mL, 0.075 mmol) was added dropwise. The mixture was stirred for 15 min at 5 °C and then water was added. Finally, the reaction was extracted with dichloromethane (x3) and the organic layers were dried over Na₂SO₄, filtered and the solvent was evaporated under reduced pressure. As result, *para*- and *ortho*-nitro regioisomers are obtained, which are separated by chromatographic column. The desired *ortho*-nitrophenols are obtained in low yields from 16% to 39%.



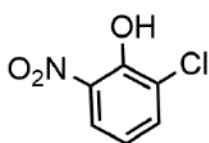
2-iodo-6-nitrophenol (1b). The product was obtained using 2-iodophenol (4.44 g, 20.2 mmol) as starting material and after column chromatographic purification (Hexane and increasing the polarity until 9Hexane/1EtOAc) as a yellow solid (1906 mg, 7.2 mmol), yield: 36%, melting point: 87 °C – 89 °C. ¹H-NMR (200 MHz, chloroform-*d*): δ 11.38 (s, 1H, -OH), 8.14 (d, *J* = 8 Hz, 1H), 8.09 (d, *J* = 8 Hz, 1H), 6.81 (t, *J* = 8.5 Hz, 1H). The characterized product is in accordance with the literature.²²⁰



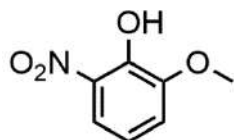
3-bromo-2-nitrophenol (1c). The product was obtained using 3-bromophenol (3.5 g, 20.18 mmol) as starting material and after column chromatographic purification (8Hexane/2EtOAc) as a yellow solid (703 mg, 3.2 mmol), yield: 16%, melting point: 65 °C - 67 °C. ¹H-NMR (400 MHz, chloroform-*d*): δ 10.62 (s, 1H, -OH), 7.98 (d, *J* = 9.0 Hz, 1H), 7.38 – 7.35 (m, 1H), 7.14 (dd, *J* = 9.1, 2.1 Hz, 1H).



2-bromo-6-nitrophenol (1d). The product was obtained using 2-bromophenol (1.75 g, 10.1 mmol) as starting material and after column chromatographic purification (9Hexane/1EtOAc increasing the polarity until 8Hexane/2EtOAc) as a yellow solid (864 mg, 3.9 mmol), yield: 39%, melting point: 65 °C – 70 °C. ¹H-NMR (400 MHz, chloroform-*d*): δ 11.17 (s, 1H, -OH), 8.11 (dd, *J* = 8.6, 1.6 Hz, 1H), 7.88 (dd, *J* = 7.8, 1.6 Hz, 1H), 6.92 (t, *J* = 8.2 Hz, 1H). The characterized product is in accordance with the literature.²²¹

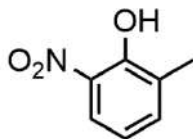


2-chloro-6-nitrophenol (1e). The product was obtained using 2-chlorophenol (3 g, 23.3 mmol) as starting material and after column chromatographic purification (2Hexane/1EtOAc) as a yellow solid (1323 mg, 7.6 mmol), yield: 33%, melting point: 65 °C – 67 °C. ¹H-NMR (400 MHz, chloroform-*d*): δ 11.04 (s, 1H, -OH), 8.07 (dd, *J* = 8.0, 1.4 Hz, 1H), 7.71 (dd, *J* = 8.0, 1.4 Hz, 1H), 6.73 (m, 1H). The characterized product is in accordance with the literature.²²²

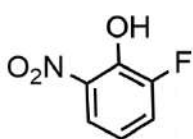


2-methoxy-6-nitrophenol (1f). The product was obtained using 2-methoxyphenol (3 g, 24.2 mmol) as starting material and after column chromatographic purification (4Hexane/1EtOAc) as an orange solid (690 mg, 4.1 mmol), yield: 17%, melting point: 58 °C – 60 °C. ¹H-NMR (200 MHz,

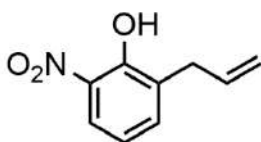
chloroform-*d*): δ 10.79 (s, 1H, -OH), 7.70 (dd, $J = 8.7, 1.5$ Hz, 1H), 7.15 (dd, $J = 8.0, 1.2$ Hz, 1H), 6.92 (t, $J = 8.4$ Hz, 1H), 3.96 (s, 3H, O-CH₃). The characterized product is in accordance with the literature.²²³



2-methyl-6-nitrophenol (1g). The product was obtained using o-cresol (3 g, 27.7 mmol) as starting material and after column chromatographic purification (9Hexane/1EtOAc) as a yellow solid (1625 mg, 10.6 mmol), yield: 38%, melting point: 65 °C – 69 °C. **¹H-NMR** (400 MHz, chloroform-*d*): δ 10.92 (s, 1H, -OH), 7.96 (d, $J = 8.6$ Hz, 1H), 7.45 (d, $J = 7.2$ Hz, 1H), 6.88 (t, $J = 7.9$ Hz, 1H), 2.33 (s, 3H, -CH₃). The characterized product is in accordance with the literature.²²²



2-fluoro-6-nitrophenol (1h). The product was obtained using 2-fluorophenol (3 g, 26.8 mmol) as starting material and after column chromatographic purification (increasing the polarity from Hexane to 9Hexane/1EtOAc) as a brown/red solid (904 mg, 5.8 mmol), yield: 22%, melting point: 90 °C – 92 °C. **¹H-NMR** (200 MHz, DMSO-*d*₆): δ 11.39 (s, 1H, -OH), 7.74 (d, $J = 9.1$ Hz, 1H), 7.53 (d, $J = 8.2$ Hz, 1H), 7.00 (t, $J = 8.6$ Hz, 1H). The characterized product is in accordance with the literature.²²⁴

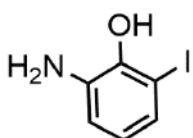


2-allyl-6-nitrophenol (1i). The product was obtained using 2-allylphenol (3 g, 22.4 mmol) as starting material and after column chromatographic purification (2Hexane/1EtOAc) as an orange oil (1019 mg, 5.7 mmol), yield: 25%. **¹H-NMR** (400 MHz, chloroform-*d*): δ 10.90 (s, 1H, -OH), 7.99 (d, $J = 8.6$ Hz, 1H), 7.46 (d, $J = 7.3$ Hz, 1H), 6.92 (t, $J = 8.0$ Hz, 1H), 6.03 – 5.93 (m, 1H), 5.13 – 5.09 (m, 2H), 3.48 (d, $J = 6.5$ Hz, 2H). The characterized product is in accordance with the literature.²²⁵

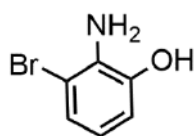
Following the retrosynthetic pathway, it was carried out the reduction of the nitro group using two different methodologies.

Procedure 1: To a solution of the nitro-derivative (25.5 mmol, 1 eq) in methanol (128 mL) was added zinc (dust) (16.71 g, 255 mmol, 10 eq). The reaction mixture was cooled to 0 °C in an ice/water bath followed by the addition of ammonium chloride (13.67 g, 255 mmol, 10 eq) portion-wise over 5 min. The heterogeneous mixture was allowed to reach room temperature and then was stirred for 30 min. The reaction was filtered through a plug of celite, and the solvent was evaporated under pressure. The obtained crude was extracted with EtOAc/H₂O/brine (x2). The organic layers were collected, dried with Na₂SO₄, filtered, and evaporated under reduced pressure.²²⁶

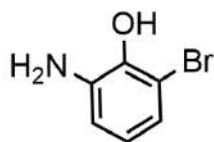
Procedure 2: In a sealed tube was added the nitro-derivative (0.5 mmol, 1 eq), methanol (5 mL) and palladium on carbon (0.01 mmol, 10% wt). Once closed the reactor was purged three times with hydrogen. The reaction was left under stirring at 1 bar from 30 to 45 min at room temperature. Then, the reaction vessel was opened, and the reaction solution was filtered through a plug of celite. The solvent was evaporated under reduced pressure and the crude was purified by column chromatography.²²⁷



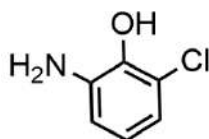
2-amino-6-iodophenol (2b). The product was obtained following *procedure 1* with 1b (1366 mg, 5.2 mmol) as substrate, and after column chromatographic purification (in CH₂Cl₂) as an orange solid (416 mg, 1.77 mmol), yield: 34%, melting point: 100 °C - 105 °C. **¹H-NMR** (200 MHz, MeOD): δ 7.02 (dd, $J = 7.9, 1.5$ Hz, 1H), 6.7 (dd, $J = 7.8, 1.5$ Hz, 1H), 6.44 (t, $J = 7.9$ Hz, 1H).



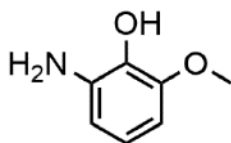
2-amino-3-bromophenol (2c). The product was obtained following *procedure 1* with 1c (403 mg, 1.8 mmol) as substrate, and after column chromatographic purification (3Hexane/2EtOAc) as a brown solid (151 mg, 0.8 mmol), yield: 43%, melting point: 138 °C. ¹H-NMR (400 MHz, chloroform-*d*): δ 7.04 (dd, J = 8.1 Hz, 1.0 Hz, 1H), 6.67 (dd, J = 7.9 Hz, 1.0 Hz, 1H), 6.53 (t, J = 8.0 Hz, 1H). The characterized product is in accordance with the literature.²²⁸



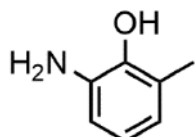
2-amino-6-bromophenol (2d). The product was obtained following *procedure 1* with 1d (1.5 g, 6.9 mmol) as substrate, and after column chromatographic purification (1Hexane/1EtOAc) as a black solid (601 mg, 3.2 mmol), yield: 46%, melting point: 84 °C – 86 °C. ¹H-NMR (400 MHz, MeOD): δ 6.80 (d, J = 8.0 Hz, 1H), 6.69 (d, J = 7.9 Hz, 1H), 6.57 (t, J = 7.9 Hz, 1H). The characterized product is in accordance with the literature.²²⁹



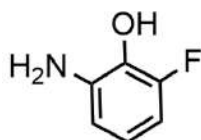
2-amino-6-chlorophenol (2e). The product was obtained following *procedure 1* with 1e (1271 mg, 7.3 mmol) as substrate, and after column chromatographic purification (2Hexane/1EtOAc) as a yellow/brown solid (632 mg, 4.4 mmol), yield: 60%, melting point: 70 °C – 73 °C. ¹H-NMR (400 MHz, chloroform-*d*): δ 6.76 – 6.70 (m, 1H), 6.68 (d, J = 8.0 Hz, 1H), 6.62 (d, J = 7.4 Hz, 1H), 5.48 (s, 1H), 3.85 (bs, 2H, -NH₂). The characterized product is in accordance with the literature.²³⁰



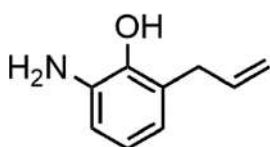
2-amino-6-methoxyphenol (2f). The product was obtained following *procedure 2* with 1f (616 mg, 3.6 mmol) as substrate, and after column chromatographic purification (1Hexane/1EtOAc) as a light brown solid (456 mg, 3.3 mmol), yield: 90%, melting point: 84 °C – 86 °C. ¹H-NMR (200 MHz, chloroform-*d*): δ 6.69 (t, J = 8.1 Hz, 1H), 6.41 (dd, J = 8.1, 0.9 Hz, 1H), 6.37 (dd, J = 8.3, 1.1 Hz, 1H), 3.85 (s, 3H, O-CH₃). The characterized product is in accordance with the literature.²³¹



2-amino-6-methylphenol (2g). The product was obtained following *procedure 2* using 3 bar of pressure, with 1g (1462 mg, 9.5 mmol) as substrate, and after column chromatographic purification (2Hexane/1EtOAc) as a pink solid (833 mg, 6.76 mmol), yield: 71%, melting point: 87 °C – 89 °C. ¹H-NMR (400 MHz, CD₃CN): δ 6.59 (t, J = 7.6 Hz, 1H), 6.53 (d, J = 8.0 Hz, 1H), 6.45 (d, J = 7.2 Hz, 1H), 3.95 (bs, 2H, -NH₂), 2.16 (s, 3H, -CH₃). The characterized product is in accordance with the literature.²³²

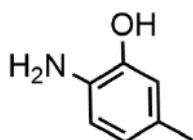


2-amino-6-fluorophenol (2h). The product was obtained following *procedure 1* with 1h (890 mg, 5.7 mmol) as substrate, and after column chromatographic purification (1Hexane/1EtOAc) as a grey solid (508 mg, 4 mmol), yield: 71%, melting point: 110 °C – 115 °C. ¹H-NMR (400 MHz, chloroform-*d*): δ 6.71 – 6.62 (m, 1H), 6.51 (d, J = 8.0 Hz, 2H), 4.04 (bs, 2H, -NH₂). The characterized product is in accordance with the literature.²³³

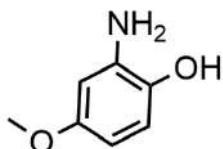


2-allyl-6-aminophenol (2i). The product was obtained following *procedure 1* using 3 eq of NH₄Cl, with 1i (510 mg, 2.8 mmol) as substrate, and after column chromatographic purification (1Hexane/1EtOAc) as a dark oil (186 mg, 1.2 mmol), yield: 44%. ¹H-NMR (400 MHz, chloroform-*d*): δ 6.74 (t, J = 7.6 Hz, 1H), 6.68 (dd, J = 7.8, 1.8 Hz, 1H), 6.57 (dd, J = 7.4, 1.8 Hz, 1H), 6.10 – 5.95 (m, 1H), 5.26 – 5.17 (m, 2H), 3.39 (dd, J = 6.3, 1.7 Hz, 2H).

It was also used aminophenols substituted in other positions to evaluate how the coupling was affected by the hindrance in the ring.

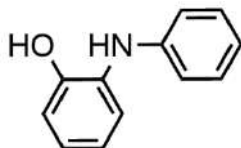


2-amino-5-methylphenol (2j). The product was obtained following *procedure 2* with the already available 5-methyl-2-nitrophenol (500 mg, 3.3 mmol) as substrate, and after column chromatographic purification (1Hexane/1EtOAc) as a yellow solid (277 mg, 2.2 mmol), yield: 69%, melting point: 157 °C – 159 °C. ¹H-NMR (200 MHz, chloroform-*d*): δ 7.27 (s, 1H), 6.70 (d, *J* = 8.3 Hz, 1H), 6.60 (d, *J* = 5.5 Hz, 1H), 2.23 (s, 3H, -CH₃). The characterized product is in accordance with the literature.²³⁴



2-amino-4-methoxyphenol (2k). The product was obtained following *procedure 2* using 1.5 bar of pressure, with the already available 4-methoxy-2-nitrophenol (500 mg, 2.9 mmol) as substrate, and after column chromatographic purification (1CH₂Cl₂/1EtOAc) as a brown solid (307 mg, 2.2 mmol), yield: 75%, melting point: 135 °C – 140 °C. ¹H-NMR (200 MHz, chloroform-*d*): δ 6.67 (d, *J* = 8 Hz, 1H), 6.35 (d, *J* = 2 Hz, 1H), 6.2 (dd, *J* = 8, 2 Hz, 1H), 3.71 (s, 3H, -CH₃). The characterized product is in accordance with the literature.²³⁵

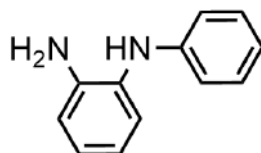
Compound **2i** was synthesized following the reported procedure from the literature.²³⁶ A flame dried flask containing a magnetic stir bar was charged under argon with 2-aminophenol (160 mg, 1.47 mmol, 1eq), phenyl iodide (82 μL, 0.73 mmol, 0.5 eq), CuI (27.9 mg, 0.14 mmol, 0.1 eq), Na₃PO₄·12H₂O (557.3 mg, 1.47 mmol, 1 eq) and DMF (1.48 mL, 19 mmol, 13 eq). The mixture was left at 80 °C for 16 hours and then was allowed to cool to room temperature. The resulting mixture was acidified with HCl (2N) to adjust the pH to 6. The aqueous fraction was extracted with EtOAc (x3). The combined organic layers were dried with Na₂SO₄, filtered, and concentrated in vacuo. The resulting residue was purified by column chromatography on aluminium oxide (from 3Hexane/1EtOAc to just EtOAc).



2-(phenylamino)phenol (2l). The product was obtained as a dark brown oil (105 mg, 0.6 mmol), yield: 39%. ¹H-NMR (400 MHz, chloroform-*d*): δ 7.26 – 7.15 (m, 3H), 7.10 (t, *J* = 7.7 Hz, 1H), 6.99 (d, *J* = 7.6 Hz, 1H), 6.89 (q, *J* = 6.8 Hz, 2H), 6.78 (d, *J* = 8.7 Hz, 2H), 5.76 (bs, 1H), 5.25 (bs, 1H). The characterized product is in accordance with the literature.²³⁶

Finally, different heterocyclic substrates were synthesized to test the catalyst ability to mimic the conversion of some HRP's enzymatic substrates. Only the *o*-phenylenediamine (**2m**) was already available from commercial sources.

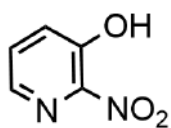
Compound **2n** was synthesized following the reported procedure from the literature.²³⁷ To a microwave vessel was added iodobenzene (136 μL, 1.22 mmol, 0.66 eq), 1,2-diaminobenzene (200 mg, 1.8 mmol, 1 eq), NiCl₂·6H₂O (15.8 mg, 0.12 mmol, 0.06 eq) and triethylamine (240 μL, 1.7 mmol, 0.9 eq). The sealed tube was subjected to microwave exposure for 20 min at 300 W or 150 °C. After the reaction was complete, the crude was diluted in CH₂Cl₂ and filtered to separate the catalyst. The filtered was concentrated and subjected to column chromatography with silica gel and a polarity of 5% EtOAc in Hexane.



1N-phenylbenzene-1,2-diamine (2n). The product was obtained as an orange solid (94 mg, 0.5 mmol), yield: 28%, melting point: 77 °C – 79 °C. ¹H-NMR (400 MHz, chloroform-*d*) δ 6.61 – 6.45 (m, 2H), 6.40 (d, *J* = 7.8 Hz, 1H), 6.29 (t, *J* = 7.6 Hz, 1H), 6.09 (t, *J* = 7.3 Hz, 3H), 6.02 (t, *J* = 7.8 Hz, 2H), 4.45 (bs, 1H, -NH-), 3.06 (bs, 2H, -NH₂). The characterized product is in accordance with the literature.²³⁸

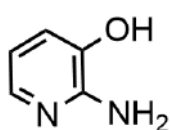
The last synthesized substrate (**2o**) was obtained in a two-step synthesis, starting with the nitration of the available *pyridin-3-ol* and its later reduction as follows:

Compound **1o** was synthesized following the reported procedure from the literature.²³⁹ In a flask under ice-cooling was added pyridin-3-ol (1250 mg, 13.1 mmol, 1 eq) in 11 mL of concentrated sulfuric acid (205.2 mmol, 15.6 eq). Next, 0.7 mL of concentrated nitric acid (16.77 mmol, 1.28 eq) was added at 0 °C over a period of 5 min. The reaction was warmed to room temperature and stirred overnight. Then, the reaction mixture was added to 25 g of ice and stirred for 30 min. The aqueous solution was extracted with CH₂Cl₂ (x3) and the collected organic fractions were dried with Na₂SO₄, filtered, and evaporated under reduced pressure.



2-nitropyridin-3-ol (1o). The product was obtained as a light-yellow solid (1584 mg, 11.3 mmol), yield: 86%, melting point: 69 °C – 70 °C. ¹H-NMR (400 MHz, chloroform-*d*): δ 10.23 (s, 1H), 8.21 (dd, *J* = 3.8, 1.8 Hz, 1H), 7.69 – 7.58 (m, 2H). The characterized product is in accordance with the literature.²⁴⁰

The consecutive reduction was done following *procedure 1* with **1o** (250 mg, 1.78 mmol) as substrate, and letting the reaction stir overnight instead of for 30 min.



2-aminopyridin-3-ol (2o). The product was obtained without further purification as a yellow oil (117 mg, 1.1 mmol), yield: 60%. ¹H-NMR (400 MHz, DMSO-*d*₆): δ 7.41 (dd, *J* = 5.5, 1.4 Hz, 1H), 7.03 (dd, *J* = 7.6, 1.4 Hz, 1H), 6.49 (dd, *J* = 7.6, 5.5 Hz, 1H), 6.32 (bs, 1H), 3.38 (bs, 2H). The characterized product is in accordance with the literature.²⁴¹

2. General procedure for the K-OMS-2 synthesis.

A solution of 5.89 g of KMnO₄ in 100 mL of water was added to a solution of 8.8 g of MnSO₄·H₂O in 30 mL of water and 3 mL concentrated HNO₃. The solution was refluxed at 100 °C for 24 h, and the product was filtered, washed with distilled water (300 mL), and dried at 120 °C. The resulting material was further calcinated at 350 °C over a period of 4h. Finally, the black stony material was finely grounded using a mortar and filtered using size exclusion sieves yielding 13 g of K-OMS-2 catalyst. Powder X-ray diffraction data were collected (Figure 54) to confirm the structure of the material.²⁴²

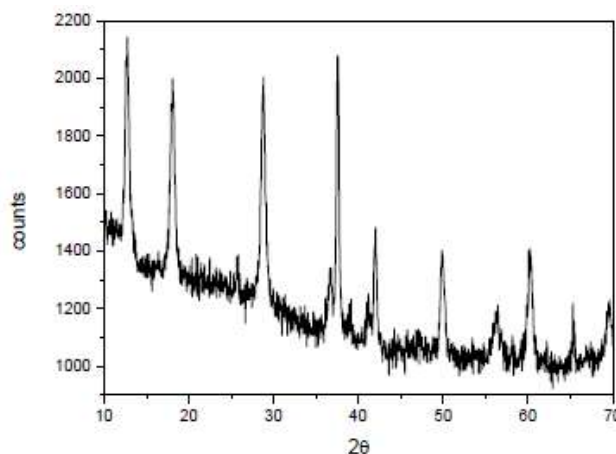


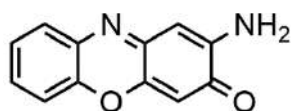
Figure 54. X-ray diffraction path for K-OMS-2.

3. General procedure used in the batch reaction optimization.

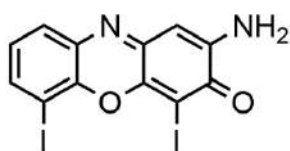
To a 10 mL vial were added the 2-aminophenol (109 mg, 1 mmol, 1 eq), the solvent 4 mL, and H₂O₂ 30% w/w in H₂O (304 μL, 3 mmol, 3 eq), followed by K-OMS-2 62% w/w Mn-loading (1.8 mg, 2 mol%, 0.02 eq). The vial was capped with a septum and wrapped with Parafilm and then, it was equipped with an O₂ balloon. The reaction mixture was stirred for the time and temperatures indicated in (Table 12 in the main text). The heterogeneous mixture was filtered over a short pad of silica eluting with the same solvent used in the reaction (2 x 5 mL). The solvent was removed under reduced pressure to afford the products.

4. General procedure used in flow synthesis and final products characterization.

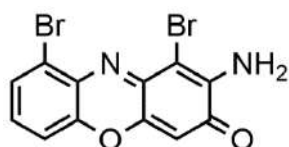
The reservoir was charged with 2 mL of CPME, the aminophenol derivative (1 mmol, 1eq), followed by H₂O₂ (304 μL, 3 mmol, 3eq). Then, the oxygen line has been set to the desired pressure and the reaction mixture started to flow through the K-OMS-2 filled reactor (filled with 70 mg of K-OMS-2). Once the reagents reservoir has been completely emptied, the system has been rinsed with CPME (2 x 2 mL). The product has been collected into the product reservoir. The CPME was recovered via distillation under reduced pressure to afford the pure product (from 93 to 98% yield).



2-amino-3H-phenoxazin-3-one (3a). The product was obtained following the flow general procedure with the 2-aminophenol starting material (109 mg, 1 mmol), and without further purification as a red powder (103 mg, 0.49 mmol), yield: 97%, melting point: 255 °C – 257 °C. **¹H-NMR** (400 MHz, DMSO-*d*₆): δ 7.70 (d, *J* = 7.6 Hz, 1H), 7.53 – 7.43 (m, 2H), 7.4 – 7.37 (m, 1H), 6.80 (s, 2H, NH₂), 6.38 – 6.36 (m, 2H). **¹³C-NMR** (101 MHz, DMSO-*d*₆): δ 180.63 (1C, -C-), 149.29 (1C, -C-), 148.65 (1C, -C-), 147.78 (1C, -C-), 142.33 (1C, -C-), 134.13 (1C, -C-), 129.22 (1C, -CH-), 128.38 (1C, -CH-), 125.69 (1C, -CH-), 116.35 (1C, -CH-), 103.84 (1C, -CH-), 98.76 (1C, -CH-). **FT-IR:** 3432, 3407, 1604, 1580, 1472, 1420, 1278, 1121, 1106, 1054 cm⁻¹. **GC-EIMS** (m/z %): 212 (100), 185 (75), 157 (20), 144 (25), 129 (20), 102 (20), 76 (35). The characterized product is in accordance with the literature.²⁴³

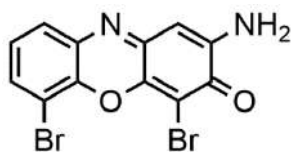


2-amino-4,6-diiodo-3H-phenoxazin-3-one (3b). The product was obtained following the flow general procedure with **2b** (470 mg, 2 mmol) as substrate, and without further purification as a red powder (454 mg, 0.98 mmol), yield: 98%, melting point: 257 °C – 260 °C. **¹H-NMR** (400 MHz, DMSO-*d*₆): δ 7.96 (dd, *J* = 7.8, 1.4 Hz, 1H), 7.73 (dd, *J* = 8.0, 1.4 Hz, 1H), 7.23 (t, *J* = 7.9 Hz, 1H), 7.06 (s, 2H, NH₂), 6.38 (s, 1H). **¹³C-NMR** (101 MHz, DMSO-*d*₆): δ 176.63 (1C, -C-), 151.13 (1C, -C-), 148.45 (1C, -C-), 146.57 (1C, -C-), 142.86 (1C, -C-), 138.32 (1C, -CH-), 135.21 (1C, -C-), 128.37 (1C, -CH-), 127.63 (1C, -CH-), 98.37 (1C, -CH-), 84.26 (1C, -C-), 81.52 (1C, -C-). **FT-IR:** 3401, 3375, 2915, 2832, 1693, 1174, 912, 742, 524 cm⁻¹. **GC-EIMS** (m/z %): 464 (100), 463 (35), 450 (50), 435 (25), 337 (65), 334 (20), 235 (25), 210 (55). The characterized product is in accordance with the literature.²¹³



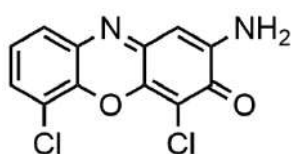
2-amino-1,9-dibromo-3H-phenoxazin-3-one (3c). The product was obtained following the flow general procedure with **2c** (376 mg, 2 mmol) as substrate, and without further purification as a red powder (359 mg, 0.97 mmol), yield: 97%, melting point: 287 °C dc. **¹H-NMR** (400 MHz, DMSO-*d*₆): δ 7.83 (d, *J* = 2.1 Hz, 1H), 7.71 (d, *J* = 8.6 Hz, 1H), 7.59 (dd, *J* = 8.6, 2.1 Hz, 1H), 7.10 (s, 2H, NH₂), 6.39 (s, 1H). **¹³C-NMR** (101 MHz, DMSO-*d*₆): δ 178.00 (1C, -C-), 149.60 (1C, -C-), 146.30 (1C, -C-), 144.66 (1C, -C-), 142.99 (1C, -C-), 132.98 (1C, -C-), 130.21 (1C, -CH-), 128.99 (1C, -CH-), 121.91 (1C, -C-), 119.18 (1C, -CH-), 103.25 (1C, -CH-), 95.12 (1C, -C-). **FT-IR:** 3405, 3375, 3318, 2920, 2850, 1644, 1173, 909, 754, 582 cm⁻¹.

GC-EIMS (m/z %): 372 (49), 370 (100), 368 (50), 359 (30), 354 (45), 290 (65), 188 (55), 186 (54), 183 (25), 109 (20), 94 (80). The characterized product is in accordance with the literature.²¹³



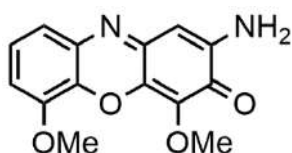
2-amino-4,6-dibromo-3H-phenoxazin-3-one (3d). The product was obtained following the flow general procedure with **2d** (376 mg, 2 mmol) as substrate, and without further purification as a red powder (363 mg, 0.98 mmol), yield: 98%, melting point: 275 °C dc.

¹H-NMR (400 MHz, DMSO- d_6): δ 7.80 – 7.73 (m, 2H), 7.38 (t, J = 7.9 Hz, 1H), 7.12 (s, 2H, NH₂), 6.40 (s, 1H). **¹³C-NMR** (101 MHz, DMSO- d_6): δ 174.91 (1C, -C-), 148.07 (1C, -C-), 147.55 (1C, -C-), 146.55 (1C, -C-), 139.48 (1C, -C-), 135.51 (1C, -C-), 132.26 (1C, -CH-), 127.82 (1C, -CH-), 126.83 (1C, -CH-), 109.25 (1C, -C-), 101.63 (1C, -C-), 98.09 (1C, -CH-). **FT-IR**: 3403, 3375, 2915, 2844, 1644, 1170, 900, 752, 580 cm⁻¹. **GC-EIMS** (m/z %): 372 (48), 370 (100), 368 (52), 359 (45), 354 (65), 290 (80), 188 (35), 186 (54), 183 (25), 94 (75). The characterized product is in accordance with the literature.²⁴⁴



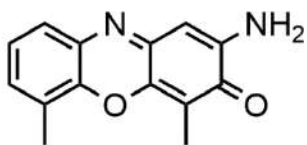
2-amino-4,6-dichloro-3H-phenoxazin-3-one (3e). The product was obtained following the flow general procedure with **2e** (287 mg, 2 mmol) as substrate, and without further purification as a red powder (275 mg, 0.98 mmol), yield: 98%, melting point: 256 °C dc.

¹H-NMR (400 MHz, DMSO- d_6): δ 7.73 – 7.65 (m, 2H), 7.44 (t, J = 8.0 Hz, 1H), 7.13 (s, 2H, NH₂), 6.40 (s, 1H). **¹³C-NMR** (101 MHz, DMSO- d_6): δ 174.75 (1C, -C-), 147.86 (1C, -C-), 147.66 (1C, -C-), 144.40 (1C, -C-), 138.20 (1C, -C-), 135.42 (1C, -C-), 129.31 (1C, -CH-), 127.34 (1C, -CH-), 126.16 (1C, -CH-), 120.27 (1C, -C-), 109.96 (1C, -C-), 97.95 (1C, -CH-). **FT-IR**: 3407, 3390, 2902, 1670, 1170, 904, 748, 510 cm⁻¹. **GC-EIMS** (m/z %): 281 (100), 279 (64), 267 (75), 252 (65), 250 (45), 242 (25), 245 (50), 212 (20), 209 (75), 143 (40), 141 (25). The characterized product is in accordance with the literature.²⁴⁴



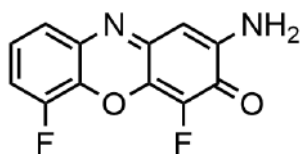
2-amino-4,6-dimethoxy-3H-phenoxazin-3-one (3f). The product was obtained following the flow general procedure with **2f** (278 mg, 2 mmol) as substrate, and without further purification as a purple powder (264 mg, 0.97 mmol), yield: 97%, melting point: 250 °C – 253 °C. **¹H-NMR** (400 MHz, DMSO- d_6): δ 7.33 – 7.28 (m, 2H), 7.20 – 7.17 (m, 1H), 6.81 (s, 2H, NH₂), 6.29 (s, 1H), 3.96 (s, 3H, -

CH₃), 3.89 (s, 3H, -CH₃). **¹³C-NMR** (101 MHz, DMSO- d_6): δ 176.42 (1C, -C-), 148.46 (1C, -C-), 147.58 (1C, -C-), 147.28 (1C, -C-), 137.62 (1C, -C-), 134.93 (1C, -C-), 134.69 (1C, -C-), 131.93 (1C, -C-), 124.68 (1C, -CH-), 120.12 (1C, -CH-), 111.85 (1C, -CH-), 96.90 (1C, -CH-), 60.21 (1C, -CH₃), 56.74 (1C, -CH₃). **FT-IR**: 3412, 3381, 2912, 2832, 1687, 1174, 1102, 909 cm⁻¹. **GC-EIMS** (m/z %): 272 (100), 258 (20), 244 (65), 243 (35), 230 (65), 223 (45), 212 (30), 210 (75). The characterized product is in accordance with the literature.²¹³

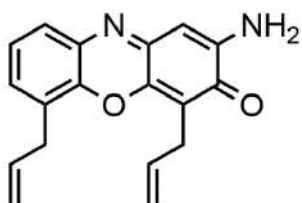


2-amino-4,6-dimethyl-3H-phenoxazin-3-one (3g). The product was obtained following the flow general procedure with **2g** (246 mg, 2 mmol) as substrate, and without further purification as a red powder (233 mg, 0.97 mmol), yield: 97%, melting point: 248 °C – 249 °C. **¹H-NMR** (400 MHz, DMSO- d_6): δ 7.53 (dd, J = 7.9, 1.7

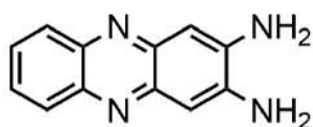
Hz, 1H), 7.35 – 7.33 (m, 1H), 7.29 – 7.25 (m, 1H), 6.74 (s, 2H, NH₂), 6.32 (s, 1H), 2.47 (s, 3H, -CH₃), 2.12 (s, 3H, -CH₃). **¹³C-NMR** (101 MHz, DMSO- d_6): δ 180.35 (1C, -C-), 148.20 (1C, -C-), 147.14 (1C, -C-), 140.95 (1C, -C-), 139.60 (1C, -C-), 133.69 (1C, -C-), 130.16 (1C, -CH-), 126.00 (1C, -CH-), 125.37 (1C, -C-), 124.75 (1C, -CH-), 111.64 (1C, -C-), 97.93 (1C, -CH-), 14.85 (1C, -CH₃), 7.98 (1C, -CH₃). **FT-IR**: 3401, 3381, 2918, 2830, 1667, 1388, 1102, 904 cm⁻¹. **GC-EIMS** (m/z %): 240 (100), 226 (30), 225 (80), 211 (65), 197 (25), 186 (20). The characterized product is in accordance with the literature.²⁴⁴



2-amino-4,6-difluoro-3H-phenoxazin-3-one (3h). The product was obtained following the flow general procedure with **2h** (254 mg, 2 mmol) as substrate, and without further purification as a purple powder (243 mg, 0.98 mmol), yield: 98%, melting point: 256 °C dc. **¹H-NMR** (400 MHz, DMSO-*d*₆): δ 7.58 (d, *J* = 8.0 Hz, 1H), 7.52 – 7.44 (m, 1H), 7.42 – 7.37 (m, 1H), 7.11 (s, 2H, NH₂), 6.34 (s, 1H). **¹³C-NMR** (101 MHz, DMSO-*d*₆): δ 172.85 (d, ²*J*_{C-F} = 16 Hz, 1C, -C-), 149.76 (d, ¹*J*_{C-F} = 248 Hz, 1C, -C-), 147.82 (1C, -C-), 147.14 (d, ⁴*J*_{C-F} = 2 Hz, 1C, -C-), 139.28 (d, ¹*J*_{C-F} = 252 Hz, 1C, -C-), 135.65 (1C, -C-), 132.63 (d, ³*J*_{C-F} = 11 Hz, -C-), 130.05 (d, ³*J*_{C-F} = 11 Hz, -C-), 125.22 (d, ³*J*_{C-F} = 7 Hz, -CH-), 124.23 (1C, -CH-), 115.84 (d, ²*J*_{C-F} = 17 Hz, -CH-), 96.94 (1C, -CH-). **¹⁹F-NMR** (282 MHz, DMSO-*d*₆): δ -137.49 (dd, *J* = 10.7, 5.6 Hz), -161.22 (s). **FT-IR**: 3404, 3388, 2902, 1670, 1298, 901, 517 cm⁻¹. **GC-EIMS** (m/z %): 248 (100), 228 (45), 208 (65), 232 (25), 230 (40), 216 (20), 212 (40), 210 (25). The characterized product is in accordance with the literature.²⁴⁴



4,6-diallyl-2-amino-3H-phenoxazin-3-one (3i). The product was obtained following the flow general procedure with **2i** (298 mg, 2 mmol) as substrate, and without further purification as a red powder (272 mg, 0.93 mmol), yield: 93%, melting point: 258 °C – 260 °C. **¹H-NMR** (400 MHz, DMSO-*d*₆): δ 7.59 (t, *J* = 4.8 Hz, 1H), 7.33 (d, *J* = 4.8 Hz, 2H), 6.78 (s, 2H, NH₂), 6.57 – 6.45 (m, 3H), 6.35 (s, 1H), 6.30 (dd, *J* = 7.2, 2.0 Hz, 1H), 6.10 – 5.84 (m, 2H), 3.64 (d, *J* = 6.4 Hz, 1H), 3.41 (d, *J* = 6.6 Hz, 1H), 3.28 (d, *J* = 6.6 Hz, 2H). **¹³C-NMR** (101 MHz, DMSO-*d*₆): δ 179.60 (1C, -C-), 148.20 (1C, -C-), 147.26 (1C, -C-), 141.47 (1C, -C-), 137.83 (1C, -C-), 129.52 (1C, -CH-), 127.54 (1C, -C-), 127.29 (1C, -C-), 125.12 (1C, -CH-), 120.43 (1C, -CH-), 117.88 (1C, -CH-), 116.82 (1C, =CH₂), 115.84 (1C, =CH₂), 115.35 (1C, -C-), 113.47 (1C, -CH-), 98.14 (1C, -CH-), 33.36 (1C, -CH₂-), 26.87 (1C, -CH₂-). **FT-IR**: 3398, 3371, 3092, 1625, 1174, 1102, 842 cm⁻¹. **GC-EIMS** (m/z %): 292 (100), 290 (35), 276 (35), 274 (60), 260 (40), 254 (45), 210 (70), 196 (20).

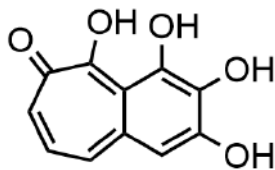


Phenazine-2,3-diamine (3m). The product was obtained following the flow general procedure with *o*-phenylenediamine (216 mg, 2 mmol) as substrate, and without further purification as a red powder (206 mg, 0.98 mmol), yield: 98%, melting point: 262 °C – 265 °C. **¹H-NMR** (400 MHz, DMSO-*d*₆): δ 7.91 – 7.89 (m, 2H), 7.65 – 7.44 (m, 2H), 6.92 (s, 2H), 6.26 (s, 4H, NH₂). **¹³C-NMR** (101 MHz, DMSO-*d*₆): δ 144.45 (2C, -C-), 142.45 (2C, -C-), 140.70 (2C, -C-), 128.28 (2C, -CH-), 126.83 (2C, -CH-), 102.58 (2C, -CH-). **FT-IR**: 3310, 3155, 1630, 1532, 1372, 1240, 890, 835 cm⁻¹. **GC-EIMS** (m/z %): 211 (45), 210 (100), 186 (20), 115 (40), 102 (20), 74 (45). The characterized product is in accordance with the literature.²⁴⁴



3-imino-N,5-diphenyl-3,5-dihydrophenazin-2-amine (3n). The product was obtained following the flow general procedure with **2n** (368 mg, 2 mmol) as substrate, and without further purification as a deep red powder (354 mg, 0.98 mmol), yield: 98%, melting point: 265 °C dc. **¹H-NMR** (400 MHz, DMSO-*d*₆): δ 7.67 (dd, *J* = 7.4, 2.0 Hz, 1H), 7.62 (t, *J* = 7.7 Hz, 2H), 7.57 – 7.50 (m, 1H), 7.41 – 7.34 (m, 2H), 7.25 – 7.11 (m, 4H), 6.89 (t, *J* = 7.4 Hz, 1H), 6.72 – 6.66 (m, 2H), 6.60 (s, 2H), 6.48 – 6.42 (m, 2H), 5.23 (s, 1H). **¹³C-NMR** (101 MHz, DMSO-*d*₆): 152.82 (1C, -C-), 151.36 (1C, -C-), 150.29 (1C, -C-), 149.86 (1C, -C-), 137.30 (1C, -C-), 136.00 (1C, -C-), 134.66 (1C, -C-), 131.27 (2C, -CH-), 130.93 (1C, -C-), 129.91 (1C, -CH-), 128.99 (2C, -CH-), 128.89 (2C, -CH-), 127.96 (1C, -CH-), 127.54 (1C, -CH-), 123.21 (1C, -CH-), 123.08 (1C, -CH-), 121.15 (2C, -CH-), 114.57 (1C, -CH-), 99.38 (1C, -CH-), 90.60 (1C, -CH-). **FT-IR**: 3312, 3134, 1630, 1532, 1375, 1248, 835, 760 cm⁻¹. **GC-EIMS** (m/z %): 363 (64), 362 (100), 273 (20), 262 (25),

184 (22), 182 (25), 174 (34), 122 (35), 108 (42). The characterized product is in accordance with the literature.²⁰⁴



2,3,4,5-tetrahydroxy-6H-benzo[7]annulen-6-one (3p). The product was obtained following the flow general procedure with **2p** (252 mg, 2 mmol) as substrate, and without further purification as an orange powder (209 mg, 0.95 mmol), yield: 95%, melting point: 274 °C – 276 °C. ¹H-NMR (400 MHz, DMSO-*d*₆): δ 7.35 (d, *J* = 11.4 Hz, 1H), 7.07 (d, *J* = 9.4 Hz, 1H), 6.90 (s, 1H), 6.74 (dd, *J* = 11.4, 9.5 Hz, 1H). ¹³C-NMR (101 MHz, DMSO-*d*₆): δ 182.65 (1C, -C-), 155.09 (1C, -C-), 152.17 (1C, -C-), 151.95 (1C, -C-), 135.11 (1C, -C-), 134.71 (1C, -CH-), 133.40 (1C, -C-), 123.98 (1C, -CH-), 116.91 (1C, -CH-), 115.25 (1C, -C-), 110.64 (1C, -CH-). **FT-IR:** 3416, 3322, 1626, 1590, 1423, 1378, 1237, 1065, 1036, 845, 802, 650 cm⁻¹. **GC-EIMS** (m/z %): 220 (100), 192 (45), 163 (20), 146 (25), 118 (35), 98 (45). The characterized product is in accordance with the literature.²⁴⁵

It could be highlighted the presence of a water peak in the proton spectra of the final products. That is due to the reduction of the oxygen peroxide used as a sacrificial oxidant.

5. Big scale flow procedure with solvent recirculation.

The reservoir was charged with 4 mL of CPME, the substrates of choice (2 mmol), followed by H₂O₂ (6 mmol, 674 mg, 608 μL). Then the oxygen line was set to 5 bar and the reaction mixture was allowed to flow through a K-OMS-2 filled reactor (filled with 70 mg of K-OMS-2) at a flow rate of 0.1 mL/min with a residence time of 30 min. Once the reagent reservoir was completely emptied, the system was rinsed with CPME (1 mL).

Once the reagent reservoir was emptied again, it was charged with the subsequent substrate (2 mmol) as a 0.5 M solution of CPME. The products were collected continuously into the product reservoir. The CPME was recovered via distillation under reduced pressure (98% of the total amount, purity confirmed by ¹H-NMR) to afford pure products.

The distilled CPME was continuously reused for the entire scope of the flow procedure. The procedure was repeated 25 times to achieve the 50 mmol of starting material transformed without lack of activity in the catalyst.

6. Analysis of the K-OMS-2 three-dimensional structure integrity after the catalytic reaction.

Powder X-ray diffraction data and HRTEM images were collected after the large-scale flow procedure to analyse if changes occur onto the structure of the K-OMS-2 catalyst (Figure 55).

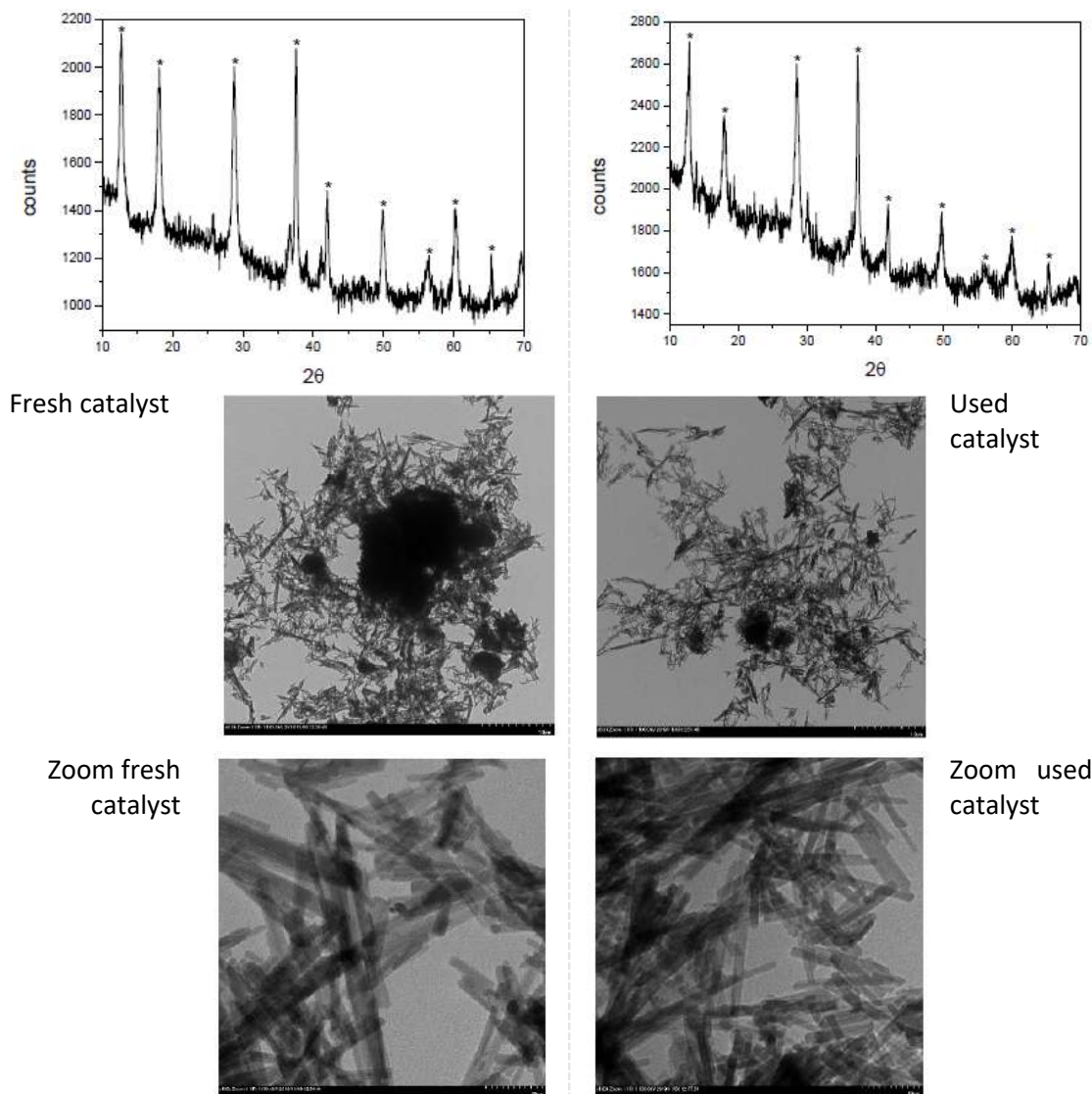


Figure 55. On the *left*, we report the XRD and HRTEM images of the fresh catalyst while on the *right* is reported the analysis of the used catalyst.

Metal leaching measures were analysed with the Agilent 4210 MP-AES equipment using aqua regia to completely digest the reaction sample contents in Mn-leaching.

7. Calculation of the green metrics.

The E-factor was calculated for both the batch and flow methodologies using the 2-aminophenol as substrate scope model. Moreover, as the solvent used can be recovered in a 98% by its distillation or by recrystallization of the final product, it has been also compared those methodologies considering the effect of the solvent recirculation in the final green values.

From the *batch procedure* (see experimental part A section 3) the calculated E-factor is:

Total amount of reactants and solvents: 109 mg (2-aminophenol) + 12082 mg (CPME) + 337 mg (hydrogen peroxide) = 12528 mg

Amount of final product: 103 mg (97% yield)

$$E\text{-factor}_{\text{BATCH-NO SOLVENT RECYCLING}} = (12528 - 103) / 103 = \mathbf{120.6}$$

Considering that the solvent is reused in the system we obtained:

$$E\text{-factor}_{\text{BATCH WITH SOLVENT RECYCLING}} = (12528 - (103 + 11840 (98\% \text{ of the total CPME used}))) / 103 = \mathbf{5.7}$$

From the *flow procedure* (see experimental part A section 4) the calculated E-factor is:

Total amount of reactants and solvents: 109 mg (2-aminophenol) + 5178 mg (6 mL CPME) + 337 mg (hydrogen peroxide) = 5624 mg

Amount of final product: 103 mg (97% yield)

$$E\text{-factor}_{\text{FLOW-NO SOLVENT RECYCLING}} = (5624 - 103) / 103 = \mathbf{53.6}$$

Considering that the solvent is reused in the system we obtained:

$$E\text{-factor}_{\text{FLOW WITH SOLVENT RECYCLING}} = (5624 - (103 + 5074 (98\% \text{ of the total CPME used}))) / 103 = \mathbf{4.3}$$

From the *big scale flow procedure* (50 mmol) with solvent recirculation (see experimental part A section 5) the calculated E-factor is:

Total amount of reactants and solvents: 218 mg (2-aminophenol) + 4315 mg (5 mL CPME) + 674 mg (hydrogen peroxide) = 5207 mg each cycle (x 25 cycles) = 130175

Amount of final product: 206 mg (97% yield) (x 25 cycles) = 5146 mg

$$E\text{-factor}_{\text{BIG-SCALE FLOW RECYCLING}} = (130175 - (5146 + 105717 (98\% \text{ of the total CPME used}))) / 5146 = \mathbf{3.7}$$

Comparing those values with literature procedures (that have a detailed experimental part) we found that our process is highly superior in terms of waste minimization.

Reference	Procedure
ACS <i>Sustainable Chem. Eng.</i> , 2019, 74, 4414-4419	According to the general procedure, the title compound was synthesized from 4,5-dimethoxy-2-nitrophenol (50 mg, 251 μmol) and palladium on activated charcoal (10 wt%, 5.00 mg, 4.70 μmol) in degassed MeOH (3 mL) and then added to a solution of 2-aminophenol (109 mg, 1.00 mmol) and aqueous H ₂ O ₂ solution (35%, 43.0 μL , 502 μmol) in degassed MeOH (3 mL). The crude product was recrystallized from water (5 mL) in order to obtain the product as a red solid (53.1 mg, 250 μmol , quant.) $E\text{-factor} = 50 \text{ mg } 4,5\text{-dimethoxy-2-nitrophenol} + 5 \text{ mg Pd/C} + 109 \text{ mg } 2\text{-aminophenol} + 16.7 \text{ mg H}_2\text{O}_2 \text{ 35\%} + 4747 \text{ mg (6 mL of MeOH)} - 53.1 \text{ mg of product} / 53.1 \text{ mg of product} = \mathbf{92}$ (Water is not considered)

<p><i>Tetrahedron Letters</i>, 2015, 56, 6104 – 6107</p>	<p>The Buchwald solution product 2-(benzyloxy)-3-nitro-N-phenylaniline (200 mg) in methanol (5 ml) was added wet 10% Pd/C (10 mg) and the reaction mixture was stirred for 5 h under the pressure of a hydrogen balloon. The reaction mixture was then filtered, washed the solids with EtOAc (20 ml), and the combined solvents were evaporated on a rotary evaporator under reduced pressure to get the crude product which was purified by column chromatography using EtOAc/Hexane (1:4) to get a red-coloured dye (60 mg, 0.28 mmol).</p>
<p>$E\text{-factor} = 200 \text{ mg } 2\text{-(benzyloxy)-3-nitro-N-phenylaniline} + 3956 \text{ mg } (5 \text{ mL MeOH}) + 10 \text{ mg Pd/C} + 20980 \text{ mg } (20 \text{ mL of EtOAc}) - 60 \text{ mg of product} / 60 \text{ mg of product} = \mathbf{418}$ (Column chromatography solvents employed were not considered in the E-factor calculation as the volume used was unspecified).</p>	

By considering the green metric Atom economy (AE), it is highlighted the efficiency of the process in which the reactive is transformed into the product with the only loss of two H atoms. The AE gives us an idea of how much of the reactants remain in the product. It is calculated by dividing the molecular mass of the desired product by the molecular mass of the reagents. In this metric it is not included solvents and auxiliary chemicals that do not appear in the stoichiometric reaction, that is why there are no different AE values between the batch and the flow processes. Moreover, it is based on a theoretical chemical yield of 100%.

$$AE = (212.21/109.13 \times 2) = \mathbf{0.97}$$

Finally, we determined the Turnover number (TON) and the Turnover frequency (TOF) of the catalyst. Those parameters indicate the maximum conversion per unit of catalyst and the conversion per unit of time, respectively, of a specific catalytic center.

TON is calculated as the number of moles of reactant consumed divided by mole of catalyst.

$$\text{TON}_{\text{BATCH}} = 1 \text{ mmol of 2-aminophenol} / 0.02 \text{ mmol of Mn} = \mathbf{50}$$

$$\text{TON}_{\text{FLOW}} = 2 \text{ mmol of 2-aminophenol} / 0.8 \text{ mmol of Mn} = \mathbf{1.6}$$

While the TOF is calculated as the TON divided by the time of reaction.

$$\text{TOF}_{\text{BATCH}} = 50 / 3 \text{ h} = \mathbf{16.6 \text{ h}^{-1}}$$

$$\text{TOF}_{\text{FLOW}} = 1.6 / 0.5 \text{ h} = \mathbf{3.2 \text{ h}^{-1}}$$

Even if the TOF in flow is lower than in the batch, it can be used continuously as indicated in the *big-scale procedure* for a period of 25 hours, showing a final TON of **80** while in batch, after three hours of reaction, we get a TON of **50**.

Results and discussion:

2. Development of sustainable synthetic pathways towards pharmaceutical scaffolds of interest.

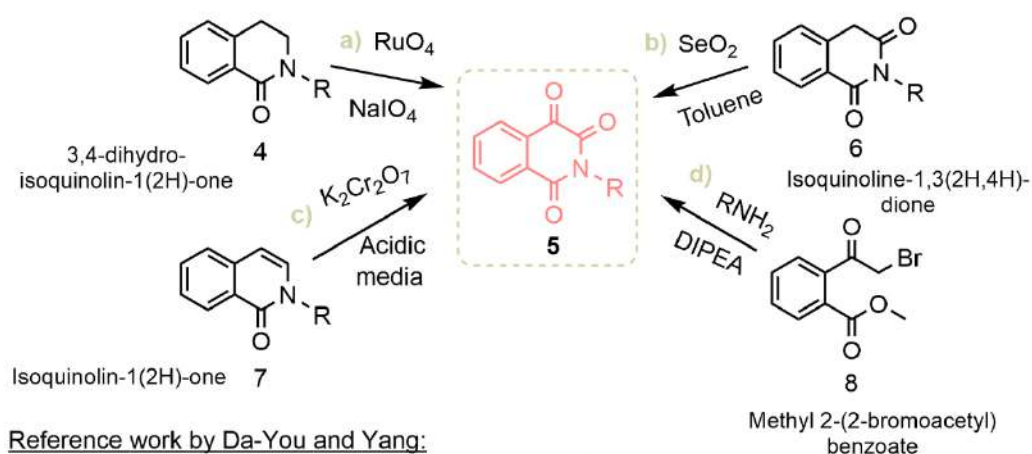
The search for new one-pot reactions is appealing due to the environmentally benign and atom economy features. In the first part of the discussion, we have used a manganese-based catalyst (KOMS-2) that mimics the function of oxidases to successfully synthesize in flow 2-aminophenoxazin-3-ones and phenazines with excellent yields.

In an effort to broaden the manganese-based catalyst applications, our group was interested in the synthesis of isoquinoline-1,3,4, (2H)-triones employing a single pot oxidation reaction. These molecules have a pharmaceutical interest as caspase inhibitors, and they are used as nerve protectors to treat neurodegenerative diseases as Alzheimer among others.^{246,247}

Nevertheless, the methods of synthesis of these compounds are limited and employ metals catalysts that cannot be recovered, producing a waste generation problem.

In literature, we can find the oxidation of 3,4-dihydroisoquinolin-1(2H)-one with ruthenium tetroxide as catalyst and NaIO₄ as the oxidant (Scheme 18, a).²⁴⁸ Other methodologies are based on the use of SeO₂²⁴⁹ and K₂Cr₂O₇²⁵⁰, which provide the oxidation of the isoquinoline-1,3(2H,4H)-dione and isoquinolin-1-one derivatives, respectively, and/or the metal-free reaction of 2-(2-bromoacetyl)benzoate with primary amines (Scheme 18, b), c) and d) respectively).²⁵¹

Procedures that employ isoquinolones or isoquinolindiones are not very straightforward because the starting material itself has to be synthesized. The limited substrate scope, the harsh reaction conditions and decomposition susceptibility make necessary the development of new methods. Instead, the proposed protocol by Da-You Ma and Yang in *Org. Biomol. Chem*, 2017,²⁵² in which it is used unfunctionalized isoquinolines as raw starting material looks more efficient from the point of view of sustainability (Scheme 18, e)).

Previous methodologies:Reference work by Da-You and Yang:

Scheme 18. Literature examples of the isoquinoline-1,3,4(2H)-triones synthesis.

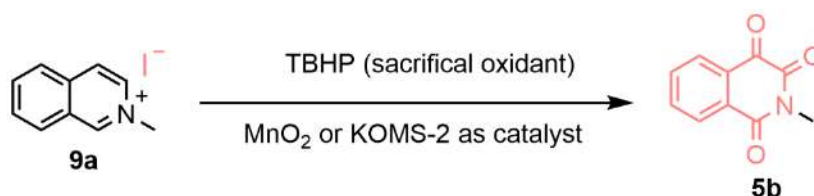
Adapted scheme from ref ²⁵¹.

The project was developed based on the opportunities that isoquinoline presents when transformed into isoquinoline-1,3,4,(2H)-trione, as a pharmaceutical scaffold. The main interest in this synthesis is the possibility to optimize the procedure, using a green manganese-based catalyst. These catalysts like the previously used (K-OMS-2), can also work as an oxidant so that we want to study the condition's reaction to its application.

2.2 Preliminary studies toward the manganese-catalyzed synthesis of isoquinoline-1,3,4,(2H)-trione.

As a starting point, we considered using a synthetic strategy similar to that reported by Da-You and co-workers²⁵², where iodine was employed as the catalyst and an excess of TBHP (tert-butyl hydroperoxide) as sacrificial oxidant. In this article takes place a multiple C-H bond transformation of isoquinolines using methylarenes. The proposed reaction mechanism is based firstly on the iodination of the benzylic sp³ C-H bond of the methyl arene to provide benzylic iodide. Then, the formation of the quaternary ammonium salt by substitution of the isoquinoline and finally, the nucleophilic addition of the TBHP.

As starting material, we used the 2-methylisoquinolinium iodide salt **9a** in order to directly tackle the oxidation reaction in the presence of TBHP as sacrificial oxidant and a manganese-based catalyst, to yield the desired isoquinoline trione **5** (Scheme 19).



Scheme 19. Synthetic strategy using the salt **9a** as starting material.

Unfortunately, when it was used TBHP in decane (3.6 eq) in the presence of MnO₂ (2 eq), a complex reaction mixture composed of 2-methylisoquinolin-1(2H)-one **10** (3%), 4-iodo-2-methylisoquinolin-1(2H)-one **11** (21%) and 2-methylphthalimide **12** (23%) as main products, was obtained (Table 14, entry 1). From these molecules, only 2-methylisoquinolin-1(2H)-one (**10**) was reported as an intermediate to obtain the further oxidated *trione*.

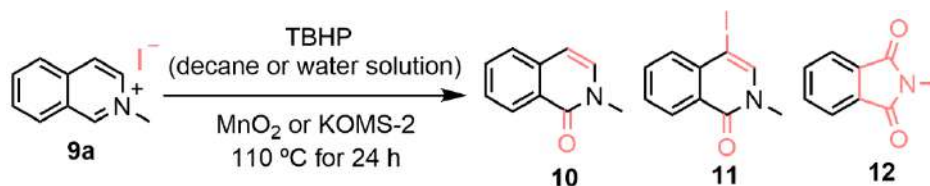
Different studies also reported that the oxygen of the C-3 carbonyl group, formed in the isoquinoline ring, is given by the H₂O in which the peroxide is dissolved^{252,253}, so that we also tried to perform the reaction using TBHP in water solution (Table 14, entry 4) but the main product was again the undesired phthalimide **12** even when increased amounts of TBHP was employed (Table 14, entries from 2 to 5).

When no MnO₂ is added, the iodide salt is also transformed into the identified products but in low yield and with some conversion to other non-recognized oxidated species (Table 14, entries 6 and 8).

Other solvents were used instead of water, as hexane and THF, which seem to form the intermediate **10** preferably (Table 14, from entry 7a to 7c).

We go further and tested the reaction condition in which the manganese catalyst is employed in catalytic amount (Table 14, from entry 9 to 13). Catalytic amounts of MnO₂ allowed less conversion of the 2-methylisoquinolinium iodide (**9a**) and no specificity for the iodide substituted product (**11**) when using TBHP in decane (Table 14, entry 9). If the reaction is left longer times (48 hours), there was not reached a better conversion rate but the equilibrium this time tents to the formation of the intermediate **11** (Table 14, entry 10).

We repeated the same experiment with the K-OMS-2 catalyst and even if we get the same identified species (**10**, **11** and **12**), there was no specificity to form **11**, and longer times result in the conversion of the products into over-oxidated species (Table 14, from entry 11 to 13).



Entry	Oxidant (eq)	Solvent (eq)	Catalyst (eq)	Yield (% and GC-MS identification)		
1	TBHP dec (3.6)	H ₂ O (6)	H ₂ O (6)	10 (3%)	11 (21%)	12 (23%)
2	TBHP aq (0.7)	H ₂ O (10)	MnO ₂ (2)	10 (6%)	11 (14%)	-
3	TBHP aq (2.5)	H ₂ O (10)	MnO ₂ (2)	10 (20%)	11 (17%)	12 (34%)
4	TBHP aq (4)	H ₂ O (10)	MnO ₂ (2)	10 (9%)	11 (11%)	12 (34%)
5	TBHP aq (7)	H ₂ O (10)	MnO ₂ (2)	-	11(6%)	12 (37%)
6	TBHP aq (7)	H ₂ O (10)	-	12 (42%) and m/z: 146 (6%)		
7a	TBHP dec (0.6)	H ₂ O (10)	MnO ₂ (2)	10 (9%)	11 (11%)	12 (6%)
7b	TBHP dec (0.6)	Hexane (10)	MnO ₂ (2)	10 (17%)	11 (6%)	12 (11%)
7c	TBHP dec (0.6)	THF (10)	MnO ₂ (2)	10 (20%)	11 (5%)	12 (3%)
8	TBHP dec (2)	H ₂ O (6)	-	10 (11%)	11 (11%)	12 (14%)
9	TBHP dec (2)	H ₂ O (6)	MnO ₂ (0.5)	10 (9%)	11 (19%)	12 (23%)
10	TBHP dec (2)	H ₂ O (6)	MnO ₂ (0.5) for 48 h	10 (6%)	11 (16%)	12 (11%)
11	TBHP dec (2)	H ₂ O (10)	K-OMS-2 (0.5)	10 (9%)	11 (11%)	12 (20%)
12	TBHP dec (2)	H ₂ O (10)	KOMS-2(0.5) for 48 h	10 (6%)	11 (8%)	12 (11%)
13	TBHP aq (1.4)	H ₂ O (10)	K-OMS-2 (0.8)	10 (17%)	11 (5%)	12 (17%)

Table 14. Conditions optimization for the further oxidation of **9a** using Mn-based catalyst.

The reaction conditions: **9a** (1 eq), solvent (10 eq), Mn-based catalyst and TBHP (70% wt in H₂O or 5.5 M in decane) stirring at 110 °C for 24 h under air atmosphere.

Despite the use of different amounts of catalyst, oxidant and different reaction times, we weren't able to obtain the desired *trione*.

The new Mn catalysed process seems to perform a chain reaction, in which the first oxidation product **10** suffer from the oxidative addition of iodine in C-4 or decarboxylation, giving **11** and **12** respectively. The outcome depends largely on the media in which the peroxide is dissolved. In Figure 56, we represented the results obtained above in Table 14, when MnO₂ (2 eq) is used. In this way, it is easy to realize that while compound **10** disappeared, compound **11** is formed when used TBHP in decane. Increasing the equivalents of peroxide lead **10** and **11** to decompose towards **12** in both decane and water.

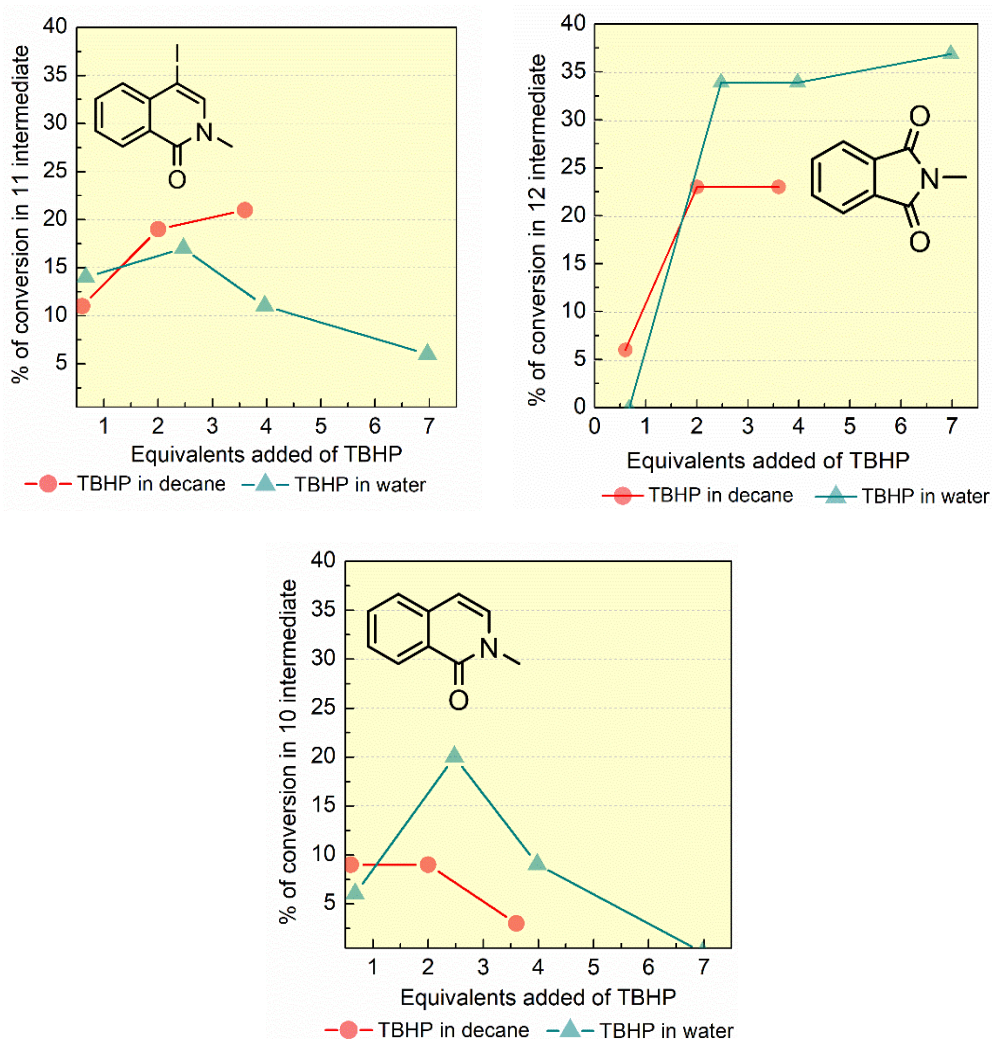
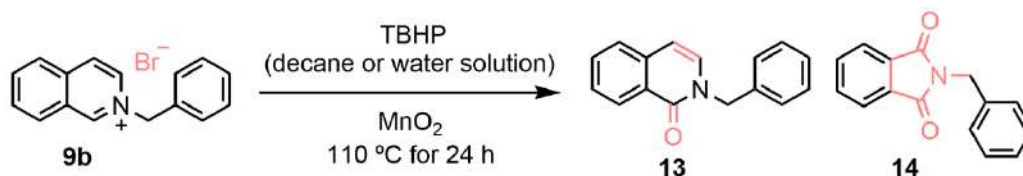


Figure 56. Representation of the yield obtained for each intermediate, while varying the employed amount of TBHP 5.5 M in decane (red) and 70% wt in water (blue).

Finally, 2-benzylisoquinolinium bromide (**9b**) was also employed as substrate in order to test the reactivity of a different starting material and also to test if the bromide counter ion could avoid halogenations in the C4-position of the isoquinolinium ring (Table 15).

Preliminary results showed that such substrate was less reactive compared to the iodide salt, probably because of the hindrance of the benzylic group.



Entry	Oxidant (eq)	Solvent (eq)	Catalyst (eq)	Yield (%)	
14	TBHP dec (3.6)	H ₂ O (10)	MnO ₂ (2)	13 (4%)	14 (8%)
15	TBHP aq (7)	H ₂ O (10)	MnO ₂ (2)	13 (6%)	14 (10%)
16	TBHP aq (7)	H ₂ O (10)	MnO ₂ (0.5)	13 (4%)	14 (6%)
17	TBHP aq (7)	H ₂ O (10)	-	-	14 (15%)

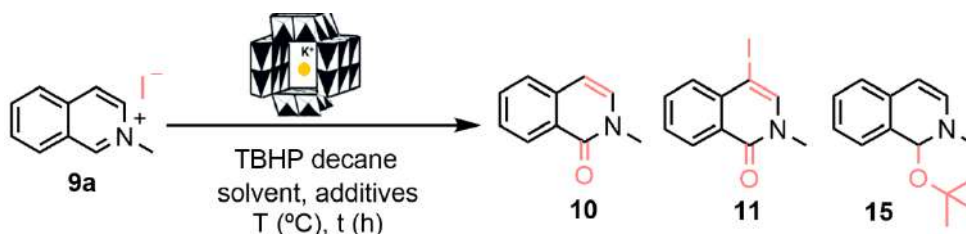
Table 15. Oxidation of the bromide benzyl isoquinolinium salt (**9b**), under the same reaction conditions.

The equilibrium of the reaction is, in all cases, displaced towards intermediate **14** that has been recognized as the 2-benzylphthalimide. Compound **13** was only obtained in low quantity and the role of the catalyst did not seem to be critical in its conversion improvement. However, when we run the reaction without MnO₂, the intermediate **13** disappeared and we got as the only product the 2-benzylphthalimide (**14**) (Table 15, entry 17).

Aryl N-substituted isoquinolinium salt gives room to low reactivity, and decomposition towards phthalimide under strong oxidative conditions. The iodide anion is a better nucleophile than bromide, which in part justified its reactivity with the isoquinoline ring in comparison to the latter.

2.3. K-OMS-2 reaction conditions optimization towards the synthesis of 11.

Even though it was not possible to propose a manganese-catalyzed protocol for the synthesis of isoquinoline trione **5**, the formation of 4-iodo isoquinolone **11** in the reaction mixture prompted us to investigate the possibility to synthesize such building block, that could be easily functionalized in the C-4 position yielding diverse bioactive molecules and drug candidates.²⁵⁴⁻²⁵⁵



Entry	Oxidant (eq)	Solvent(1mL)/addt.	Catalyst (eq)	T (°C), t (h)	Yield (%)	
1	TBHP dec (2)	CH ₃ CN	K-OMS-2 (0.5)	70 °C, 24 h	11 (25%)	10 (37%)
2 ^a	TBHP dec (2)	CH ₃ CN/acid	K-OMS-2 (0.5)	70 °C, 24 h	11 (22%)	10 (31%)
3	TBHP dec (2)	CH ₃ CN	K-OMS-2 (0.5)	70 °C, 6 h	11 (27%)	10 (48%)
4	TBHP dec (2)	-	K-OMS-2 (0.5)	70 °C, 6 h	11 (30%)	10 (9%)
5	TBHP dec (2)	-	K-OMS-2 (0.5)	70 °C, 3 h	11 (37%)	10 (20%)
6	TBHP dec (2)	-	-	70 °C, 3 h	11 (32%)	10 (23%)
7	TBHP dec (2)	I ₂ (0.5)	K-OMS-2 (0.5)	70 °C, 3 h	11 (25%)	10 (17%)
8	TBHP dec (2)	KI (1)	K-OMS-2 (0.5)	70 °C, 3 h	11 (13%)	10 (31%)
9	TBHP dec (2)	NaIO ₄ (0.5)	K-OMS-2 (0.5)	70 °C, 3 h	11 (25%)	10 (20%)
10	H ₂ O ₂ aq (2.4)	-	K-OMS-2 (0.5)	70 °C, 3 h	No reaction	
11	TBHP dec (2)	-	K-OMS-2 (0.5)	50 °C, 8 h	11 (33%)	10 (23%)
12	PIDA (1.5)	MeOH (0.1 mL)	K-OMS-2 (0.5)	50 °C, 4 h	11 (31%)	10 (8%)
13	TBHP dec (2)	-	K-OMS-2 (0.5)	rt, 1 h	15 (39%)	
14	TBHP dec (2)	-	K-OMS-2 (0.5)	120 °C, 3 h	11 (16%)	10 (23%)
15 ^b	TBHP dec 3.6	-	K-OMS-2 (0.5)	70 °C, 3 h	11 (40%)	10 (23%)

Table 16. Optimization of the reaction conditions with the K-OMS catalyst.

^aAs acid we used HCl 2N (pH from 3 to 4). ^bThere was a 28% of a mixture of **12** and iododecane. Reaction conditions: To a sealed reaction vessel was added **9a** (1 eq), K-OMS-2 (62% loading, 0.5 eq), solvent (1 mL unless otherwise noted), TBHP in decane (5.5 M) or another sacrificial oxidant and iodide source. The reaction was heated for the described time and temperature and purified under column chromatography.

Based on the previous experience, we observed that avoiding the use of water as a solvent, the presence of compound **12** in the reaction mixture was irrelevant. Aprotic solvents as acetonitrile have been previously used in OMS catalysed reactions, showing more suitability for oxidation processes than polar solvents that could compete for binding in the active site of the catalyst.¹⁸⁶ Also, the temperature was reduced to avoid the decarboxylation process that leads to phthalimide formation. Application of these reaction conditions (Table 16, entries 1 and 3) gave better results than those previously obtained.

Acid conditions were reported to enhance oxidation¹⁸⁹ but, in our system, seems to slightly diminish the conversion (Table 16, entry 2).

Since the best solvent in green chemistry is no-solvent we used the oxidant TBHP in decane as the reaction media itself without adding any other external solvent. The best result (**11**, 37%) was obtained at 70 °C for 3 h, however, it was noticed that the catalyst plays a marginal role in

the formation of **11** since the uncatalyzed reaction yield an only slightly lower amount of **11** (32%) (Table 16, entries 5 and 6 respectively).

In order to increase the amount of **11**, we tested the use of different iodide sources as I₂, KI and NaIO₄, which could enhance the iodide oxidative C-4 addition. However, the use of none of them showed better results (Table 16, entry from 7 to 9).

The use of hydrogen peroxide (30% w/w in water) as oxidant instead of TBHP gave no reaction¹⁹⁶ while decreasing the reaction temperature at 50 °C, only made the reaction slower (Table 16, entries 10 and 11 respectively).

Hypervalent iodide PIDA (phenyliodine (III) diacetate) was used with those mild conditions in accordance with the literature²⁵⁷, but without success (Table 16, entry 12).

In an approach towards greener conditions, we tested the reaction at room temperature (Table 16, entry 13), however, the formation of a new product, namely the tertbutyl ether **15**, took place. It was isolated in moderate yield and unequivocally identified by ¹H- and ¹³C-NMR (see experimental part B. 10.). This experiment sheds light on the possible mechanism of reaction by the radical attack of TBHP on the C-1 position and its latter oxidation to form **10**.

Finally, stronger temperatures and oxidation conditions were tested (Table 16, entries 14 and 15). Higher temperatures (120 °C) gave lower conversion and more equivalents of TBHP (3.6 eq) slightly increased the amount of **11**.

Authors from the reported literature, have proposed that this type of reaction occurred *via* radical attack of peroxides and then the further nucleophilic addition of the iodine contra ion.^{257,253} In fact, Yang's *group* pointed out the by-product formation of **10** and **11** when isoquinolinium was the starting material under strong oxidative conditions.^{258,259}

To support this hypothesis, the reaction conditions reported in Table 16, entry 5, were carried out with the radical scavenger TEMPO (2 eq). Compounds **10** and **11** were obtained in 27% and 20% yield, respectively, which highlights the nucleophilic nature of the process.

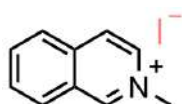
In conclusion, we studied the oxidative performance of the Mn-based catalyst K-OMS-2 in the conversion of 2-methyl isoquinolinium iodide (**9a**) to 4-iodo-2-methyl-isoquinolinone (**11**). Unfortunately, the desired product was obtained in moderate yield and always along with the by-product **10**, so additional purification steps were necessary. Further research needs to be done to improve yield and selectivity of this reaction.

Experimental part B: *Greenest* synthetic pathway towards pharmaceuticals scaffolds of interest.

8. Synthesis of the starting materials.

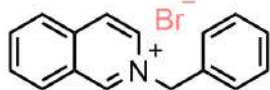
The isoquinolinium salts **9a** and **9b** were synthesized from well-known procedures in the literature.

Compound **9a** was synthesized as follows²⁶⁰: Isoquinoline (500 mg, 3.87 mmol, 1 eq) and methyl iodide (501.3 μ L, 8.05 mmol, 2.1 eq) were added to ethanol (7.5 mL, 33 eq), and the mixture was heated at reflux for 2 hours. On cooling the reaction, yellow needles were formed. The precipitated solid was filtered obtaining the desired product in 77 % yield.



2-methylisoquinolin-2-ium iodide (9a). The final product was obtained without further purification as a yellow solid (808 mg, 3 mmol), yield: 77%, melting point: 160 °C – 163 °C. ¹H-NMR (400 MHz, DMSO-*d*₆): δ 10.02 (s, 1H), 8.70 (d, *J* = 6.7 Hz, 1H), 8.57 (d, *J* = 6.8 Hz, 1H), 8.48 (d, *J* = 8.3 Hz, 1H), 8.35 (d, *J* = 8.4 Hz, 1H), 8.25 (t, *J* = 7.7 Hz, 1H), 8.07 (t, *J* = 7.7 Hz, 1H), 4.48 (s, 3H). The characterized product is in accordance with the literature.²⁶¹

Compound **9b** was synthesized as follows²⁶²: The isoquinoline (200 mg, 1.6 mmol, 1 eq), acetonitrile (3 mL, 37 eq) and benzyl bromide (139 μ L, 1.7 mmol, 1.1 eq) reaction mixture, was heated at reflux for 3 hours. Then, the reaction was cooled to room temperature and the solvent was removed under vacuum giving the final product in 48% yield.



2-benzylisoquinolin-2-ium bromide (9b). The final product was obtained after purification in silica gel column chromatography (9.5 CH₂Cl₂/ 0.5 MeOH) as a light-orange solid (238 mg, 0.8 mmol), yield: 48%, melting point: 106 °C – 108 °C. ¹H-NMR (400 MHz, DMSO-*d*₆): δ 10.33 (s, 1H), 8.85 (d, *J* = 6.0 Hz, 1H), 8.61 (d, *J* = 5.9 Hz, 1H), 8.55 (d, *J* = 7.8 Hz, 1H), 8.41 – 8.19 (m, 2H), 8.14 – 8.01 (m, 1H), 7.67 – 7.52 (m, 2H), 7.49 – 7.34 (m, 3H), 6.00 (bs, 2H). The characterized product is in accordance with the literature.²⁶³

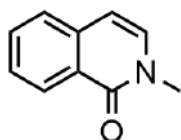
9. General procedure of the optimization reaction.

All the reactions were carried out in a sealed reaction vessel successively charged with **9a** or **9b** (0.22 mmol, 1 eq), the equivalents of MnO₂ or K-OMS-2 (62% loading) indicated in each case, and the TBHP (5.5 M in decane or 70% in aq) and deionized water (40 μ L, 2.21 mmol, 10 eq) The reaction was warmed at 110°C - 120°C for 24 hours in a holey metal plaque. We follow the reaction at 1, 4 and 24 hours by routine CG-MS and TLC. The resulting crude solution is filtered with cotton and celite to separate the remaining catalyst and purified by silica gel column chromatographic (2Hexane/ 1EtOAc), giving the three main products **10**, **11** and **12** in different yields.

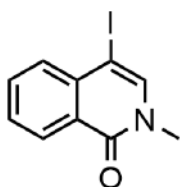
10. Optimized catalytic reaction with K-OMS-2 and final products characterization.

A sealed reaction vessel was successively charged with **9a** (60 mg, 0.221 mmol, 1 eq), K-OMS-2 at 62% loading (9.8 mg, 0.5 eq) and TBHP 5.5 M in decane (74 μ L, 0.664 mmol, 2 eq). The reaction was heated in a holey metal plaque at 70°C for 3 h. The resulting crude solution is filtered with cotton and celite to separate the remaining catalyst and purified by silica gel column chromatographic (2Hexane/ 1EtOAc), giving the main products **10** and **11** in 20% and 37% yields, respectively.

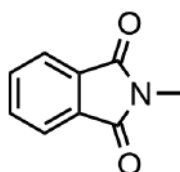
Next, the obtained intermediates products from **9a** and **9b** under the above reaction conditions are characterized and identified in agreement with references found in the literature:



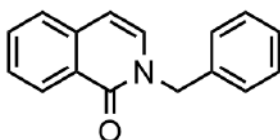
2-Methylisoquinolin-1(2H)-one (10). The final product was obtained from **9a** after purification in a silica gel column chromatographic (2Hexane/ 1EtOAc) as a yellow oil. $^1\text{H-NMR}$ (400 MHz, DMSO- d_6): δ 8.22 (d, J = 7.8 Hz, 1H), 7.73 – 7.60 (m, 2H), 7.52 – 7.42 (m, 2H), 6.61 (d, J = 7.3 Hz, 1H), 3.51 (s, 3H). The characterized product is in accordance with the literature.²⁶⁴



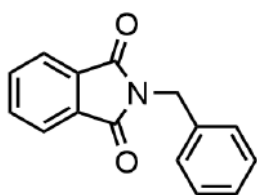
4-iodo-2-methylisoquinolin-1(2H)-one (11). The final product was obtained from **9a** after purification in a silica gel column chromatographic (2Hexane/ 1EtOAc) as an orange solid, melting point: 115 °C – 120 °C. $^1\text{H-NMR}$ (400 MHz, DMSO- d_6): δ 8.21 (d, J = 8.0 Hz, 1H), 8.01 (s, 1H), 7.85 – 7.77 (m, 1H), 7.62 (d, J = 8.6 Hz, 1H), 7.57 (t, J = 7.6 Hz, 1H), 3.50 (s, 3H). The characterized product is in accordance with the literature.²⁵⁷



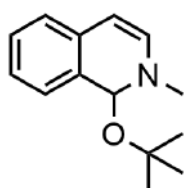
N-Methylphthalimide (12). The final product was obtained from **9a** after purification in a silica gel column chromatographic (2Hexane/ 1EtOAc) as a white solid, melting point: 115°C – 125°C. $^1\text{H-NMR}$ (400 MHz, CDCl₃): δ 7.84 (dd, J = 5.5, 3.0 Hz, 2H), 7.70 (dd, J = 5.5, 3.0 Hz, 2H), 3.18 (s, 3H). The characterized product is in accordance with the literature.²⁶⁵



2-benzylisoquinolin-1(2H)-one (13). The final product was obtained from **9b** after purification in a silica gel column chromatographic (2Hexane/ 1EtOAc) as a yellow oil. $^1\text{H-NMR}$ (400 MHz, CDCl₃): δ 8.40 (d, J = 7.5 Hz, 1H), 7.57 (td, J = 7.5, 1.2 Hz, 1H), 7.44 (d, J = 7.4 Hz, 2H), 7.28 – 7.23 (m, 5H), 7.03 (d, J = 7.4 Hz, 1H), 6.43 (d, J = 7.4 Hz, 1H), 5.17 (s, 2H). The characterized product is in accordance with the literature.²⁵⁸



N-Benzylphthalimide (14). The final product was obtained from **9b** after purification in a silica gel column chromatographic (2Hexane/ 1EtOAc) as a white solid, melting point: 115 °C – 117 °C. $^1\text{H-NMR}$ (400 MHz, CDCl₃): δ 7.95 – 7.80 (m, 2H), 7.78 – 7.67 (m, 2H), 7.43 (d, J = 7.0 Hz, 2H), 7.36 – 7.24 (m, 3H), 4.85 (s, 2H). The characterized product is in accordance with the literature.²⁶⁶



1-(tert-butoxy)-2-methyl-1,2-dihydroisoquinoline (15). The final product was obtained from **9a** at rt, after purification in a silica gel column chromatographic (2Hexane/ 1EtOAc) as a red oil. $^1\text{H-NMR}$ (400 MHz, CDCl₃): δ 8.07 (d, J = 7.6 Hz, 1H), 7.49 – 7.31 (m, 4H), 5.78 (d, J = 1.9 Hz, 1H), 5.45 (d, J = 1.9 Hz, 1H), 3.33 (s, 3H), 1.12 (s, 9H). $^{13}\text{C-NMR}$ (101 MHz, CDCl₃): δ 138.35 (1C, -C-), 132.64 (1C, -CH-), 128.97 (1C, -CH-), 128.83 (1C, -CH-), 127.74 (1C, -CH-), 126.79 (1C, -C-), 96.23 (1C, -CH-), 81.76 (1C, -C-), 35.96 (1C, -CH-),

26.33 (3C, -CH₃), 25.92 (1C, -CH-), 19.72 (1C, -CH₃). The characterized product is in accordance with the literature.²⁶⁷

Conclusions

In the research towards more environmentally friendly processes, we have contributed with the development of an on flow and heterogeneous catalytic green system.

The K-OMS-2 is an excellent heterogeneous and robust catalyst able to mimic enzymatic reactions of peroxidases and oxidases, surpassing the latter limitations of substrate selectivity and pH and temperature degradation.

The reusability of K-OMS-2 in flow and its compatibility with greener solvents as CPME has allowed the obtention of phenoxazinones and phenazines in high yields and regioselectivity via an oxidative C–H cyclization pathway.

Scalability, speed, and low metal leaching bring this system closer to an industrial application.

The analysis of the green metrics E-factor, AE, and the catalytic TON and TOF further support the convenience of the developed methodology.

However, the usage of K-OMS-2 in the oxidation of isoquinolines salts was unable to form the isoquinoline-1,3,4, (2H)-*trione*. Instead, we identified interesting building blocks widely used in the pharmaceutical industry as the 4-iodo-2-methylisoquinolin-1(2H)-one.

Mild synthetic conditions were found, but the catalyst was not selective enough to the desired product. Although K-OMS-2 has desirable properties, its reaction outcome leads to a mixture of two products and the need for purification steps are undesirable.

In view of the results, further experiments could be done with doped or ion exchange (H⁺) OMS-2, which could lead to an enhancement in its oxidative performance while maintaining the heterogeneity.

Conclusiones

En el Capítulo 1, siguiendo la filosofía basada en el green-by-design, hemos sintetizado dos librerías nuevas de inhibidores de la Colino Quinasa siguiendo los Principios de la Química Verde. La librería **PL** está compuesta por 13 moléculas que contienen un enlazador ditioetano, mientras que la librería **FP** compuesta por 9 inhibidores, contine un enlazador disulfuro.

La sostenibilidad de las síntesis se ha evaluado usando métricas verdes como E-factor y EcoScale.

Desde el punto de vista de la capacidad inhibitoria, la librería disulfuro (**FP**) parece tener una mayor actividad que la ditioetano (**PL**). Sin embargo, los compuestos **FP** son más susceptibles de ser metabolizados en las células.

Ambas librerías mejoran su actividad cuando los enlazadores ditioetano y disulfuro están unidos a las cabezas catiónicas [2,3-d] tienopirimidina y [3,2-b] tienopiridina, sustituidas en posición 4 por cicloalquilaminas voluminosas (azepano > piperidina > pirrolidina). Los compuestos **PL 55** y **FP 3** destacaron convirtiéndose en los compuestos líder de cada librería.

Los ensayos de docking relacionan la actividad inhibitoria de la librería **PL** con su interacción con el Mg^{2+} en el sitio catalítico, mientras que en la librería **FP**, el enlace disulfuro más pequeño y rígido presenta mejores valores de S-score debido a la mejor interacción en bolsillo de la colina y a la menor exposición de las cabezas catiónicas fuera del sitio catalítico.

Sorprendentemente, el compuesto **FP 16** presentó un modo de unión inédito, en el que los átomos de S del enlazador se coordinaban al Mg^{2+} .

Los ensayos de antiproliferación en células tumorales MCF-7 y HepG2, determinaron que el enlazador ditioetano era mejor que el disulfuro.

Las moléculas con la cabeza catiónica [2,3-d] tienopirimidina, mostraron valores de acción antiproliferativa en consonancia con los valores de inhibición enzimática, mientras que las cabezas de [3,2-d] tienopirimidina y las quinolónicas parecen interaccionar con otras rutas apoptóticas o tienen problemas de permeabilidad. Las cabezas [3,2-b] tienopiridina, presentaron una buena inhibición enzimática pero una baja actividad antiproliferativa. Esto se podría deber a una posible interacción con los transportadores de colina en la membrana.

Por último, las cabezas piridínicas fueron demasiado polares, mostrando valores bajos de inhibición enzimática y antiproliferativos, además de problemas de solubilidad en la librería **PL**.

La librería **PL**, que presentaba mejores valores en la inhibición del crecimiento de células tumorales, mostró fluorescencia en algunos compuestos. De manera que se pudo determinar si la acumulación de los inhibidores en la membrana de las células neoplásicas era la razón de la discordancia entre los valores de inhibición enzimática y de antiproliferación en algunos de estos compuestos.

Los análisis con FLIM demostraron la existencia de un mecanismo de acción dual en la librería **PL** (interacción en la membrana y en la Colino Quinasa citosólica). Por tanto, dichos compuestos podrían ser mejores en el tratamiento de diferentes líneas tumorales ya que su función no depende únicamente de su permeabilidad a la membrana.

Para finalizar, y dado que la fluorescencia es una característica de las moléculas con PAINS, se realizó una evaluación in silico de las posibles estructuras interferentes en las librerías. De hecho, las cargas positivas y el enlace disulfuro fueron señalados como características indeseables. Sin embargo, mientras que las cargas positivas de las cabezas catiónicas son necesarias para la selectividad en el sitio de la colina, el puente disulfuro podría efectivamente romperse y metabolizarse en las células.

Además, las predicciones farmacodinámicas mostraron baja absorción de los compuestos líder **PL 55** y **FP 3** en el tracto gastrointestinal. Por esa razón, se necesitan más estudios para mejorar las propiedades ADME de dichos compuestos y para el diseño de nuevos inhibidores que puedan desplazar al Mg^{2+} o unirse a él para inhibir la reacción de catálisis enzimática de forma más efectiva.

En el Capítulo 2, se ha llevado a cabo la transformación de procesos químicos hacia modelos más sostenibles con el desarrollo de un sistema en flujo que emplea un catalizador heterogéneo y benigno.

El K-OMS-2 es un excelente catalizador heterogéneo y robusto capaz de imitar las reacciones de oxidación enzimáticas realizadas por peroxidasas y oxidasas, superando limitaciones de las anteriores como: la selectividad del sustrato, la sensibilidad al pH y la degradación a altas temperaturas.

La reutilización del K-OMS-2 en química de flujo y su compatibilidad con disolventes verdes como el CPME, ha permitido la obtención de fenoxacionas y fenacinas con altos rendimientos y regioselectividad, mediante C-H oxidación y ciclación.

La escalabilidad, rapidez y baja lixiviación del Mn hacen que este sistema tenga un gran interés para la industria.

El análisis de las métricas verdes respecto a la síntesis, como el E-factor, AE, y al catalizador, como el TON y TOF, sostienen las ventajas medioambientales de la metodología en flujo desarrollada.

Sin embargo, el uso del K-OMS-2 para la oxidación de sales de isoquinolina no dio lugar a la formación de la deseada isoquinolina-1,3,4, (2H)-triona. En su lugar, se identificó la formación de estructuras químicas de gran interés para la industria farmacéutica como el 4-yodo-2-metil isoquinolinona.

Se encontraron condiciones de síntesis sostenibles con el medio ambiente, pero la reacción catalítica no formaba selectivamente el producto deseado. Aunque el catalizador K-OMS-2 tiene unas propiedades muy deseables, el resultado de la reacción daba lugar a una mezcla de dos productos y por tanto a la necesidad de procesos de purificación, lo cual es indeseable.

En vista de los resultados, futuros estudios podrían desarrollarse con el uso de catalizadores OMS-2 dopados o modificados mediante intercambio iónico con H^+ , lo cual podría mejorar su capacidad oxidativa, manteniendo al mismo tiempo su heterogeneidad.

Appendix:

1. The search of the catalytic pocket.

We started comparing the catalytic site of diverse crystallographic structures of the Human ChoK α 1 in complex with different inhibitors, using the align tool of Pymol. As reported in [Figure 57](#), the catalytic pocket maintains the same conformation except for PDB: 2CKQ, in deep salmon color, that shows a closed loop 1 in the catalytic pocket.

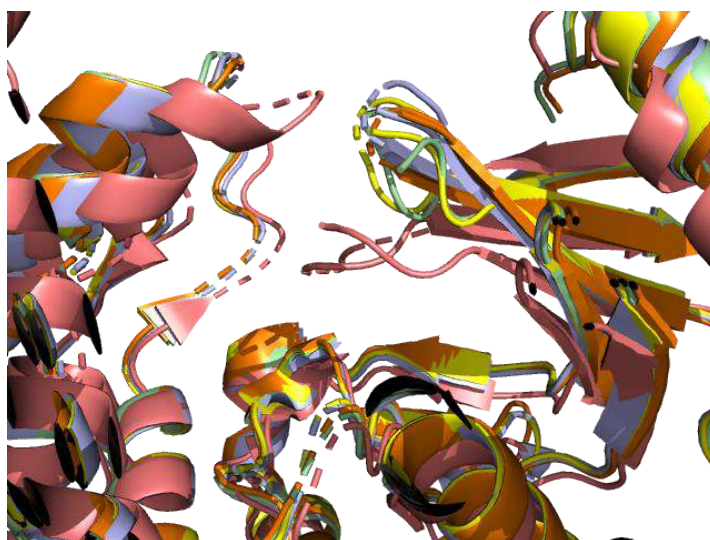


[Figure 57](#). Aligned crystallographic structures and their comparison to PDB: 3G15 (light blue color).

PDB: 4BR3 (green color, rmsd = 0.58 Å), PDB: 4CGA (orange color, rmsd = 0.82 Å), PDB: 5EQY (yellow color, rmsd = 0.44 Å) and PDB: 2CKQ (deep salmon color, rmsd = 2.05 Å).

We decided to use the PDB: 3G15 crystallographic structure as a template for docking because when aligned to the other crystal complexes the RMSD values are < 2 Å so that all maintain the semi-open conformation.

Choline Kinase is crystallized as a dimeric enzyme and each monomer has a catalytic site where the docking of the new ligands could be done. However, when both monomer chains were superimposed, we realized that chain A is more complete, and it was chosen to test the binding of the new libraries ([Scheme 20](#)).

Structure ID	Description	Sequence Length	Modeled residues	Coverage
3G15 A	Choline kinase alpha	401	354	86%
3G15 B	Choline kinase alpha	401	306	100%

ChoK alpha 1 reported crystallographic residues of chains A and B of the dimer.

	RMSD	TM-score	Score	SI%	SS%	Length	
	0.47	0.86	396.95	100	100	305	
32	RRRAYLWCKEFLP	GAWRGLREDEFHISVIRGGLSN	MLFQCSLPDTTATLG	81			
32	RRRAYLWCKEFLP	-AW-----	MLFQC-----	71			
82	DEPRK	VLLRLYGAAEAMVLESVMFAILAERSLGP	KLYGIFPQGRLEQFIP	154			
87	-----	VLLRL-----	MVLESVMFAILAERSLGP	KLYGIFPQGRLEQFIP	154		
155	SRRLDTEELS	LPDISAEIAEKMATFHGMKMPFNKEPKWLF	GTMEKYLKEV	204			
155	SRRLDTEELS	LPDISAEIAEKMATFHGMKMPFNKEPKWLF	GTMEKYLKEV	204			
205	LRIKFTEESRIK	KLHKLLSYNLPLELENLRSLL	ESTPSPVVFCHNDCQEG	254			
205	LRIKFTEESRIK	KLHKLLSYNLPLELENLRSLL	ESTPSPVVFCHNDCQEG	254			
255	NILLLEGRENSEK	QKLMLIDFEYSSNYRGF	DIGNHFCEWMDYSYEKYP	304			
255	NILLLEGRENSEK	QKLMLIDFEYSSNYRGF	DIGNHFCEWMDYSYEKYP	304			
305	FFRANIRKYPT	TKKQQLHF	FISSYLP	PAFQ	NDFENL	STEEKSIIKEEMLLEV	354
305	FFRANIRKYPT	TKKQQLHF	FISSYLP	PAFQ	NDFENL	STEEKSIIKEEMLLEV	354
355	RFALASHFLWGL	WSIVQAKISSIEFGYMDYA	QARFDAYFHQ	KRKLG			400
355	RFALASHFLWGL	WSIVQAKISSIEFGYMDYA	QARFDAYFHQ	KRKLG			400

Scheme 20. Superimposed amino acid sequence of the Choline Kinase $\alpha 1$ (PDB: 3G15) monomers A and B.

Pairs of residues that are structurally equivalent, are colored in orange (chain A) and blue (chain B).

Data collected from the RCSB PDB “Analysed” option, Pairwise Structure Alignment.

Some reported information is related to: RMSD (root mean square deviation); TM-score (template modelling score), a value > 0.5 indicates the same folding; SI% (sequence identity percentage); SS% (sequence similarity percentage); Length is the number of equivalent residues in the alignment.

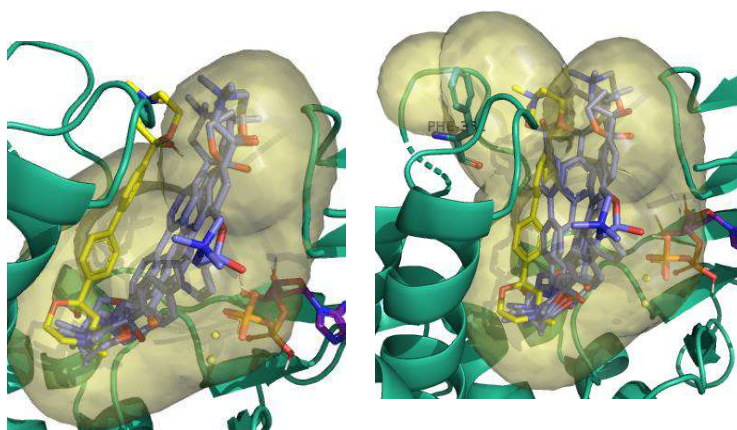


Figure 58. (Left part) Pocket designed by using the Flapsite algorithm and the poses of the docked HC-3. (Right part) Pocket designed with Phe 361 merged with the latter and the poses obtained while docking the crystallographic ligand. The crystallographic ligand has yellow carbon atoms.

pocket and involved the uncovered fragment of the ligand. It was chosen Glu 434, Phe 361 and a combination of both to create a new pocket with whom merge the pocket designed by default. Results pointed out that the Phe 361 residue constituted the best pocket using an extension of 6 and a thickness of 7.

Next, the catalytic pocket was searched with the Flapsite algorithm. To test its validation, we performed the docking of the crystallographic ligand HC-3 with the default parameters.

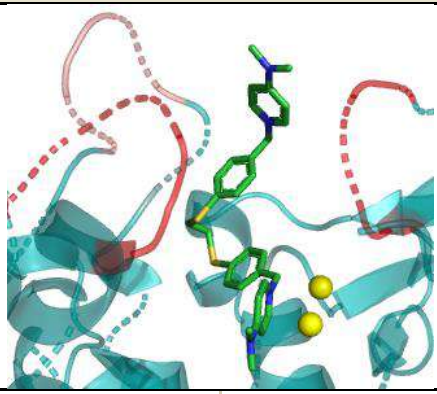
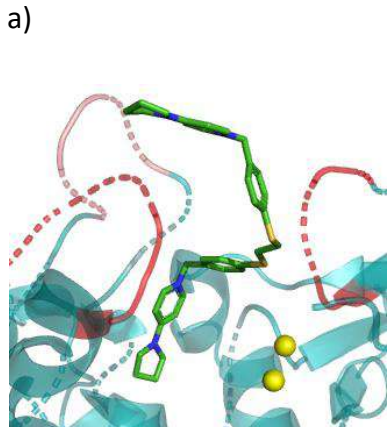
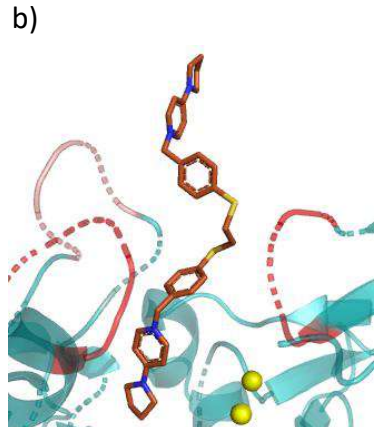
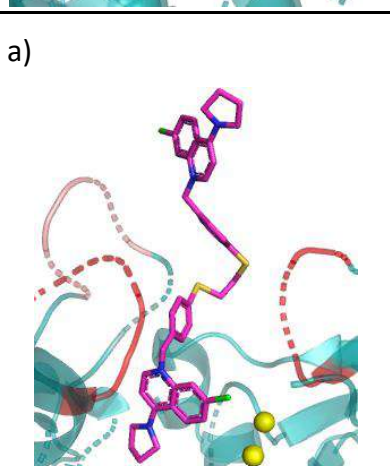
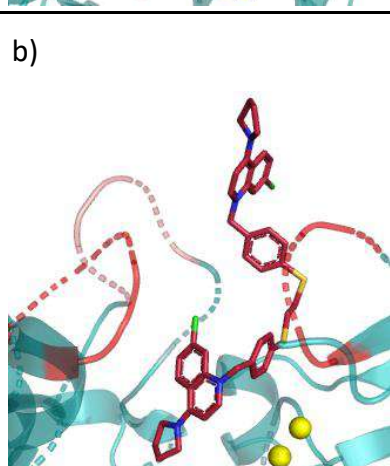
Unfortunately, the pocket didn't involve the whole ligand and, the second positively charged ring was left out. As so, none of the five poses generated was arranged in the correct position (as in the crystal) (Figure 58, left part).

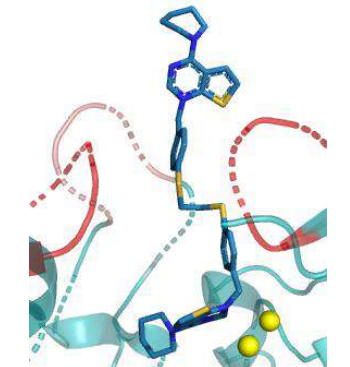
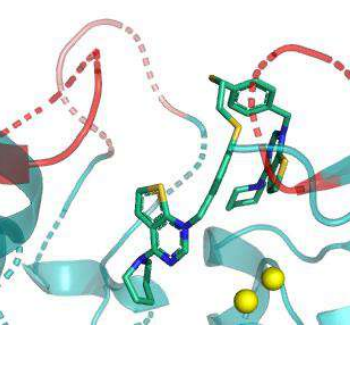
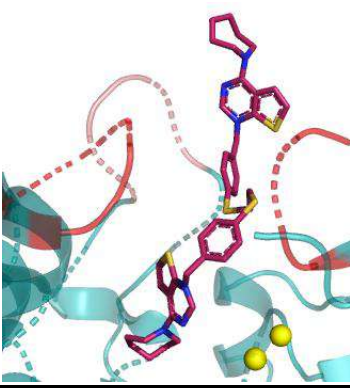
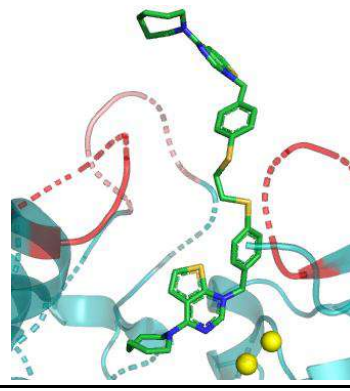
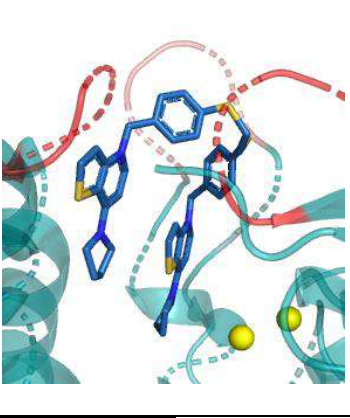
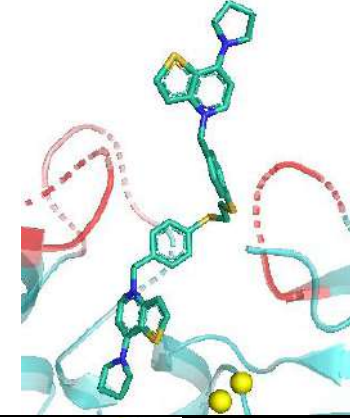
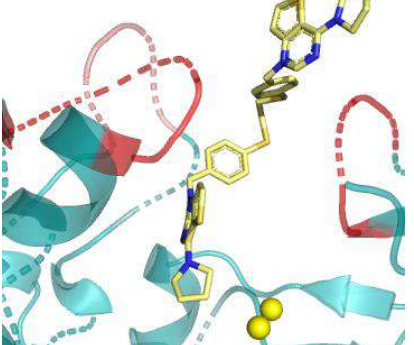
Given that, we selected one amino acid residue to be merged with the default

This time, when docking **HC-3** with the default parameters, at least one of the five poses generated overlaps the crystallographic pose (Figure 58, right part). For that reason, it was defined as the catalytic pocket and will be used to study the binding of the synthesized library of compounds.

2. The inhibitors' probability to adopt the pose.

The following Tables 17 and 18 show the most probable poses for each ligand.

Compound	Pose	Probability (%)
40		100
46	a)  b) 	a) 60 b) 40
48	a)  b) 	a) 50 b) 50

54	a) 	b) 	a) 80 b) 20
55	a) 	b) 	a) 20 b) 80
65	a) 	b) 	a) 40 b) 60
68			100

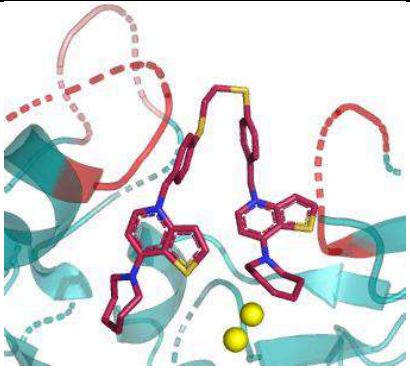
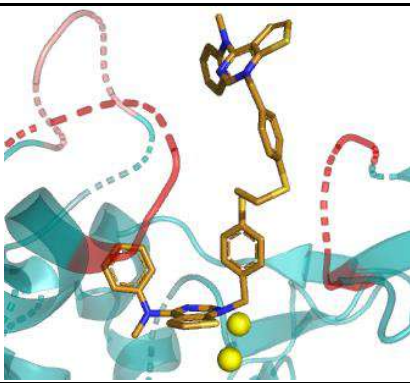
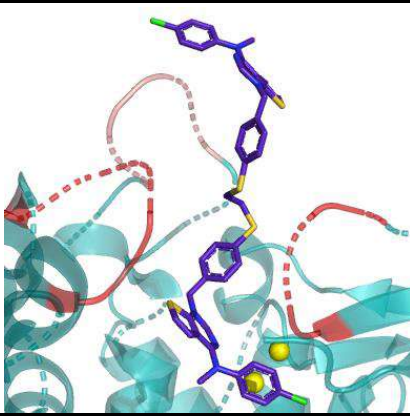
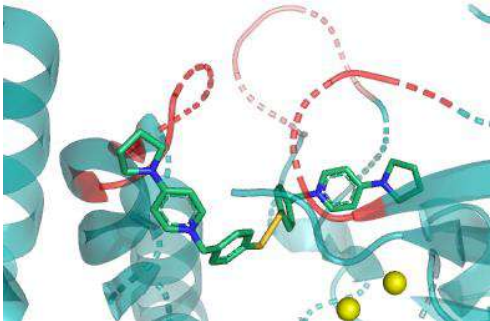
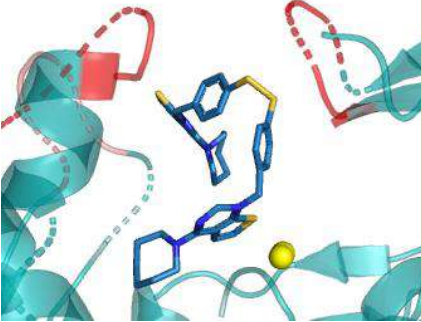
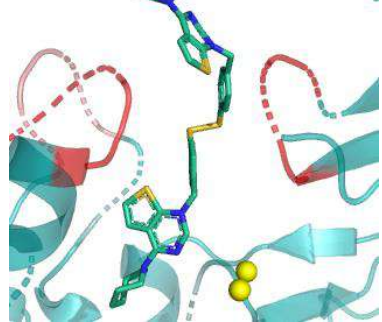
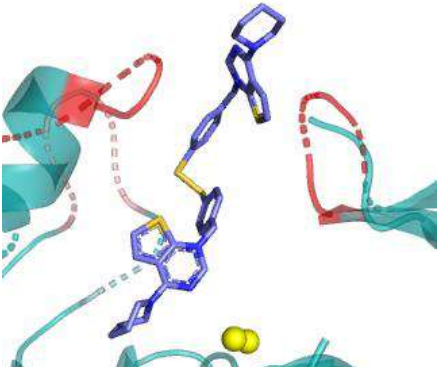
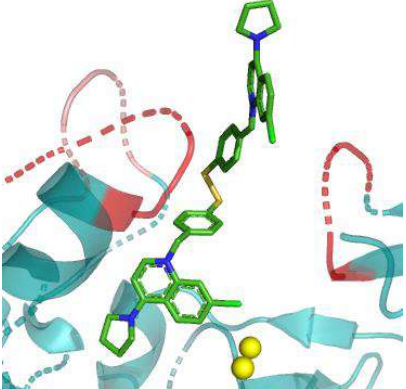
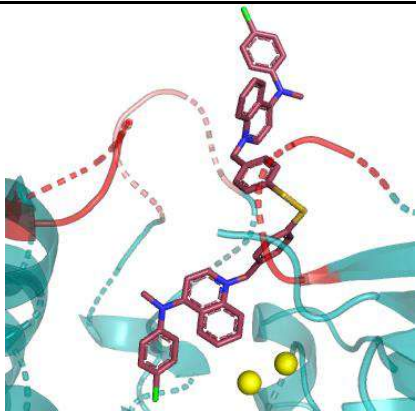
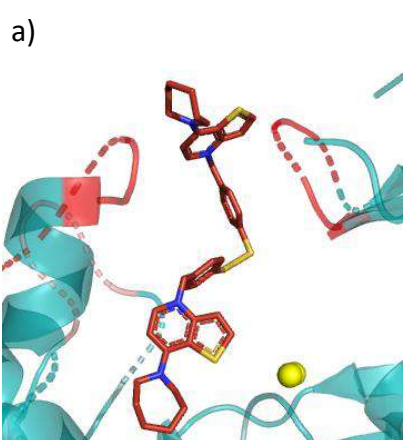
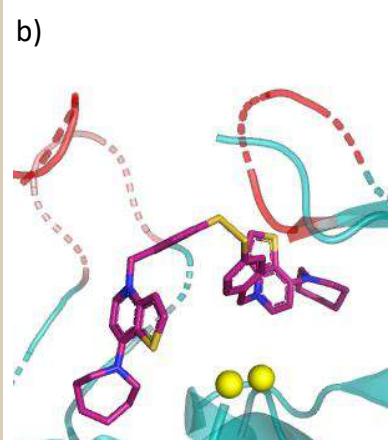
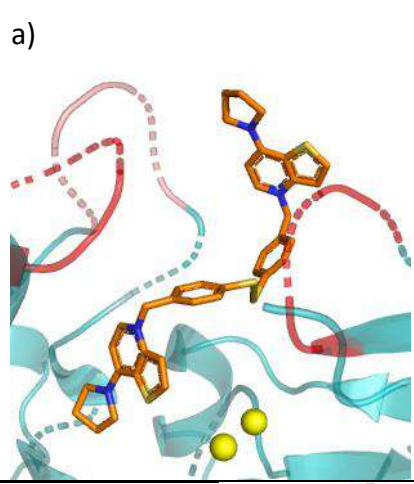
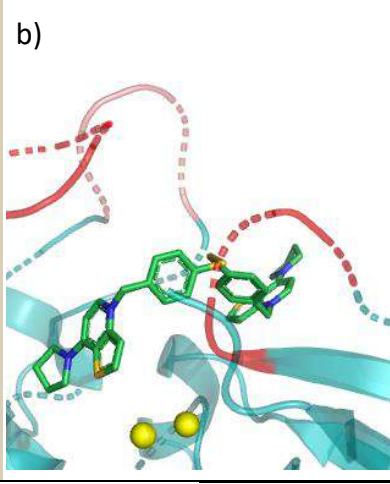
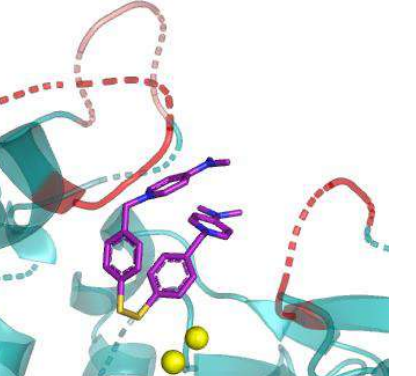
69	 Molecular docking pose 69 showing a ligand (red and yellow sticks) bound to a protein (teal ribbon). Two magnesium atoms are represented as yellow spheres. Delimited loops are shown as red dashed lines.	100
71	 Molecular docking pose 71 showing a ligand (yellow and blue sticks) bound to a protein (teal ribbon). Two magnesium atoms are represented as yellow spheres. Delimited loops are shown as red dashed lines.	100
73	 Molecular docking pose 73 showing a ligand (purple and yellow sticks) bound to a protein (teal ribbon). Two magnesium atoms are represented as yellow spheres. Delimited loops are shown as red dashed lines.	100

Table 17. Main poses obtained for the dithioethane library.
Mg atoms are represented as yellow spheres and delimited loops are coloured in red.

Compound	Pose	Probability (%)
FP 2	 A 3D molecular docking model showing a ligand (FP 2) in a protein binding pocket. The protein backbone is shown as a cyan ribbon, and the binding site is represented by a semi-transparent cyan surface. The ligand is shown in a stick representation with green and blue atoms. Two yellow spheres are visible in the binding site. Dotted lines indicate hydrogen bonds between the ligand and the protein.	
FP 3	<p>a)  b) </p> Two 3D molecular docking models of FP 3. Model (a) shows the ligand in a blue stick representation, and model (b) shows it in a green stick representation. Both models show the ligand bound to the protein binding site (cyan surface) with two yellow spheres. Dotted lines indicate hydrogen bonds.	
FP 4	 A 3D molecular docking model showing a ligand (FP 4) in a protein binding pocket. The protein backbone is shown as a cyan ribbon, and the binding site is represented by a semi-transparent cyan surface. The ligand is shown in a stick representation with blue and yellow atoms. Two yellow spheres are visible in the binding site. Dotted lines indicate hydrogen bonds.	
FP 5	 A 3D molecular docking model showing a ligand (FP 5) in a protein binding pocket. The protein backbone is shown as a cyan ribbon, and the binding site is represented by a semi-transparent cyan surface. The ligand is shown in a stick representation with green and blue atoms. Two yellow spheres are visible in the binding site. Dotted lines indicate hydrogen bonds.	

FP 7	 A 3D molecular model showing a ligand (red and blue sticks) bound to a protein (teal ribbon). The protein structure is partially shown, with the ligand interacting with a specific site. Two yellow spheres are visible at the bottom.	100
FP 14	<p>a)  3D molecular model of FP 14 (a) showing a ligand (red and blue sticks) bound to a protein (teal ribbon). The protein structure is partially shown, with the ligand interacting with a specific site. Two yellow spheres are visible at the bottom.</p> <p>b)  3D molecular model of FP 14 (b) showing a ligand (purple and blue sticks) bound to a protein (teal ribbon). The protein structure is partially shown, with the ligand interacting with a specific site. Two yellow spheres are visible at the bottom.</p>	a) 75 b) 25
FP 15	<p>a)  3D molecular model of FP 15 (a) showing a ligand (orange and blue sticks) bound to a protein (teal ribbon). The protein structure is partially shown, with the ligand interacting with a specific site. Two yellow spheres are visible at the bottom.</p> <p>b)  3D molecular model of FP 15 (b) showing a ligand (green and blue sticks) bound to a protein (teal ribbon). The protein structure is partially shown, with the ligand interacting with a specific site. Two yellow spheres are visible at the bottom.</p>	a) 60 b) 40
FP 16	 A 3D molecular model showing a ligand (purple and blue sticks) bound to a protein (teal ribbon). The protein structure is partially shown, with the ligand interacting with a specific site. Two yellow spheres are visible at the bottom.	100

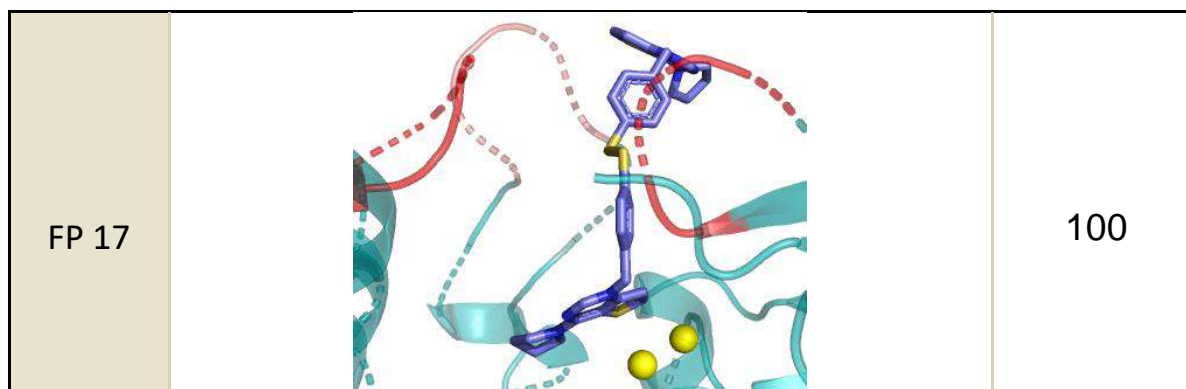


Table 18. Main poses obtained for the disulphide library.
Mg atoms are represented as yellow spheres and delimited loops are coloured in red.

3. Similarity and energetic values obtained by FLAP.

Herein, we report the most important parameter's values obtained when docking with FLAPdock. For simplicity, it was only reported the first three results that correspond with the highest S-scores and the mainly poses adopted in the defined pocket. When there is only one result is due to a sole solution was obtained (Tables 19 and 20). Next, it is reported the definition of each parameter to a better understanding of the obtained values.

S-score: The similarity score is a global score that includes terms from the GRID MIF similarities (hydrogen-bonding interactions, hydrophobic interactions, and shape), the LJ non-polar attractive and repulsive interactions, and the electrostatic (Q) interactions.

H, O, N1, DRY (probes score): represent the degree of overlap between the catalytic site MIFs and the compound molecular pseudo-fields, for each probe individually. It is calculated for a given superposition by directly comparing the volumes of the oriented MIFs. All similarities range from 0.0 (bad) to 1.0 (good).

Global Sum: is produced by summing all the scores of the individual probes together.

Global Product: is produced by multiplying all the scores of the individual probes together.

POSI: Each heavy atom in the ligand is mapped to its corresponding GRID probe and then, the probe energy is calculated at that position. The energies are summed across all heavy atoms to give a binding score.

POSI norm: POSI normalized values to be able of comparing them among compounds.

Etot: is the total energy of interaction at each GRID point, calculated as a sum of the LJ interactions, electrostatic effects, and hydrogen bond potential.

Compound	S-score	H	O	N1	DRY	GlobP	GlobSum	POSI	POSI norm	Etot
HC-3	1.001	1	0.425	0.451	0.577	0.329	1.221	47.93	0.116	0.113
40	0.902	0.976	0	1	0.406	0	1.118	40.389	0.078	0.171
	0.878	0.973	0	1	0.369	0	1.125	40.157	0.078	0.153
	0.857	0.976	0	1	0.377	0	1.12	38.804	0.075	0.131
46	0.863	0.784	0	1	0.512	0	1.282	64.029	0.113	0.168
	0.837	0.887	0	1	0.507	0	1.267	46.281	0.081	0.083
	0.817	0.806	0	1	0.391	0	1.173	44.945	0.079	0.142
48	0.698	0.779	0	1	0.361	0	1.226	50.85	0.069	0.045
	0.693	0.765	0	1	0.358	0	1.106	46.325	0.063	0.055
	0.585	0.835	0	1	0.37	0	1.222	45.944	0.062	-0.096
54	1.052	0.807	0.567	1	0.313	0.413	1.043	50.645	0.071	0.178
	1.045	0.839	0.449	1	0.32	0.417	1.057	47.124	0.066	0.189
	1.026	0.951	0.327	1	0.525	0.402	1.293	65.898	0.093	0.089
55	1.163	0.933	0.495	1	0.46	0.474	1.29	70.144	0.095	0.198
	1.062	0.864	0.404	1	0.342	0.415	1.102	60.178	0.081	0.191
	0.957	0.768	0.364	1	0.379	0.419	1.143	60.255	0.082	0.127
65	0.885	0.939	0	1	0.59	0	1.366	78.405	0.115	0.086
	0.813	0.885	0	1	0.541	0	1.351	73.501	0.108	0.051
	0.748	0.732	0	1	0.533	0	1.312	58.096	0.085	0.063
68	0.987	0.821	0.496	1	0.398	0.336	0.997	46.896	0.069	0.09
	0.957	0.838	0.507	1	0.374	0.361	0.966	46.943	0.069	0.074
	0.944	0.866	0.478	1	0.368	0.375	1.017	45.478	0.067	0.063
69	1.007	0.977	0	1	0.484	0.335	1.448	77.427	0.105	0.201
71	1.007	0.916	0.416	1	0.096	0.47	1.252	62.988	0.083	0.135
73	0.958	0.889	0.441	1	0.272	0.385	1.055	65.664	0.08	0.106
67	UNABLE TO BE DOCKED									
70	UNABLE TO BE DOCKED									
72	UNABLE TO BE DOCKED									

Table 19. S-score, MIFs, and energetic values for the dithioethane compounds library.

Compound	S-score	H	O	N1	DRY	GlobP	GlobSum	POSI	POSI norm	Etot
HC-3	1.001	1	0.425	0.451	0.577	0.329	1.221	47.93	0.116	0.113
FP 2	0.756 0.754	0.841 0.845	0.032 0.032	1 1	0.368 0.365	0.327 0.33	1.033 1.038	43.19 43.335	0.08 0.08	0.096 0.093
FP 3	1.265 1.186 0.986	0.995 0.986 0.761	0.441 0.484 0.452	1 1 1	0.526 0.547 0.445	0.493 0.493 0.414	1.346 1.334 1.118	69.576 71.895 56.329	0.098 0.101 0.079	0.243 0.149 0.114
FP 4	1.184 1.046 0.974	0.98 0.813 0.932	0.391 0.335 0.541	1 1 1	0.502 0.341 0.444	0.344 0.304 0.443	1.177 0.982 1.208	53.258 42.03 55.266	0.078 0.062 0.081	0.213 0.261 0.097
FP 5	0.997 0.884 0.872	0.81 0.805 0.855	1 0.032 0.2	1 1 1	0.44 0.489 0.475	0.71 0 0	1.315 1.32 1.266	45.931 58.171 51.004	0.065 0.082 0.072	-0.098 0.165 0.095
FP 7	0.546 0.532	0.845 0.921	0.032 0.612	1 1	0.396 0.385	0.293 0.31	1.301 1.373	56.56 72.595	0.072 0.093	-0.149 -0.34
FP 14	1.015 0.897 0.829	0.929 0.903 0.776	0.672 0.032 0.032	1 1 1	0.484 0.528 0.486	0.406 0.391 0.396	1.275 1.271 1.204	58.238 69.081 67.258	0.082 0.097 0.095	0.019 0.126 0.133
FP 15	0.885 0.853 0.76	0.895 0.778 0.78	0.362 0.435 0.302	1 1 1	0.391 0.437 0.407	0.431 0.364 0.413	1.22 1.125 1.128	50.927 55.395 42.668	0.078 0.085 0.065	0.089 -0.004 0.031
FP 16	1.013	1	0.5	1	0.539	0.498	1.322	39.904	0.082	0.023
FP 17	1.138 1.128 1.106	0.903 0.81 0.774	0.376 0.646 0.636	1 1 1	0.361 0.453 0.469	0.403 0.407 0.46	1.061 1.065 1.118	53.522 56.94 64.668	0.082 0.087 0.099	0.272 0.18 0.167

Table 20. S-score, MIFs and energetic values for the disulphide library of compounds.

References

1. World Health Organization (WHO). Geneva. *WHO Report on Cancer: Setting Priorities, Investing Wisely and Providing Care for All.*; 2020.
2. Luengo A, Gui DY, Vander Heiden MG. Targeting Metabolism for Cancer Therapy. *Cell Chem Biol.* 2017;24(9):1161-1180. doi:10.1016/j.chembiol.2017.08.028
3. Katz-Brull R, Margalit R, Bendel P, Degani H. Choline metabolism in breast cancer; ²H-, ¹³C- and ³¹P-NMR studies of cells and tumors. *Magn Reson Mater Physics, Biol Med.* 1998;6(1):44-52. doi:10.1016/S1352-8661(98)00009-X
4. Glunde K, Bhujwala ZM, Ronen SM. Choline metabolism in malignant transformation. *Nat Rev Cancer.* 2011;11:835-848. doi:10.1038/nrc3162
5. Gabellieri C, Belouèche-Babari M, Jamin Y, Payne GS, Leach MO, Eykyn TR. Modulation of choline kinase activity in human cancer cells observed by dynamic ³¹P NMR. *NMR Biomed.* 2009;22(4):456-461. doi:10.1002/nbm.1361
6. Ramírez De Molina A, Rodríguez-González A, Lacal JC. From Ras signalling to ChoK inhibitors: A further advance in anticancer drug design. *Cancer Lett.* 2004;206(2):137-148. doi:10.1016/j.canlet.2003.08.031
7. Ryan MB, Corcoran RB. Therapeutic strategies to target RAS-mutant cancers. *Nat Rev Clin Oncol.* 2018;15(11):709-720. doi:10.1038/s41571-018-0105-0
8. Hernández-Alcoceba R, Fernández F, Lacal JC. In vivo antitumor activity of choline kinase inhibitors: A novel target for anticancer drug discovery. *Cancer Res.* 1999;59:3112-3118. doi:10.1016/s0959-8049(99)80913-7
9. Hernández-Alcoceba R, Saniger L, Campos J, et al. Choline kinase inhibitors as a novel approach for antiproliferative drug design. *Oncogene.* 1997;15(19):2289-2301. doi:10.1038/sj.onc.1201414
10. Gallego-Ortega D, de Molina AR, Ramos MA, et al. Differential role of human choline kinase α and β enzymes in lipid metabolism: Implications in cancer onset and treatment. *PLoS One.* 2009;4(11). doi:10.1371/journal.pone.0007819
11. Gibellini F, Smith TK. The Kennedy pathway-de novo synthesis of phosphatidylethanolamine and phosphatidylcholine. *IUBMB Life.* 2010;62(6):414-428. doi:10.1002/iub.337
12. Cheng M, Bhujwala ZM, Glunde K. Targeting phospholipid metabolism in cancer. *Front Oncol.* 2016;6:266. doi:10.3389/fonc.2016.00266
13. Price BD, Morris JDH, Marshall CJ, Hall A. Stimulation of phosphatidylcholine hydrolysis, diacylglycerol release, and arachidonic acid production by oncogenic ras is a consequence of protein kinase C activation. *J Biol Chem.* 1989;264(28):16638-16643. doi:10.1016/s0021-9258(19)84753-1
14. Báñez-Coronel M, de Molina A, Rodríguez-González A, et al. Choline Kinase Alpha Depletion Selectively Kills Tumoral Cells. *Curr Cancer Drug Targets.* 2008;8(8):709-719. doi:10.2174/156800908786733432
15. De Molina AR, Báñez-Coronel M, Gutiérrez R, et al. Choline kinase activation is a critical requirement for the proliferation of primary human mammary epithelial cells and breast tumor progression. *Cancer Res.* 2004;64(18):6732-6739. doi:10.1158/0008-5472.CAN-04-0489
16. Hernando E, Sarmentero-Estrada J, Koppie T, et al. A critical role for choline kinase- α in the aggressiveness of bladder carcinomas. *Oncogene.* 2009;28(26):2425-2435. doi:10.1038/onc.2009.91
17. Ramírez de Molina A, Rodríguez-González A, Gutiérrez R, et al. Overexpression of choline kinase is a frequent feature in human tumor-derived cell lines and in lung, prostate, and colorectal human cancers. *Biochem Biophys Res Commun.* 2002;296:580-583. doi:10.1016/S0006-291X(02)00920-8
18. Wittenberg J, Kornberg A. Choline phosphokinase. *J Biol Chem.* 1953;202(1):431-444. doi:10.1016/s0021-9258(19)57144-7

19. Brostrom MA, Browning ET. Choline kinase from brewers' yeast. Partial purification, properties, and kinetic mechanism. *J Biol Chem.* 1973;248(7):2364-2371. doi:10.1016/S0021-9258(19)44118-5
20. Kee-Hong Kim, Dennis R. Voelker, Mark T. Flocco and GMC. Expression, purification, and characterization of choline kinase product of the CKI gene from *Saccharomyces cerevisiae*. *J Biol Chem.* 1998;273(12):6844-6852. doi:10.1074/jbc.273.12.6844
21. Peisach D, Gee P, Kent C, Xu Z. The crystal structure of choline kinase reveals a eukaryotic protein kinase fold. *Structure.* 2003;11(6):703-713. doi:10.1016/S0969-2126(03)00094-7
22. Yuan C, Kent C. Identification of Critical Residues of Choline Kinase A2 from *Caenorhabditis elegans*. *J Biol Chem.* 2004;279:17801-17809. doi:10.1074/jbc.M401382200
23. Milanese L, Espinosa A, Campos JM, Gallo MA, Entrena A. Insight into the inhibition of human choline kinase: Homology modeling and molecular dynamics simulations. *ChemMedChem.* 2006;1:1216-1228. doi:10.1002/cmdc.200600158
24. Malito E, Sekulic N, Too WCS, Konrad M, Lavie A. Elucidation of Human Choline Kinase Crystal Structures in Complex with the Products ADP or Phosphocholine. *J Mol Biol.* 2006;364(2):136-151. doi:10.1016/j.jmb.2006.08.084
25. Hong BS, Allali-Hassani A, Tempel W, et al. Crystal structures of human choline kinase isoforms in complex with Hemicholinium-3: Single amino acid near the active site influences inhibitor sensitivity. *J Biol Chem.* 2010;285:16330-16340. doi:10.1074/jbc.M109.039024
26. Sahún-Roncero M, Rubio-Ruiz B, Saladino G, et al. The mechanism of allosteric coupling in choline kinase α 1 revealed by the action of a rationally designed inhibitor. *Angew Chem Int Ed.* 2013;52:4582-4586. doi:10.1002/anie.201209660
27. Sahún-Roncero M, Rubio-Ruiz B, Saladino G, et al. The mechanism of allosteric coupling in choline kinase α 1 revealed by the action of a rationally designed inhibitor. *Angew Chemie - Int Ed.* 2013;52(17):4582-4586. doi:10.1002/anie.201209660
28. Hudson CS, Knegtel RM, Brown K, Charlton PA, Pollard JR. Kinetic and mechanistic characterisation of Choline Kinase- α . *Biochim Biophys Acta - Proteins Proteomics.* 2013;1834:1107-1116. doi:10.1016/j.bbapap.2013.02.008
29. Rubio-Ruiz B, Serrán-Aguilera L, Hurtado-Guerrero R, Conejo-García A. Recent advances in the design of choline kinase α inhibitors and the molecular basis of their inhibition. *Med Res Rev.* 2021;41:902-927. doi:10.1002/med.21746
30. Hamza M, Lloveras J, Ribbes G, Soula G, Douste-Blazy L. An in vitro study of hemicholinium-3 on phospholipid metabolism of Krebs II ascites cells. *Biochem Pharmacol.* 1983;32:1893-1897. doi:10.1016/0006-2952(85)90377-6
31. Cannon JG. Structure-Activity aspects of Hemicholinium-3 (HC-3) and its analogs and congeners. *Med Res Rev.* 1994;14(5):505-531. doi:10.1002/med.2610140503
32. Hernández-Alcoceba R, Saniger L, Campos J, et al. Choline kinase inhibitors as a novel approach for antiproliferative drug design. *Oncogene.* 1997;15(19):2289-2301. doi:10.1038/sj.onc.1201414
33. Campos J, Nunez M, Conejo-Garcia A, et al. QSAR-Derived Choline Kinase Inhibitors: How Rational can Antiproliferative Drug Design Be? *Curr Med Chem.* 2005;10(13):1095-1112. doi:10.2174/0929867033457539
34. Campos JM, Núez MC, Sánchez RM, et al. Quantitative structure-activity relationships for a series of symmetrical bisquaternary anticancer compounds. *Bioorganic Med Chem.* 2002;10(7):2215-2231. doi:10.1016/S0968-0896(02)00054-8
35. Conejo-García A, Báñez-Coronel M, Sánchez-Martín RM, et al. Influence of the linker in bispyridium compounds on the inhibition of human choline kinase. *J Med Chem.* 2004;47(22):5433-5440. doi:10.1021/jm0496537
36. Sánchez-Martín R, Campos JM, Conejo-García A, et al. Symmetrical bis-quinolinium compounds: New human choline kinase inhibitors with antiproliferative activity against the HT-29 cell line. *J Med Chem.* 2005;48(9):3354-3363. doi:10.1021/jm049061o

37. Rodríguez-González A, De Molina AR, Fernández F, Lacal JC. Choline kinase inhibition induces the increase in ceramides resulting in a highly specific and selective cytotoxic antitumoral strategy as a potential mechanism of action. *Oncogene*. 2004;23:8247-8259. doi:10.1038/sj.onc.1208045
38. Lacal JC, Campos JM. Preclinical characterization of RSM-932A, a novel anticancer drug targeting the human choline kinase alpha, an enzyme involved in increased lipid metabolism of cancer cells. *Mol Cancer Ther*. 2015;14:31-39. doi:10.1158/1535-7163.MCT-14-0531
39. TCD Pharma. Study of Intravenous TCD-717 in Patients With Advanced Solid Tumors. <https://clinicaltrials.gov/ct2/show/NCT01215864>
40. Conejo-García, Ana; Campos, Joaquín; Sánchez, Rosario M.; Rodríguez-González, Agustín; Lacal, Juan C.; Gallo, Miguel A.; Espinosa A. Choline kinase inhibitory effect and antiproliferative activity of new 1,1',1''-(benzene-1,3,5-triylmethylene)tris{4-[(disubstituted)amino]pyridinium} tribromides. *Eur J Med Chem*. 2003;38:109-116. doi:10.1016/s0223-5234(02)00004-1
41. Conejo-García A, Campos JM, Sánchez-Martín RM, Gallo MA, Espinosa A. Bispyridinium Cyclophanes: Novel Templates for Human Choline Kinase Inhibitors. *J Med Chem*. 2003;46:3754-3757. doi:10.1021/jm030792i
42. Conejo-García A, Campos J, Eder C, Entrena A, Gallo MA, Espinosa A. Synthesis and NMR studies on a C3-symmetrical triquinolina triscationic bicyclophane. *J Org Chem*. 2005;70:5748-5751. doi:10.1021/jo050554q
43. Rubio-Ruiz B, Conejo-García A, Ríos-Marco P, et al. Design, synthesis, theoretical calculations and biological evaluation of new non-symmetrical choline kinase inhibitors. *Eur J Med Chem*. 2012;50:154-162. doi:10.1016/j.ejmech.2012.01.050
44. Trousil S, Carroll L, Kalusa A, Aberg O, Kaliszczak M, Aboagye EO. Design of symmetrical and nonsymmetrical N,N-dimethylaminopyridine derivatives as highly potent choline kinase alpha inhibitors. *Med Chem Commun*. 2013;4:693-696. doi:10.1039/c3md00068k
45. Schiaffino-Ortega S, López-Cara LC, Ríos-Marco P, et al. New non-symmetrical choline kinase inhibitors. *Bioorganic Med Chem*. 2013;21(22):7146-7154. doi:10.1016/j.bmc.2013.09.003
46. Rubio-Ruiz B, Ramos-Torrecillas J, Capitán-Cañadas F, et al. Antiproliferative activity, cell cycle, and apoptosis studies of a series of 6-substituted 9H-purin-9-yl-pyridinium derivatives on a human cervical carcinoma cell line. *ChemMedChem*. 2013;8(8):1266-1269. doi:10.1002/cmdc.201300171
47. Schiaffino-Ortega S, Mariotto E, Luque-Navarro PM, et al. Anticancer and structure activity relationship of non-symmetrical choline kinase inhibitors. *Pharmaceutics*. 2021;13:1360. doi:10.3390/pharmaceutics13091360
48. Rubio-Ruiz B, Figuerola-Conchas A, Ramos-Torrecillas J, et al. Discovery of a new binding site on human choline kinase α 1: Design, synthesis, crystallographic studies, and biological evaluation of asymmetrical bispyridinium derivatives. *J Med Chem*. 2014;57:507-515. doi:10.1021/jm401665x
49. Rubbini G, Buades-Martín AB, Kimatrai-Salvador M, et al. Lead optimization-hit expansion of new asymmetrical pyridinium/quinolinium compounds as choline kinase α 1 inhibitors. *Future Med Chem*. 2018;10:1769-1786. doi:10.4155/fmc-2018-0059
50. Castro-Navas FF, Schiaffino-Ortega S, Carrasco-Jimenez MP, et al. New more polar symmetrical bipyridinic compounds: new strategy for the inhibition of choline kinase α 1. *Future Med Chem*. 2015;7:417-436.
51. Schiaffino-Ortega S, Baglioni E, Mariotto E, et al. Design, synthesis, crystallization and biological evaluation of new symmetrical biscationic compounds as selective inhibitors of human Choline Kinase α 1 (ChoK α 1). *Sci Rep*. 2016;6:23793. doi:10.1038/srep23793
52. Serrán- Aguilera L, Mariotto E, Rubbini G, et al. Synthesis, biological evaluation, in silico modeling and crystallization of novel small monocationic molecules with potent antiproliferative activity by dual mechanism. *Eur J Med Chem*. 2020;207:112797. doi:10.1016/j.ejmech.2020.112797
53. Estévez-Braun A, Ravelo AG, Pérez-Sacau E, Lacal JC. A new family of choline kinase inhibitors with antiproliferative and antitumor activity derived from natural products. *Clin Transl Oncol*. 2015;17:74-84. doi:10.1007/s12094-014-1260-0

54. Martín-Cantalejo Y, Sáez B, Monterde MI, Murillo MT, Braña MF. Synthesis and biological activity of new bispyridinium salts of 4,4'-bispyridyl-5,5'-perfluoroalkyl-2,2'-bisoxazoles. *Eur J Med Chem.* 2011;46:5662-5667. doi:10.1016/j.ejmech.2011.09.046
55. Arlauckas SP, Popov A V., Delikatny EJ. Direct inhibition of choline kinase by a near-infrared fluorescent carbocyanine. *Mol Cancer Ther.* 2014;13:2149-2158. doi:10.1158/1535-7163.MCT-14-0085
56. Clem BF, Clem AL, Yalcin A, et al. A novel small molecule antagonist of choline kinase- α that simultaneously suppresses MAPK and PI3K/AKT signaling. *Oncogene.* 2011;30:3370-3380. doi:10.1038/onc.2011.51
57. Chand P, Chesney JA, Clem BF, Tapolsky GH, Telang S, Trent JO. US2011/0257211 Small-molecule Choline Kinase inhibitors as anti-cancer therapeutics. Published online 2011.
58. Mortimore M, Everitt S, Rutherford A, Knegtel R. WO2013/043961 Compounds useful as inhibitors of Choline Kinase. Published online 2013.
59. Serrán-Aguilera L, Nuti R, López-Cara LC, et al. Pharmacophore-Based Virtual Screening to Discover New Active Compounds for Human Choline Kinase α 1. *Mol Inform.* 2015;34(6-7):458-466. doi:10.1002/minf.201400140
60. Zech SG, Kohlmann A, Zhou T, et al. Novel Small Molecule Inhibitors of Choline Kinase Identified by Fragment-Based Drug Discovery. *J Med Chem.* 2016;59(2):671-686. doi:10.1021/acs.jmedchem.5b01552
61. Zech SG, Kohlmann A, Li F, et al. WO2014/151761 Novel Choline Kinase Inhibitors. Published online 2013.
62. Casale E, Corti E, Gnocchi P, et al. WO2018/019681A1 Purine and 3-deazapurine analogues as Choline Kinase inhibitors. Published online 2017.
63. González-Díaz H, Viña D, Santana L, De Clercq E, Uriarte E. Stochastic entropy QSAR for the in silico discovery of anticancer compounds: Prediction, synthesis, and in vitro assay of new purine carbanucleosides. *Bioorganic Med Chem.* 2006;14(4):1095-1107. doi:10.1016/j.bmc.2005.09.039
64. Badari A, Casale E, Nesi M, Quartieri F. WO2019-011715 Pyrazolo-Quinazoline derivatives as Choline Kinase inhibitors. Published online 2018.
65. Felder ER, Badari A, Disingrini T, et al. The generation of purinome-targeted libraries as a means to diversify ATP-mimetic chemical classes for lead finding. *Mol Divers.* 2012;16(1):27-51. doi:10.1007/s11030-012-9361-6
66. Mariotto E, Bortolozzi R, Volpin I, et al. EB-3D a novel choline kinase inhibitor induces deregulation of the AMPK-mTOR pathway and apoptosis in leukemia T-cells. *Biochem Pharmacol.* 2018;155(July):213-223. doi:10.1016/j.bcp.2018.07.004
67. Mariotto E, Viola G, Ronca R, et al. Choline kinase alpha inhibition by EB-3D triggers cellular senescence, reduces tumor growth and metastatic dissemination in breast cancer. *Cancers (Basel).* 2018;10:391. doi:10.3390/cancers10100391
68. Yalcin A, Clem B, Makoni S, et al. Selective inhibition of choline kinase simultaneously attenuates MAPK and PI3K/AKT signaling. *Oncogene.* 2010;29(1):139-149. doi:10.1038/onc.2009.317
69. Trousil S, Kaliszczak M, Schug Z, et al. The novel choline kinase inhibitor ICL-CCIC-0019 reprograms cellular metabolism and inhibits cancer cell growth. *Oncotarget.* 2016;7(24):37103-37120. doi:10.18632/oncotarget.9466
70. Sola-Leyva A, López-Cara LC, Ríos-Marco P, Ríos A, Marco C, Carrasco-Jiménez MP. Choline kinase inhibitors EB-3D and EB-3P interferes with lipid homeostasis in HepG2 cells. *Sci Rep.* 2019;9:5109. doi:10.1038/s41598-019-40885-z
71. Jabalera Y, Sola-Leyva A, Peigneux A, et al. Biomimetic magnetic nanocarriers drive choline kinase alpha inhibitor inside cancer cells for combined chemo-hyperthermia therapy. *Pharmaceutics.* 2019;11:408. doi:10.3390/pharmaceutics11080408
72. Kall SL, Delikatny EJ, Lavie A. Identification of a Unique Inhibitor-Binding Site on Choline Kinase α .

- Biochemistry*. 2018;57:1316-1325. doi:10.1021/acs.biochem.7b01257
73. Falcon SC, Hudson CS, Huang Y, et al. A non-catalytic role of choline kinase alpha is important in promoting cancer cell survival. *Oncogenesis*. 2013;2:e38. doi:10.1038/oncsis.2013.2
 74. Miyake T, Parsons SJ. Functional interactions between Choline kinase α , epidermal growth factor receptor and c-Src in breast cancer cell proliferation. *Oncogene*. 2012;31:1431-1441. doi:10.1038/onc.2011.332
 75. Kall SL, Whitlatch K, Smithgall TE, Lavie A. Molecular basis for the interaction between human choline kinase alpha and the SH3 domain of the c-Src tyrosine kinase. *Sci Rep*. 2019;9:17121. doi:10.1038/s41598-019-53447-0
 76. Guma M, Sanchez-Lopez E, Lodi A, et al. Choline kinase inhibition in rheumatoid arthritis. *Ann Rheum Dis*. 2015;74(7):1399-1407. doi:10.1136/annrheumdis-2014-205696
 77. Li H, Zhu W, Zhang L, et al. The metabolic responses to hepatitis B virus infection shed new light on pathogenesis and targets for treatment. *Sci Rep*. 2015;5:8421. doi:10.1038/srep08421
 78. Zimmerman T, Lacal JC, Ibrahim SA. Choline Kinase Emerges as a Promising Drug Target in Gram-Positive Bacteria. *Front Microbiol*. 2019;6:2146. doi:10.3389/fmicb.2019.02146
 79. Mwakingwe-Omari A, Healy SA, Lane J, et al. Two chemoattenuated PfSPZ malaria vaccines induce sterile hepatic immunity. *Nature*. 2021;595:289-294. doi:10.1038/s41586-021-03684-z
 80. Minkah NK, Kappe SHI. Malaria vaccine gets a parasite boost in the liver. *Nature*. 2021;595:173-174. doi:10.1038/d41586-021-01720-6
 81. *World Malaria Report: 20 Years of Global Progress and Challenges*. Geneva:World Health Organization; 2020. <https://www.who.int/publications/i/item/9789240015791>
 82. Venugopal K, Hentzschel F, Valkiūnas G, Marti M. Plasmodium asexual growth and sexual development in the haematopoietic niche of the host. *Nat Rev Microbiol*. 2020;18:177-189. doi:10.1038/s41579-019-0306-2
 83. Vial HJ, Thuet MJ, Ancelin ML, Philippot JR, Chavis C. Phospholipid metabolism as a new target for malaria chemotherapy. Mechanism of action of D-2-amino-1-butanol. *Biochem Pharmacol*. 1984;33(17):2761-2770. doi:10.1016/0006-2952(84)90693-2
 84. Peyrottes S, Caldarelli S, Wein S, Périgaud C, Pellet A, Vial H. Choline Analogues in Malaria Chemotherapy. *Curr Pharm Des*. 2012;18:3454-3466. doi:10.2174/138161212801327338
 85. Martínez-Peinado N, Lorente-Macías Á, García-Salguero A, et al. Novel purine chemotypes with activity against Plasmodium Falciparum and Trypanosoma Cruzi. *Pharmaceuticals*. 2021;14(7):638. doi:10.3390/ph14070638
 86. Jiang X, Yuan Y, Huang J, et al. Structural Basis for Blocking Sugar Uptake into the Malaria Parasite Plasmodium falciparum. *Cell*. 2020;183:258-268. doi:10.1016/j.cell.2020.08.015
 87. Brancucci NMB, Gerdt JP, Wang CQ, et al. Lysophosphatidylcholine Regulates Sexual Stage Differentiation in the Human Malaria Parasite Plasmodium falciparum. *Cell*. 2017;171(7):1532-1544.e15. doi:10.1016/j.cell.2017.10.020
 88. Torretta A, Lopez-Cara LC, Parisini E. Crystal structure of the apo and the ADP-bound form of Choline Kinase from Plasmodium Falciparum. *Crystals*. 2020;10(7):613. doi:10.3390/cryst10070613
 89. Zimmerman T, Moneriz C, Diez A, et al. Antiplasmodial activity and mechanism of action of RSM-932A, a promising synergistic inhibitor of Plasmodium falciparum choline kinase. *Antimicrob Agents Chemother*. 2013;57(12):5878-5888. doi:10.1128/AAC.00920-13
 90. Serrán-Aguilera L, Denton H, Rubio-Ruiz B, et al. Plasmodium falciparum Choline Kinase Inhibition Leads to a Major Decrease in Phosphatidylethanolamine Causing Parasite Death. *Sci Rep*. 2016;6:33189. doi:10.1038/srep33189
 91. Rubio-Ruiz B, Castillo-Acosta VM, Pérez-Moreno G, et al. In vitro antiplasmodial and cytotoxic activities of asymmetrical pyridinium derivatives. *Eur J Med Chem*. 2014;85:289-292. doi:10.1016/j.ejmech.2014.07.105

92. Schiafino-Ortega S, Baglioni E, Pérez-Moreno G, et al. 1,2-Diphenoxiethane salts as potent antiplasmodial agents. *Bioorganic Med Chem Lett*. 2018;28(14):2485-2489. doi:10.1016/j.bmcl.2018.05.060
93. Aguilar-Troyano FJ, Torretta A, Rubbini G, et al. New Compounds with Bioisosteric Replacement of Classic Choline Kinase Inhibitors Show Potent Antiplasmodial Activity. *Pharmaceutics*. 2021;13(11):1842. doi:10.3390/pharmaceutics13111842
94. Wengelnik K, Vidal V, Ancelin ML, et al. A class of potent antimalarials and their specific accumulation in infected erythrocytes. *Science*. 2002;295:1311-1314. doi:10.1126/science.1067236
95. Hamzé A, Rubi E, Arnal P, et al. Mono- and Bis-Thiazolium Salts Have Potent Antimalarial Activity. *J Med Chem*. 2005;48:3639-3643.
96. Caldarelli SA, Boisbrun M, Alarcon K, et al. Exploration of potential prodrug approach of the bis-thiazolium salts T3 and T4 for orally delivered antimalarials. *Bioorganic Med Chem Lett*. 2010;20(13):3953-3956. doi:10.1016/j.bmcl.2010.05.001
97. Caldarelli SA, Duckert JF, Wein S, et al. Synthesis and evaluation of bis-thiazolium salts as potential antimalarial drugs. *ChemMedChem*. 2010;5(7):1102-1109. doi:10.1002/cmdc.201000097
98. Baroni M, Cruciani G, Sciabola S, Perruccio F, Mason JS. A Common Reference Framework for Analyzing / Comparing Proteins and Ligands . Fingerprints for Ligands And Proteins (FLAP): Theory and Application. *J Chem Inf Model*. 2007;47:279-294. doi:10.1021/ci600253e
99. Daina A, Michielin O, Zoete V. SwissADME: A free web tool to evaluate pharmacokinetics, drug-likeness and medicinal chemistry friendliness of small molecules. *Sci Rep*. 2017;7:42717. doi:10.1038/srep42717
100. Romagnoli R, Baraldi PG, Lopez-Cara C, et al. Concise Synthesis and Biological Evaluation of 2-Aroyl-5-Amino Benzo[b]thiophene Derivatives As a Novel Class of Potent Antimitotic Agents. *J Med Chem*. 2013;56:9296-9309. doi:10.1021/jm4013938
101. Sola-Leyva A, López-Cara LC, Ríos-Marco P, Ríos A, Marco C, Carrasco-Jiménez MP. Choline kinase inhibitors EB-3D and EB-3P interferes with lipid homeostasis in HepG2 cells. *Sci Rep*. 2019;9:5109. doi:10.1038/s41598-019-40885-z
102. Brenk R, Schipani A, James D, et al. Lessons learnt from assembling screening libraries for drug discovery for neglected diseases. *ChemMedChem*. 2008;3:435-444. doi:10.1002/cmdc.200700139
103. Zhang J, Yang PL, Gray NS. Targeting cancer with small molecule kinase inhibitors. *Nat Rev Cancer*. 2009;9:28-39. doi:10.1038/nrc2559
104. Russowsky D, Canto RFS, Sanches SAA, et al. Synthesis and differential antiproliferative activity of Biginelli compounds against cancer cell lines: Monastrol, oxo-monastrol and oxygenated analogues. *Bioorg Chem*. 2006;34:173-182. doi:10.1016/j.bioorg.2006.04.003
105. Chavarria D, Fernandes C, Silva T, et al. Bioisosteric OH- to SH-replacement changes the antioxidant profile of ferulic acid. *Org Biomol Chem*. 2019;17:9646. doi:10.1039/c9ob01875a
106. Hevey R. Bioisosteres of carbohydrate functional groups in glycomimetic design. *Biomimetics*. 2019;4:53. doi:10.3390/biomimetics4030053
107. Liu Z, Wang Y, Lin H, et al. Design, synthesis and biological evaluation of novel thieno[3,2-d]pyrimidine derivatives containing diaryl urea moiety as potent antitumor agents. *Eur J Med Chem*. 2014;85:215-227. doi:10.1016/j.ejmech.2014.07.099
108. Chauhan A, Khan T. Focal adhesion kinase—An emerging viable target in cancer and development of focal adhesion kinase inhibitors. *Chem Biol Drug Des*. 2021;97:774-794. doi:10.1111/cbdd.13808
109. Romagnoli R, Prencipe F, Oliva P, et al. Design, Synthesis, and Biological Evaluation of 6-Substituted Thieno[3,2-d]pyrimidine Analogues as Dual Epidermal Growth Factor Receptor Kinase and Microtubule Inhibitors. *J Med Chem*. 2019;62:1274-1290. doi:10.1021/acs.jmedchem.8b01391

110. Pingali SRK, Upadhyay SK, Jursic BS. Microwave-assisted benzyl mono- and dibromination in diethyl carbonate as environmentally friendly alternative to radical bromination in carbon tetrachloride. *Green Chem.* 2011;13(4):928-933. doi:10.1039/c0gc00794c
111. Jiang X, Shen M, Tang Y, Li C. Chemoselective monobromination of alkanes promoted by unactivated MnO₂. *Tetrahedron Lett.* 2005;46(3):487-489. doi:10.1016/j.tetlet.2004.11.113
112. Niculescu VC, Muresan N, Salageanu A, et al. Novel 2,3-disubstituted 1,4-naphthoquinone derivatives and their metal complexes - Synthesis and in vitro cytotoxic effect against mouse fibrosarcoma L929 cells. *J Organomet Chem.* 2012;700:13-19. doi:10.1016/j.jorganchem.2011.10.036
113. Hu ZJ, Sun PP, Li L, et al. Two novel π -conjugated carbazole derivatives with blue two-photon-excited fluorescence. *Chem Phys.* 2009;355:91-98. doi:10.1016/j.chemphys.2008.10.031
114. Lechuga-Eduardo H, Zarza-Acuña E, Romero-Ortega M. Synthesis of 3-substituted 2-cyclohexenones through umpoled functionalization. *Tetrahedron Lett.* 2017;58(33):3234-3237. doi:10.1016/j.tetlet.2017.07.007
115. Conejo-García A, Báñez-Coronel M, Sañchez-Martín RM, et al. Influence of the linker in bispyridium compounds on the inhibition of human choline kinase. *J Med Chem.* 2004;47(22):5433-5440. doi:10.1021/jm0496537
116. Sánchez-Martín R, Campos JM, Conejo-García A, et al. Symmetrical bis-quinolinium compounds: New human choline kinase inhibitors with antiproliferative activity against the HT-29 cell line. *J Med Chem.* 2005;48(9):3354-3363. doi:10.1021/jm049061o
117. Strappaveccia G, Ismalaj E, Petrucci C, et al. A biomass-derived safe medium to replace toxic dipolar solvents and access cleaner Heck coupling reactions. *Green Chem.* 2015;17:365-372. doi:10.1039/c4gc01677g
118. Horváth IT. Solvents from nature. *Green Chem.* 2008;10:1024-1028. doi:10.1039/b812804a
119. Li X, Xu J. Effects of the Microwave Power on the Microwave-assisted Esterification. *Curr Microw Chem.* 2017;4(2):158-162. doi:10.2174/2213335603666160906151018
120. Anastas, P. T.; Warner JC. *Green Chemistry Theory and Practice*. Oxford University Press; 1998.
121. Trost BM. The atom economy - A search for synthetic efficiency. *Science.* 1991;254(5037):1471-1477. doi:10.1126/science.1962206
122. Sheldon RA. The E factor 25 years on: the rise of green chemistry and sustainability. *Green Chem.* 2017;19(1):18-43. doi:10.1039/c6gc02157c
123. Eissen M, Metzger JO. Environmental performance metrics for daily use in synthetic chemistry. *Chem - A Eur J.* 2002;8(16):3580-3585. doi:10.1002/1521-3765(20020816)8:16<3580::AID-CHEM3580>3.0.CO;2-J
124. Van Aken K, Strekowski L, Patiny L. EcoScale, a semi-quantitative tool to select an organic preparation based on economical and ecological parameters. *Beilstein J Org Chem.* 2006;2(3). doi:10.1186/1860-5397-2-3
125. Oost, Thorsten; Anderskewitz, Ralf; Hamprecht, Dieter Wolfgang; Hoenke, Christoph; Martyres D et al. Pyrazole Compounds as CRTH2 antagonists. WO2011092140. 2011;(August).
126. Jimenez-Gonzalez C, Ponder CS, Broxterman QB, Manley JB. Using the right green yardstick: Why process mass intensity is used in the pharmaceutical industry to drive more sustainable processes. *Org Process Res Dev.* 2011;15(4):912-917. doi:10.1021/op200097d
127. Goodford PJ. A Computational Procedure for Determining Energetically Favorable Binding Sites on Biologically Important Macromolecules. *J Med Chem.* 1985;28:849-857. doi:10.1021/jm00145a002
128. Carosati E, Sciabola S, Cruciani G. Hydrogen bonding interactions of covalently bonded fluorine atoms: From crystallographic data to a new angular function in the GRID force field. *J Med Chem.* 2004;47:5114-5125. doi:10.1021/jm0498349
129. Siragusa L, Luciani R, Borsari C, et al. Comparing Drug Images and Repurposing Drugs with BioGPS

- and FLAPdock: The Thymidylate Synthase Case. *ChemMedChem*. 2016;11:1653-1666. doi:10.1002/cmdc.201600121
130. Gabriele Cruciani, Raimund Mannhold, Hugo Kubinyi GF. *Molecular Interaction Fields. Applications in Drug Discovery and ADME Prediction*. Wiley-VCH; 2006.
131. Spyraakis F, Santucci M, Maso L, et al. Virtual screening identifies broad-spectrum β -lactamase inhibitors with activity on clinically relevant serine- and metallo-carbapenemases. *Sci Rep*. 2020;10:12763. doi:10.1038/s41598-020-69431-y
132. Massari S, Bertagnin C, Pismataro MC, et al. Synthesis and characterization of 1,2,4-triazolo[1,5-a]pyrimidine-2-carboxamide-based compounds targeting the PA-PB1 interface of influenza A virus polymerase. *Eur J Med Chem*. 2021;209:112944. doi:10.1016/j.ejmech.2020.112944
133. Chessum N, Jones K, Pasqua E, Tucker M. *Recent Advances in Cancer Therapeutics*. Vol 54. 1st ed. Elsevier B.V.; 2015. doi:10.1016/bs.pmch.2014.11.002
134. Hille C, Berg M, Bressel L, et al. Time-domain fluorescence lifetime imaging for intracellular pH sensing in living tissues. *Anal Bioanal Chem*. 2008;391:1871-1879. doi:10.1007/s00216-008-2147-0
135. Jiang N, Fan J, Xu F, et al. Ratiometric fluorescence imaging of cellular polarity: Decrease in mitochondrial polarity in cancer cells. *Angew Chemie - Int Ed*. 2015;54:2510-2514. doi:10.1002/anie.201410645
136. Wang K-N, Liu L-Y, Mao D, et al. Polarity-Sensitive Ratiometric Fluorescence Probe for Monitoring Lipid Droplets/Nucleus change during Ferroptosis. *Angew Chem Int Ed*. 2021;60:15095-15100. doi:10.1002/anie.202104163
137. Kuimova MK, Yahioglu G, Levitt JA, Suhling K. Molecular rotor measures viscosity of live cells via fluorescence lifetime imaging. *J Am Chem Soc*. 2008;130:6672-6673. doi:10.1021/ja800570d
138. Espinar-Barranco L, Luque-Navarro P, Strnad MA, et al. A solvatofluorochromic silicon-substituted xanthene dye useful in bioimaging. *Dye Pigment*. 2019;168:264-272. doi:10.1016/j.dyepig.2019.04.024
139. Baell J, Walters MA. Chemistry: Chemical con artists foil drug discovery. *Nature*. 2014;513:481-483. doi:10.1038/513481a
140. Baell JB. Observations on screening-based research and some concerning trends in the literature. *Future Med Chem*. 2010;2:1529-1546. doi:10.4155/fmc.10.237
141. Li YG, Li L, Yang MY, He G, Kantchev EAB. A Bulky Disulfoxide Ligand for Pd-Catalyzed Oxidative Allylic C-H Amination with 2,2,2-Trichloroethyl Tosyl Carbamate. *J Org Chem*. 2017;82(9):4907-4917. doi:10.1021/acs.joc.6b03089
142. Little MA, Loughrey JJ, Santoro A, Halcrow MA, Hardie MJ. Hexasulfanyl analogues of cyclotrimeratrylene. *Tetrahedron Lett*. 2014;55(15):2530-2533. doi:10.1016/j.tetlet.2014.03.025
143. Fekner T, Gallucci J, Chan MK. Ruffling-Induced Chirality: Synthesis, Metalation, and Optical Resolution of Highly Nonplanar, Cyclic, Benzimidazole-Based Ligands. *J Am Chem Soc*. 2004;126:223-236. doi:10.1021/ja030196d
144. Wang Y, Du Y, Huang X, et al. Carbene-Catalyzed Reductive Coupling of Nitrobenzyl Bromide and Nitroalkene via the Single-Electron-Transfer (SET) Process and Formal 1,4-Addition. *Org Lett*. 2017;19(3):632-635. doi:10.1021/acs.orglett.6b03792
145. Arnold Lee, Daniel and Murphy Eric A. Heterocyclic compounds useful for Kinase inhibition. Published online 2011:156. WO 2011/119894
146. Grice, R. and Owen LN. Cytotoxic Compounds. Part IV. Substituted Benzyl Halides. *J Chem Soc*. Published online 1963:1947-1954. doi:10.1039/JR9630001947
147. Alagic A, Koprianiuk A, Kluger R. Hemoglobin - Superoxide Dismutase - Chemical Linkages That Create a Dual-Function Protein. *J Am Chem Soc*. 2005;127(22):8036-8043. doi:10.1021/ja050339r
148. Curran D, Dada O, Müller-Bunz H, et al. Synthesis and cytotoxicity studies of novel NHC*-gold(I) complexes derived from lepidiline A. *Molecules*. 2018;23(8):2031.

- doi:10.3390/molecules23082031
149. Xie Q, Ni C, Zhang R, Li L, Rong J, Hu J. Efficient Difluoromethylation of Alcohols Using TMSCF₂Br as a Unique and Practical Difluorocarbene Reagent under Mild Conditions. *Angew Chemie - Int Ed.* 2017;56(12):3206-3210. doi:10.1002/anie.201611823
 150. Aoyama E, Fuchida H, Oshikawa Y, Uchinomiya S, Ojida A. Intracellular delivery of chemical probes using a glutathione-responsive traceless tag. *Chem Commun.* 2016;52(49):7715-7718. doi:10.1039/c6cc03336a
 151. Dumur F, Roubaud V, Dumas E, Mayer CR. Efficient syntheses of thiophenol derivatives. *Synlett.* 2010;(16):2477-2481. doi:10.1055/s-0030-1258058
 152. Aguilar-Troyano FJ, Torretta A, Rubbini G, Fasiolo A et al. New Compounds with Bioisosteric Replacement of Classic Choline Kinase Inhibitors Show Potent Antiplasmodial Activity. *Pharmaceutics.* 2021;13(11):1842. doi:https://doi.org/10.3390/pharmaceutics13111842
 153. Chen P, Luo K, Yu X, et al. Cu-Catalyzed Direct Amination of Cyclic Amides via C-OH Bond Activation Using DMF. *Org Lett.* 2020;22(16):6547-6551. doi:10.1021/acs.orglett.0c02320
 154. Gill RK, Singh H, Raj T, Sharma A, Singh G, Bariwal J. 4-Substituted thieno[2,3-d]pyrimidines as potent antibacterial agents: Rational design, microwave-assisted synthesis, biological evaluation and molecular docking studies. *Chem Biol Drug Des.* 2017;90(6):1115-1121. doi:10.1111/cbdd.13028
 155. Robba, M.; Lecomte, J.M; Cugnon de Sévricourt M. Thienopyrimidines II. Etude de la thiéno [3.2-d] pyrimidine et de quelques dérivés. *Tetrahedron.* 1971;27:487-499. doi:https://doi.org/10.1016/S0040-4020(01)90718-5
 156. Entrena Guadix, Antonio José; López Cara, Luisa Carlota; Espinosa Ubeda, Antonio; Schiaffino Ortega, Santiago; Marco de la Calle, Carmen; Carrasco Jiménez, María Paz; Ríos Marco, Pablo; Viola, Giampetro; Bortolozzi, Roberta and Basso G. Inhibidores polares simétricos de Colina Cinasa con actividad antitumoral. Published online 2015. ES2482290B1
 157. Abou-Shehada S, Teasdale MC, Bull SD, Wade CE, Williams JMJ. Lewis acid activation of pyridines for nucleophilic aromatic substitution and conjugate addition. *ChemSusChem.* 2015;8(6):1083-1087. doi:10.1002/cssc.201403154
 158. Sheldon RA. Organic Synthesis: Past, Present and Future. *Chem Ind.* 1992;23:903-906.
 159. Sheldon RA. Metrics of Green Chemistry and Sustainability: Past, Present, and Future. *ACS Sustain Chem Eng.* 2018;6:32-48. doi:10.1021/acssuschemeng.7b03505
 160. Zimmerman JB, Anastas PT, Erythropel HC, Leitner W. Designing for a green chemistry future. *Science.* 2020;367:397-400. doi:10.1126/science.aay3060
 161. de Gonzalo G, Alcántara AR, Domínguez de María P. Cyclopentyl Methyl Ether (CPME): A Versatile Eco-Friendly Solvent for Applications in Biotechnology and Biorefineries. *ChemSusChem.* 2019;12:2083-2097. doi:10.1002/cssc.201900079
 162. Clarke CJ, Tu WC, Levers O, Bröhl A, Hallett JP. Green and Sustainable Solvents in Chemical Processes. *Chem Rev.* 2018;118:747-800. doi:10.1021/acs.chemrev.7b00571
 163. Regalbutto JR. Engineering: Cellulosic biofuels - Got gasoline? *Science.* 2009;325:822. doi:10.1126/science.1174581
 164. Hauenstein O, Agarwal S, Greiner A. Bio-based polycarbonate as synthetic toolbox. *Nat Commun.* 2016;7:11862. doi:10.1038/ncomms11862
 165. Thompson GD, Dutton R, Sparks TC. Spinosad – a case study : an example from a natural products discovery programme. *Pest Manag Sci.* 2000;56:696-702. doi:10.1002/1526-4998(200008)56:8<696::AID-PS182>3.0.CO;2-5
 166. Bogdan AR, Dombrowski AW. Emerging Trends in Flow Chemistry and Applications to the Pharmaceutical Industry. *J Med Chem.* 2019;62:6422-6468. doi:10.1021/acs.jmedchem.8b01760
 167. Luque Navarro PM, Lanari D. Flow synthesis of biologically-relevant compound libraries. *Molecules.* 2020;25:909. doi:10.3390/molecules25040909

168. Alam MP, Bilousova T, Spilman P, et al. A Small Molecule Mimetic of the Humanin Peptide as a Candidate for Modulating NMDA-Induced Neurotoxicity. *ACS Chem Neurosci*. 2018;9:462-468. doi:10.1021/acscchemneuro.7b00350
169. Ferlin F, Lanari D, Vaccaro L. Sustainable Flow Approaches to Active Pharmaceutical Ingredients. *Green Chem*. 2020;22:5937-5955. doi:10.1039/d0gc02404j
170. Shanmugam, S.; Gouni, L. R.; Tammireddy GN. TM. An improved process for the preparation of an antihistamine agent. WO2018/002696 A1. 2011;44(8):1-8.
171. Borukhova S, Noël T, Hessel V. Continuous-Flow Multistep Synthesis of Cinnarizine, Cyclizine, and a Buclizine Derivative from Bulk Alcohols. *ChemSusChem*. 2016;9:67-74. doi:10.1002/cssc.201501367
172. Vaccaro L, Curini M, Ferlin F, et al. Definition of green synthetic tools based on safer reaction media, heterogeneous catalysis, and flow technology. *Pure Appl Chem*. 2018;90:21-33. doi:10.1515/pac-2017-0409
173. Schmidt SB, Husted S. The biochemical properties of manganese in plants. *Plants*. 2019;8:381. doi:10.3390/plants8100381
174. Shen YF, Zenger RP, Suib SL, McCurdy L, Potter DI, O'Young CL. Octahedral molecular sieves: Preparation, characterization and applications. *J Chem Soc Chem Commun*. 1992;17:1213-1214. doi:10.1039/C39920001213
175. DeGuzman RN, Shen YF, Neth EJ, et al. Synthesis and Characterization of Octahedral Molecular Sieves (OMS-2) Having the Hollandite Structure. *Chem Mater*. 1994;6:815-821. doi:10.1021/cm00042a019
176. Ching S, Roark JL, Duan N, Suib SL. Sol-Gel Route to the Tunneled Manganese Oxide Cryptomelane. *Chem Mater*. 1997;9:750-754. doi:10.1021/cm960460k
177. Kim SH, Kim SJ, Oh SM. Preparation of layered MnO₂ via thermal decomposition of KMnO₄ and its electrochemical characterizations. *Chem Mater*. 1999;11:557-563. doi:10.1021/cm9801643
178. Qiu G, Huang H, Dharmarathna S, Benbow E, Stafford L, Suib SL. Hydrothermal synthesis of manganese oxide nanomaterials and their catalytic and electrochemical properties. *Chem Mater*. 2011;23:3892-3901. doi:10.1021/cm2011692
179. Malinger KA, Ding Y-S, Sithambaram S, Espinal L, Gomez S, Suib SL. Microwave frequency effects on synthesis of cryptomelane-type manganese oxide and catalytic activity of cryptomelane precursor. *J Catal*. 2006;239:290-298. doi:10.1016/j.jcat.2006.02.005
180. Ding Y-S, Shen X-F, Sithambaram S, et al. Synthesis and catalytic activity of cryptomelane-type manganese dioxide nanomaterials produced by a novel solvent-free method. *Chem Mater*. 2005;17:5382-5389. doi:10.1021/cm051294w
181. Dharmarathna S, King'ondeu CK, Pedrick W, Pahalagedara L, Suib SL. Direct sonochemical synthesis of manganese octahedral molecular sieve (OMS-2) nanomaterials using cosolvent systems, their characterization, and catalytic applications. *Chem Mater*. 2012;24:705-712. doi:10.1021/cm203366m
182. Ming S, Wang P, Liu P, et al. Promotional effect of metal cations doping on OMS-2 catalysts for NH₃-SCR reaction. *Chem Eng J*. 2020;379:122287. doi:10.1016/j.cej.2019.122287
183. Suib SL. Porous Manganese Sieves and Octahedral Layered Materials. *Acc Chem Res*. 2008;41:479-487. doi:https://doi.org/10.1021/ar7001667
184. Shen X-F, Ding Y-S, Liu J, et al. A magnetic route to measure the average oxidation state of mixed-valent manganese in manganese oxide octahedral molecular sieves (OMS). *J Am Chem Soc*. 2005;127:6166-6167. doi:10.1021/ja043406a
185. Opembe NN, Son Y-C, Srisakandakumar T, Suib SL. Kinetics and mechanism of 9H-fluorene oxidation catalyzed by manganese oxide octahedral molecular sieves. *ChemSusChem*. 2008;1:182-185. doi:10.1002/cssc.200700094
186. Sithambaram S, Nyutu EK, Suib SL. OMS-2 catalyzed oxidation of tetralin: A comparative study of

- microwave and conventional heating under open vessel conditions. *Appl Catal A Gen.* 2008;348:214-220. doi:10.1016/j.apcata.2008.06.046
187. Kumar R, Sithambaram S, Suib SL. Cyclohexane oxidation catalyzed by manganese oxide octahedral molecular sieves-Effect of acidity of the catalyst. *J Catal.* 2009;262:304-313. doi:10.1016/j.jcat.2009.01.007
188. Yodsa-nga A, Millanar JM, Neramittagapong A, Khemthong P, Wantala K. Effect of manganese oxidative species in as-synthesized K-OMS 2 on the oxidation of benzene. *Surf Coatings Technol.* 2015;271:217-224. doi:10.1016/j.surfcoat.2014.12.025
189. Wang S, Huang Y, Meng X, Liu X. Highly efficient and heterogeneous OMS-2 for the directly oxidative degradation of organic dyes under acidic condition. *Inorg Chem Commun.* 2020;117:107969. doi:10.1016/j.inoche.2020.107969
190. Son Y-C, Makwana VD, Howell AR, Suib SL. Efficient, catalytic, aerobic oxidation of alcohols with octahedral molecular sieves. *Angew Chemie - Int Ed.* 2001;40:4280-4283. doi:10.1002/1521-3773(20011119)40:22<4280::AID-ANIE4280>3.0.CO;2-L
191. Schurz F, Bauchert JM, Merker T, Schleid T, Hasse H, Gläser R. Octahedral molecular sieves of the type K-OMS-2 with different particle sizes and morphologies: Impact on the catalytic properties in the aerobic partial oxidation of benzyl alcohol. *Appl Catal A Gen.* 2009;355:42-49. doi:10.1016/j.apcata.2008.11.014
192. Iyer A, Galindo H, Sithambaram S, King'ondeu C, Chen CH, Suib SL. Nanoscale manganese oxide octahedral molecular sieves (OMS-2) as efficient photocatalysts in 2-propanol oxidation. *Appl Catal A Gen.* 2010;375:295-302. doi:10.1016/j.apcata.2010.01.012
193. Sithambaram S, Ding Y, Li W, Shen X, Gaenzler F, Suib SL. Manganese octahedral molecular sieves catalyzed tandem process for synthesis of quinoxalines. *Green Chem.* 2008;10:1029-1032. doi:10.1039/b805155k
194. Dharmarathna S, King'ondeu CK, Pahalagedara L, Kuo CH, Zhang Y, Suib SL. Manganese octahedral molecular sieve (OMS-2) catalysts for selective aerobic oxidation of thiols to disulfides. *Appl Catal B Environ.* 2014;147:124-131. doi:10.1016/j.apcatb.2013.08.002
195. Kumar R, Garces LJ, Son Y-C, Suib SL, Malz RE. Manganese oxide octahedral molecular sieve catalysts for synthesis of 2-aminodiphenylamine. *J Catal.* 2005;236:387-391. doi:10.1016/j.jcat.2005.10.024
196. Meng X, Wang Y, Chen B, Chen G, Jing Z, Zhao P. OMS-2/H₂O₂/Dimethyl Carbonate: An Environmentally-Friendly Heterogeneous Catalytic System for the Oxidative Synthesis of Benzoxazoles at Room Temperature. *Org Process Res Dev.* 2017;21:2018-2024. doi:10.1021/acs.oprd.7b00315
197. Grasselli RK. Fundamental principles of selective heterogeneous oxidation catalysis. *Top Catal.* 2002;21:79-88. doi:10.1023/A:1020556131984
198. Poyraz AS, Huang J, Cheng S, et al. Effective recycling of manganese oxide cathodes for lithium based batteries. *Green Chem.* 2016;18:3414-3421. doi:10.1039/c6gc00438e
199. Zhang T, Liu J, Sun DD. A novel strategy to fabricate inorganic nanofibrous membranes for water treatment: Use of functionalized graphene oxide as a cross linker. *RSC Adv.* 2012;2:5134-5137. doi:10.1039/c2ra20300f
200. Mardazad N, Khorshidi A, Fallah Shojaei A. Efficient one-pot synthesis and dehydrogenation of tricyclic dihydropyrimidines catalyzed by OMS-2-SO₃H, and application of the functional-chromophore products as colorimetric chemosensors. *RSC Adv.* 2021;11:12349-12360. doi:10.1039/d1ra01005k
201. Janusz G, Pawlik A, Świdarska-Burek U, et al. Laccase properties, physiological functions, and evolution. *Int J Mol Sci.* 2020;21:966. doi:10.3390/ijms21030966
202. Bruyneel F, Dive G, Marchand-Brynaert J. Non-symmetrically substituted phenoxazinones from laccase-mediated oxidative cross-coupling of aminophenols: An experimental and theoretical insight. *Org Biomol Chem.* 2012;10:1834-1846. doi:10.1039/c1ob05795b

203. Sousa AC, Oliveira MC, Martins LO, Robalo MP. Towards the rational biosynthesis of substituted phenazines and phenoxazinones by laccases. *Green Chem.* 2014;16:4127-4136. doi:10.1039/c4gc00901k
204. Sousa AC, Conceição Oliveira M, Martins LO, Robalo MP. A Sustainable Synthesis of Asymmetric Phenazines and Phenoxazinones Mediated by CotA-Laccase. *Adv Synth Catal.* 2018;360:575-583. doi:10.1002/adsc.201701228
205. Veitch NC. Horseradish peroxidase: A modern view of a classic enzyme. *Phytochemistry.* 2004;65:249-259. doi:10.1016/j.phytochem.2003.10.022
206. Kour H, Paul S, Singh PP, Gupta R. A mild and simple method for the synthesis of substituted phenazines. *Synlett.* 2014;25:495-500. doi:10.1055/s-0033-1340478
207. Mitra M, Kundu T, Kaur G, et al. Catecholase and phenoxazinone synthase activities of a ferromagnetically coupled tetranuclear Cu (II). *RSC Adv.* 2016;6:58831-58838. doi:10.1039/C6RA11433D
208. Yu L, Zhou X, Wu D, Xiang H. Synthesis of phenazines by Cu-catalyzed homocoupling of 2-halogen anilines in water. *J Organomet Chem.* 2012;705:75-78. doi:10.1016/j.jorganchem.2011.12.030
209. Giurg M, Piekalska K, Gebala M, et al. Catalytic Oxidative Cyclocondensation of o-Aminophenols to 2-Amino-3H-phenoxazin-3-ones. *Synth Commun.* 2007;37:1779-1789. doi:10.1080/00397910701316136
210. Gao L, Zhuang J, Nie L, et al. Intrinsic peroxidase-like activity of ferromagnetic nanoparticles. *Nat Nanotechnol.* 2007;2:577-583. doi:10.1038/nnano.2007.260
211. Khairy M, Mahmoud AH, Khalil KMS. Synthesis of highly crystalline LaFeO₃ nanospheres for phenoxazinone synthase mimicking activity. *RSC Adv.* 2021;11:17746-17754. doi:10.1039/d1ra02295d
212. Birkner N, Navrotsky A. Thermodynamics of manganese oxides: Sodium, potassium, and calcium birnessite and cryptomelane. *PNAS.* 2017;114(7):1046-1053. doi:10.1073/pnas.1620427114
213. Ferlin F, Marini A, Ascani N, Ackermann L, Lanari D, Vaccaro L. Heterogeneous Manganese-Catalyzed Oxidase C-H/C-O Cyclization to Access Pharmaceutically Active Compounds. *ChemCatChem.* 2020;12(2):449-454. doi:10.1002/cctc.201901659
214. Strappaveccia G, Ismalaj E, Petrucci C, et al. A biomass-derived safe medium to replace toxic dipolar solvents and access cleaner Heck coupling reactions. *Green Chem.* 2015;17:365-372. doi:10.1039/c4gc01677g
215. Ghosh K, Chattopadhyay S. Synthetic stratagem and structures of two heteroleptic cobalt(III) complexes acting as biomimetic catalysts: Role of co-ligands in catalytic activities. *Polyhedron.* 2019;170:495-507. doi:10.1016/j.poly.2019.05.062
216. Bakshi R, Kumar R, Mathur P. Bis-benzimidazole diamide iron (III) complexes as mimics of phenoxazinone synthase. *Catal Commun.* 2012;17:140-145. doi:10.1016/j.catcom.2011.10.017
217. Yadav A, Mathur P. p-Quinoneimine as an intermediate in the oxidative coupling of 2-amino-5-methylphenol to 4a,7-dimethyldihydro-2-aminophenoxazinone catalyzed by a monomeric copper (II) complex. *Catal Commun.* 2014;55:1-5. doi:10.1016/j.catcom.2014.06.001
218. Sang S, Lambert JD, Tian S, et al. Enzymatic synthesis of tea theaflavin derivatives and their anti-inflammatory and cytotoxic activities. *Bioorganic Med Chem.* 2004;12:459-467. doi:10.1016/j.bmc.2003.10.024
219. Touzeau F, Arrault A, Guillaumet G, et al. Synthesis and Biological Evaluation of New 2-(4, 5-Dihydro-1H-imidazol-2-yl)-3, 4-dihydro-2H-1, 4-benzoxazine Derivatives. *J Med Chem.* 2003;46:1962-1979. doi:10.1021/jm021050c
220. Gershon H, Clarke DD, Gershon M. Antifungal activity of halophenols and halonitrophenols. *Monatshefte für Chemie.* 1995;126:1161-1166. doi:10.1007/BF00811385
221. Hofmann LE, Mach L, Heinrich MR. Nitrogen Oxides and Nitric Acid Enable the Sustainable Hydroxylation and Nitrohydroxylation of Benzenes under Visible Light Irradiation. *J Org Chem.*

- 2018;83:431-436. doi:10.1021/acs.joc.7b02333
222. Zhang W, Zhang J, Ren S, Liu Y. Palladium-catalyzed aromatic C-H bond nitration using removable directing groups: Regiospecific synthesis of substituted o -nitrophenols from related phenols. *J Org Chem*. 2014;79:11508-11516. doi:10.1021/jo502145v
223. Jong L, NG R, Collins N. Lipoxygenase inhibitors. WO2021/195346. Published online 2021.
224. Clewley RG, Cross GG, Fischer A, Henderson GN. Formation of 4-Halo-4-nitrocyclohexa-2, 5-dienones on Nitration of p-Halophenols and p-Halophenyl Acetates. *Tetrahedron*. 1989;45(5):1299-1310.
225. Olea AF, Espinoza L, Sedan C, et al. Synthesis and in vitro growth inhibition of 2-allylphenol derivatives against *Phytophthora cinnamomi* rands. *Molecules*. 2019;24:4196. doi:10.3390/molecules24224196
226. Costales A, Mathur M, Ramurthy S, et al. 2-Amino-7-substituted benzoxazole analogs as potent RSK2 inhibitors. *Bioorganic Med Chem Lett*. 2014;24:1592-1596. doi:10.1016/j.bmcl.2014.01.058
227. Chan WN, Hadley MS, Harling JD, et al. Evaluation of a series of anticonvulsant 1,2,3,4-tetrahydroisoquinoliny-benzamides. *Bioorganic Med Chem*. 2000;8:2085-2094. doi:10.1016/S0968-0896(00)00149-8
228. Yang X, Shan G, Rao Y. Synthesis of 2-aminophenols and heterocycles by Ru-catalyzed C-H mono- and dihydroxylation. *Org Lett*. 2013;15(10):2334-2337. doi:10.1021/ol400437a
229. Janssen FJ, Baggelaar MP, Hummel JJA, et al. Comprehensive Analysis of Structure-Activity Relationships of α -Ketoheterocycles as sn-1-Diacylglycerol Lipase α Inhibitors. *J Med Chem*. 2015;58:9742-9753. doi:10.1021/acs.jmedchem.5b01627
230. Connelly S, Mortenson DE, Choi S, et al. Semi-quantitative models for identifying potent and selective transthyretin amyloidogenesis inhibitors. *Bioorg Med Chem Lett*. 2017;27:3441-3449. doi:10.1016/j.bmcl.2017.05.080
231. Kohara T, Tanaka H, Kimura K, Horiuchi H. Synthesis of Thieno [2,3-b][1,5]benzoxazepine Derivatives. *J Heterocycl Chem*. 2002;39:163. doi:https://doi.org/10.1002/jhet.5570390124
232. Boyer J, Arnoult E, Médebelle M, Guillemont J, Unge J, Jochmans D. Difluoromethylbenzoxazole pyrimidine thioether derivatives: A novel class of potent non-nucleoside HIV-1 reverse transcriptase inhibitors. *J Med Chem*. 2011;54:7974-7985. doi:10.1021/jm200766b
233. Rynearson KD, Charrette B, Gabriel C, et al. 2-Aminobenzoxazole ligands of the hepatitis C virus internal ribosome entry site. *Bioorganic Med Chem Lett*. 2014;24:3521-3525. doi:10.1016/j.bmcl.2014.05.088
234. Vasilikogiannaki E, Gryparis C, Kotzabasaki V, Lykakis IN, Stratakis M. Facile Reduction of Nitroarenes into Anilines and Nitroalkanes into Hydroxylamines via the Rapid Activation of Ammonia· Borane Complex by Supported Gold Nanoparticles. *Adv Synth Catal*. 2013;355(5):907-911. doi:10.1002/adsc.201200983
235. Mietke T, Cruchter T, Winterling E, Tripp M, Harms K, Meggers E. Suzuki Cross-Coupling for Post-Complexation Derivatization of Non-Racemic Bis-Cyclometalated Iridium(III) Complexes. *Chem Eur J*. 2017;23:12363-12371. doi:10.1002/chem.201701758
236. Li Y, Wang H, Jiang L, Sun F, Fu X, Duan C. Copper-catalyzed direct synthesis of di- and triphenylamines: A dramatic accelerating effect of 2-aminophenols. *European J Org Chem*. 2010;36:6967-6973. doi:10.1002/ejoc.201001113
237. Gupta AK, Rao GT, Singh KN. NiCl₂·6H₂O as recyclable heterogeneous catalyst for N-arylation of amines and NH-heterocycles under microwave exposure. *Tetrahedron Lett*. 2012;53:2218-2221. doi:10.1016/j.tetlet.2012.02.081
238. Ryu HJ, Yang SJ, Lee GH, Gong YD. Construction of Druglike 2-Amido Benzo[d]imidazole Analogues via Desulfurative Cyclization of Thiourea Intermediate Resin on Solid-Phase. *ACS Comb Sci*. 2018;20:282-291. doi:10.1021/acscombsci.8b00004
239. Vakalopoulos A, Hartung I, Follmann M, et al. Hydroxy-substituted imidazo[1,2-A]

- pyridinecarboxamides and their use. US2014128386A1. Published online 2014.
240. Juárez-Ornelas KA, Jiménez-Halla JOC, Kato T, Solorio-Alvarado CR, Maruoka K. Iodine(III)-Catalyzed Electrophilic Nitration of Phenols via Non-Brønsted Acidic NO₂⁺ Generation. *Org Lett*. 2019;21:1315-1319. doi:10.1021/acs.orglett.8b04141
241. Chen XL, Ai BR, Dong Y, Zhang XM, Wang JY. Hexafluoro-2-propanol-assisted quick and chemoselective nitro reduction using iron powder as catalyst under mild conditions. *Tetrahedron Lett*. 2017;58:3646-3649. doi:10.1016/j.tetlet.2017.08.009
242. DeGuzman RN, Shen YF, Neth EJ, et al. Synthesis and Characterization of Octahedral Molecular Sieves (OMS-2) Having the Hollandite Structure. *Chem Mater*. 1994;6:815-821. doi:10.1021/cm00042a019
243. Kühlbörn J, Konhäuser M, Groß J, Wich PR, Opatz T. Xylochemical Synthesis of Cytotoxic 2-Aminophenoxazinone-Type Natural Products Through Oxidative Cross Coupling. *ACS Sustain Chem Eng*. 2019;7:4414-4419. doi:10.1021/acssuschemeng.8b06353
244. Zhou J, Ma ZY, Shonhe C, Ji SH, Cai YR. TEMPO-catalyzed electrochemical dehydrogenative cyclocondensation of o-aminophenols: Synthesis of aminophenoxazinones as antiproliferative agents. *Green Chem*. 2021;23:8566-8570. doi:10.1039/d1gc02908h
245. Inui T, Nakahara K, Uchida M, et al. Oxidation of ethanol induced by simple polyphenols: Prooxidant property of polyphenols. *Bull Chem Soc Jpn*. 2004;77:1201-1207. doi:10.1246/bcsj.77.1201
246. Chen Y-H, Zhang Y-H, Zhang H-J, et al. Design, Synthesis, and Biological Evaluation of Isoquinoline-1,3,4-trione Derivatives as Potent Caspase-3 Inhibitors. *J Med Chem*. 2006;49:1613-1623. doi:10.1021/jm050896o
247. Kudelova J, Fleischmannova J, Adamova E, Matalova E. Pharmacological caspase inhibitors: Research towards therapeutic perspectives. *J Physiol Pharmacol*. 2015;66:473-382. doi:10.1177/1461444810365020
248. Yoshifuji S, Arakawa Y. Ruthenium Tetroxide Oxidation of 3,4-Dihydroisoquinolin-1(2H)-ones: An Efficient Synthesis of Isoquinoline-1,3,4(2H)-triones. *Chem Pharm Bull*. 1989;37 (12):3380-3381. doi:https://doi.org/10.1248/cpb.37.3380
249. Buu-Hoi NP, Saint-Ruf G, Bourgeade JC. Phthalonimides (1,3,4-Trioxo-1,2,3,4-tetrahydroisoquinolines) of Potential Biological Interest. *J Heterocycl Chem*. 1968;5:545-547. doi:https://doi.org/10.1002/jhet.5570050416
250. Mitchell G, Clarke ED, Ridley SM, Greenhow DT, Gillen KJ, Vohra SK. 1,3,4(2H)-Isoquinolinetrione Herbicides: Novel Redox Mediators of Photosystem I*. *Pestic Sci*. 1995;44:49-58. doi:10.1002/ps.2780440108
251. Di Mola A, Tedesco C, Massa A. Metal-Free Air Oxidation in a Convenient Cascade Approach for the Access to Isoquinoline-1,3,4(2H)-triones. *Molecules*. 2019;24:2177. doi:10.3390/molecules24112177
252. Zhu D, Luo WK, Yang L, Ma DY. Iodine-catalyzed oxidative multiple C-H bond functionalization of isoquinolines with methylarenes: An efficient synthesis of isoquinoline-1,3,4(2H)-triones. *Org Biomol Chem*. 2017;15:7112-7116. doi:10.1039/c7ob01539a
253. Tang J, Chen X, Zhao C, et al. Iodination/Amidation of the N-Alkyl (Iso)quinolinium Salts. *J Org Chem*. 2021;86:716-730. doi:https://doi.org/10.1021/acs.joc.0c02321
254. Martin L, Steurer S, Cockcroft X-L. New Pyridinones and Isoquinolinones as Inhibitors of the Bromodomain BRD9. WO 2016/139361 A1. Published online 2016.
255. Kaila N, Follows B, Leung L, et al. Discovery of isoquinolinone indole acetic acids as antagonists of chemoattractant receptor homologous molecule expressed on TH2 cells (CRTH2) for the treatment of allergic inflammatory diseases. *J Med Chem*. 2014;57:1299-1322. doi:10.1021/jm401509e
256. Shin S, Kim Y, Kim K, Hong S. A copper-mediated cross-coupling approach for the synthesis of 3-heteroaryl quinolone and related analogues. *Org Biomol Chem*. 2014;12:5719-5726.

- doi:10.1039/c4ob00939h
257. Fang Z, Wang Y, Wang Y. Synthesis of 4-Iodoisoquinolin-1(2H)-ones by a Dirhodium(II)-Catalyzed 1,4-Bisfunctionalization of Isoquinolinium Iodide Salts. *Org Lett.* 2019;21:434-438. doi:10.1021/acs.orglett.8b03614
258. Luo W, Shi X, Zhou W, Yang L. Iodine-Catalyzed Oxidative Functionalization of Azaarenes with Benzylic C(sp³)-H Bonds via N-Alkylation/Amidation Cascade: Two-Step Synthesis of Isoindolo[2,1-b]isoquinolin-7(5H)-one. *Org Lett.* 2016;18:2036-2039. doi:10.1021/acs.orglett.6b00646
259. Luo W-K, Xu C-L, Yang L. I₂/TBHP mediated multiple C-H bonds functionalization of azaarenes with methylarenes to synthesize iodoisoquinolinones via iodination/N-benylation/amidation sequence. *Tetrahedron Lett.* 2019;60:151328. doi:10.1016/j.tetlet.2019.151328
260. Blagg J, Coote SJ, Davies SG, Mobbs BE. Tetrahydroisoquinolines. Part 2. Synthesis of 4-Substituted N-Methyl-1,2,3,4-tetrahydroisoquinolines via Regio- and Stereo-selective Elaboration of Tricarbonyl(N-methyl-1,2,3,4-tetrahydroisoquinoline)chromium. *J Chem Soc Perkin Trans 1.* 1986;1:2257-2261. doi:https://doi.org/10.1039/P19860002257
261. Yang X, Sun R, Li S, et al. Regioselective Direct C-H Trifluoromethylation of Pyridine. *Org Lett.* 2020;22:7108-7112. doi:10.1021/acs.orglett.0c02413
262. Tamayo NA, Bo Y, Gore V, et al. Fused Piperidines as a Novel Class of Potent and Orally Available Transient Receptor Potential Melastatin Type 8 (TRPM8) Antagonists. *J Med Chem.* 2012;55:1593-1611. doi:10.1021/jm2013634
263. Xu JH, Zheng SC, Zhang JW, Liu XY, Tan B. Construction of Tropane Derivatives by the Organocatalytic Asymmetric Dearomatization of Isoquinolines. *Angew Chemie - Int Ed.* 2016;55:11834-11839. doi:10.1002/anie.201605736
264. Liu J, Wang SM, Qin HL. Light-induced [2+2] cycloadditions for the construction of cyclobutane-fused pyridinyl sulfonyl fluorides. *Org Biomol Chem.* 2020;18:4019-4023. doi:10.1039/d0ob00814a
265. D'Alterio MC, Yuan YC, Bruneau C, Talarico G, Gramage-Doria R, Poater A. Base-controlled product switch in the ruthenium-catalyzed protodecarbonylation of phthalimides: A mechanistic study. *Catal Sci Technol.* 2020;10:180-186. doi:10.1039/c9cy02047k
266. Ding G, Li C, Shen Y, Lu B, Zhang Z, Xie X. Potassium Hydroxide-Catalyzed Chemoselective Reduction of Cyclic Imides with Hydrosilanes: Synthesis of ω -Hydroxylactams and Lactams. *Adv Synth Catal.* 2016;358:1241-1250. doi:10.1002/adsc.201501093
267. Schöneboom JC, Groetsch S, Christl M, Engels B. Computational assessment of the electronic structure of 1-azacyclohexa-2,3,5-triene (3 δ 2-1H-pyridine) and its benzo derivative (3 δ 2-1H-quinoline) as well as generation and interception of 1-methyl-3 δ 2-1H-quinoline. *Chem Eur J.* 2003;9:4641-4649. doi:10.1002/chem.200305000